Politecnico di Milano

DEPARTMENT OF CHEMISTRY, MATERIALS AND CHEMICAL ENGINEERING
Ph.D. Industrial Chemistry and Chemical Engineering

Doctoral thesis

An interface-resolved methodology for the evaporation and combustion modeling of isolated fuel droplets

Candidate:
Abd Essamade Saufi

Advisor:
prof. Alberto Cuoci

Doctoral cycle XXXII, 2016-2020

Tra le molte virtù di Chuang-Tzu c'era l'abilità nel disegno. Il re gli chiese il disegno di un granchio. Chuang-Tzu disse che aveva bisogno di cinque anni di tempo e d'una villa con dodici servitori. Dopo cinque anni il disegno non era cominciato. "Ho bisogno di altri cinque anni" disse Chuang-Tzu. Il re glieli accordò. Allo scadere dei dieci anni, Chuang-Tzu prese il pennello e in un istante, con un solo gesto, disegnò un granchio, il più perfetto granchio che si fosse mai visto.

Chuang-Tzu, IV secolo a.C.

Contents

Abstract

Multiphase flows are extensively used for power generation (e.g. internal combustion engines, gas turbines, industrial burners), due to the high energy density of liquid fuels. The combustion of a liquid is generally carried out through an atomization process, transforming the liquid in a spray of droplets, followed by the fuel vaporization, ignition and gas-phase combustion. The improvement and control of a spray system is not only beneficial from an economical point of view, but it significantly impacts its efficiency in terms of pollutants emission.

The collective vaporization of the droplets ensemble directly influences the burning rate and the combustion chamber performance. The simplest and physically meaningful configuration we can extract from a spray system is represented by an *isolated droplet*: this allows to put aside the physical interaction phenomena typically involved in gas-liquid dispersed flows (breakups, coalescence, fragmentation etc.), obtaining an ideal system for the analysis of vaporization, ignition and combustion of liquid fuels. Isolated droplets are mainly studied assuming a spherical symmetry of the system in order to simplify the mathematical modeling and leave room for a more detailed chemistry description: this approach paved the way for the study of crucial aspects related to microgravity combustion, such as cool flames, multiple ignitions and extinction regimes. The main drawback is that external convection, internal circulation, interface deformations and other essential phenomena cannot be described, despite their fundamental role in droplet vaporization.

This work aims at addressing these issues, proposing and discussing a numerical model for the combustion of isolated droplets based on an *interface-resolved* approach, i.e. including momentum equations for the velocity field and the advection of the fluid interface, abandoning the sphero-symmetric hypothesis. The main novelty is the extension of the two-phase fluid dynamic core to include (i) heat and mass transfer rates based on the resolution of the boundary layer (without the use of semi-empirical correlations), (ii) a detailed treatment of thermodynamics at the interface, (iii) multicomponent fuels, (iv)

the phase-change process, (v) the gas-phase combustion and (vi) the thermal interaction with the suspending fiber. In addition, one of the main critical problems in the CFD modeling of evaporating droplets is the numerical treatment of surface tension, due to the persistent presence of an artificial velocity field (spurious currents) which destabilizes the interface. In this work this problem has been approached introducing (vii) a suspending force, directed towards the droplet center, which stabilizes the droplet against gravity and eliminates the spurious currents instabilities.
The resulting code is called `DropletSMOKE++` and it shows a very good agreement with the experiments in a wide range of operating conditions, both in natural and forced convection. The comparison with the microgravity condition highlights the impact of the external fluid flow on the evaporation mechanism, while non-ideal thermodynamics is shown to be fundamental to model high pressure systems and multicomponent droplets. The analysis of droplet combustion is reported in terms of standoff ratio, flame temperature, internal circulation and water condensation, exhibiting a satisfactory agreement with experiments in terms of diameter decay, temperature profiles and sensitivity to the gas-phase oxygen concentration. In particular, the multiregion approach is shown to be essential to describe the conjugate heat transfer between the solid fiber and the fluid phase, which enhances the burning rate and causes a partial quenching of the flame close to the wall.
Finally, the problem of spurious currents has been approached in a more rigorous way: `DropletSMOKE++` is extended to include a stable and accurate methodology for surface tension, based on a combination of the Ghost Fluid Method (GFM) and Height Functions (HF). The method is able to reduce spurious currents almost to machine accuracy and accurate results are obtained for additional cases such as translating droplets, capillary oscillations, rising bubbles, sessile droplets and suspended droplets.

Keywords: Droplet; Evaporation; Combustion; VOF; Convection; Fiber; Surface tension;

Sommario

I flussi multifase sono largamente utilizzati per la generazione di energia (motori a combustione interna, turbine a gas, bruciatori industriali), grazie alla loro elevata densità energetica. La combustione di un liquido è generalmente iniziata da un processo di atomizzazione, trasformando il liquido in uno spray, seguita dalla vaporizzazione del combustibile, l' ignizione e la combustione in fase gas. Il miglioramento e il controllo di un sistema spray non è solo vantaggioso dal punto di vista economico, ma impatta in modo significativo l'efficienza in termini di emissioni inquinanti. A causa dell'intrinseca complessità degli spray, le simulazioni numeriche giocano un ruolo fondamentale nello studio e ottimizzazione di questi sistemi, rivelando meccanismi e dettagli fisici spesso non visualizzabili sperimentalmente.

L'evaporazione collettiva di un insieme di goccioline influenza direttamente la velocità di conversione dell'energia e, in ultima analisi, le prestazioni della camera di combustione. La più semplice, ma fisicamente significativa configurazione estraibile da un sistema spray è rappresentata da una *goccia isolata*: questo permette di mettere da parte i fenomeni di interazione fisica tipici dei flussi bifase dispersi (breakup, coalescenze, frammentazioni etc.), ottenendo un sistema ideale per l'analisi dell'evaporazione, ignizione e combustione di combustibili liquidi. Le gocce isolate sono principalmente studiate assumendo una simmetria sferica del sistema, per semplificare la modellazione matematica, lasciando spazio ad un maggior dettaglio dal punto di vista chimico: questo approccio ha permesso di studiare in dettaglio fenomeni fondamentali della combustione in microgravità, come fiamme fredde, ignizioni multiple e regimi di estinzione. L'inconveniente principale è che la convezione, la circolazione interna, le deformazioni dell'interfaccia e altri importanti fenomeni non possono essere descritti, nonostante il loro ruolo fondamentale nell'evaporazione di gocce.

Questo lavoro di tesi mira ad affrontare questi problemi, con lo sviluppo di un modello di combustione di una gocciolina isolata basato su un approccio *interface-resolved*, cioè includendo nel modello la soluzione dei campi di velocità e il trasporto dell'interfaccia,

abbandonando l'ipotesi di simmetria sferica. La principale novità del lavoro è l'estensione di questo modello fluidodinamico bifase per includere (i) i fenomeni di scambio termico e materiale basati sulla soluzione dello strato limite (senza quindi l'utilizzo di correlazioni), (ii) una descrizione dettagliata della termodinamica all'interfaccia, (iii) combustibili multicomponente, (iv) il passaggio di fase, (v) la combustione in fase gas e (vi) l'interazione termica con la fibra. Il codice risultante è chiamato `DropletSMOKE++`, concepito per la modellazione dell'evaporazione e combustione di gocce di combustibile in regime di convezione esterna. `DropletSMOKE++` presenta un ottimo accordo con i dati sperimentali in un ampio spettro di condizioni operative, sia in convezione naturale che forzata. Il confronto con i dati in microgravità evidenzia l'impatto della convezione esterna sul meccanismo di evaporazione, mentre la non-idealità della termodinamica si è rivelata fondamentale per modellare sistemi ad alta pressione o gocce multicomponente. L'analisi della combustione è riportata in termini di diametro di fiamma, temperatura massima, circolazione interna e condensazione di acqua. L'accordo con i dati sperimentali è soddisfacente per quanto riguarda i profili temporali del diametro, della temperatura e della sensitività all'ossigeno in fase gas. In particolare, l'approccio multiregione è essenziale per descrivere lo scambio termico tra la fibra e il fluido bifase, il quale incrementa la velocità di combustione e causa il parziale spegnimento della fiamma vicino alla superficie solida.
Uno degli aspetti più critici nella modellazione CFD di gocce è la tensione superficiale, a causa della presenza di velocità artificiali (*spurious currents*) che destabilizzano l'interfaccia. `DropletSMOKE++` è esteso per includere una metodologia accurata per la tensione superficiale, ovvero una combinazione di Ghost Fluid Method (GFM) e Height Functions (HF). Il metodo è in grado di ridurre significativamente queste correnti, permettendo simulazioni numeriche stabili. Risultati accurati sono stati ottenuti per altri casi test, come gocce in movimento uniforme, oscillazioni capillari, bolle immerse in un liquido e gocce sospese.

Parole chiave: Goccia; Evaporazione; Combustione; VOF; Convezione; Fibra; Tensione superficiale;

Preface

The objective of this thesis work is the numerical modeling of the evaporation and combustion of small fuel droplets in convective conditions. The thesis is structured in *three parts*:

1. An introduction, containing the main concepts, methods and an updated state of the art of the numerical simulation of multiphase flows, with a particular emphasis on the application to isolated droplets, as well as the main motivations for the present work;

2. A collection of four papers, in which the work is presented and discussed in detail. The papers are well connected and they are reported following a logical order of increasing complexity of the work:

   - **Paper 1.** A. Saufi, A. Frassoldati, T. Faravelli, A. Cuoci *DropletSMOKE++: a comprehensive multiphase CFD framework for the evaporation of multidimensional fuel droplets* International Journal of Heat and Mass Transfer, 131 (2019), pp. 836-853
   - **Paper 2.** A. Saufi, R. Calabria, F. Chiariello, A. Frassoldati, A. Cuoci , T. Faravelli, P. Massoli *An experimental and CFD modeling study of suspended droplets evaporation in buoyancy driven convection* Chemical Engineering Journal, 375 (2019), 122006
   - **Paper 3.** A. Saufi, A. Frassoldati, T. Faravelli, A. Cuoci *Direct numerical simulation of the combustion of a suspended droplet in normal gravity* Combustion and Flame (submitted)
   - **Paper 4.** A. Saufi, O. Desjardins, A. Cuoci *An accurate methodology for surface tension modeling in OpenFOAM®* International Journal of Multiphase Flow (submitted)

3. A conclusion, where the main achievements of the thesis are summarized and used to define possible outlooks and propose additional analyses to further advance the work.

Contribution of the authors

The advisor of this thesis is prof. Alberto Cuoci from Politecnico di Milano.
This is a numerical work, based on the development and application of a multiphase CFD code. In particular:

- The code has been entirely developed by Abd Essamade Saufi (AES) over the course of the PhD program at Politecnico di Milano and at Cornell University. All the numerical simulations and numerical analyses have been carried out by AES, as well as the writing of all the papers;
- The experimental work for Paper 2 have been carried out at Istituto Motori in Naples, by Raffaella Calabria, Fabio Chiariello and Patrizio Massoli;
- Feedbacks on papers and on potential directions of the work have been provided by profs. Alessio Frassoldati, Tiziano Faravelli, Alberto Cuoci (from Politecnico di Milano), Perrine Pepiot and Olivier Desjardins (from Cornell University).

Conferences

Part of this thesis work has been presented at the following conferences:

- Poster presentation: *A CFD framework for the evaporation of fuel droplets in a gravity field,* 41st meeting of the Italian Section of the Combustion Institute, Sorrento, Italy (2018);
- Poster presentation: *DropletSMOKE++: a multiphase CFD framework for the evaporation of multidimensional fuel droplets*, International Symposium on Combustion, Dublin, Ireland (2018)
- Oral presentation: *Evaporation of multicomponent fuel droplets in buoyancy driven convection*, International Conference on Smart Energy Carriers, Napoli, Italy (2019)
- Oral presentation: *The role of preferential vaporization in Fast Pyrolysis Bio Oil (FPBO) droplets evaporation*, 42nd meeting of the Italian Section of the Combustion Institute, Ravenna, Italy (2019)

Part I

Introduction

Chapter 1

Multiphase flows

A multiphase flow is characterized by the presence of two or more thermodynamic phases which coexist simultaneously. The most general classification includes (i) liquid-liquid flows, (ii) gas-liquid flows and (iii) fluid-solid flows. These systems can be characterized by the presence of a sharp interface which separates two continuous phases, defining a *separated* flow, or by a dispersion of finite elements (bubbles, droplets or solid particles) in a continuous fluid phase, defining a *dispersed flow*.

1.1 Examples of multiphase flows

Having this in mind, it is clear that our encounters with multiphase systems are very frequent:

- In Nature, an impressive number of phenomena are related to multiphase flows: formation and motion of clouds, atmospheric precipitation (e.g. rain, snow), ocean waves, waterfalls, geysers, volcanic eruptions, sandstorms, soil erosion etc. A comprehensive knowledge of these phenomena finds an immediate practical application in weather forecasting, with all the consequent implications in terms of protection of life and property, rational agricultural planning, safety of air and marine traffic. The entrainment of spume droplets over the ocean has a strong effect on the species mass transfer between the atmosphere and the water and has a direct influence on climate change dynamics;

- From a technological perspective, a very large number of modern industrial applications involve the use of multiphase flows: gas-liquid systems are ubiquitous in modern engineering processes including chemical and nuclear reactors, phase sep-

arators, distillation columns and heat transfer systems (condensers, evaporators, cooling towers). Gas-liquid systems are often preferable as dispersed flows, due to the large surface area per unit volume, in the form of *sprays* (medicine coating, painting, irrigation devices and pesticides for agriculture) and *bubbly flows* (absorbers, boiling heat transfer systems). Fluid-solid configurations are also widely represented: fluidized beds for catalytic processes, dust collectors and spray dryers constitute important unit operations in chemical engineering. It is estimated that more than a half of the products of a modern industrial society depend on a multiphase process [1]. The revenues of these industries are of the order of tens of billions of dollars and it is clear that even a small optimization in the design of these systems can lead to immense economical savings;

- A significant portion of the current energy demand is satisfied by the combustion of a liquid fuel (in the form of a spray). Internal combustion engines, gas turbines, industrial burners are extensively used for power generation, transportation and aerospace applications. The improvement and the control of these systems is not only beneficial from an economical point of view, but it can significantly impact their efficiency in terms of pollutants emission (soot, unburned hydrocarbons, NO_x and CO) with positive feedbacks on human health.

This work deals with gas-liquid multiphase flows. In order to illustrate in a general manner the typical physical phenomena occurring in a gas-liquid multiphase flow, it is interesting to briefly analyze a specific example with a minimum level of detail.

1.1.1 The combustion of a spray

A burning spray is one of the most interesting systems to analyze within a gas-liquid flow context. It gives a very complete overview on the main physical phenomena exhibited by multiphase systems, which are also in common with other configurations. The most important process is the *atomization* of the fuel. Smaller droplets are necessary to increase the specific surface area of the fuel and help to increase the overall evaporation rate and improve the efficiency of the combustion system. The atomization of a liquid jet involves the breakup of the macroscale liquid structure into a large number of small droplets by using a co-flowing air stream at high velocity. Alternatively, only the liquid phase can be injected at high pressure. The physical mechanism is extremely complicated and many theories have been proposed. In general, we can identify some fundamental steps:

- Spray formation is generally initiated by a shear instability of the jet which pro-

duces interfacial ondulations. The Kevin-Helmotz theory was originally used to investigate the surface stability of a cylindrical liquid jet subjected to perturbations using a first-order linear theory [2]. The amplitude of this ondulations increases and destabilizes the interface, forming ligaments and sheets. This is called *primary breakup*;

- These fragments are further stretched and broken into droplets mainly by capillary instability. This is called *secondary breakup*, which typically occurs farther from the nozzle;
- In addition, the coalescence mechanism partially aggregates the liquid structures affecting the droplet size distribution and the atomization rate. Cavitation phenomena are also expected if the pressure variations ahead of the nozzle are large, providing the nucleation and growth of bubbles in the liquid structures.

The atomization process always generates a turbulent flow and a significant research effort is devoted to understand the contribution of turbulence effect in the in the breakup of the liquid jet, both concerning primary and secondary atomization.
Sprays are widely used for energy conversion purposes. At high temperatures, the liquid evaporates from the surface, generating a Stefan flow which modifies the local flow and influences the motion of the surrounding droplets. Vaporization is of primary importance since it is often the controlling phenomena for spray combustion, because of the larger time scale with respect to mixing or chemical reactions. A very uniform droplet size distribution is desirable for the improvement of the vaporization efficiency and the rate of energy production. The fuel vapors can then ignite and undergo a combustion process, forming additional species and pollutants and creating large spatial temperature and concentration gradients. If the droplets are small enough, it is reasonable to assume the reactive step as a pure gas-phase process. However, liquid-phase reactions might occur, especially if heavy fuels are adopted or a non-uniform droplet size distribution is obtained from the atomization.

From this brief description it is immediate to understand that multiphase flows are inherently *complex*. First of all, the complexity arises from the single phenomena involved, summarized in Table 1.1. The description of the physical mechanism of each isolated phenomenon is already a challenging task and some remain not fully understood even after years of study from the scientific community. Furthermore:

- The phenomena are *strongly coupled*: the fluid dynamics and the interaction among

Fluid dynamics	interfacial instabilities, surface tension effects, shape distortion, gas-liquid boundary layers, internal circulation, turbulence.
Structures interactions	breakup, coalescence, collisions, capillary instability, shattering, fragmentation.
Thermodynamics	evaporation, condensation, multiphase heat transfer, radiation, cavitation, nucleation, bubbles growth.
Chemistry	gas-phase combustion, liquid-phase chemistry.

Table 1.1: Summary of the main physical and chemical phenomena occurring in a combustion of a spray.

the liquid structures influence each other. The evaporation process modifies the flow field (Stefan flow), together with the temperature and density gradients induced by the combustion process. On the other hand, the phase-change and the reactive processes directly depend on the local fluid dynamics through the development of boundary layers at the interface;

- There is a very wide range of *spatial scales* to be considered. The typical droplet sizes span from few tens to few hundreds micrometers. This means that the analysis of the internal flow and of the gas-phase boundary layers would require at least a submicrometer scale, whereas typical combustion chambers can be of the orders of meters (i.e. a disparity up to 5-6 orders of magnitude). The same is valid for the temporal scales, where very fast processes (e.g. due to very fast chemistry of some radical species) have to be integrated for a long time in order to obtain significant statistical quantities on complex flows. In the presence of a turbulent flow (most common situation) the disparity in the magnitudes of the scales increases even more.

This complexity does not allow to to approach multiphase problems with analytical methods. While this can be done for extremely simplified flows (at the limit of zero or infinite Reynolds numbers), the simple coupling between two phenomena or the study of intermediate Reynolds number regimes makes the use of analytical methods not possible. Even when it is possible, the numerous hypothesis and simplifications required make the final results not particularly interesting for practical applications. On the other hand, the experimental work, though of primary importance, suffers from non-trivial issues when dealing with multiphase flows. The smallest scales associated with atomization processes

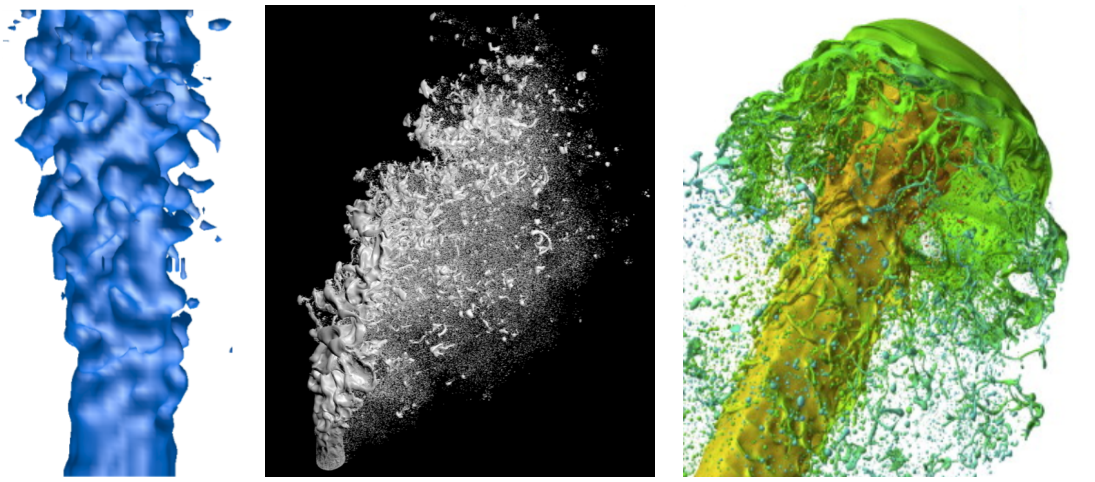

(a) (b) (c)

Figure 1.1: Turbulent atomization of a liquid jet. Pictures from Bianchi [4] et al. (a), Owkes et al. [5] (b) and Shinjo et al. [6] (c).

make accurate measurements very difficult and some phenomena occur at time scales which are just impossible to visualize experimentally. Even with modern laser diagnostic the optical access to the whole flow remains limited: for instance, primary atomization takes place in a region where the spray is very dense (the liquid volume fraction is $\sim$1) and the liquid surface topology is very complex. Therefore, it is very difficult to get experimental results to characterize this region [3].

The immediate conclusion is that the improvement and optimization of spray combustion systems can not be achieved solely adopting an empirical engineering approach, at least working within reasonable time scales at an acceptable economical cost. The physics is too complex and too many different variables have to be taken into account to make a reliable prediction of the overall effect of each single modification.

1.2 Numerical simulations

In this context, numerical simulations are a fundamental tool for the analysis of multiphase flows. Numerical simulations provide a very detailed (virtual) visualization of the process in time and space and allow to get an insight into the physical mechanism of the resolved phenomena. The sensitivity at different physical parameters can be easily investigated in cases in which it is not possible in any other way (e.g. the effect of gravity,

surface tension). The mathematical models, whatever their complexity, are always based on universal conservation laws (mass, energy and momentum) which makes them totally general. We can go one step further and claim that, on principle, a full Direct Numerical Simulation (DNS[1]) of a multiphase flow can replace a real experiment, at much lower costs and in a totally reproducible manner. In practice, a DNS is not performed when a complex systems is investigated: first of all the numerical resolution of all the spatial and temporal scales is strongly limited by the computational power available. Second, for many applications the detailed knowledge of the flow field or the exact position of every interface in a dispersed flow is often not necessary, whereas some sort of averaging of the main physical quantities would have a more practical utility. Hence, the numerical modeling of complex flows (e.g. burning sprays, fluidized beds, turbulent systems) is mainly based on reduced mathematical descriptions (e.g. LES) and this will probably remain the standard approach in the foreseeable future [7]. However:

- In the last years the available computational power has increased very rapidly. Full three-dimensional simulations of dispersed flows are becoming more affordable with the development of massively-parallel supercomputers and advanced algorithms [8]. In 2004 Bianchi et al. [4] modeled an atomization process using ~ 6 million cells (Figure 1.1 a), while the more recent simulations from Owkes and Desjardins [5] and Shinjo [6] used respectively 2 and 6 *billion* cells to simulate the turbulent atomization of a liquid jet: an impressive improvement within ten years. The addition of more complex physics (e.g. heat transfer, phase change, combustion) to the fluid-dynamic core is still out of our reach, but significant progresses in the field are, probably, just a matter of time;

- Reduced models for practical applications can benefit from the numerical analysis of simpler systems, for which a DNS can be feasible at reasonable costs. For instance, sprays are commonly treated as a collection of zero-dimensional points tracked in a Lagrangian way. The coupling between the turbulent flow and the material particles requires accurate subgrid scale (SGS) models for (i) the turbulent modeling, (ii) the droplet source terms (e.g. heat and mass fluxes) and (iii) the particle-flow interaction (e.g. drag force). These closure models need to be developed and validated based on the DNS results of simpler configurations, such as droplet arrays or single droplets. A relevant example is the work of Helenbrook and

[1] In this work DNS is meant as the Direct Numerical Resolution of the governing equations, adopting computational grids fine enough to resolve the smallest space and time scales. This does not necessarily involve the presence of a turbulent flow (as usually implied when dealing with DNS), but only the absence of sub-grid scale models.

Edwards [9]: adopting a moving mesh technique within an hybrid finite element-spectral methodology, they simulated over 3000 cases of axisymmetric droplets in a uniform gas stream. They observed different steady-state droplet shapes (prolate, oblate and dimpled) and they identified the fluid-dynamic conditions that caused them. Finally, they could recover accurate correlations for the drag on the droplet, including the effects of internal circulation and interface deformation. The DNS of reduced configurations helped them analyzing the individual phenomena involved and to build physics-based reduced models to be applied in real systems.

1.3 From sprays to droplets

Concerning the importance of sprays for energy generation purposes, it is evident that the collective vaporization of the droplets ensemble has a direct influence on the overall burning rate, on pollutants emission and, ultimately, on the combustion chamber performance. In this sense, the simplest and physically meaningful configuration we can imagine is the vaporization and combustion of an *isolated droplet*. The study of a single fuel droplet is scientifically interesting from many points of view: (i) it allows to focus on the phase-change and reactive processes, decoupling these phenomena from the interactions typically involved in a spray such as breakups, coalescence and fragmentation; (ii) it provides a basis for refining the current understanding of vaporization, ignition and extinction processes and allows to quantitatively assess the capability to predict these phenomena; (iii) it serves as a simplified system to investigate the sensitivity of the different parameters included in the model. A common example is the development of detailed kinetic mechanisms for combustion chemistry: typically, ideal system are used to investigate the quality and the effect of the kinetic schemes (like ideal reactors, 1D flames or 2D laminar flames), even though real combustion systems are much more complex and usually operate in a turbulent regime. In the same way, it is clear that real spray combustion systems cannot be described as the sum of isolated droplets which burn individually. The typical droplet sizes generated by a spray atomizer are two orders of magnitude smaller than those used in isolated droplet experiments (between 10 and 100 μm), and they are usually completely vaporized before the gas-phase ignition. The kinetics entirely governs the ignition of the spray. Conversely, due to the relatively large droplets considered in this work (~ 1 mm), the evaporation process is *always* the limiting step.

In fact, an isolated droplet must be thought as an *ideal system* in which the physico-chemical interaction of individual phenomena can be studied and parametric analyses on

the different variables can be carried out, e.g. (i) the interaction between diffusion and chemistry (ii) the effect of buoyancy on evaporation (iii) the role of radiative heat transfer (iv) the effect of the fuel type on the ignition properties etc., are typical examples, which cannot be studied in real spray systems.

It is clear, however, that the first step is the development and validation of computational models for isolated droplets. Hence, the need of high quality experimental data at different operating conditions and accurate mathematical models (and numerical methodologies) able to describe of the physico-chemical phenomena involved.

Chapter 2

Isolated droplets (I)

Sphero-symmetric models

The vaporization and combustion of isolated droplets have been studied for nearly 70 years from an experimental, theoretical and numerical perspective. Nevertheless, the problem is far from being completely understood and several aspects are still unclear. The improvement of the experimental devices, together with new computational models, allowed scientists to clarify important phenomena, but continuously shed light on new ones previously unknown. This chapter is an attempt to reflect this dynamics, providing a brief overview of the main models for isolated droplets.

2.1 A brief history

In this section the numerical modeling of isolated droplets is presented adopting the fundamental assumption of *spherical symmetry* of the system. Some notes on the experimental works are given as well.

The classical theory

The systematic study of isolated droplets started in the early '50s with the works of Spalding [10] and Godsave [11], elucidating the main mechanism of droplet vaporization at low and high temperatures. The first experimental works consisted in suspending a fuel droplet on a silica filament, following its consumption both for pure evaporation and combustion processes. The mathematical model was based on a sphero-symmetric droplet vaporizing in an unbounded atmosphere, summarized in Table 2.1, which allowed a 1D description along the radial coordinate. Initial attempts to solve the equations were

	Equation (for $j = l, g$)
Mass	$\frac{\partial \rho_j}{\partial t} + \frac{1}{r^2}\frac{\partial}{\partial r}\left(r^2 \rho_j v_j\right) = 0; \qquad \bar{\rho}_l \frac{dR}{dt} + \frac{R}{3}\frac{d\bar{\rho}_l}{dt} = -\dot{m}$
Energy	$\rho_g C_{p,j}\left(\frac{\partial T_j}{\partial t} + v_j \frac{\partial T_j}{\partial r}\right) = \frac{1}{r^2}\frac{\partial}{\partial r}\left(r^2 k_j \frac{\partial T_j}{\partial r}\right)$
Species	$\rho_j\left(\frac{\partial \omega_{i,j}}{\partial t} + v_j \frac{\partial \omega_{i,j}}{\partial r}\right) = \frac{1}{r^2}\frac{\partial}{\partial r}\left(r^2 \rho_j \mathcal{D}_{i,j} \frac{\partial \omega_{i,j}}{\partial r}\right)$

Table 2.1: Equations for the modeling of the vaporization of a spherically symmetric droplet, solving for density ρ, droplet radius R, temperature T and species mass fraction ω in both gas (g) and liquid (l) phases. $\dot{m}$ is the vaporization rate. This model must be coupled with boundary conditions which describe the conservation of the material and heat fluxes at the interface. Pressure is constant.

analytical, assuming that:

- There is no relative motion between the phases;
- The liquid temperature remains constant and equal to the boiling temperature;
- The initial unsteady period is much faster than the total droplet lifetime.

On these hypotheses relies the *classical theory* of droplet vaporization, extensively reviewed by several works, including Kuo [12], Williams [13] and Faeth [14]. The so called "D^2 law" was introduced, stating that the square of the droplet diameter decreases linearly with time during the vaporization process:

$$\frac{dD^2}{dt} = -k \tag{2.1}$$

Relaxations of these hypotheses were the main objective of the subsequent works. An excellent paper by Williams [15] identifies the weak points of the theory and its failure in predicting essential features in droplet vaporization. Experiments were often not in agreement with the theoretical prediction, since the influence of natural convection on the burning process was too severe to be neglected, making a direct comparison scientifically meaningless. Two approaches were followed in parallel:

- Experimentally, it made more sense to observe the combustion of droplets in a field with little or no gravitational acceleration, in order to provide a process that corresponds to that of a spherically symmetric combustion model. Kumagai [16] was the first to adopt free-falling chambers, in which buoyancy effects were greatly reduced. This condition (called *microgravity*) was then used by the same authors [17, 18, 19] providing useful experimental data for model comparison;

- The agreement with theoretical models was slightly improved, but yet not satisfactory. The results from Okajima's system clearly showed the presence of unsteady effects, either due to the gas-phase transport or to the transient liquid heating, while the classical theory did not include these effects. Hence, the need of a pushing the research also on the modeling side, in order to include the additional physics needed to describe the heat transfer unsteadiness and the external convection.

Heat transfer, internal and external convection

Once reached the capability to numerically solve the Equations in Table 2.1, more complex analyses were possible. The unsteady droplet heating was originally investigated by Law [20, 21]: he described how the heat flux to the surface is partially used to vaporize the fuel, while the remaining part increases the liquid temperature. The droplet vaporizes faster, slowing the increase of the surface temperature, reaching a situation in which the incoming heat flux is entirely used to vaporize the liquid. The droplet temperature stabilizes at a constant value called the "wet bulb temperature". Law showed that the combustion characteristics (i.e. burning rate, flame position) are greatly affected by these transient thermal effects and that droplet heating should be included in any attempt to investigate the burning behavior of an initially cold droplet [22].
The first approach was to consider thermal conduction as the only heat transfer mechanism in the liquid phase (*conduction limit model*). However, numerous experimental works showed that the time needed to reach a steady-state burning rate was systematically over-predicted by theoretical analyses, suggesting that the internal heat transfer should have been much faster than what could be provided by conduction alone [20]. El Wakil [23, 24] was among the firsts to introduce the idea of an intense convection inside the liquid phase, considering the internal transport occurring at infinite rate and a uniform liquid temperature distribution (*rapid mixing model*). It was clear, however, that the real condition was bounded between the two extremes and significant results were reached later with the works of Winnikow [25] and Harper [26]: assuming an inviscid flow, it was shown the internal motion to be similar to a Hill's spherical vortex [27] caused by the continuity of tangential velocity at the droplet surface. This was called *vortex model*, successfully adopted by Sirignano [28, 29] to modify the energy equation and investigate the effect of the internal circulation on the droplet heating.

The internal motion is due to the surface shear stress induced by the gas-phase, hence it necessarily implies the presence of some form of convection in the gas-phase

(either natural or forced). External convection develops a thin boundary layer at the interface, modifying the heat and mass transfer mechanisms and inducing a drag force on the droplet. The Equations in Table 2.1 are not valid anymore, since the spherical symmetry is lost. Due to the difficulty of solving the fluid flow and, more importantly, the gas-phase boundary layer, most of the approaches to include external convection in a the model relied on empirical correlations. The Ranz-Marshall correlation was one of the first proposed, based on wetted-spheres experiment [30]:

$$Nu = 2 + 0.552 Re^{1/2} Pr^{1/3} \tag{2.2}$$

$$Sh = 2 + 0.552 Re^{1/2} Sc^{1/3} \tag{2.3}$$

in which the Nusselt and Sherwood numbers from the classical vaporization theory (Nu, Sh=2) are corrected to account for the external fluid dynamics (through the Reynolds number), and the gas-phase properties (through the Prandtl and Schmidt numbers). However, serious flaws characterize these correlations: they do not account for transient heating, internal circulation and the dynamics of the regressing interface. Another strict limitation is the hypothesis of small evaporation fluxes. The large density variation due to the phase-change process induces a radial convective flux (*Stefan flow*), which is dominant when the vaporization flux is high (e.g. in combustion cases). This radial flow leads to a significant thickening of the gas-phase boundary layer, slowing the droplet heating and decreasing the drag coefficient on the droplet [31, 32]. Several corrections have been proposed over time for specific cases, at the price of a lack of generality. In this context, the most rigorous methodology for droplet convective evaporation was reached by Abramzon and Sirignano [33, 34]. It provides numerous correlations for the heat and mass transfer rates, including external convection, approximate models for internal circulation and the effect of the Stefan flow and it is nowadays one of the most used to formulate source terms for spray calculations.

ISS experiments and combustion chemistry

The study of gas-phase chemistry has always been one of the main challenges in droplet science: (i) combustion chemistry is characterized by several reactions (thousands) and for each one the reaction rate in function of temperature and species concentrations is needed; (ii) source terms have to be added to the energy and species equations (Table 2.1) in order to describe the generation/consumption of species and the heat re-

(a) (b) (c)

Figure 2.1: n-Heptane droplet combustion experiment in microgravity conditions, from the Flame Extinguishment Experiments (FLEX) project: 0.1 s before ignition (a), 0.12 s after ignition (b) and 2.3 s after ignition (c). Pictures from Dietrich et al. [35].

lease/absorption due to the reactions; (iii) this makes the direct resolution of the Equations extremely difficult, since the reactions rates dependence on temperature and species concentration is highly non-linear. Originally, a *flame-sheet combustion* regime was assumed to simplify the problem, in which the chemistry is frozen everywhere except at the infinitesimally-thin region where a single-step irreversible combustion reaction occurs at infinite rate [14, 15]. A diffusion flame is established, in which fuel and oxidizer diffuse towards the flame front where their concentration is zero due to the fast reaction. However, in some regions the characteristic times of diffusion and reaction can be similar and finite-rate chemistry effects were already evident from experiments [36]. Moreover, it was clear that certain features of droplet combustion could only be described accounting for a finite kinetics (e.g. ignition, NO_x formation).

In the early nineties, innovative experiments started to be conducted aboard the International Space Station (ISS) for the study of evaporation and multi-stage combustion phenomena in microgravity conditions [37, 35]. As reported in the comprehensive review by Ronney on microgravity combustion [38], the absence of gravity eliminates buoyancy and allows to focus on physical aspects such as differential species diffusion, radiation effects and combustion kinetics. This enabled the measurement of droplet and flame histories over an unprecedented range of conditions, shedding light on phenomena such as radiative and diffusive extinctions, flame oscillations and quasi-steady combustion sustained by cool flames (Figure 2.1). These experiments have provided a wealth of new data for improving the understanding of droplet combustion and offered important measurements to be compared with computational models. Indeed, significant results were reached when the growing available computational power and the rapid development of

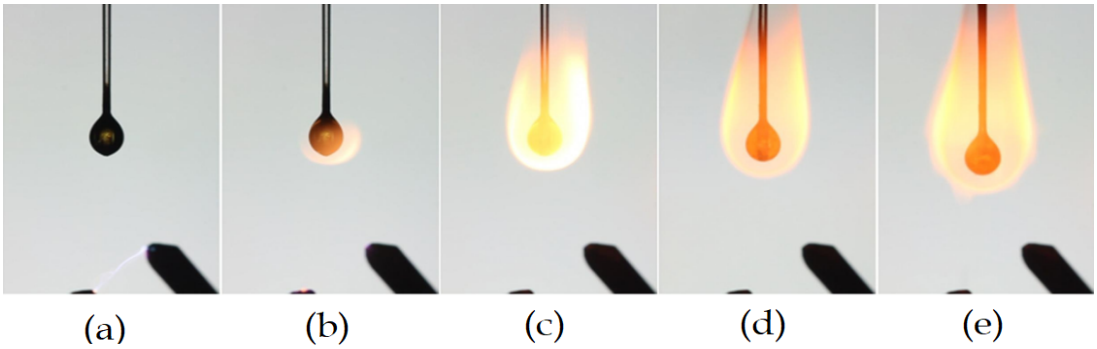

Figure 2.2: Fuel droplet combustion experiment in normal gravity conditions, from Sankaranarayanan et al. [48].

detailed kinetic mechanisms allowed to include a complex chemistry within numerical models. The initial modeling works by Cho and Dryer [39, 40], followed by Marchese [41, 42], were directed to the detailed 1D modeling of spherical fuel droplets (methanol, heptane, hexadecane) in microgravity, including up to tens of species and hundreds of reactions. Cuoci et al. [43] were one of the firsts to include a detailed kinetic mechanism (∼200 species, ∼5000 reactions) to investigate the low-temperature chemistry effects in n-alkane droplets, focusing on ignition delay times, extinction diameters and defining oxidation regions. The work was intensively carried out by other authors in the following years [44, 45, 46], also further extending the kinetics including soot formation and thermophoresis [47]. The coupling of detailed kinetic mechanisms and 1D models for microgravity droplets significantly advanced the field, defining the role of low-temperature chemistry, the formation of oxidized species and the effect of pressure on the chemical behavior, reaching results that were unthinkable just ten years before.

Current works

Nowadays, the research on droplets is still active: new diagnostic devices allow to analyze the thermal field and pollutants (e.g. soot) formation and distribution with an unprecedented level of detail [49]. Most of the experiments are performed under gravity, since experimental devices are much cheaper and the operating conditions are closer to the real ones where droplets are commonly adopted (Figure 2.2). The most recent works (2000s) mainly focus on defining the role of the supporting fiber [50, 51] and the investigation of complex mixtures combustion [52, 53], with a particular attention towards alternative fuels (e.g. bio-oil, heavy fuel oils). In these systems liquid-phase reactions can occur, as it is evident from the combustion residues after the droplet consumption

	Equation (for $j = l, g$)
Mass	$\frac{\partial \rho_j}{\partial t} + \nabla \cdot (\rho_j \mathbf{v}_j) = 0; \qquad \frac{\partial}{\partial t} \int_{V_L} \rho_L dV_L = -\dot{m}$
Energy	$\rho_j C_{p,j} \left(\frac{\partial T_j}{\partial t} + \mathbf{v}_j \nabla T_j \right) = \nabla \cdot (k_j \nabla T_j)$
Species	$\rho_j \left(\frac{\partial \omega_{i,j}}{\partial t} + \mathbf{v}_j \nabla \omega_{i,j} \right) = \nabla \cdot (\rho_j \mathcal{D}_{i,j} \nabla \omega_{i,j})$
Momentum	$\frac{\partial (\rho_j \mathbf{v}_j)}{\partial t} + \nabla \cdot (\rho_j \mathbf{v}_j \otimes \mathbf{v}_j) = \nabla \cdot \mu_j \left(\nabla \mathbf{v}_j + \nabla \mathbf{v}_j^T \right) + \left(\frac{2}{3} \mu_i - \zeta_i \right) (\nabla \cdot \mathbf{v}) \underline{\underline{\mathbf{I}}} - \nabla p + \rho_j \mathbf{g}$

Table 2.2: Equations for the modeling of the vaporization of a generic liquid volume V_L, solving for density ρ, droplet total mass, temperature T, species mass fraction ω and velocity $\mathbf{v}$ in both gas (g) and liquid (l) phases. $\dot{m}$ is the vaporization rate. This model must be coupled with boundary conditions which describe the conservation of the material and heat fluxes at the interface. See Appendix A for more details.

and the formation of cenospheres. The physical behind these phenomena is still largely unknown and deserves proper analyses.

2.2 Towards interface-resolved simulations

When looking at more complex configurations (e.g. strongly deformed interfaces, suspended droplets, high relative gas velocity), the aforementioned models do not maintain their validity. The assumption of spherical symmetry is the main *limiting factor*, from different points of view:

- External convection and additional forces (e.g. gravity) cannot be included in the numerical modeling, even though they have a significant impact in determining the heat and mass transfer phenomena;
- The phase-boundary is assumed spherical throughout the droplet lifetime and its motion is limited to the regression due to the vaporization. However, external convection and forces (e.g. gravity, surface tension) can modify the interface shape, which should be generally considered as a deformable surface;
- In convective conditions, the calculation of the heat and mass transfer rates must be based on semi-empirical correlations. The capability to solve the fluid flow and the physics at the boundary layer, especially for laminar flows, would make the vaporization model totally general and equally applicable to a wide range of operating conditions, including transition regimes;

- The internal circulation cannot be modeled, even though it is known to be a crucial factor. It enhances the liquid heat transfer, but for multicomponent fuels (commonly used for energy generation) the effect is much more interesting because it directly affects the preferential vaporization of the species [54];
- The thermal effect of the suspending fiber cannot be included in the model. Many recent studies have as a main objective the optimization of the tethering system (e.g. to minimize the interference with the droplet vaporization) and numerical simulations can represent a fundamental support for these analyses.

The only way to address these issues is to abandon the spherical symmetry assumption and move towards a CFD approach, in particular: (i) the model in Table 2.1 must be extended to a three-dimensional system (Table 2.2), (ii) Navier-Stokes equations must be solved to provide the velocity fields in both phases and (iii) the position of the interface must be found as a function of the fluid flow.

Chapter 3

Isolated droplets (II)

Interface-resolved models

In this section we focus on *interface resolved simulation*, in which the position of the phase-boundary is generally unknown and has to be found as part of the numerical solution. This is fundamental if we want to actually solve (and not only model) the fluid-dynamic interaction between the fluid flow and the droplet, as well as the heat and mass transfer phenomena involved. The main methods for the interface advection, surface tension calculation and the implementation of heat and mass transfer phenomena are described, with an emphasis on the application to isolated droplets.

3.1 Advection of a fluid interface

The numerical methodologies for interface advection can be divided in two main categories: *interface tracking* and *interface capturing* methods. Both methods rely on a fixed Eulerian grid to solve the governing equations, using a single set of equations for both the phases. This is called *one-fluid formulation*, in which interfacial effects (e.g. surface tension, surface heat fluxes) are described by a singular distribution (i.e. Dirac delta δ_s) in the governing equations. A scalar marker function is needed to identify which phase is present in each computational cell and define the local fluid properties. The way this marker function is updated makes the difference between tracking and capturing methods.

- In the interface tracking methods the interface is represented by Lagrangian marker points that are moved by the fluid. The fluid front requires the use of a dedicated grid to be tracked and the fluid-flow is solved on an underlying fixed grid. The

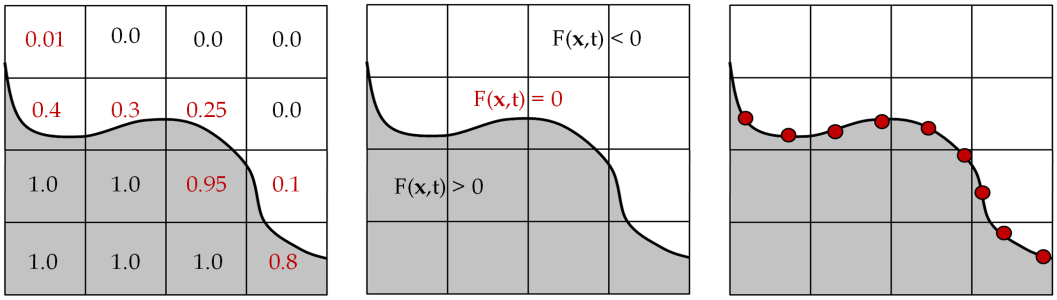

Figure 3.1: Interface advection methods: Volume of Fluid (VOF) (a), Level-Set (b) and Front-Tracking (c).

fluid front includes the description of the interfacial forces (e.g. surface tension) and a continuous transfer of information is required between the Lagrangian and the fixed grid. The marker function is then reconstructed from the position of the front, already defined by the marker points.

- In the interface capturing methods the marker function is advected directly, solving a transport equation for it. The exact position of the interface is then reconstructed from the marker function.

Since no assumption on the fluid front connectivity is assumed, interface capturing methods automatically include topology changes and better describe large deformation of the interface, while in interface tracking methods this has to be artificially enforced. However, the main difficulty of interface capturing is that the interface reconstruction from the marker function is not straightforward and accurate geometrical methods can be fairly complex.

Volume of Fluid (VOF)

In the VOF method the marker function α represents the volume fraction of the liquid in the computational cell. From a mathematical point of view it is a Heaviside function: it assumes value 0 in the gas phase, value 1 in the liquid phase with the discontinuity localized at the interface. The properties χ of the fluids are updated with the marker function itself:

$$\chi = \alpha\chi_L + (1-\alpha)\,\chi_G \tag{3.1}$$

From a numerical perspective, the marker function actually goes from 0 to 1 in a smooth way, considering computational cells with intermediate α values ($0< \alpha <1$) to contain the interface (Figure 3.1 a). This does not provide any information on the exact position of the interface in the cell, which has to be reconstructed based on the values of the marker function in neighboring cells. The VOF method was originally proposed by Hirt and Nichols [55] in 1981 and it is so far one of the most adopted methodologies for multiphase flows. Early implementations suffered from significant diffusion of the interface, which was almost completely eliminated by the introduction of more sophisticated reconstruction methods [56, 57]. VOF methods are widely used because of their boundedness and excellent mass conservation properties, as well as the possibility to efficiently handle topology changes (e.g. breakups, coalescence). However, the accurate representation of surface tension remained for a long time the main weak point of VOF methods [58, 59], mainly because of the discontinuous nature of α.

Level-set method

A smooth function $F(\mathbf{x}, t)$ is used to identify the two different phases. It assumes a positive value in one fluid and a negative value in the other fluid, while the isosurface $F(\mathbf{x}, t) = 0$ represent the interface (Figure 3.1 b). In this case surface tension implementation results to be easier due to the continuous nature of F. The material properties are updated with a marker function I reconstructed from the level-set function:

$$I = \begin{cases} 0 & \text{if } F < -\epsilon\Delta x \\ \frac{1}{2}\left(1 + (F/\epsilon\Delta x) + \frac{1}{\pi} sin\left(\pi F/\epsilon\Delta x\right)\right) & \text{if } |F| \leq \epsilon\Delta x \\ 1 & \text{if } F > -\epsilon\Delta x \end{cases} \tag{3.2}$$

where ϵ is an empirical parameter representing half of the interface thickness. The level-set method has been introduced in 1988 by Osher [60], but the actual application to multiphase interface transport was developed by Sussman in 1994 [61]. The level set-function F requires the maintaining of its shape (constant thickness) close to the interface in order to properly reconstruct the marker function I. Simply advecting F with a transport equation does not guarantee this condition, therefore re-initialization methods are always required in level-set methods [61, 62]. An additional equation is solved at each time step to make F a distance function and to maintain the gradient at the interface. The re-initialization procedure was one of the main issue in multiphase flows calculation, together with the continuous effort in developing methods to improve mass conservation in level set-methods [63]. This also lead to interesting hybrid solutions

between VOF and level-set techniques [64].

Front tracking

The front-tracking method for multiphase flows was introduced by Unverdi and Tryggvason in 1992 [65]. Marker points are used to advect the interface, while the fluid flow is solved on an Eulerian fixed grid (Figure 3.1 c). It is clear that some form of communication is needed between the front and the flow and this is usually done assuming a smooth transition between the fluids at the interface and applying interfacial forces with a singular smoothed source term. Front tracking has been successfully used over the years to model drops and bubbles motion [66, 67] and to efficiently implement surface tension [68]. Differently from VOF and level-set methods, the changes in topology (breakups and merging) are not automatically handled and require to change the connection of the marker points at the front.

Other methods

VOF, level-set and front-tracking methods represent the large majority of the computational approaches for interface advection in multiphase flows. Alternative methods within the "one-fluid" category include the phase-field method [69, 70], where a thermodynamic consistence is enforced within the front advection, and the CIP method [71] in which the transition between the fluid is described by a cubic polynomial. Both methods found a discrete success in modeling floating solids or solidification processes, while the use for two-fluid systems seems to be relatively limited.

3.2 Velocity field

In the sphero-symmetric modeling of droplets the only velocity field is the radial one generated by the Stefan flow, which is propagated in the gas-phase with the continuity equation. An interface-resolved approach requires a momentum equation for the two-phase velocity field, which can be written following the "one-fluid" approach:

$$\frac{\partial(\rho\mathbf{v})}{\partial t} + \nabla\cdot(\rho\mathbf{v}\otimes\mathbf{v}) = \nabla\cdot\mu\left(\nabla\mathbf{v} + \nabla\mathbf{v}^T\right) - \nabla p + \rho\mathbf{g} + \sigma\kappa\delta_s\mathbf{n} \tag{3.3}$$

where $\sigma\kappa\delta_s\mathbf{n}$ is the surface tension force (next section). The momentum equation must be coupled with a continuity equation, which includes the velocity jump due to the phase change [72]:

$$\frac{1}{\rho}\frac{D\rho}{Dt} + \nabla \cdot \mathbf{v} = \dot{m}\left(\frac{1}{\rho_L} - \frac{1}{\rho_G}\right) \tag{3.4}$$

where $\dot{m}$ represents the vaporization flux per unit volume, only applied at the interface. In all CFD codes Equations 3.3 and 3.4 are solved together with an iterative algorithm (e.g. SIMPLE [73]) through the solution of an intermediate Laplacian equation for the pressure field.

3.3 Surface tension

The modeling of surface tension is one of the most critical issues in multiphase flows at small scales, because of the singular nature of this force. The adoption of a "one fluid" approach requires to include surface tension as a volumetric force in the Navier-Stokes equations, using a smoothed Dirac delta distribution to impose it at the interface. The classical approach is called Continuous Surface Force (CSF), proposed by Brackbill in 1992 [58] and still widely used. Its quality relies on its simplicity, computing the surface tension force $\mathbf{f}_s$ as[1]:

$$\mathbf{f}_s = \sigma\kappa\delta_s\mathbf{n} \tag{3.5}$$

and the interface curvature κ as the discrete divergence of the interface normal $\mathbf{n}$. It is natural to assume the discretization of the Dirac delta $\delta_s\mathbf{n}$ equal to the derivative of the discretized Heaviside function (i.e. the marker function α):

$$\delta_s\mathbf{n} = \nabla\alpha \tag{3.6}$$

$\mathbf{f}_s$ is directly added to the Navier-Stokes equation as a body force. From a numerical perspective this method is known to have critical issues, i.e. (i) the numerical discretization of the surface tension force and (ii) the evaluation of the interface curvature.

Numerical discretization and spurious currents

The surface tension force only exists at the liquid-gas interface, posing a great problem concerning the discretization of $\delta_s\mathbf{n}$. It is well known that incorrect, approximate or trivial discretizations of the surface tension force lead to the formation of unphysical

[1] Since this work is based on the VOF methodology, only surface tension implementation in interface capturing techniques is considered.

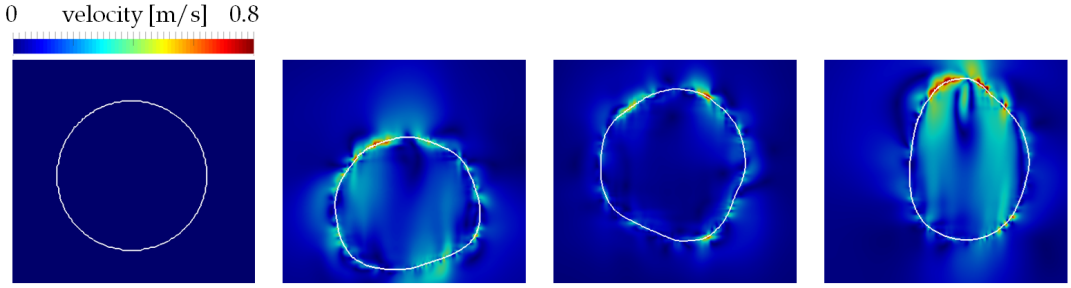

Figure 3.2: Spurious currents on a droplet of water ($D = 1$ mm, white contour) using the CSF method for surface tension. Times t = 0 (a), 0.04 (b), 0.1 (c) and 0.2 (d) s. Results from the `interFoam` multiphase solver available in `OpenFOAM`® [74].

velocities around the interface (called spurious currents) due to the local numerical imbalance between the pressure gradient and the surface tension force [75, 76, 77]. The simplest case is given by a motionless spherical droplet at zero gravity, described by the following (continuous) equation:

$$\frac{\partial (\rho \mathbf{v})}{\partial t} = -\nabla p + \sigma \kappa \delta_s \mathbf{n} = \mathbf{0} \tag{3.7}$$

If the numerical discretizations of the pressure gradient ∇p and surface tension force $\sigma \kappa \delta_s \mathbf{n}$ do not cancel out:

$$\frac{\partial (\rho \mathbf{v})}{\partial t} = -\nabla p + \sigma \kappa \delta_s \mathbf{n} \neq \mathbf{0} \tag{3.8}$$

a non-physical flow field (spurious current) will be generated as a consequence of this numerical imbalance. This flow generally grows in time, eventually destroying the droplet (Figure 3.2). Alternative methods directly approach the sharp discontinuity, such as the *Ghost Fluid Method* (GFM). The main strategy is an explicit treatment of the discontinuity, including the jump conditions directly in the numerical discretization. Introduced by Fedwik et al. [78] to handle discontinuities in compressible solvers, it has been extended to study detonations [79], to efficiently solve variable coefficients Poisson equations [80] and finally to treat the large density ratio typical of multiphase flows [81, 82, 83, 84].

Curvature evaluation

The surface tension force is directly proportional to the interface curvature (Equation 3.7). Even if the surface tension force is discretized with a perfectly balanced method, this is generally not enough to eliminate spurious currents. The curvature gradients along the interface generate a flow, which may be physical (e.g. when a deformed droplet tends towards a spherical shape) or unphysical, when these variations are actually due to numerical errors in the curvature evaluation [58, 85]. This issue is particularly evident within a VOF method, because it requires the differentiation of a discontinuous function (e.g. α):

$$\kappa = \nabla \cdot \mathbf{n} = \nabla \cdot \left(\frac{\nabla \alpha}{|\nabla \alpha|} \right) \tag{3.9}$$

First solutions relied on the filtering of the α function, in order to handle smoother functions [86, 87]. However these methods can be hardly generalized (uncertainty on the number-type of filters, choice of the interface thickness etc.) and many studies showed the inaccuracy and non-consistency of these methods [72]. Widely used are *Height Functions* [85, 88], in which local heights are computed (from volume fractions) and differentiated in order to obtain the curvature. The main conditions is to have well defined heights, usually available when the droplet is well resolved. When this is not possible, *least-squares methods* can be used, based on discrete surfaces differentiation [89, 90, 82]. The interface is locally approximated by a quadratic form, from which the curvature can be analytically computed.

3.4 Additional fields and physics

Droplets are commonly used in sprays, where the two-phase fluid dynamics is not the only relevant physical phenomena. Extending the physics is not only limited to the addition of new fields and equations, but also brings new time and length scales. Due to the mathematical complexity of interface-resolved simulations, including additional physics to the main fluid-dynamic core remains a challenging task.

Heat and mass transfer

Heat transfer is generally the easiest phenomenon to include in a multiphase model, due to the temperature continuity at the interface guaranteed by the thermodynamic equilibrium. Following the "one fluid" approach, a single energy equation can be written

for both phases:

$$\rho C_p \left(\frac{\partial T}{\partial t} + \mathbf{v} \nabla T \right) = \nabla \cdot (k \nabla T) + \dot{q} \delta_s \tag{3.10}$$

where the term $\dot{q}\delta_s$ accounts for heat fluxes localized at the interface (typically due to the phase-change). Noteworthy applications include the ones of Davidson [91] and Gupta [92].
On the other hand, mass transfer is much more challenging: (i) there is a discontinuity in species concentrations at the interface due to thermodynamic equilibrium and (ii) the equality of the material fluxes at the interface must be imposed. This makes the "one-fluid" approach for species equation extremely difficult to implement in a stable way. An interesting approach is proposed by Marschall et al. [93, 94], including the concentration jump directly in the governing equations. Other authors prefer to adopt a variable transformation to make the concentration profile continuous [95, 96] and enforcing the interfacial condition dictated by thermodynamic equilibrium. There is no definitive solution on this issue and the research is still very open.

Phase-change

The phase-change process is one of the most important for droplets [2]. The implementation within a multiphase framework presents, however, some difficulties:

- The vaporization (or condensation) rate $\dot{m}_i$ of the i-th species has to be calculated based on the available fields. The easiest approach is to consider the interface at a steady-state temperature and calculate $\dot{m}$ simply as the ratio between the heat flux $\dot{q}$ and the latent heat $\Delta h_{ev,i}$:

$$\dot{m}_i = -\frac{\dot{q}}{\Delta h_{ev,i}} \tag{3.11}$$

  However, this approach is not able to describe the heating transient period. The most rigorous approach consists in considering the diffusive and convective material fluxes at the interface:

$$\dot{m}_i = \rho \mathcal{D}_i \nabla \omega_i \nabla \alpha + \dot{m} \omega_i \tag{3.12}$$

  for monocomponent liquids $\dot{m}_i = \dot{m}$, so:

[2] Phase-change in both direction: evaporation and condensation.

$$\dot{m} = \frac{\rho \mathcal{D}_i \nabla \omega_i}{1 - \omega_i} \nabla \alpha \tag{3.13}$$

Equation 3.13 is widely used in literature [97, 98], but necessarily requires the solution of a species equation for the ω_i profile, which is not easy to obtain within a "one-fluid" formulation (see mass transfer);

- Equation 3.4 provides a discontinuous velocity field at the phase-boundary. The gas-phase radial velocity stretches the interface, making its advection numerically difficult. The problem is further complicated by the presence of surface tension, which is very sensitive to instabilities in the interface advection [99]. A common solution is the extension of each phase velocity proposed by Nguyen et al. for incompressible flame discontinuities [100]. The liquid (gas) velocity field is extended towards the gas (liquid) phase and used to discretize the liquid (gas) side momentum equation respecting the jump conditions (as done in GFM). This has been recently generalized to multiphase flows [101, 102] using the extended liquid velocity field to advect the interface. The methodology involves multiple steps (including an additional Poisson equation) and it is quite complex. Another possibility is the explicit extrapolation [103] (constant, linear or quadratic) of the liquid velocity in a narrow band around the interface. Whereas the implementation is much easier, it includes uncertainties on the liquid cells chosen for the extrapolation. Moreover, in both methods additional effort is required to obtain a free-divergence extended velocity [104] to enforce mass conservation.

Initial attempts to include phase-change within an interface-resolved simulation include the works of Welch [105, 106, 107] in the early 2000s, mainly applied to the study of boiling processes and bubbles growth adopting a VOF capturing method. Front-tracking methods have been used by Tryggvason [66, 108], exploiting their accuracy in describing the interface shape, which is particularly convenient for phase-change simulation. Conversely, Level-set method applications [109, 101] are less diffused for phase-change, probably due to the need to handle mass-conservation issues. Recent numerical strategies include smoothing for the source term [110] and the implementation of gradient augmented level-set method to approach the phase-change [111]. The issue of the velocity jump has only been very recently addressed by Shlottke [97], Palmore [98] and Reutzsch [112].

Combustion

Due to the aforementioned difficulties of implementing phase-change, the combustion process has been even less studied within an interface-resolved approach. Combustion chemistry is characterized by a highly non-linear dependence on temperature and species concentration and presents a wide range of temporal scales. This stiff nature of combustion chemistry make the direct numerical resolution of the governing equations (energy and species) extremely difficult. Available works are mainly based on non-shrinking, motionless droplets [113] or adopt one-step/global schemes for chemistry [114]. Recently, a skeletal mechanism ($\sim$20 reactions) was used by Ghata et al. [115] within a multiphase approach, limiting however the application to zero gravity conditions. The high temperatures typical of combustion processes require the adoption of a radiation model for heat transfer, further complicating the problem.

Chapter 4

Motivation of the work

The previous chapters defined the two approaches for the modeling of isolated droplet: sphero-symmetric models and interface-resolved models. Both methods are widely used, with different purposes:

- **Sphero-symmetric** simulations allow a relatively simple numerical modeling: (i) the governing equations can be written in one-dimension, using a single radial coordinate; (ii) no momentum equation is needed for the velocity field; (iii) the interface is not transported; (iv) surface tension is neglected. Therefore:
  - The main advantage is the possibility to push the chemistry complexity, adopting detailed kinetic mechanisms for combustion (up to hundreds of species and thousands of reactions), variable fluid properties, detailed thermodynamics and complex radiation models. This allows to analyze in detail complex phenomena such as ignitions, extinctions, cool flames, soot formation, thermophoresis etc. Most of the works and advances are on the application side rather than the model development, which is solid and well-established by now;
  - The main drawbacks are (i) the necessity of expensive microgravity experiments for the validation and (ii) the incapability of describing phenomena such as convection, internal circulation, interface deformation and the droplet-fiber interaction.
- **Interface-resolved** simulations are based on a CFD approach, considering: (i) a three-dimensional geometry of the system; (ii) momentum equations for the velocity field; (iii) advection methods for the interface transport; (iv) stable and accurate methodologies for surface tension. Therefore:

- The main advantage is the predictive power of the computational model, which can provide a detailed knowledge of the internal and external velocity fields, as well as the numerical description of the boundary layers. The interface deformations are automatically included. Experimental data for validation are obtainable at low cost (e.g. suspended droplets);
- The main drawback is the mathematical and numerical complexity, which poses severe limits to the application. The model development is still an open area of research and most of the works put the emphasis on the implementation of consistent and stable numerical methods (advection, phase-change, surface tension etc.) with less attention to the systematic validation against experiments and application to real systems. The chemistry description is often not considered.

Objectives

This work aims at building a bridge between the two methods, exploiting their respective advantages.

- The first objective is the development of a multiphase CFD solver for isolated droplets vaporization and combustion, based on an interface-resolved methodology, including:

  1. An advection method for the interface transport;
  2. Governing equations for velocity, temperature and species concentration;
  3. A general phase-change model which does not require the use of semi-empirical correlations (based on the solution of the boundary layer);

  The aim is to further extend this model, adding sub-models typically included only in sphero-symmetric models:

  4. The modeling of multicomponent droplets;
  5. A detailed thermodynamic description of the interface;
  6. The description of combustion chemistry and radiative heat transfer;
  7. Variable fluid properties, in function of temperature, pressure and composition;
  8. The description of the thermal perturbation of the fiber;

- Points 4 to 8 allow allow to face our second objective: the systematic and extensive validation of the model against experiments, rarely done despite the wide availability of data. The possibility to model real systems (e.g. suspended droplets) generally requires large domains (with respect to the droplet) and unstructured computational grids. The simulations should cover a wide range of operating conditions including the fuel type, gas temperature, ambient pressure, droplet diameter, natural and forced convection. This includes the numerical analysis on the effect of the physical phenomena involved such as convection, gravity, the thermal perturbation of the fiber etc.;

The aim to to obtain a predictive numerical tool for the detailed analysis of the phenomena involved in the vaporization and combustion of an isolated fuel droplet. This is a fundamental step for the development of physics-based sub-models to be used in reduced descriptions of complex configurations.

Fluid dynamic regimes and non-dimensional numbers

In this thesis work several non-dimensional numbers will be adopted to identify the properties of the multiphase flow. The Reynolds number is defined as:

$$Re = \frac{\rho D v}{\mu} \tag{4.1}$$

which quantifies the relative contribution of inertia and viscous forces. Since this work deals with isolated droplets, the characteristic length is the droplet diameter D. In this work the flow regime is always *laminar*, with Reynolds number values between 5 and 50 (actually overestimated). Turbulent simulations could be designed adopting appropriate subgrid-scale models for reduced descriptions (e.g. LES) or further refining the mesh to resolve the Kolmogorov scale.

Within a multiphase system, the gas-liquid interaction is governed by several non-dimensional numbers. The shape of the droplet generally depends on (i) surface tension, (ii) droplet weight and (iii) external convection. The Weber number:

$$We = \frac{\rho D v^2}{\sigma} \tag{4.2}$$

defines the ratio between inertial forces and surface tension. The Eotvos number:

$$Eo = \frac{\Delta \rho g D^2}{\sigma} \tag{4.3}$$

evaluates the ratio between the droplet weight and surface tension forces. For the cases of our interest (small suspended droplets) very small Weber numbers are expected, due to surface tension dominance ($\sim$ 0.02 in typical cases), as well as small Eotvos numbers ($\sim$ 0.1 in typical cases). As a consequence the droplet deformation due to convection and/or gravity will be very limited, providing a practically *spherical* droplet. Finally, it is worth introducing non-dimensional numbers to compare the viscous forces with surface tension. The Laplace number:

$$La = \frac{\sigma \rho D}{\mu^2} \tag{4.4}$$

and the capillary number:

$$Ca = \frac{\mu v}{\sigma} \tag{4.5}$$

The main difference is that the capillary number used a characteristic velocity to define the viscous stresses, while a characteristic length is used for the Laplace number. Quantifying spurious currents for surface tension driven flows is typically done defining cases ad different Laplace numbers and evaluating the results in terms of capillary numbers.

Bibliography

[1] Andrea Prosperetti and Grétar Tryggvason. *Computational methods for multiphase flow*. Cambridge university press, 2009.

[2] Jennifer C Beale and Rolf D Reitz. "Modeling spray atomization with the Kelvin-Helmholtz/Rayleigh-Taylor hybrid model". In: *Atomization and sprays* 9.6 (1999), pp. 623–650.

[3] Romain Lebas et al. "Numerical simulation of primary break-up and atomization: DNS and modelling study". In: *International Journal of Multiphase Flow* 35.3 (2009), pp. 247–260.

[4] Gian Marco Bianchi et al. *Improving the knowledge of high-speed liquid jets atomization by using quasi-direct 3D simulation*. Tech. rep. SAE Technical Paper, 2005.

[5] Mark Owkes, Madhusudan Pai, and Olivier Desjardins. "Large-eddy simulation study of injector geometry on liquid jet in cross-flow and validation with experiments". In: *52nd Aerospace Sciences Meeting*. 2014, p. 1186.

[6] J Shinjo and A Umemura. "Simulation of liquid jet primary breakup: Dynamics of ligament and droplet formation". In: *International Journal of Multiphase Flow* 36.7 (2010), pp. 513–532.

[7] Said Elghobashi. "Direct numerical simulation of turbulent flows laden with droplets or bubbles". In: *Annual Review of Fluid Mechanics* 51 (2019), pp. 217–244.

[8] Kun Luo et al. "Level set method for atomization and evaporation simulations". In: *Progress in Energy and Combustion Science* 73 (2019), pp. 65–94.

[9] BT Helenbrook and CF Edwards. "Quasi-steady deformation and drag of uncontaminated liquid drops". In: *International journal of multiphase flow* 28.10 (2002), pp. 1631–1657.

[10] Dudley Brian Spalding. "The combustion of liquid fuels". In: *Symposium (International) on combustion*. Vol. 4. 1. Elsevier. 1953, pp. 847–864.

[11] GAE Godsave. "Studies of the combustion of drops in a fuel spray–the burning of single drops of fuel". In: *Symposium (International) on Combustion*. Vol. 4. 1. Elsevier. 1953, pp. 818–830.

[12] Kenneth K Kuo. "Principles of Combustion. John Wiley &Sons". In: *New York, USA* (1986), pp. 261–227.

[13] A Williams. *Combustion of sprays of liquid fuels*. Elek Science London, UK, 1976.

[14] GM Faeth. "Current status of droplet and liquid combustion". In: *Energy and Combustion Science*. Elsevier, 1979, pp. 149–182.

[15] FA Williams. "On the assumptions underlying droplet vaporization and combustion theories". In: *The Journal of Chemical Physics* 33.1 (1960), pp. 133–144.

[16] S Kumagai. "Combustion of fuel droplets in falling chamber". In: *Symposium (International) on Combustion*. Vol. 6. 1. Elsevier. 1957, pp. 726–731.

[17] S Okajima and S Kumagai. "Further investigations of combustion of free droplets in a freely falling chamber including moving droplets". In: *Symposium (International) on Combustion*. Vol. 15. 1. Elsevier. 1975, pp. 401–407.

[18] S Kumagai, T Sakai, and S Okajima. "Combustion of free fuel droplets in a freely falling chamber". In: *Symposium (International) on Combustion*. Vol. 13. 1. Elsevier. 1971, pp. 779–785.

[19] S Okajima and S Kumagai. "Experimental studies on combustion of fuel droplets in flowing air under zero-and high-gravity conditions". In: *Symposium (International) on Combustion*. Vol. 19. 1. Elsevier. 1982, pp. 1021–1027.

[20] CK Law. "Unsteady droplet combustion with droplet heating". In: *Combustion and Flame* 26 (1976), pp. 17–22.

[21] CK Law and WA Sirignano. "Unsteady droplet combustion with droplet heating—II: Conduction limit". In: *Combustion and flame* 28 (1977), pp. 175–186.

[22] CK Law. "Recent advances in droplet vaporization and combustion". In: *Progress in Energy and Combustion Science* 8.3 (1982), pp. 171–201.

[23] MM El Wakil, OA Uyehara, and PS Myers. *A theoretical investigation of the heating-up period of injected fuel droplets vaporizing in air*. Tech. rep. University of Wisconsin, 1954.

[24] MM El Wakil et al. *Experimental and calculated temperature and mass histories of vaporizing fuel drops*. Tech. rep. University of Wisconsin, 1956.

[25] S Winnikow and BT Chao. "Droplet motion in purified systems". In: *the Physics of Fluids* 9.1 (1966), pp. 50–61.

[26] JF Harper and DW Moore. "The motion of a spherical liquid drop at high Reynolds number". In: *Journal of Fluid Mechanics* 32.2 (1968), pp. 367–391.

[27] Horace Lamb. *Hydrodynamics*. Dover Publications, New York, 1945.

[28] S Prakash and WA Sirignano. "Liquid fuel droplet heating with internal circulation". In: *International Journal of Heat and Mass Transfer* 21.7 (1978), pp. 885–895.

[29] WA Sirignano. "Fuel droplet vaporization and spray combustion theory". In: *Progress in Energy and Combustion Science* 9.4 (1983), pp. 291–322.

[30] WE Ranz and WR Marshall. "Evaporation from drops". In: *Chemical Engineering Progress* 48.3 (1952), pp. 141–146.

[31] John K Dukowicz. "Drag of evaporating or condensing droplets in low Reynolds number flow". In: *The Physics of fluids* 27.6 (1984), pp. 1351–1358.

[32] M Renksizbulut and MC Yuen. "Numerical study of droplet evaporation in a high-temperature stream". In: *Journal of Heat Transfer* 105.2 (1983), pp. 389–397.

[33] B Abramzon and WA Sirignano. "Droplet vaporization model for spray combustion calculations". In: *International Journal of Heat and Mass Transfer* 32.9 (1989), pp. 1605–1618.

[34] WA Sirignano. *Fluid dynamics and transport of droplets and sprays*. Cambridge university press, 1999.

[35] Daniel L Dietrich et al. "Droplet combustion experiments aboard the international space station". In: *Microgravity Science and Technology* 26.2 (2014), pp. 65–76.

[36] JW Aldred, JC Patel, and A Williams. "The mechanism of combustion of droplets and spheres of liquid n-heptane". In: *Combustion and Flame* 17.2 (1971), pp. 139–148.

[37] Daniel L Dietrich et al. "Droplet combustion experiments in spacelab". In: *Symposium (International) on Combustion*. Vol. 26. 1. Elsevier. 1996, pp. 1201–1207.

[38] Paul D Ronney. "Understanding combustion processes through microgravity research". In: *Symposium (International) on Combustion*. Vol. 27. 2. Elsevier. 1998, pp. 2485–2506.

[39] SY Cho, Richard A Yetter, and FL Dryer. "Mathematical modelling of liquid droplet combustion in micro-gravity". In: *Mathematical and Computer Modelling* 14 (1990), pp. 790–794.

[40] SY Cho, Richard A Yetter, and FL Dryer. "A computer model for one-dimensional mass and energy transport in and around chemically reacting particles, including complex gas-phase chemistry, multicomponent molecular diffusion, surface evaporation, and heterogeneous reaction". In: *Journal of Computational Physics* 102.1 (1992), pp. 160–179.

[41] Anthony J Marchese and Frederick L Dryer. "The effect of liquid mass transport on the combustion and extinction of bicomponent droplets of methanol and water". In: *Combustion and Flame* 105.1-2 (1996), pp. 104–122.

[42] Anthony J Marchese, Frederick L Dryer, and Vedha Nayagam. "Numerical modeling of isolated n-alkane droplet flames: initial comparisons with ground and space-based microgravity experiments". In: *Combustion and Flame* 116.3 (1999), pp. 432–459.

[43] A Cuoci et al. "Autoignition and burning rates of fuel droplets under microgravity". In: *Combustion and Flame* 143.3 (2005), pp. 211–226.

[44] Tanvir I Farouk and Frederick L Dryer. "Isolated n-heptane droplet combustion in microgravity: cool flames–two-stage combustion". In: *Combustion and Flame* 161.2 (2014), pp. 565–581.

[45] TI Farouk et al. "Isolated n-decane droplet combustion–dual stage and single stage transition to "Cool Flame" droplet burning". In: *Proceedings of the Combustion Institute* 36.2 (2017), pp. 2523–2530.

[46] Alberto Cuoci et al. "Flame extinction and low-temperature combustion of isolated fuel droplets of n-alkanes". In: *Proceedings of the Combustion Institute* 36.2 (2017), pp. 2531–2539.

[47] Alessandro Stagni et al. "Numerical investigation of soot formation from microgravity droplet combustion using heterogeneous chemistry". In: *Combustion and Flame* 189 (2018), pp. 393–406.

[48] Anand Sankaranarayanan et al. "Droplet combustion studies on two novel energetic propellants, an RP-1 surrogate fuel, and their blends". In: *Fuel* 255 (2019), p. 115836.

[49] RS Volkov and PA Strizhak. "Research of temperature fields and convection velocities in evaporating water droplets using Planar Laser-Induced Fluorescence and Particle Image Velocimetry". In: *Experimental Thermal and Fluid Science* 97 (2018), pp. 392–407.

[50] C Chauveau et al. "An experimental study on the droplet vaporization: effects of heat conduction through the support fiber". In: *Proceedings of 22 nd Annual Conference on Liquid Atomization and Spray Systems (ILASS Europe 2008)*. Vol. 59. 2008, p. 61.

[51] D Shringi, HA Dwyer, and BD Shaw. "Influences of support fibers on vaporizing fuel droplets". In: *Computers & Fluids* 77 (2013), pp. 66–75.

[52] Anja Oasmaa, Cordner Peacocke, et al. *A guide to physical property characterisation of biomass-derived fast pyrolysis liquids*. Technical Research Centre of Finland Espoo, 2001.

[53] SS Sazhin et al. "Modelling of biodiesel fuel droplet heating and evaporation". In: *Fuel* 115 (2014), pp. 559–572.

[54] CK Law. "Multicomponent droplet combustion with rapid internal mixing". In: *Combustion and Flame* 26 (1976), pp. 219–233.

[55] Cyril W Hirt and Billy D Nichols. "Volume of fluid (VOF) method for the dynamics of free boundaries". In: *Journal of computational physics* 39.1 (1981), pp. 201–225.

[56] Nasser Ashgriz and JY Poo. "FLAIR: Flux line-segment model for advection and interface reconstruction". In: *Journal of computational physics* 93.2 (1991), pp. 449–468.

[57] Yuriko Renardy and Michael Renardy. "PROST: a parabolic reconstruction of surface tension for the volume-of-fluid method". In: *Journal of computational physics* 183.2 (2002), pp. 400–421.

[58] JU Brackbill, Douglas B Kothe, and Charles Zemach. "A continuum method for modeling surface tension". In: *Journal of computational physics* 100.2 (1992), pp. 335–354.

[59] Bruno Lafaurie et al. "Modelling merging and fragmentation in multiphase flows with SURFER". In: *Journal of Computational Physics* 113.1 (1994), pp. 134–147.

[60] Stanley Osher and James A Sethian. "Fronts propagating with curvature-dependent speed: algorithms based on Hamilton-Jacobi formulations". In: *Journal of computational physics* 79.1 (1988), pp. 12–49.

[61] Mark Sussman, Peter Smereka, Stanley Osher, et al. "A level set approach for computing solutions to incompressible two-phase flow". In: *Journal of computational physics* 114.1 (1994), pp. 146–159.

[62] Mark Sussman et al. "An improved level set method for incompressible two-phase flows". In: *Computers & Fluids* 27.5-6 (1998), pp. 663–680.

[63] Mark Sussman et al. "An adaptive level set approach for incompressible two-phase flows". In: *Journal of Computational Physics* 148.1 (1999), pp. 81–124.

[64] Mark Sussman and Elbridge Gerry Puckett. "A coupled level set and volume-of-fluid method for computing 3D and axisymmetric incompressible two-phase flows". In: *Journal of computational physics* 162.2 (2000), pp. 301–337.

[65] Salih Ozen Unverdi and Grétar Tryggvason. "A front-tracking method for viscous, incompressible, multi-fluid flows". In: *Journal of Computational Physics* 100.1 (1992), pp. 25–37.

[66] Damir Juric and Grétar Tryggvason. "Computations of boiling flows". In: *International journal of multiphase flow* 24.3 (1998), pp. 387–410.

[67] Grétar Tryggvason et al. "A front-tracking method for the computations of multiphase flow". In: *Journal of Computational Physics* 169.2 (2001), pp. 708–759.

[68] Stéphane Popinet and Stéphane Zaleski. "A front-tracking algorithm for accurate representation of surface tension". In: *International Journal for Numerical Methods in Fluids* 30.6 (1999), pp. 775–793.

[69] David Jacqmin. "Calculation of two-phase Navier–Stokes flows using phase-field modeling". In: *Journal of Computational Physics* 155.1 (1999), pp. 96–127.

[70] Maykel Verschueren, FN Van De Vosse, and HEH Meijer. "Diffuse-interface modelling of thermocapillary flow instabilities in a Hele-Shaw cell". In: *Journal of Fluid Mechanics* 434 (2001), pp. 153–166.

[71] H Takewaki, A Nishigushi, and T Yabe. "Cubic Interpolated Pseudo-Particle Method (CIP) for Solving Hyperbolic Type equation". In: *Journal of Computational Physics* 61.2 (1985), pp. 261–268.

[72] Grétar Tryggvason, Ruben Scardovelli, and Stéphane Zaleski. *Direct numerical simulations of gas–liquid multiphase flows*. Cambridge University Press, 2011.

[73] Suhas V Patankar and D Brian Spalding. "A calculation procedure for heat, mass and momentum transfer in three-dimensional parabolic flows". In: *Numerical prediction of flow, heat transfer, turbulence and combustion*. Elsevier, 1983, pp. 54–73.

[74] Christopher J Greenshields. "OpenFOAM user guide". In: *OpenFOAM Foundation Ltd, version* 3.1 (2015).

[75] Marianne M Francois et al. "A balanced-force algorithm for continuous and sharp interfacial surface tension models within a volume tracking framework". In: *Journal of Computational Physics* 213.1 (2006), pp. 141–173.

[76] Stéphane Popinet. "An accurate adaptive solver for surface-tension-driven interfacial flows". In: *Journal of Computational Physics* 228.16 (2009), pp. 5838–5866.

[77] Stéphane Popinet. "Numerical models of surface tension". In: *Annual Review of Fluid Mechanics* 50 (2018), pp. 49–75.

[78] Ronald P Fedkiw et al. "A non-oscillatory Eulerian approach to interfaces in multimaterial flows (the ghost fluid method)". In: *Journal of computational physics* 152.2 (1999), pp. 457–492.

[79] Ronald P Fedkiw, Tariq Aslam, and Shaojie Xu. "The ghost fluid method for deflagration and detonation discontinuities". In: *Journal of Computational Physics* 154.2 (1999), pp. 393–427.

[80] Xu-Dong Liu, Ronald P Fedkiw, and Myungjoo Kang. "A boundary condition capturing method for Poisson's equation on irregular domains". In: *Journal of computational Physics* 160.1 (2000), pp. 151–178.

[81] Elin Olsson and Gunilla Kreiss. "A conservative level set method for two phase flow". In: *Journal of computational physics* 210.1 (2005), pp. 225–246.

[82] Olivier Desjardins, Vincent Moureau, and Heinz Pitsch. "An accurate conservative level set/ghost fluid method for simulating turbulent atomization". In: *Journal of Computational Physics* 227.18 (2008), pp. 8395–8416.

[83] Wurigen Bo and John W Grove. "A volume of fluid method based ghost fluid method for compressible multi-fluid flows". In: *Computers & Fluids* 90 (2014), pp. 113–122.

[84] Vuko Vukčević, Hrvoje Jasak, and Inno Gatin. "Implementation of the Ghost Fluid Method for free surface flows in polyhedral Finite Volume framework". In: *Computers & Fluids* 153 (2017), pp. 1–19.

[85] Sharen J Cummins, Marianne M Francois, and Douglas B Kothe. "Estimating curvature from volume fractions". In: *Computers & structures* 83.6-7 (2005), pp. 425–434.

[86] Mahmoud Aboukhedr et al. "Simulation of micro-flow dynamics at low capillary numbers using adaptive interface compression". In: *Computers & Fluids* 165 (2018), pp. 13–32.

[87] Ali Q Raeini, Martin J Blunt, and Branko Bijeljic. "Modelling two-phase flow in porous media at the pore scale using the volume-of-fluid method". In: *Journal of Computational Physics* 231.17 (2012), pp. 5653–5668.

[88] G Bornia et al. "On the properties and limitations of the height function method in two-dimensional Cartesian geometry". In: *Journal of Computational Physics* 230.4 (2011), pp. 851–862.

[89] Robert Chiodi and Olivier Desjardins. "A reformulation of the conservative level set reinitialization equation for accurate and robust simulation of complex multiphase flows". In: *Journal of Computational Physics* 343 (2017), pp. 186–200.

[90] Emilie Marchandise et al. "A stabilized finite element method using a discontinuous level set approach for the computation of bubble dynamics". In: *Journal of Computational Physics* 225.1 (2007), pp. 949–974.

[91] Malcolm R Davidson and Murray Rudman. "Volume of fluid calculation of heat or mass transfer across deforming interfaces in two-fluid flow". In: *Numerical Heat Transfer: Part B: Fundamentals* 41.3-4 (2002), pp. 291–308.

[92] Raghvendra Gupta, David F Fletcher, and Brian S Haynes. "CFD modelling of flow and heat transfer in the Taylor flow regime". In: *Chemical Engineering Science* 65.6 (2010), pp. 2094–2107.

[93] Daniel Deising, Holger Marschall, and Dieter Bothe. "A unified single-field model framework for Volume-Of-Fluid simulations of interfacial species transfer applied to bubbly flows". In: *Chemical Engineering Science* 139 (2016), pp. 173–195.

[94] Holger Marschall et al. "Numerical simulation of species transfer across fluid interfaces in free-surface flows using OpenFOAM". In: *Chemical engineering science* 78 (2012), pp. 111–127.

[95] J Petera and LR Weatherley. "Modelling of mass transfer from falling droplets". In: *Chemical Engineering Science* 56.16 (2001), pp. 4929–4947.

[96] Jianfeng Wang et al. "Numerical simulation of unsteady mass transfer by the level set method". In: *Chemical Engineering Science* 63.12 (2008), pp. 3141–3151.

[97] Jan Schlottke and Bernhard Weigand. "Direct numerical simulation of evaporating droplets". In: *Journal of Computational Physics* 227.10 (2008), pp. 5215–5237.

[98] John Palmore Jr and Olivier Desjardins. "A volume of fluid framework for interface-resolved simulations of vaporizing liquid-gas flows". In: *Journal of Computational Physics* 399 (2019), p. 108954.

[99] Thomas Abadie, Joelle Aubin, and Dominique Legendre. "On the combined effects of surface tension force calculation and interface advection on spurious currents within Volume of Fluid and Level Set frameworks". In: *Journal of Computational Physics* 297 (2015), pp. 611–636.

[100] Duc Q Nguyen, Ronald P Fedkiw, and Myungjoo Kang. "A boundary condition capturing method for incompressible flame discontinuities". In: *Journal of Computational Physics* 172.1 (2001), pp. 71–98.

[101] Lucia Rueda Villegas et al. "A Ghost Fluid/Level Set Method for boiling flows and liquid evaporation: Application to the Leidenfrost effect". In: *Journal of Computational Physics* 316 (2016), pp. 789–813.

[102] Sébastien Tanguy et al. "Benchmarks and numerical methods for the simulation of boiling flows". In: *Journal of Computational Physics* 264 (2014), pp. 1–22.

[103] Tariq D Aslam. "A partial differential equation approach to multidimensional extrapolation". In: *Journal of Computational Physics* 193.1 (2004), pp. 349–355.

[104] Sébastien Tanguy, Thibaut Ménard, and Alain Berlemont. "A level set method for vaporizing two-phase flows". In: *Journal of Computational Physics* 221.2 (2007), pp. 837–853.

[105] Samuel WJ Welch. "Direct simulation of vapor bubble growth". In: *International Journal of Heat and Mass Transfer* 41.12 (1998), pp. 1655–1666.

[106] Samuel WJ Welch and John Wilson. "A volume of fluid based method for fluid flows with phase change". In: *Journal of computational physics* 160.2 (2000), pp. 662–682.

[107] Samuel WJ Welch and Thami Rachidi. "Numerical computation of film boiling including conjugate heat transfer". In: *Numerical Heat Transfer: Part B: Fundamentals* 42.1 (2002), pp. 35–53.

[108] Asghar Esmaeeli and Grétar Tryggvason. "Computations of film boiling. Part I: numerical method". In: *International Journal of Heat and Mass Transfer* 47.25 (2004), pp. 5451–5461.

[109] Frédéric Gibou et al. "A level set based sharp interface method for the multiphase incompressible Navier–Stokes equations with phase change". In: *Journal of Computational Physics* 222.2 (2007), pp. 536–555.

[110] S Hardt and F Wondra. "Evaporation model for interfacial flows based on a continuum-field representation of the source terms". In: *Journal of Computational Physics* 227.11 (2008), pp. 5871–5895.

[111] Lakshman Anumolu and Mario F Trujillo. "Gradient augmented level set method for phase change simulations". In: *Journal of Computational Physics* 353 (2018), pp. 377–406.

[112] Jonathan Reutzsch, Corine Kieffer-Roth, and Bernhard Weigand. "A consistent method for direct numerical simulation of droplet evaporation". In: *Journal of Computational Physics* 413 (2020), p. 109455.

[113] Bosen Wang et al. "Fully resolved DNS of droplet array combustion in turbulent convective flows and modelling for mixing fields in inter-droplet space". In: *Combustion and Flame* 189 (2018), pp. 347–366.

[114] Y Jin and BD Shaw. "Computational modeling of n-heptane droplet combustion in air–diluent environments under reduced-gravity". In: *International Journal of Heat and Mass Transfer* 53.25-26 (2010), pp. 5782–5791.

[115] Narugopal Ghata and Benjamin D Shaw. "Computational modeling of unsupported and fiber-supported n-heptane droplet combustion in reduced gravity: a study of fiber effects". In: *Combustion Science and Technology* 187.1-2 (2015), pp. 83–102.

Part II

Papers

Summary

This work is entirely based on the development, validation and subsequent application of DropletSMOKE++, a CFD multiphase solver conceived for the analysis of small fuel droplets evaporation and combustion in convective conditions. The code is based on the OpenFOAM® framework, which allows to build customized solvers for specific applications and provides numerical tools for the discretization, boundary conditions and the management of unstructured grids.
The work is presented as a cohesive series of four papers, written during the PhD program, each one conceived and developed as the natural continuity of the previous: (i) The first paper presents the main mathematical model, the DropletSMOKE++ code structure and its validation; (ii) in the second paper the code is extended for multicomponent fuels and including a multiregion approach to model the fiber. The application is focused on the modeling of an experimental device at Istituto Motori in Naples; (iii) the third paper presents an important extension of the model to include the droplet combustion, boiling and radiative heat transfer, including validation with experiments; (iv) the fourth paper focuses on the rigorous modeling of surface tension for droplets and the implementation in DropletSMOKE++ for future applications.

Summary of the papers

The following section contains a concise description of each paper, including motivation, methods and main results.

Paper 1

In the first paper the solver is presented and described in detail. DropletSMOKE++ is a comprehensive computational framework, based on OpenFOAM®, conceived for the evaporation of small fuel droplets under the influence of a gravity field and an external fluid flow. The Volume Of Fluid (VOF) methodology is adopted to track the interface posi-

tion, coupled with the solution of energy and species equations. The evaporation rate is directly evaluated based on the vapor concentration gradient at the phase boundary, with no need of semi-empirical evaporation sub-models.
The strong surface tension forces often prevent to model small droplets evaporation, because of the presence of parasitic currents. In this work we by-pass the problem, eliminating surface tension and introducing a suspending force directed toward the center of the droplet. This expedient represents a major novelty of this work, which allows to numerically suspend a droplet on a fiber in normal gravity conditions without modeling surface tension. Parasitic currents are completely suppressed, allowing to accurately model the evaporation process whatever the droplet size. The `DropletSMOKE++` code is then validated against experimental data in literature, showing an excellent agreement in a wide range of operating conditions, for different fuels and initial droplet diameters (both in natural and forced convection). The comparison with the same cases modeled in microgravity conditions highlights the impact of an external fluid flow on the evaporation mechanism, especially at high pressures. Non-ideal thermodynamics for phase-equilibrium is included to correctly capture evaporation rates at high pressures, otherwise not well predicted by an ideal gas assumption. Finally, the presence of flow circulation in the liquid phase is discussed, as well as its influence on the internal temperature field.

Paper 2

In the second paper, the `DropletSMOKE++` code is adopted to model an experimental device at "Istituto Motori" in Naples, performing a detailed analysis on the evaporation of acetic acid and ethylene glycol suspended droplets. An isolated droplet is positioned in a combustion chamber, suspended on a thin thermocouple and evaporated in buoyancy driven convection, following the thermal history throughout the droplet lifetime. The experiments provide quantitative and qualitative data on the evaporation physics of acetic acid, ethylene glycol and their mixture. The data are then modeled adopting the multiphase CFD code `DropletSMOKE++`, describing the flow field around the droplet, the heating rate and the evaporation process. The main novelty introduced in the computational work is a multiregion approach to describe the thermal perturbation of the suspending fiber. This extension allows to model the conjugate heat transfer with the liquid and the gas phase, as well as its impact on the droplet evaporation. `DropletSMOKE++` results show a good agreement with the experimental data, regarding both the diameter decay and the liquid temperature, whose internal distribution in the liquid is shown to be highly affected by the heat flux from the fiber (which can contribute up to 30/40%

in the total heat flux on the droplet). The effect of the thermocouple on the evaporation rate has been highlighted simulating the same experiments considering the solid as adiabatic, showing in this case a large underprediction of the vaporization rate and confirming the need of a detailed model for the tethering system to correctly predict the vaporization phenomenon. The mixture evaporation has been investigated, emphasizing the importance of adopting a detailed thermodynamic model (which includes activity coefficients) and the impact of the non-ideality of the mixture on the evaporation process. The droplet also exhibits preferential vaporization, facilitated by the internal convection in the liquid phase.

Paper 3

The third paper presents a further extension and application of `DropletSMOKE++` in order to account for *gas-phase combustion*, introducing: (i) an operator-splitting methodology to efficiently solve the gas-phase chemistry with large kinetic mechanisms, (ii) a model for the flame radiative heat transfer and (iii) a double vaporization model to account for possible boiling. This allows to simulate the combustion of suspended fuel droplets in normal gravity with a detailed description of the gas-phase chemistry, representing the novelty and the main objective of this work. The numerical model is applied to simulate the vaporization, ignition and combustion of a methanol droplet suspended on a quartz fiber at different oxygen concentrations. The numerical results are compared with recent experimental data, showing a satisfactory agreement in terms of diameter decay, radial temperature profiles and sensitivity to the oxygen concentration in the gas-phase. In particular, the burning rate is found to be significantly affected by thermal conduction from the fiber, due to its relatively large size and the high temperatures involved in the combustion process. On the other hand the fiber perturbs the flame itself, providing a partial quenching close to its surface. The relative flame position with respect to the droplet surface has been compared to the one predicted in microgravity conditions, evidencing a lower standoff ratio and a higher flame temperature due to the strong flow driven by buoyancy. The chemistry of the system has been briefly analyzed in terms of distribution of the main species in the gas phase, showing a local accumulation of (i) intermediate oxidation products at the fiber (due to the flame quenching) and (ii) water at the surface. This latter phenomenon leads to the partial condensation of water in the liquid phase, which pushes the flame farther from the droplet and slightly increases the surface temperature.

Paper 4

The surface tension force was neglected in the previous works, due its complexity and the difficulty to implement it in OpenFOAM® (see Chapter 2). The purpose of the fourth paper is to address this issue and to extend DropletSMOKE++ to include a rigorous treatment of the surface tension force, with a particular emphasis on the implementation in the OpenFOAM® framework. Due to the extensive numerical testing necessary to validate the method, the paper only focuses on the surface tension force disregarding heat transfer, phase change and variable fluid properties.
The methodology relies on a combination of (i) a well-balanced approach based on the Ghost Fluid Method (GFM), including the jump of density and pressure directly in the numerical discretization of the pressure equation, and (ii) the Height Functions method to evaluate the interface curvature, implemented, to the authors' knowledge, for the first time in OpenFOAM®. The method is able to significantly reduce spurious currents (almost to machine accuracy) for a stationary droplet, showing second order convergence both for the curvature and the interface shape. Accurate results are also obtained for additional test cases such as translating droplets, capillary oscillations and rising bubbles, for which numerical results are comparable to what obtained by other numerical codes in the same conditions. Finally, the Height Functions method is extended to include the treatment of contact angles, both for sessile droplets and droplets suspended under gravity, comparing the numerical results with the theoretical prediction.

Paper 1

DropletSMOKE++: a comprehensive multiphase CFD framework for the evaporation of multidimensional fuel droplets

A.E. Saufi, A. Frassoldati, T. Faravelli, A. Cuoci

Department of Chemistry, Materials, and Chemical Engineering "G. Natta", P.zza Leonardo da Vinci 32, Milano, Italy

International Journal of Heat and Mass Transfer (2019), vol. **131**, 836-853

Abstract

This paper aims at presenting the DropletSMOKE++ solver, a comprehensive multidimensional computational framework for the evaporation of fuel droplets, under the influence of a gravity field and an external fluid flow. The Volume Of Fluid (VOF) methodology is adopted to dynamically track the interface, coupled with the solution of energy and species equations. The evaporation rate is directly evaluated based on the vapor concentration gradient at the phase boundary, with no need of semi-empirical evaporation sub-models. The strong surface tension forces often prevent to model small droplets evaporation, because of the presence of parasitic currents. In this work we by-pass the problem, eliminating surface tension and introducing a suspending force directed towards the center of the droplet. This expedient represents a major novelty of this work, which allows to numerically hang a droplet on a fiber in normal gravity conditions without modeling surface tension. Parasitic currents are completely suppressed, allowing to accurately model the evaporation process whatever the droplet size. DropletSMOKE++ shows an excellent agreement with the experimental data in a wide range of operating conditions, for various fuels and initial droplet diameters, both in natural and forced convection. The comparison with the same cases modeled in microgravity conditions highlights the impact of an external fluid flow on the evaporation mechanism, especially at high pressures. Non-ideal thermodynamics for phase-equilibrium is included to correctly capture evaporation rates at high pressures, otherwise not well predicted by an ideal gas assumption. Finally, the presence of flow circulation in the liquid phase is discussed, as well as its influence on the internal temperature field. DropletSMOKE++ will be released as an open-source code, open to contributions from the scientific community.

Keywords: droplet, evaporation, VOF, buoyancy, convection, OpenFOAM

1 Introduction

The high energy density of liquid fuels is nowadays exploited in many engineering devices such as diesel engines and industrial burners. Spray injection systems are widely used in order to disperse the liquid fuel in an oxidizing environment and the control of this process is currently an active area of research. In particular, the study of a single isolated droplet allows to neglect complex interaction phenomena (coalescence, breakup, etc.) among droplets and to focus on the evaporation and combustion mechanisms. In the last decades the numerical modeling of droplets evaporation and combustion has considerably improved. Starting from the works of Spalding [1] and Godsave [2] concerning the well known "d^2 law", derived under the hypothesis of a perfectly spherical, motionless and constant liquid temperature droplet, Abramzon and Sirignano [3, 4] started to account for a convective flow, providing numerous correlations for the heat and mass transfer outside and within the droplet in presence of a relative gas motion. In this context, Dwyer et al. analyzed the droplet dynamics in high T fields [5, 6]. In particular, the transient surface heating has been investigated by Law [7], assuming a constant spatial liquid temperature, while Kotake and Okazaki [8] started to analyze the influence of the liquid internal circulation on the vaporization rate. More recently, Sazhin et al. analyzed the heating and evaporation process [9, 10], as well as the effect of thermal radiation [11].

With the growing available computational power, the direct numerical solution of the equations governing the evolution of isolated fuel droplets became affordable, allowing the detailed 1D modeling of spherical fuel droplets in microgravity conditions [12, 13, 14]. Microgravity conditions can be reproduced conducting the experiments in free-falling chambers [15, 16, 17], both for suspended and free droplets. Recently, some experiments have been conducted aboard the International Space Station (ISS) for the study of evaporation and multi-stage combustion phenomena. The absence of gravity allows to adopt a simple 1D mathematical description and to focus on physical aspects such as differential species diffusion, non-ideal thermodynamics and combustion kinetics. In particular, the implementation of detailed mechanisms for gas-phase chemistry in 1D models has paved the way for a better understanding of low-T chemistry [18, 19, 20] , ignition and extinction phenomena [21, 22].

However, most of experiments on droplets are conducted under the influence of a gravity field, since experimental devices are much cheaper and the operating conditions are closer to the real ones where droplets are commonly adopted. 1D models are intrinsically not able to predict physical phenomena such as buoyancy, droplet deformation, relative

gas motion and internal circulation, which are always present in real conditions. In particular, the external flow field (both induced and forced) around the droplet strongly modifies the evaporation rate at the interface, while the liquid circulation governs the internal heat transfer.

From the modeling point of view, the description of these phenomena requires at least a 2D multiphase model, able to predict the anisotropic deformation of the droplet and to provide both liquid and gas velocity fields. This must be coupled with a reliable evaporation model to describe the droplet shrinking, the diffusion of vapor towards the gas-phase and its further transport, both by the external convection and by the induced Stefan flow. The energy transfer between the two phases is also necessary, as well as proper correlations for the fluid properties.

Among the several methods available for multiphase flows, the Volume Of Fluid (VOF) methodology [23] is widely known for its simplicity, robustness and especially for the excellent mass conservation properties. Its application for evaporation and condensation phenomena has been investigated in recent years [24, 25, 26, 27]. However, most of these works rely on phase-change models based on experimental data, kinetic theories and semi-empirical correlations. A more general evaporation model based on the interface concentration gradient has been implemented by Shlottke [28], neglecting however the detailed characterization of thermodynamic equilibrium at the interface and without a comparison of the results with experimental data. More recently, Gatha et al. [29, 30] used a VOF technique to model droplet evaporation and combustion, limiting however the investigation to microgravity conditions.

A major numerical issue of VOF method concerns surface tension. Small droplets dynamics involve strong surface tension forces, which are extremely difficult to model due to the presence of the so-called parasitic currents [31]. These currents tend to numerically deform and eventually destroy the droplet, due to inaccuracies on the evaluation of the surface curvature. Some techniques [32, 33] have been developed to mitigate parasitic currents for particular cases (e.g. rising bubbles, inviscid static droplets, capillary oscillations), but small droplets evaporation still suffers from this issue. The rapid size reduction of the droplet makes surface tension to be more and more dominant, further amplifying the problem. Even if some works concerning droplets vaporization with VOF methodology are available in literature [34, 35, 36], the problem of parasitic currents is often not even mentioned. These works are based on commercial CFD codes (mainly `Ansys FLUENT`® and `COMSOL`®), making very difficult to reproduce the results with open-source codes since the adopted numerical algorithms are not provided in detail. Concerning the numerical framework, promising results have been reached by codes such

as FS3D [37] and Gerris [38], whereas the OpenFOAM® environment is still lacking in comprehensive solvers for the detailed analysis of droplets evaporation.
This work aims at presenting an open-source general computational tool (called DropletSMOKE++) for the modeling of isolated droplets evaporation under convective conditions in the presence of a gravity field, overcoming the aforementioned limits of the currently available solvers. In particular it includes:

- An accurate interface tracking method, based on a geometrical advection, coupled with the Navier-Stokes equations, numerically solved for both liquid and gas phase.
- A reliable evaporation model based on the surface mass flux, coupled with a species equation, with no need of semi-analytical approaches or correlations based on mass-heat transfer dimensionless numbers.
- The detailed description of the vapor-liquid equilibrium thermodynamics, including fugacity coefficients and Poynting correction calculation using a cubic Equation of State.
- A numerical technique which suppresses parasitic currents and by-passes the problem of curvature evaluation, introducing an external suspending force to mimic surface tension effects.

The DropletSMOKE++ code is fully implemented within the open-source OpenFOAM® framework to manage the computational mesh and the discretization of governing equations. The numerical code will be freely available and open for contributions from the scientific community. The code version used for this work is provided in the supplementary material.
The paper organization includes a thorough description of the mathematical model, as well as the numerical methodology adopted. The suspending force substituting surface tension is discussed in detail, including its numerical implementation, its effect on the droplet shape and how it impacts evaporation.
A quantitative assessment of the code has been performed, comparing the DropletSMOKE++ results with a reference finite-differences based solver for droplets evaporation in microgravity conditions [13]. Afterwards, the gravity field has been introduced, allowing the analysis of the natural and forced convection regime.
An extensive validation with available experimental data has been carried on for n-heptane, n-decane and n-hexadecane droplets in a very wide range of operating conditions, both for natural and forced convection. Experimental data from various authors

include the normalized equivalent diameter decay and some data on the surface temperature behavior, which have been compared with the `DropletSMOKE++` numerical results. Equivalent numerical cases (with the same initial conditions) have been simulated also in microgravity conditions in order to highlight the main differences between the models and the intrinsic inability of microgravity solvers to correctly predict the experimental data. Finally, the presence of internal circulation in the liquid phase is briefly analyzed.

2 Mathematical model

2.1 Interface advection

The VOF methodology is often referred to as a "one-fluid" approach, where the two phases are treated as a single fluid whose properties vary abruptly at the phase boundary. A scalar marker function α represents the liquid volumetric fraction, varying from value 0 in the gas-phase to value 1 in the liquid phase. The α advection equation in the most general form is:

$$\frac{\partial(\rho\alpha)}{\partial t} + \nabla \cdot (\rho\alpha\mathbf{v}) = -\dot{m} \tag{1}$$

The source term $\dot{m}$ represents the evaporation/condensation contribution to the liquid. Rewriting the equation in function of α:

$$\frac{\partial\alpha}{\partial t} + \nabla \cdot (\mathbf{v}\alpha) = -\frac{\dot{m}}{\rho} - \frac{\alpha}{\rho}\frac{D\rho}{Dt} \tag{2}$$

This equation is solved in two steps, treating the advection and the source terms in a segregated approach, similarly to what happens in an operator-splitting technique. The interface tracking is solved first, using the `isoAdvector` library developed by Roenby and Jasak [39] :

$$\frac{\partial\alpha}{\partial t} + \nabla \cdot (\mathbf{v}\alpha) = 0 \tag{3}$$

`isoAdvector` performs a geometric advection of the interface, whose quality is superior (Figure 1) to the MULES (Multidimensional Universal Limiter with Explicit Solution) compressive scheme by Weller [41] usually used in `OpenFOAM`® multiphase solvers. The source terms are included in a second step:

$$\frac{\partial\alpha}{\partial t} = -\frac{\dot{m}}{\rho} - \frac{\alpha}{\rho}\frac{D\rho}{Dt} \tag{4}$$

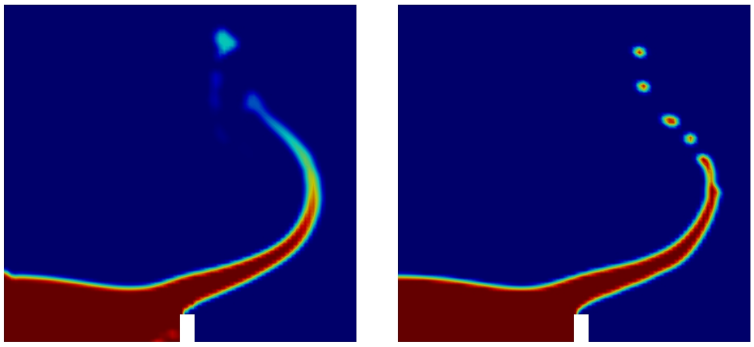

(a) (b)

Figure 1: Comparison of the interface resolution between the MULES compressive scheme (Figure a) and `isoAdvector` (Figure b) for the well known `damBreak` case [40].

where the first term accounts for the evaporation, while the second term describes the liquid density variation, and eventually the droplet expansion due to external heating.

2.2 Pressure and velocity fields

A single Navier-Stokes equation is solved for both phases:

$$\frac{\partial(\rho\mathbf{v})}{\partial t} + \nabla\cdot(\rho\mathbf{v}\otimes\mathbf{v}) = \nabla\cdot\mu\left(\nabla\mathbf{v} + \nabla\mathbf{v}^T\right) - \nabla p + \rho\mathbf{g} \tag{5}$$

It is convenient to separate the hydrostatic pressure $\rho\mathbf{g}\cdot\mathbf{r}$ from the total pressure p, in order to simplify the definition of boundary conditions for pressure:

$$\frac{\partial(\rho\mathbf{v})}{\partial t} + \nabla\cdot(\rho\mathbf{v}\otimes\mathbf{v}) = \nabla\cdot\mu\left(\nabla\mathbf{v} + \nabla\mathbf{v}^T\right) - \nabla p_{rgh} - \mathbf{g}\cdot\mathbf{r}\nabla\rho \tag{6}$$

where $p_{rgh} = p - \rho\mathbf{g}\cdot\mathbf{r}$ is the dynamic pressure and $\mathbf{r}$ is the position vector.
The continuity equation (needed for the pressure-velocity coupling) accounts for the density variations and for the abrupt change of density at the interface occurring during the evaporation, generating the Stefan flow:

$$\frac{\alpha}{\rho_L}\frac{D\rho_L}{Dt} + \frac{1-\alpha}{\rho_G}\frac{D\rho_G}{Dt} + \dot{m}\left(\frac{1}{\rho_L} - \frac{1}{\rho_G}\right) + \nabla\cdot\mathbf{v} = 0 \tag{7}$$

In case of constant density and no evaporation Equation 7 reduces to the continuity equation for incompressible flows $\nabla\cdot\mathbf{v} = 0$.

2.3 Temperature and species fields

Additionally, energy and species equations are included:

$$\rho C_p \left(\frac{\partial T}{\partial t} + \mathbf{v} \nabla T \right) = \nabla \cdot (k \nabla T) + \beta \frac{Dp}{Dt} - \sum_{i=0}^{Ns} \mathbf{j}_{d,i} C_{p,i} \nabla T - \sum_{i=0}^{Ns_L} \dot{m}_i \Delta h_{ev,i} \tag{8}$$

$$\rho \left(\frac{\partial \omega_i}{\partial t} + \mathbf{v} \nabla \omega_i \right) = -\nabla \cdot \mathbf{j}_{d,i} \tag{9}$$

The last term in Equation 8 accounts for the interface cooling during evaporation. The diffusion fluxes $\mathbf{j}_{d,i}$ are discussed in the next section.

2.4 Evaporation model

In this work, the mass evaporation flux is calculated based on the interface concentration gradient of the vapor. Its evaluation is not trivial, since it strongly depends on how the diffusion coefficients are computed. The species diffusion coefficients $\mathcal{D}_i$ in the mixture are evaluated based on the binary diffusion coefficients and the mole fractions:

$$\mathcal{D}_i = \frac{\sum_{j \neq i} y_j M_{w,j}}{M_w \sum_{j \neq i} \frac{y_i}{\mathcal{D}_{i,j}}} \tag{10}$$

which means that the diffusion velocities $\mathbf{v}_{d,i}$ must be evaluated based on the mole fraction gradient of the species [42]:

$$\mathbf{v}_{d,i} = -\mathcal{D}_i \frac{\nabla y_i}{y_i} \tag{11}$$

The diffusion fluxes $\mathbf{j}_{d,i}$ are defined as:

$$\mathbf{j}_{d,i} = \rho \omega_i \mathbf{v}_{d,i} = -\rho \omega_i \mathcal{D}_i \frac{\nabla y_i}{y_i} = -\rho \mathcal{D}_i \frac{M_{w,i}}{M_w} \nabla y_i \tag{12}$$

This expression of the diffusion flux is also used in Equation 9.

A convective flux $\mathbf{j}_{c,i}$ is generated by the interfacial density change during the evaporation process, as stated in Equation 7:

$$\mathbf{j}_{c,i} = \rho \omega_i \mathbf{v} \tag{13}$$

The total evaporating flux $\mathbf{j}_i$ is the sum of diffusive and convective fluxes:

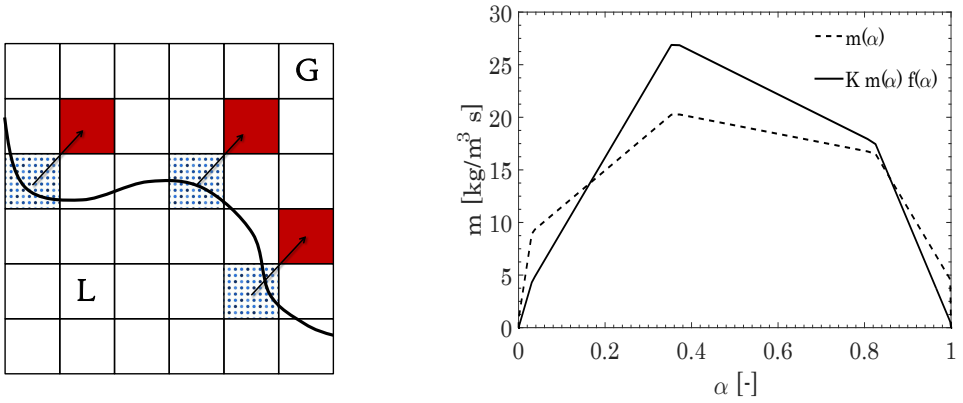

(a) (b)

Figure 2: Calculation of $\dot{m}_i = \mathbf{j}_i|\nabla\alpha|$ in Figure (a): interface cells (in dotted blue) associated to the adjacent gas-phase cells (in red). In Figure (b): evaporation flux $\dot{m}$ distribution over the interface for standard implementation (dashed line, Equation 16) and corrected implementation (solid line, Equation 19).

$$\mathbf{j}_i = \mathbf{j}_{d,i} + \mathbf{j}_{c,i} \tag{14}$$

The local surface area per unit volume is usually computed from the α function as $|\nabla\alpha|$, since its volume integral is the surface area by definition:

$$S = \int_V |\nabla\alpha| dV \tag{15}$$

The evaporation rate for species i is then:

$$\dot{m}_i = \mathbf{j}_i \nabla\alpha \tag{16}$$

It is important to point out that $|\nabla\alpha|$ is calculated at the interface cells (where $|\nabla\alpha| \neq 0$), while $\mathbf{j}_i$ must be computed at the gas cells adjacent to the interface cells. Referring to Figure 2 (a), a specific algorithm has been developed to associate every cell at the interface (represented in dotted blue) to the closest cell in the gas-phase (represented in red) along the interface normal (black arrow). Indicating with subscript *int* a generic interface cell and with *adj* the closest adjacent gas-phase cell with respect to *int*, we have:

$$\dot{m}_i|_{int} = \mathbf{j}_i|_{adj}|\nabla\alpha|_{int} \tag{17}$$

which has to be evaluated for every cell at the interface.

The total evaporation rate $\dot{m}$ is the sum over the liquid (evaporating) species:

$$\dot{m} = \sum_{i=0}^{Ns_L} \dot{m}_i \tag{18}$$

When solving Equation 4 it is important to ensure a sharp interface. However, it is possible for α to reach negative values in certain cells, especially if $\dot{m}$ is high enough. In order to avoid this, $\dot{m}$ is multiplied by a proper function of α, whose aim is to force $\dot{m}$ to be zero when α approaches zero. Differently from previous works [27], the evaporating flux is evaluated as follows:

$$\dot{m} = Kf(\alpha) \sum_{i=0}^{Ns_L} \dot{m}_i \tag{19}$$

where the constant K is introduced to ensure the conservation of the integral mass flux $\int_V \dot{m} dV$. It is simply recovered equaling Equations 18 and 19 after a volume integration:

$$K = \frac{\int_V \dot{m} dV}{\int_V f(\alpha) \dot{m} dV} \tag{20}$$

We have chosen the function $f(\alpha)$ as follows:

$$f(\alpha) = \sqrt{\alpha (1 - \alpha)} \tag{21}$$

which is a redistribution of $\dot{m}$ over the interface, as shown in Figure 2. This function goes to 0 and to 1 much faster, which helps to maintain a sharp interface after Equation 4 solution.

2.5 Thermodynamic equilibrium

The characterization of equilibrium thermodynamics at the phase boundary is crucial for a correct prediction of experimental data, especially for non-ideal mixtures and high pressure cases. In this work a detailed thermodynamics is included, based on Peng and Robinson equation of state [43] for the evaluation of the compressibility factor Z and the fugacity coefficients ϕ_i.
The vapor-liquid equilibrium relation for a two-phase systems is [44]:

$$p_i^0(T) x_i \phi_i \left(T, p_i^0\right) e^{\int_{p_i^0}^{p} \frac{v_{L,i}}{RT} dp} = p y_i \hat{\phi}_i(T, p, y_i) \tag{22}$$

where $p_i^0(T)$ is the vapor pressure of species i, ϕ_i is the gas-phase fugacity coefficient for the pure species and $\hat{\phi}_i$ is the gas-phase mixture fugacity coefficient. The exponential term represents the Poynting correction, while x_i and y_i are the liquid and gas mole fractions of species i. The gaseous mole fraction y_i is evaluated in a segregated approach, from equation 22:

$$y_i = \frac{p_i^0(T)\phi_i\left(T, p_i^0\right) e^{\int_{p_i^0}^{p} \frac{v_{L,i}}{RT} dp}}{p\hat{\phi}_i(T, p, y_i)} x_i \tag{23}$$

This saturation mole fraction is assigned to the whole liquid phase and then advected in the gas phase through Equation 9, following the approach described in [45].
The gas density is calculated by:

$$\rho_G = \frac{pM_w}{Z(T, p, y_i)RT} \tag{24}$$

where Z is provided by the Peng-Robinson cubic equation of state.
The molar volume v_L in the Poynting correction is simply evaluated as:

$$v_{L,i} = \frac{M_{w,i}}{\rho_L} \tag{25}$$

2.6 The problem of surface tension: introduction of the suspending force field

The droplet-gas interaction is characterized by high density ratios between the two phases and strong surface tension forces, particularly enhanced in small droplet sizes. Even though VOF methods are widely recognized for the great efficiencies in describing topologically complex interfaces, the accurate representation of surface tension is still a major problem in multiphase flows [33].
The continuous representation of surface tension force $\mathbf{f}_s$ by Brackbill [31] requires an accurate evaluation of the interface curvature κ:

$$\mathbf{f}_s = \sigma\kappa\nabla\alpha \tag{26}$$

where curvature κ is evaluated as:

$$\kappa = \nabla \cdot \left(\frac{\nabla\alpha}{|\nabla\alpha|}\right) \tag{27}$$

The α gradient evaluation is numerically challenging, because of the discontinuous nature of the α function. A direct implementation of Equation 26 creates a numerical

imbalance between the surface tension force $\mathbf{f}_s$ and the pressure gradient ∇p in the Navier-Stokes equation. As a consequence, unphysical flows and pressure spikes are generated around the interface, whose magnitude is proportional to σ and inversely proportional to the droplet size. For the typical droplet diameters of the experiments (usually no more than 1-1.5 mm) these flows can strongly deform the interface and eventually break the droplet apart. Several methods have been proposed in this context, such as balanced force algorithms [46] to reduce the numerical imbalance in surface tension force evaluation, height functions [46] to compute the interface curvature directly from the α field and artificial viscosity methods [47]. A sophisticated combination of quad/octree spatial discretization, height functions and balanced algorithms has been implemented by Popinet [38] in Gerris solver.
Concerning the `OpenFOAM`® environment, Albadawi [48] proposed a coupled VOF-Level Set to mitigate the parasitic currents, while Raeini [49] introduced smoothing factors for κ field combined with the introduction of a capillary pressure equation and a curtailing of the α marker. Even if these latter methods significantly improve the modeling of surface tension forces, they have been validated on bubbles growth, stationary droplets and capillary flows, whereas no test case can be found on small droplets dynamics. Their application on the cases of our interest did not provide satisfactory results, mainly because the droplet shrinking due to the evaporation exponentially amplified the problem: the lower was the droplet size, the stronger were the parasitic currents around the interface, even if the initial stationary droplet was stabilized enough.

In this work, in order to avoid these problems, parasitic currents have been suppressed directly from their source imposing zero surface tension. In presence of a gravity field surface tension is essential to hang the droplet on a fiber or a wire. Therefore, its elimination required the introduction of an additional force to compensate the droplet weight.
A small spherical fiber is initially introduced inside the liquid droplet. A suspending force directed towards the center of the fiber have been imposed, defined as:

$$\mathbf{f}_m = \rho \alpha \nabla \xi \tag{28}$$

where ξ is a scalar potential field defined as:

$$\xi = \xi_0 \frac{D_f}{2r} \tag{29}$$

where D_f is the fiber radius ($D_f = 0.05$ mm in this work), r is the distance from the fiber center and ξ_0 the intensity of the potential field. The α term in Equation 28 forces

$\mathbf{f}_m$ to be applied to the sole liquid phase and makes $\mathbf{f}_m$ to be proportional to the droplet volume, as it is for gravity forces.
The result is a force field directed towards the droplet center and only applied to the liquid phase, similarly to what happens in a magnetic attraction of a ferrofluid. The Navier-Stokes equation becomes:

$$\frac{\partial(\rho\mathbf{v})}{\partial t} + \nabla\cdot(\rho\mathbf{v}\otimes\mathbf{v}) = \nabla\cdot\mu\left(\nabla\mathbf{v} + \nabla\mathbf{v}^T\right) - \nabla p_{rgh} - \mathbf{g}\cdot\mathbf{r}\nabla\rho + \mathbf{f}_m \tag{30}$$

It is important to notice that the combination of a geometrical advection (i.e. `isoAdvector`) and the absence of surface tension σ allows to track the interface maintaining a very high resolution, without any additional correction (such as filtering kernels, smoothing factors etc.) usually needed in the VOF methodology because of the strong gradients involved. The detailed numerical description and the implementation of the suspending force $\mathbf{f}_m$ are presented in the next section, as well as a sensitivity analysis on the value ξ_0 to be used in the simulations. The effect of the initial droplet shape on the evaporation will be also discussed.

2.7 Fluid properties

The evaluation of transport and thermodynamics properties is based on the OpenSMOKE++ library [50]. Gas properties (diffusion coefficients, thermal conductivity, heat capacities and viscosity) are based on the kinetic theory of gases, while liquid properties (vapor pressure, density, conductivity, heat capacity, viscosity and vaporization heat) are evaluated based on the correlations available in the Yaws database [51].
Mixture properties to be used in the governing equations can be then computed. For a generic property χ:

$$\chi = \chi_L\alpha + \chi_G\left(1-\alpha\right) \tag{31}$$

with $\chi = \rho, \mu, C_p, k, \mathcal{D}_i$.

3 Numerical methodology

3.1 Description of the DropletSMOKE++ solver

The `DropletSMOKE++` code is embedded within the `OpenFOAM`® framework which allows to manage the spatial discretization of the governing equations on arbitrary geometries. The PIMPLE algorithm [40], a combination between SIMPLE (Semi-Implicit Method for Pressure-Linked Equations) and PISO (Pressure Implicit Splitting of Operators), is

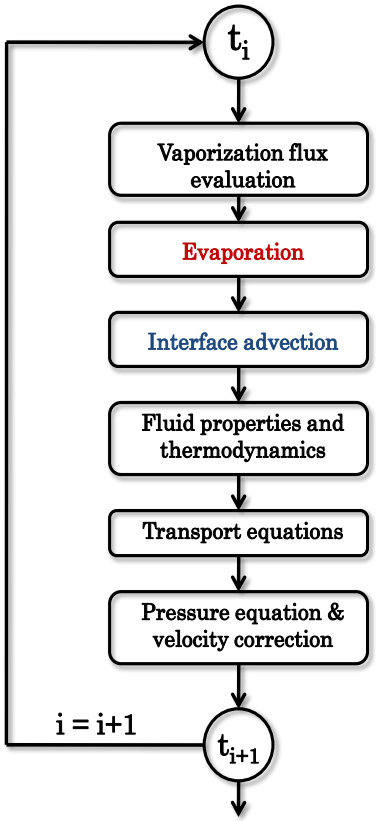

Figure 3: Steps of the numerical algorithm used in `DropletSMOKE++`

Boundary	α	$\mathbf{v}$	T, ω_i	p_{rgh}
inlet (natural convection)	$\alpha = 0$	inletOutlet	inletOutlet	$p_{rgh} = p_{ext}$
inlet (forced convection)	$\alpha = 0$	$\mathbf{v} = \mathbf{v}_{ext}$	$T, \omega_i = T_{ext}, \omega_{i,ext}$	$\nabla p_{rgh} = 0$
outerWall	$\alpha = 0$	noSlip	$\nabla T, \nabla \omega = 0$	$\nabla p_{rgh} = 0$
outlet	$\alpha = 0$	inletOutlet	inletOutlet	$p_{rgh} = p_{ext}$
sphere	$\nabla \alpha = 0$	noSlip	$\nabla T, \omega = 0$	$\nabla p_{rgh} = 0$

Table 1: Boundary conditions for α, velocity, temperature, species i and pressure field, to be compared with Figure 4.

used to manage the pressure-velocity coupling, computing a velocity field which satisfies both momentum and continuity equation through an iterative procedure.
For every time step, `DropletSMOKE++` encompasses the following steps in a segregated approach (Figure 3):

1. Evaluation of the evaporation flux (Equation 16)
2. Liquid evaporation or expansion (Equation 4)
3. Interface advection (Equation 3)
4. Update of gas-liquid properties and thermodynamics
5. Momentum, temperature and species equation (Equations 30, 8, 9)
6. Iterative calculation of the pressure field (Equation 7) and velocity correction

The time discretization follows an implicit Euler method, where the time step is automatically computed based on a threshold Courant number. As reported by Brackbill et al. [31], the VOF time step constraint states that $\Delta t < \left[\frac{\rho(\Delta x)^3}{2\pi\sigma}\right]^{\frac{1}{2}}$, which depends on surface tension. It is worth noticing that the suppression of surface tension introduced in this work alleviates this constraint, allowing larger time steps to be used.
Finally, Gauss linear upwind scheme is used for spatial discretization of convective terms, while an orthogonal correction is adopted for Laplacian terms.

3.1.1 Computational mesh

The computational mesh used for all the numerical cases proposed in this work has been built with the commercial CFD code `Ansys FLUENT`® v17.2. The geometry is 2D and axisymmetric, representing a slice of a cylinder having a radius $W = 5$ mm and a height

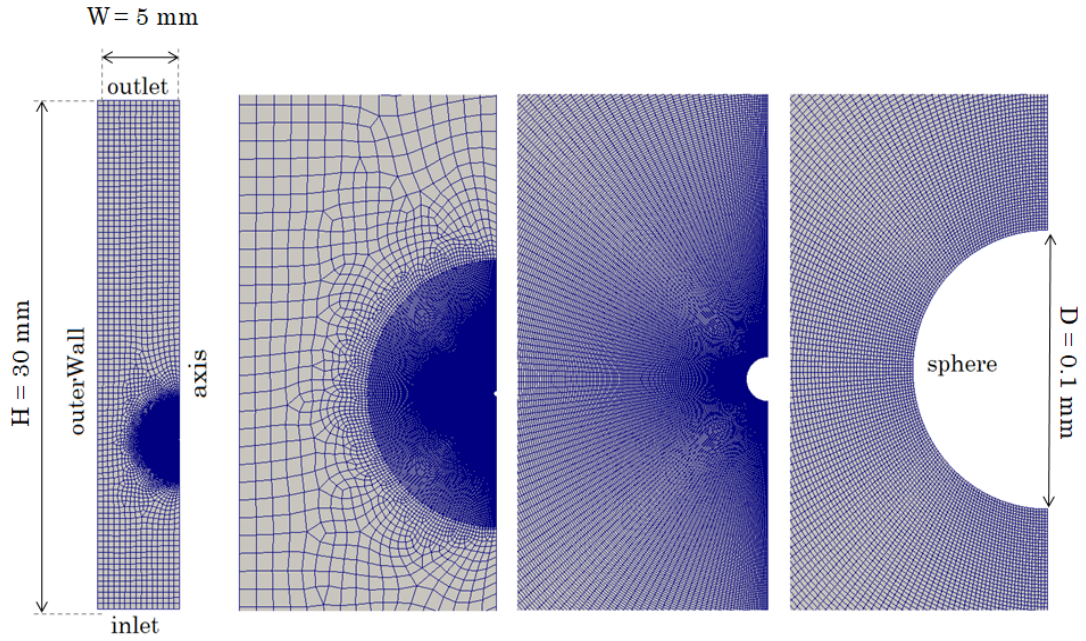

Figure 4: Computational mesh represented in increasing levels of detail, from left to right. The boundary names are also shown, to be compared with Table 1.

$H = 30$ mm. At 10 mm from the base a spherical fiber (diameter $D = 0.1$ mm) is introduced, which is needed as a source for the force field $\mathbf{f}_m$ previously described. The liquid droplet will be place around this small spherical fiber. The geometry is meshed in a non-structured way (Figure 4), with a particular attention to the gas-liquid boundary: the mesh is structured and orthogonal on the cylinder boundaries. The region including the liquid droplet and the gas in its proximity is meshed with a concentric pattern, getting finer while approaching the inner fiber. Therefore, the presence of a spherical boundary is also necessary for the mesh construction.
In this work, the mesh is composed by 70,000 cells, with a maximum mesh non-orthogonality equal to 56.6 and a maximum Skewness of 1.3. It has been verified that the numerical solution does not change doubling the number of cells, proving mesh independence (Appendix A).

3.2 Boundary conditions

The definition of proper boundary conditions is fundamental to reach reliable results. The geometry has four boundaries, shown in Figure 4:

1. outerWall: external lateral surface of the cylinder

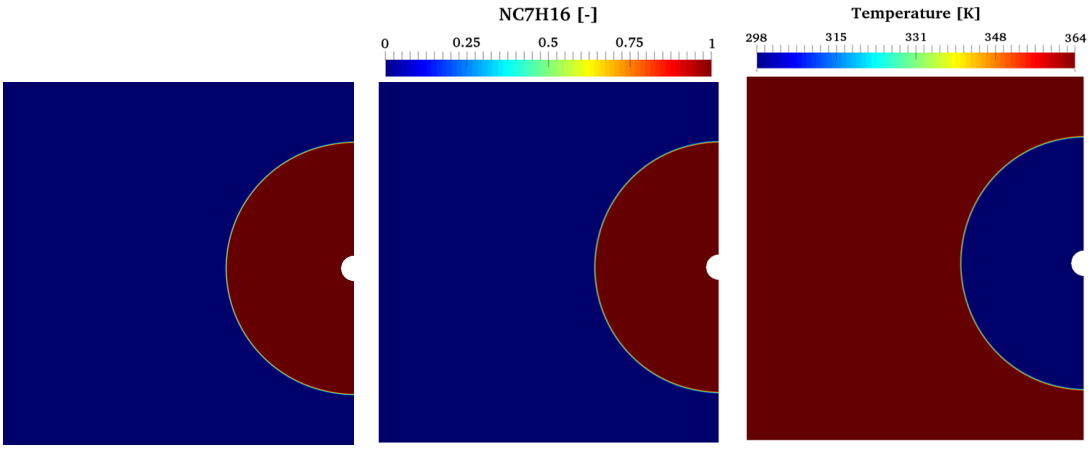

(a) (b) (c)

Figure 5: Example of initial conditions in droplet evaporation simulations. Liquid volume fraction (α field) in Figure (a), n-heptane mass fraction in Figure (b) and temperature field in Figure (c).

2. inlet: the bottom base surface of the cylinder

3. outlet: the upper base of the cylinder

4. sphere: the spherical fiber surface

The boundary conditions are summarized in Table 1. The *inlet* boundary conditions change depending on the case (natural or forced convection). The *inletOutlet* condition is basically a zero gradient condition, that switches to a fixed value condition if the velocity vector next to the boundary points inside the domain (backward flow). The *noSlip* condition imposes a zero relative velocity between the fluid and the boundary. It is worth noticing that the separation of the hydrostatic pressure, allows a simple definition of boundary conditions for p_{rgh}.

3.3 Initial conditions

Referring to the mesh presented in Figure 4, the liquid droplet must be positioned around the spherical fiber. In Figure 5 the initial conditions for the evaporation of a cold n-heptane droplet in a hot environment are presented as an example.

Case	Species	D_0 [mm]	T_L [K]	T_G [K]	p [atm]	Results [Figure 6]
1	n-Decane	0.5	435	435	1	(a, b, c)
2	n-Heptane	0.5	360	360	1	(d, e, f)
3	n-Heptane	1.03	300	364	20	(g, h, i)
4	Water	0.7	360	360	1	(j, k, l)

Table 2: Numerical cases for the comparison with 1D model [13]. The related plots are reported in Figure 6.

3.4 Code parallelization

The numerical cases presented in this work are run on a multi-processor (Intel Xeon X5675, 3.07 GHz) machine. The Domain Decomposition Method is used to split the mesh into sub-domains and allocate them to separate processors. The `DropletSMOKE++` code can then run in parallel mode, with communication between processors with MPI communication protocol, allowing a significant reduction of the computational time. The optimal number of processors is found to be around 12, which corresponds to an average of 6000 cells for each processor and a speed-up performance ~ 6 times higher with respect to the serial mode.
The simulations required from 2 to 20 hours, depending on the operating conditions.

4 Validation of microgravity cases

In this section `DropletSMOKE++` is validated in microgravity conditions (imposing $\mathbf{g} = \mathbf{0}$), against the numerical results of the solver developed by Cuoci et al. [13]. This latter code has been validated in a wide range of operating conditions over the last 10 years [22, 21] and represents a reliable reference for comparison. This validation is done in order to assess the validity of the equations (in terms of diameter decay, temperature profiles and vaporization velocity) before the activation of the gravity field. Obviously, the suspending force $\mathbf{f}_m = 0$ in these cases.

The 4 numerical cases analyzed are listed in Table 2. Three liquids have been chosen (n-decane, n-heptane and water) at different temperature and pressure conditions. Numerical results are summarized in Figure 6.
For each case (lines) three plots are reported (columns): the temporal evolution of the droplet size, the liquid surface temperature and the vaporization velocity. More precisely, this latter is the convective velocity of the gas generated at the phase boundary.

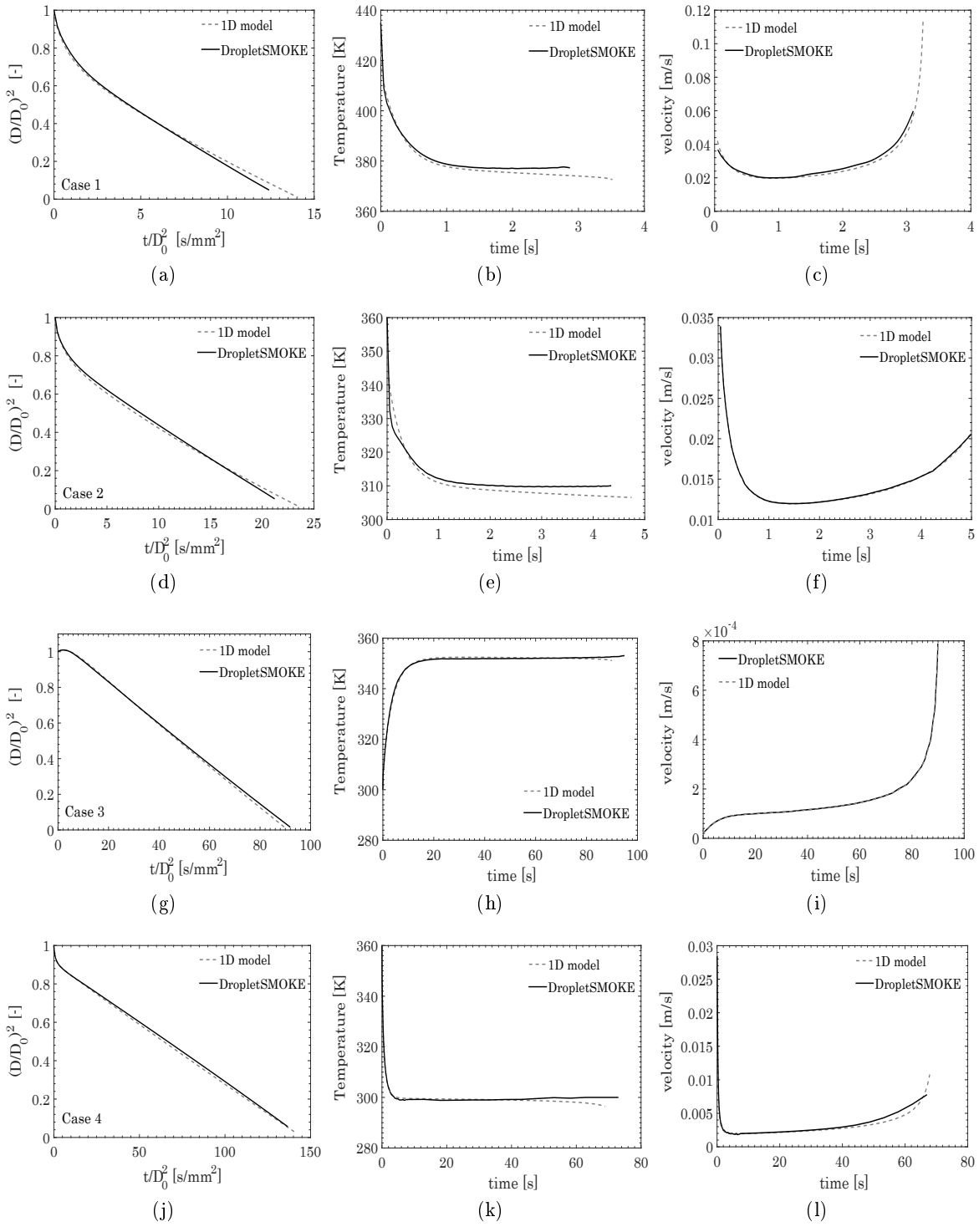

Figure 6: Numerical comparison of the 1D model of Cuoci et al. [13] and `DropletSMOKE++` (Table 2).

4.1 Results and discussion

For all cases the squared diameter, after the initial transient period, reduces linearly with time, as the d^2 law states. A wet-bulb temperature is reached by the interface and maintained along the whole evaporation process, due to the equilibrium between the incoming heat flux and the outcoming vaporization enthalpy. The transient period depends on the initial conditions. In cases 1-2-4 (initially isothermal) the interface is immediately cooled, diminishing the vaporization flux. In case 3 the liquid is firstly heated (reducing ρ_L and increasing the droplet size) providing an increasing vaporization flux.
The agreement between the models can be considered satisfactory, even if small differences exist. In particular the surface temperature tends to be slightly over-predicted, especially in the final steps of the evaporation. This is probably due to the spherical boundary of the fiber in the `DropletSMOKE++` simulations (Figure 4), which is absent in the 1D model. The presence of a small sphere inside the liquid provides a lower droplet mass if compared to a 1D droplet with the same initial diameter. As can be seen in Figure 6 its effect is completely negligible for most of the simulation (the "missing" mass is less than 0.01% of the initial total mass). While the droplet surface approaches the fiber, this effect becomes important: the incoming heating flux is now distributed over a lower liquid mass, providing a slightly higher equilibrium temperature. This will not be a problem when modeling evaporation under convection, since fibers are always present in experiments to hang liquid droplets.

5 Implementation of the suspending force $\mathbf{f}_m$

In order to sustain the droplet against the gravity field, a suspending force $\mathbf{f}_m$ (Equation 28) is introduced, based on a potential ξ defined by Equation 29, represented in Figure 7 (a) and previously described in the mathematical model. The liquid droplet is then fixed around the fiber (Figure 7 b). Inside the droplet a small pressure gradient is established (from $\sim$100 to $\sim$500 Pa, depending on the value ξ_0), similarly to what happens for a liquid column subjected to a gravity field (Figure 7 c). This is actually consistent with surface tension forces, which provide an internal pressure higher than the external one (capillary pressure).

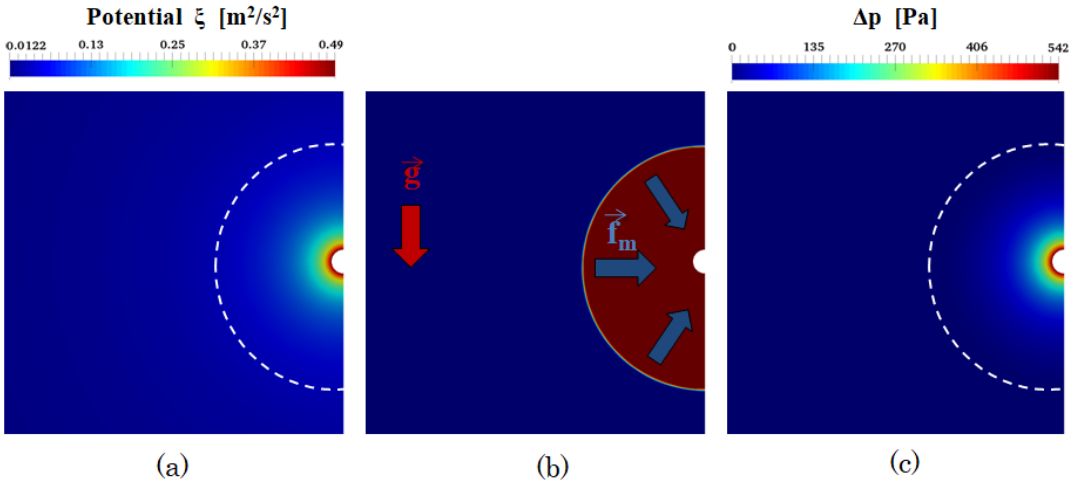

Figure 7: Potential field ξ (Figure a) around fiber, evaluated with $\xi_0 = 1\ m^2/s^2$. In Figure (b) the droplet is placed around the fiber and sustained against gravity $\mathbf{g}$ by the force $\mathbf{f}_m = \rho\alpha\nabla\xi$. The $\Delta p = p - p_{ext}$ field is presented in Figure (c). The white dashed lines in (a,c) represent the droplet surface.

5.1 Control of the droplet shape

A droplet suspended under the effect of a gravity field reaches a steady-state shape imposed by the equilibrium between the liquid weight, the pressure gradient and the surface tension forces:

$$-\nabla p + \sigma\kappa\nabla\alpha + \rho\mathbf{g} = \mathbf{0} \tag{32}$$

In this work surface tension in not considered, and the suspending force $\mathbf{f}_m$ governs the equilibrium shape of the droplet:

$$-\nabla p + \mathbf{f}_m + \rho\mathbf{g} = \mathbf{0} \tag{33}$$

The intensity of $\mathbf{f}_m$ can be controlled by the value of the constant ξ_0, which defines the potential field ξ (Equation 29). Figure 8 shows the equilibrium shape assumed by a n-heptane droplet (1 mm diameter, ambient T) for different values of ξ_0, from 0.35 to 2 $\frac{m^2}{s^2}$. For values $\xi_0 < 0.35\ \frac{m^2}{s^2}$ the droplet falls down, while for $\xi_0 > 2\ \frac{m^2}{s^2}$ the droplet shape remains spherical. These threshold values have been found to be nearly the same for different liquids.

The effect is very similar to surface tension forces: for low values of ξ_0 (or surface tension σ) the droplet tends to assume an elongated shape, because of the dominant gravity forces. Increasing ξ_0 (or surface tension σ), the droplet approaches a spherical geometry.

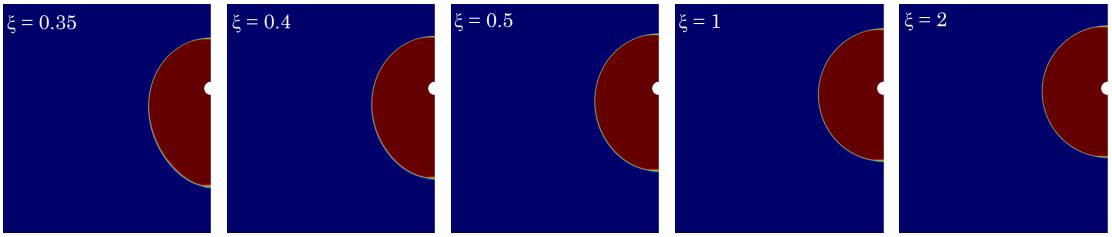

(a) (b) (c) (d) (e)

Figure 8: Equilibrium shape of a n-heptane droplet ($D_0 = 1$ mm, ambient T) under the effect of gravity $\mathbf{g}$ and different intensities of the potential field $\xi_0 \left[\frac{m^2}{s^2}\right]$.

In this work ξ_0 represents a degree of freedom of the problem, which we can saturate imposing a ξ_0 value that better describes the droplet shape of the experimental cases.

5.2 Effect of the droplet shape on evaporation

In order to set a proper initial shape of the droplet, a sensitivity analysis on the evaporation process has been carried out. Two numerical simulations of an evaporating n-heptane droplet have been run for the threshold values $\xi_0 = 0.35\ \frac{m^2}{s^2}$ and $\xi_0 = 2\ \frac{m^2}{s^2}$, (Figures 8 a, e). The initial droplet diameter $D_0 = 1$ mm, the liquid temperature is $T_L = 300$ K, the ambient temperature is $T_G = 364$ K and the pressure is $p = 20$ bar.
From Figure 9 we can see that the droplet shape does not have a major impact on the evaporation process. The surface area increases for lower values of ξ_0, explaining the slightly larger evaporation rates (Figure 9 c), while the surface temperature (Figure 9 b) is almost insensitive to ξ_0.
We expect the experimental cases of our interest to behave somewhere in-between these two cases, closer to the upper limit described by the black lines in Figure 9
In order to verify this hypothesis, a simple analysis has been conducted on the droplet shapes usually involved in experiments. 10 pictures of suspended droplets available in literature from experimental works [52, 53, 54, 55, 56, 57, 58] have been collected (Figure 10 b) and organized based on two dimensionless numbers, the sphericity ψ and the Eötvös number Eo, defined as:

$$\psi = \frac{D_y}{D_x} \tag{34}$$

$$Eo = \frac{(\rho_L - \rho_G)\, g D^2}{\sigma} \sim \frac{\rho_L g D^2}{\sigma} \tag{35}$$

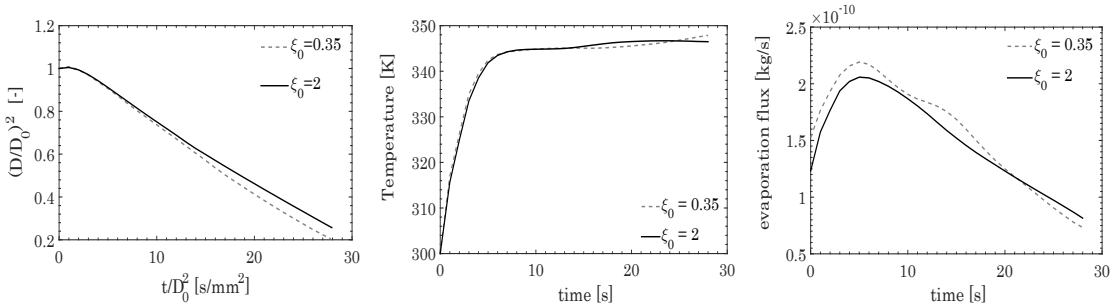

(a) (b) (c)

Figure 9: Effect of the droplet shape on the evaporation process. The dashed grey line corresponds to Figure 8 (a), while the black line refers to Figure 8 (e).

where D_y and D_x are the maximum lengths of the droplet, in vertical and horizontal directions. The sphericity ψ is a measure of how the droplet shape approaches that of a perfect sphere (which has $\psi = 1$). The Eötvös number Eo is the ratio between gravitational and surface tension forces. A further classification is introduced based on the tipe of supporting fiber (vertical, horizontal or cross fiber). The 10 experimental cases are reported in Figure 10 (a), together with the black line $\psi = 1$, representing a perfect sphere (Figure 8 e), and the gray line $\psi = 1.2$ representing the limit case in Figure 8 (a).

The Eötvös number is below 1 for all cases, indicating that surface tension forces always dominate over gravity. The sphericity $0.86 < \psi < 1.12$ indicates nearly spherical shapes for all the droplets, especially when cross fibers are used (black points). As expected, the horizontal fibers tend to slightly deform the droplet along D_x direction, providing $\psi < 1$ (white points) while the vertical ones along D_y, providing $\psi > 1$ (orange points). Figure 10 clearly shows that most of experimental cases lay between the two lines $\psi = 1$ (Figure 8 e) and $\psi = 1.2$ (Figure 8 a). A rigorous modeling of the surface topology would require different computational meshes to describe the large variety of fibers used to support the droplets (vertical, horizontal, thermocouples, cross fibers...), as well as precise data regarding the dynamic contact angle between the solid and the different liquids. In order to simplify the problem and based on Figures 9 and 10, we assume the evaporation regime not to be significantly influenced by small deviations of the droplet shape from the spherical one, which probably better describes on average the different experimental cases analyzed in this work. For these reasons we decided to adopt an intermediate value $\xi_0 = 1 \frac{m^2}{s^2}$ (Figure 8 d).

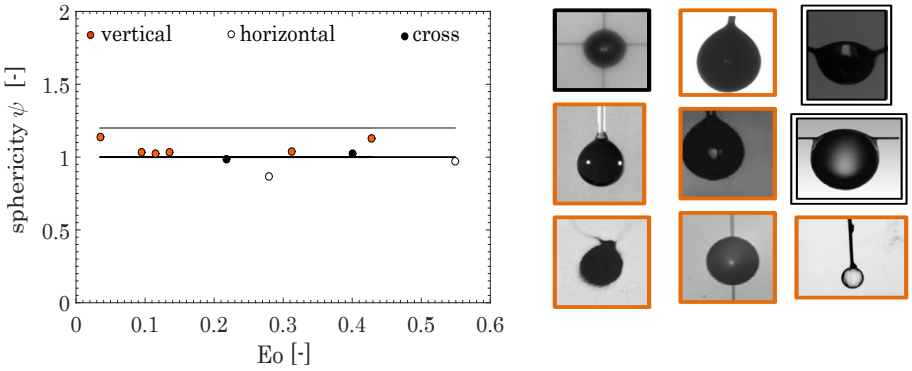

(a) (b)

Figure 10: Scatterplot of experimental cases of suspended droplets (Figure a), based on their Eötvös number $Eo = \frac{\rho_L g D^2}{\sigma}$ and sphericity $\psi = \frac{D_y}{D_x}$. Colors represent the supporting fiber: vertical (orange), horizontal (white) and cross fiber (black). The black line represents a perfect sphere ($\psi = 1$), the gray line represents the limit case in Figure 8 a ($\psi = 1.2$). Figure (b) reports the 9 of the 10 droplet pictures, signed with the same colors for comparison.

6 Cases in natural convection

6.1 Description of the experimental cases

The numerical model is now validated against 11 sets of experimental data in natural convection regime, taken from 4 papers in literature from 1997 to 2018. All the experimental cases are summarized in Table 3.

Ghassemi [52] used a fine quartz fiber of 0.125 mm of diameter (similarly to the spherical fiber used in our simulations) to hang and evaporate small n-heptane droplets in a hot nitrogen environment. Nomura et al. [59] examined the evaporation of cold n-heptane droplets in a hot air environment from 300 K to 450 K at various pressures (from 5 atm to 50 atm). The experimental data are taken from the paper of Gogos et al. [60], who proposed a very complex axysimmetric model to model them. An aluminum cross-fiber support frame has been utilized by Verwey et al. [61], in order to maintain a spherical shape of the droplet. N-decane and n-heptane evaporation has been investigated. Finally, n-hexadecane droplets evaporation was examined through a horizontal fiber by Han et al. [55]. Where needed, electric furnaces have been used to heat up the environment and nitrogen to pressurize the vessel. High-speed video cameras have been adopted to follow the droplet lifetime. For all cases, the experimental data provided concern the droplet "equivalent" diameter decay. Han et al. [55] also provided some data on the

Case	Species	D_0 [mm]	T_L [K]	T_G [K]	p [atm]	Refs.	Results
1	n-Heptane	1	300	773	10	[52]	Figure 12 (a)
2	n-Heptane	1	300	673	10	[52]	Figure 12 (b)
3	n-Heptane	0.698	300	398	50	[59]	Figure 13 (a)
4	n-Heptane	0.607	300	474	10	[59]	Figure 13 (b)
5	n-Heptane	0.604	300	450	5	[59]	Figure 13 (c)
6	n-Decane	0.546	300	373	10	[61]	Figure 14 (a)
7	n-Heptane	0.539	300	300	5	[61]	Figure 14 (b)
8	n-Decane	0.5	300	300	1	[61]	Figure 14 (c)
9	n-Decane	0.245	300	300	10	[61]	Figure 14 (d)
10	n-Hexadecane	1	300	773	1	[55]	Figure 15 (a, b, c)
11	n-Hexadecane	1	300	673	1	[55]	Figure 15 (d, e, f)

Table 3: Experimental cases in natural convection regime examined in this work.

mean droplet temperature by using a thermocouple as a fiber.
To our knowledge, the cases from Verwey et al. [61] and Han et al. [55] have never been modeled. Experimental data from Ghassemi et al. [52] and Nomura et al. [59] have only been approached so far either with simplified semi-analytical methods, or specific correlations based on mass-heat transfer dimensionless numbers for the evaporation sub-model [62, 63].
In principle, the `DropletSMOKE++` code can handle the thermal perturbation of the fiber on the droplet. This could be done either imposing a heat flux of the sphere boundary (Figure 5) which mimics its presence, or directly meshing the fiber geometry and solve the multi-region heat transfer between the fluid and the solid. Because of the small size of the fibers used in the experiments and the relatively low temperatures involved (since we are not modeling combustion processes), we found the evaporation process to be marginally affected by the thermal perturbation of the fiber, deciding to neglect it and postponing the problem to future works.

6.2 Numerical simulations: results and discussion

For each one of the cases presented in Table 3, an equivalent simulation (imposing the same initial conditions) has been performed with the microgravity solver of Cuoci et al. [13] in order to highlight the impact of gravity on the numerical simulation and better support the need of a multidimensional CFD model.
In Figure 11 the numerical results of the simulation of case 1 of Ghassemi et al. [52] are

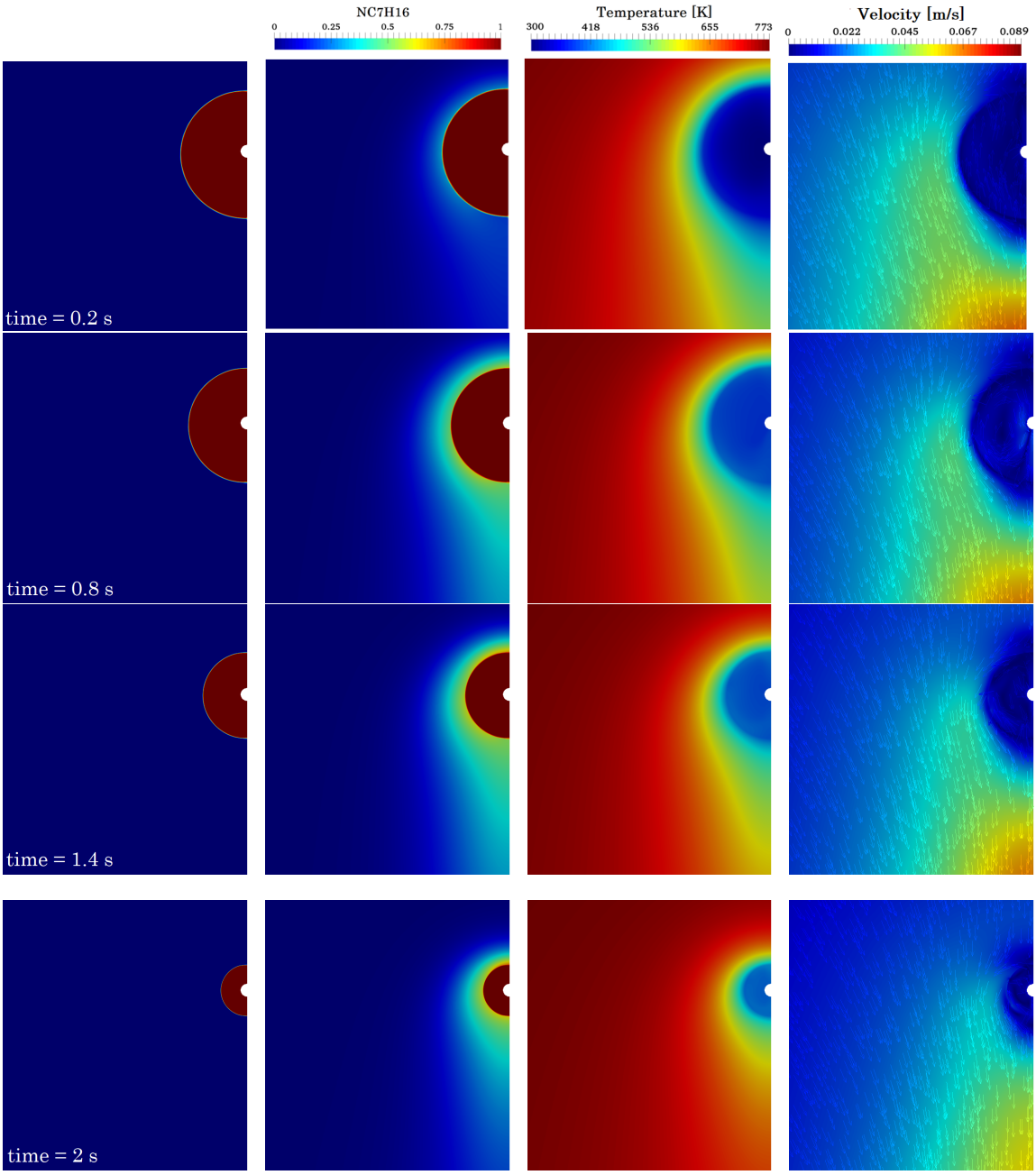

Figure 11: α (a), n-heptane mass fraction (b), temperature (c) and velocity vector fields (d) evolution. Numerical simulation of case 1 from Ghassemi et al. [52].

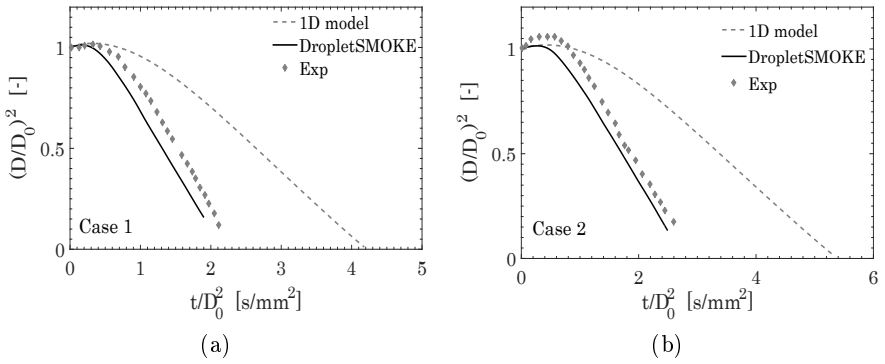

Figure 12: Model prediction of the experimental data of Ghassemi et al. [52], cases 1, 2 of Table 3.

reported as a reference example for a qualitative analysis. The liquid volume fraction (α), the n-heptane mass fraction field, the temperature and the vectorial velocity field are reported respectively in Figures 11.
The droplet is initially at an ambient temperature $T_L = 300$ K and it is progressively heated by the external environment at $T_G = 773$ K (Figure 11 c). A small amount of vapor is released from the droplet surface (Figure 11 b). The gas around the droplet is cooler than T_G and the n-heptane vapor has a higher density. This density gradient induces a downward flow field (Figure 11 d) around the droplet, generating a laminar natural convection regime. After a transient period, an equilibrium temperature is reached since the equilibrium mass fraction vapor in Figure 11 (b) reaches a steady state value.

Figure 12 reports the numerical results of the cases from Ghassemi et al. [52] (cases 1, 2), compared against the available experimental data. `DropletSMOKE++` can predict the experimental data with a reasonable accuracy for both cases. The linear behavior of the squared diameter can be easily recognized, as well as its initial increase due to the droplet heating shown in Figure 11.

The numerical simulations of the cases from Nomura et al. [59] (cases 4, 5, 6) are reported in Figure 13. There is a good agreement with the experimental data, especially if compared to the model prediction of the 1D model which largely overpredicts evaporation times. The velocity field around the droplet increases both heat and mass transfer rates from the liquid surface, providing a much lower evaporation time with respect to the microgravity case. This effect is particularly enhanced at high pressure (case 3, Figure 13 a) where the droplet evaporates ~ 4 times faster under the influence of gravity.

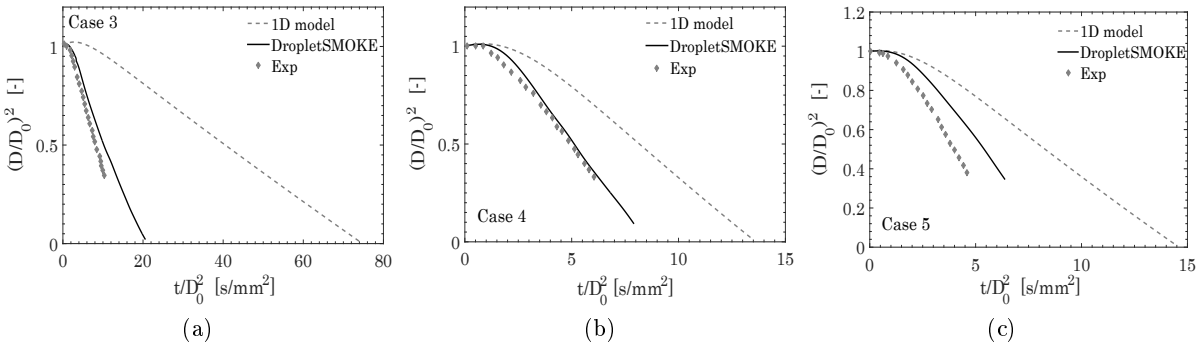

(a) (b) (c)

Figure 13: Model prediction of the experimental data of Nomura et al. [59], cases 3, 4, 5 of Table 3.

The reason is straightforward: the Grashof number increases with the gas density (with a power 2), which is proportional to pressure:

$$Gr = \frac{\rho^2 g D^3 \beta \Delta T}{\mu^2} \sim p^2 \tag{36}$$

Therefore, the presence of natural convection has a stronger impact in high pressures cases, if compared with the same cases in microgravity (where $Gr = 0$).
In Case 5 (Figure 13 c) we slightly overpredict the droplet lifetime, especially if compared to the other cases from the same author. It is worth noticing that this experimental case has been also modeled by Gogos et al. [60], using a complex non-VOF axisymmetric model and assuming a perfectly spherical droplet. His model generally shows good agreement with experiments, but the results of this specific case show deviation from the experimental data very similar to ours.

The cases from Verwey et al. [61] are carried out in mild conditions, characterized by a low vaporization rate due to the low temperatures and moderately high pressures involved. This is clear from Figure 14, where the evaporation times are much longer with respect to the previous cases. Cases 8 and 9 are particularly interesting, since the microgravity solver predicts a quasi steady-state condition. An evaporation flux is still present, but it is extremely low due to the purely diffusive regime involved (the Stefan flow in this conditions is completely negligible). It is interesting to point out that the velocity flow around the droplet has a maximum magnitude value of only 0.5-0.6 mm/s (not shown). Despite this small convective flow, the evaporation rate is strongly enhanced.

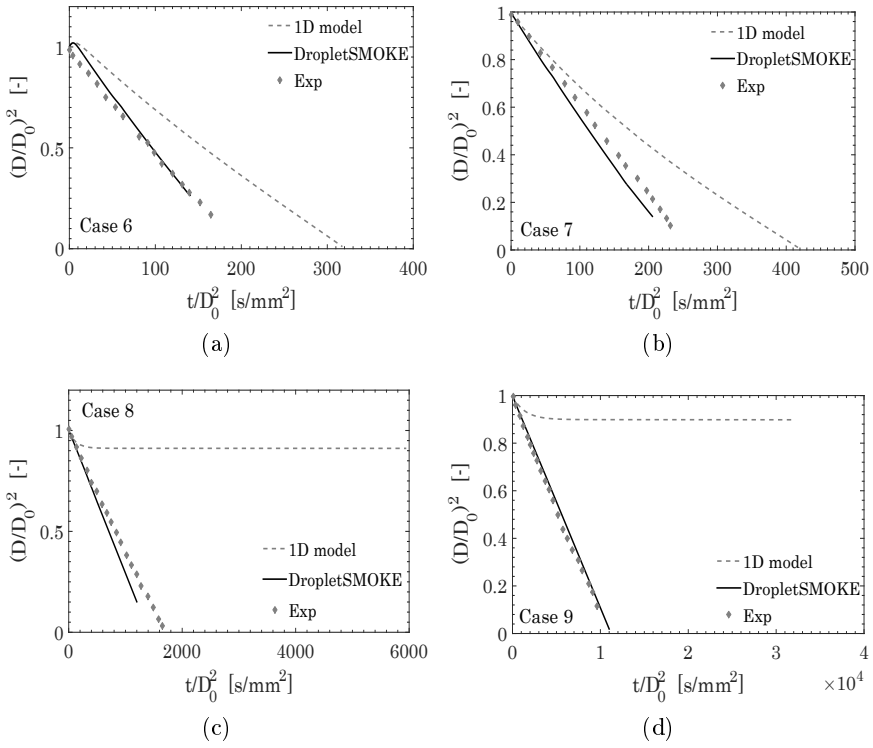

Figure 14: Model prediction of the experimental data of Verwey et al. [61], cases 6, 7, 8, 9 of Table 3.

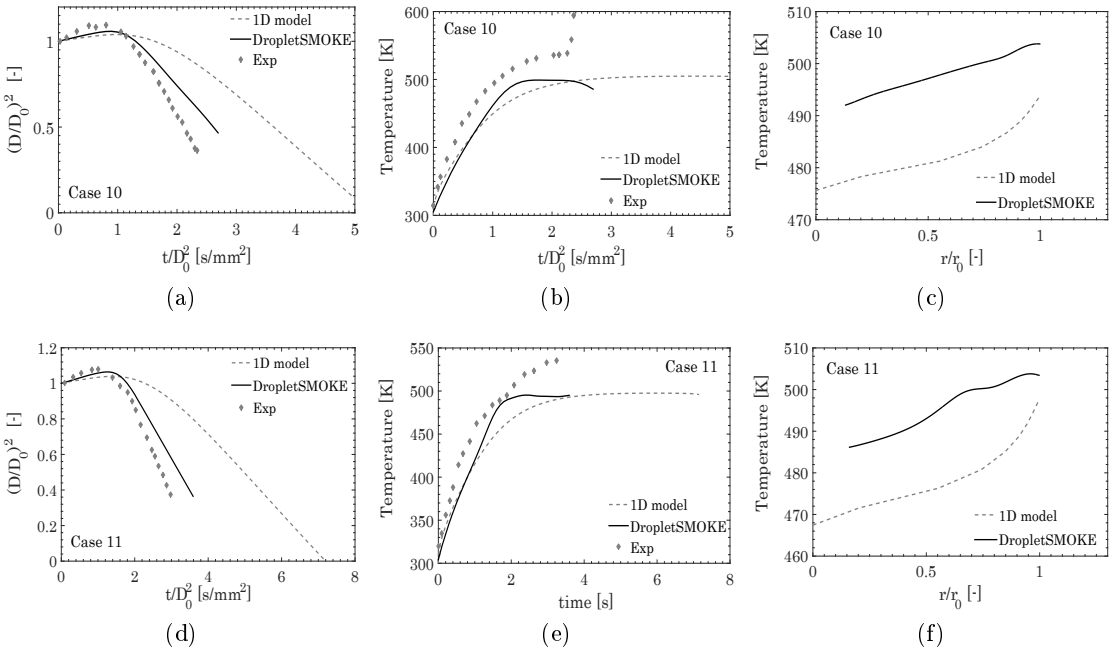

Figure 15: Figures (a), (b), (d), (e) show the model prediction of the experimental data of Han et al. [55], cases 10, 11 of Table 3. Figures (c), (f) report the liquid temperature distribution predited by `DropletSMOKE++` and by the 1D model for cases 10, 11 (time = 2 s).

This can be easily analyzed by scaling arguments: in case 8 (Figure 14 c) the initial droplet diameter is $D_0 = 0.5$ mm, while the surrounding convective flow has an average magnitude of 0.5 mm/s. This means that, taking the droplet diameter D_0 as a characteristic length of the system, the complete replacement of vapor cloud around the droplet lasts ~ 1 s, while for the pure diffusion case is practically infinite.

n-Hexadecane droplets evaporation from Han et al. [55] have been modeled (Figure 15). Experimental data on the mean droplet temperature are also available. There is a good agreement with the experimental results. The droplet temperature is slightly underestimated, especially towards the end of the simulation. Experimentally, this is due to the exposure of the thermocouple to the hot gas when the droplet is almost entirely consumed, or to the additional heat flux on the droplet given by the heat conduction from the fiber.

Figures 15 (c), (f) show the liquid temperature distribution inside the droplet predicted with the 1D model and with `DropletSMOKE++`, for both Cases 10-11, at time $t = 2$ s. The heat flux on the droplet surface is rapidly redistributed inside the liquid phase because

of the internal circulation, as will be further discussed later. This provides an average liquid temperature which is higher if compared to the 1D model. Moreover, the temperature distribution predicted by `DropletSMOKE++` is more homogeneous, while stronger T gradients characterize the 1D model.

Whereas the evaporation rate and the droplet lifetime are strongly influenced by natural convection, in terms of droplet surface temperature there is no significant deviation between the 1D model and `DropletSMOKE++`. More precisely, the initial droplet heating is faster (since evaporation is here negligible), but the steady state wet-bulb temperature is the same. The experimental data confirm this fact (Figure 15 b, e).
In steady state conditions, there is an equilibrium between the heat flux on the droplet surface and the evaporating flux enthalpy:

$$h_T \left(T_G - T_s\right) = h_M \left(\rho_{i,s} - \rho_{i,G}\right) \Delta h_{ev,i} \tag{37}$$

where $\rho_{i,s} = \frac{p_i^0(T_s) M_{w,i}}{RT_s}$ is the surface vapor concentration, while $\rho_{i,G} \sim 0$. h_T is the external heat transfer coefficient, while h_M is the external mass transfer coefficient. It is possible to derive one coefficient from the other through the Chilton-Colburn factor J [42]:

$$J_M = \frac{Sh}{ReSc^{\frac{1}{3}}} = J_T = \frac{Nu}{RePr^{\frac{1}{3}}} \tag{38}$$

from which it is easy to derive h_M in function of h_T:

$$h_M = \frac{\mathcal{D}_i}{k} \left(\frac{Sc}{Pr}\right)^{\frac{1}{3}} h_T \tag{39}$$

substituting h_M in Equation 37:

$$T_G - T_s = \frac{\mathcal{D}_i}{k} \left(\frac{Sc}{Pr}\right)^{\frac{1}{3}} \frac{p_i^0 \left(T_s\right) M_{w,i}}{RT_s} \Delta h_{ev,i} \tag{40}$$

The resolution of this equation provides the equilibrium temperature T. Equation 40 clearly indicates that the wet-bulb temperature does not depend on the external fluid flow, but only on the properties of the fluids and on the bulk temperature T_G.

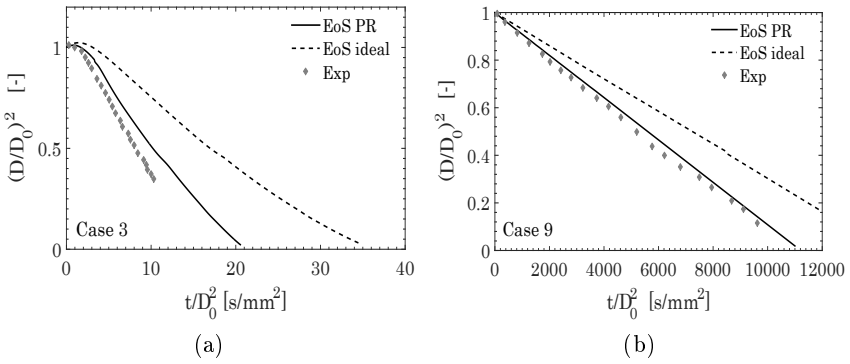

(a) (b)

Figure 16: Model prediction of the experimental data of Nomura et al. [59] case 3 (Figure a) and Verwey et al. [61] case 9 (Figure b) using both Peng-Robinson EoS and ideal EoS.

6.3 Effect of non-ideal thermodynamics

To complete the study in natural convection, the effect of real gas behavior has been investigated in high pressure and low temperature cases (Case 3 and Case 9). It is well known that in this conditions the ideal Equation of State fails in predicting fluid volumetric properties and the vapor-liquid equilibrium at the interface. The Peng-Robinson equation has been shown to be very accurate in modeling of linear alkanes [64] with respect to other equations, therefore it has been used to compute the compressibility factor Z for density evaluation and the fugacity coefficients ϕ.

Figure 16 reports case 3 (Figure 16 a) and case 9 (Figure 16 b) conducted respectively at 50 atm and 10 atm. The ideal and the Peng-Robinson equations of state are compared against the experimental data.

The model prediction is significantly improved when considering real gas effects. In the present conditions the gas fugacity coefficient $\hat{\phi}_i(T, p, y_i)$ reaches values of $\sim 0.6 - 0.7$, which leads to a vapor concentration at the interface increased by a factor $1.3 - 1.4$ (Equation 23). The Poynting correction, normally negligible at low pressures, becomes important in these cases:

$$e^{\int_{p^0}^{p} \frac{v_L}{RT} dP} \sim 1.2 - 1.3 \tag{41}$$

which further increases the interfacial vapor mass fraction. Finally, the higher density (Equation 24) of the real gas enhances the heat and mass transport coefficients. These effects lead to a higher vaporization rate that significantly reduces the droplet lifetime.

Case	Species	D_0 [mm]	T_L [K]	T_G [K]	p [atm]	$\|\mathbf{v}\|$ [m/s]	Refs.	Results
1	n-Heptane	0.7	300	490	1	0.7	[65]	Figure 17 (a)
2	n-Hexadecane	0.7	300	490	1	0.7	[65]	Figure 17 (b)

Table 4: Experimental cases in forced convection regime examined in this work.

7 Cases in forced convection

7.1 Description of the experimental cases

To conclude this work, two cases in forced convection have been simulated and compared with experimental results taken from Yang et al. [65]. According to our knowledge, this is the first time that these cases are numerically modeled. n-heptane and n-hexadecane droplets have been evaporated in an upward hot gas flow generated by a heating coil. The experimental data are given for different supporting fibers diameters. The data chosen for comparison refer to a fiber diameter of 0.15 mm, which is the closest to the fiber dimension used in this work ($D = 0.1$ mm). The experimental cases are summarized in Table 4.

7.2 Numerical results and discussion

The boundary conditions presented in Table 1 impose a fixed upward velocity at the *inlet* boundary, as well as a fixed temperature value. In Figure 17 (c) we can see the upward velocity field and the relative effect on the vapor cloud around the droplet and on the temperature field.
The agreement with the experimental data (Figure 17 a, b) is satisfactory, with a slight overestimation of the initial heat up in case 2.

From Figure 17 (c), it is clear that the liquid phase can be considered almost uniform in these conditions. This is further analyzed in Figure 18: the flow field streamlines are reported for the liquid phase, colored by the velocity magnitude (Figure 18 a) and temperature (Figure 18 b) for case 2 (Table 4) at time $t = 3$ s. The external convective flow induces a shear stress on the surface providing a strong circulation inside the droplet, with a maximum magnitude of ~ 2 cm/s. The resulting toroidal structure is well known in literature, and it is usually approximated as an inviscid Hill's spherical vortex [4, 66] to derive sub-models of droplet heating. It has been demonstrated that internal circulation needs to be included in modeling droplet vaporization [8], and this is usually accomplished with effective conductivity models [3]. Since the entire flow field is directly solved in this

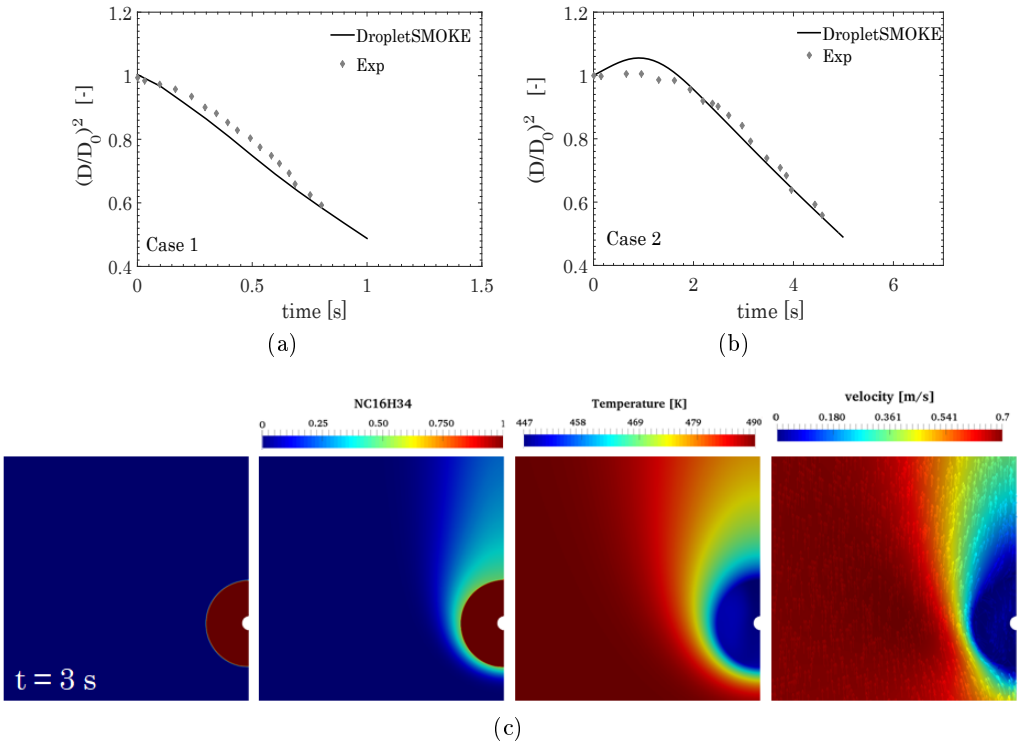

Figure 17: Figure (a): model prediction of the experimental data of Yang et al. [65], cases 1 (a) and 2 (b) of Table 4. Figure (c): α, n-hexadecane mass fraction, temperature and velocity fields at time $t = 3$ s, of the numerical simulation of case 2.

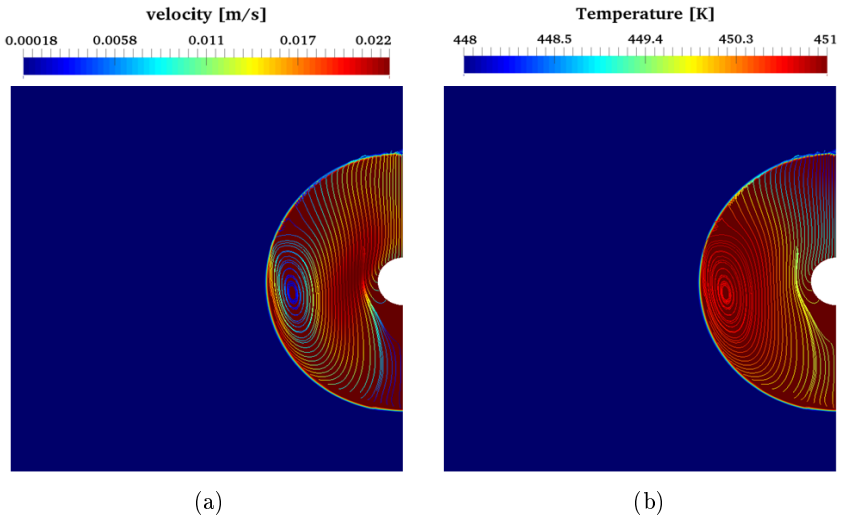

Figure 18: Flow field streamlines in the liquid phase for case 2 (Table 4), time $t = 3$ s. Colored by velocity magnitude (a) and temperature (b).

work, the internal temperature field can be predicted with no need of such additional sub-models. The maximum temperature difference inside the liquid phase is only ~ 3 K (Figure 18 b). As expected, a more intense heat transfer occurs at the bottom of the droplet, where the flow field impacts the liquid.
Finally, it is important to point out that the suppression of surface tension forces adopted in this work could in principle affect the internal motion in the liquid phase, because of the different the tangential shear stress at the interface. However, our comparative analyses in this sense, not reported in this work, show that the results obtained with `DropletSMOKE++` are in a reasonable agreement both with experimental [67, 68] and numerical [36, 69] works not based on the VOF methodology. These investigations are still preliminary, but indicate that even neglecting surface tension the internal circulation phenomenon can be quantitatively and qualitatively captured with a reasonable accuracy.

8 Conclusions

In this work we presented a multidimensional CFD numerical framework for the evaporation of isolated fuel droplets. The solver (called `DropletSMOKE++`) accounts for the presence of external flow field and for the influence of a gravity field, allowing to numerically model the evaporation of droplets both in natural and forced convection. The code is embedded within the well-known `OpenFOAM`® framework, open for contributions from the scientific community.
The core of the code is based on the VOF (Volume Of Fluid) methodology, widely known for its simplicity and mass conservation properties. The interface is geometrically advected and subjected to source terms to account both for evaporation and liquid expansion. This main solver is coupled with an evaporation model, which directly computes the vaporization rate from the interface molar fraction gradient, and with energy and species equations.
The main novelty of this work is the surface tension treatment. The parasitic currents, still an open problem for the modeling of small droplets dynamics, have been completely suppressed by-passing the modeling of surface tension effects. A suspending force directed towards the droplet center has been introduced to stabilize the droplet position against the gravity force. This expedient allowed to accurately model the evaporation process, whatever the droplet size. By tuning this suspending force, it is possible to modify the initial droplet shape to better match the experimental conditions (where the droplets are nearly spherical).
The `DropletSMOKE++` simulations has been compared with a well-known 1D microgravity

solver, in order to verify the correct implementation of the governing equations, obtaining a very good agreement between the models. Afterwards an extensive validation against experimental data has been carried out, both for natural and forced convection cases available in literature, over a very wide range of temperature, pressure and initial diameter conditions.
The agreement with experimental data was excellent and allowed to analyze the impact of an external flow field on the evaporation process, in particularly compared to the same cases modeled with a 1D model. The droplet lifetimes are largely overpredicted by the 1D model, while the CFD simulations carried out with `DropletSMOKE++` are able to correctly reproduce the data. This difference between the models is particularly enhanced at high pressures and in slow evaporating conditions (low temperature and high pressure).
Finally, the effect of the liquid internal circulation has been highlighted. In particular a much more uniform temperature field is provided by the internal heat transfer, strongly enhanced by the vortical structure of the internal flow field.
Future works will concern the introduction of a gas-phase kinetic mechanism to simulate the combustion process in presence of a convective flow, as well as the investigation of the liquid phase chemistry.

Acknowledgments

The authors acknowledge the support by the European Union's Horizon 2020 research and innovation program (Residue2Heat, G.A. No. 654650). The authors also would like to thank the Modeling and Scientific Computing (MOX) group at Politecnico di Milano for the useful and inspiring discussions.

These following appendices are not part of the published paper, but it is worth including them in this manuscript to better support the numerical methodology of the work.

Appendix A Boundary layers

This appendix is focused on the calculation of the boundary layers thickness for (i) heat transfer and (ii) mass transfer, for a small droplet immersed in a convective laminar flow. This estimation is important to determine the grid to be used for the simulations. The calculations follow the procedure reported in Abramzon and Sirignano work os spray

modeling [3].

A.1 Boundary layers

The definition of heat exchange coefficient h is:

$$h = \frac{-\kappa \nabla T}{\Delta T} \sim \frac{\kappa \Delta T}{\delta_T \Delta T} \sim \frac{\kappa}{\delta_T} \tag{42}$$

And the Nusselt number:

$$Nu = \frac{hD}{\kappa} \sim \frac{D}{\delta_T} \tag{43}$$

so:

$$\delta_T = \frac{D}{Nu} \tag{44}$$

in the same way:

$$\delta_M = \frac{D}{Sh} \tag{45}$$

Using:

$$Nu = 0.552 Re^{1/2} Pr^{1/3} \tag{46}$$

$$Sh = 0.552 Re^{1/2} Sc^{1/3} \tag{47}$$

The Shmidt and the Prandtl number in the gas phase have been calculated in a range of temperatures from $T = 300$ K to $T = 573$ K, for typical fuels (methanol, heptane, decane). The percentage variation was $\sim 10\%$, we take the average values:

$$Sc = \frac{\mu}{\rho \mathcal{D}_i} \sim 0.9 \tag{48}$$

$$Pr = \frac{\mu Cp}{k} \sim 0.65 \tag{49}$$

At the initial condition 0 (usually initial droplet diameters $D \sim 1$ mm) with $v = 0.5$ m/s (overestimated for our interests):

$$Re_0 = \frac{\rho v D}{\mu} \sim 50 \tag{50}$$

$$\delta_{T,0} \sim 3 \cdot 10^{-4} \text{ m} \tag{51}$$

$$\delta_{M,0} \sim 2.6 \cdot 10^{-4} \text{ m} \tag{52}$$

For the final condition f (usually simulations are stopped at $D = 0.1$ mm):

$$Re_f \sim 5 \tag{53}$$

$$\delta_{T,f} \sim 9.3 \cdot 10^{-5} \text{ m} \tag{54}$$

$$\delta_{M,f} \sim 8.4 \cdot 10^{-5} \text{ m} \tag{55}$$

These values represent a *minimum* conservative limit. The actual thickness is larger, due the presence of the Stefan flow which expands the boundary layer[1]. It is possible to take into consideration this effect, with appropriate correction factors (through the Spalding heat and mass transfer numbers B_T and B_M). Alternatively, it is sufficient to satisfy the condition without the Stefan flow, since it is more restrictive.

A.2 Mesh construction

We adopt in all our simulations a maximum cell size of $\Delta = 1 \cdot 10^{-5}$ m (inside the droplet and the region around it), to properly resolve the minimum gas film thickness (Equations 54, 55). This corresponds to a droplet resolution (for an initial diameter of $D = 1$ mm):

$$\frac{D}{\Delta} \sim 100 \tag{56}$$

This resolution is not maintained for the entire computational domain, because it is generally much larger than the droplet. Therefore:

- The mesh is built in 2D adopting the mesh generator implemented in `Ansys FLUENT`® v19.2, defining two separate regions at different resolutions: a fine one in the droplet region, a coarser one outside of it;
- The fluid regions are then connected, forming a polyhedral unstructured grid;

[1] Typically, the boundary layer is expanded by a factor 1.2-1.3, as reported by Abramzon and Sirignano.

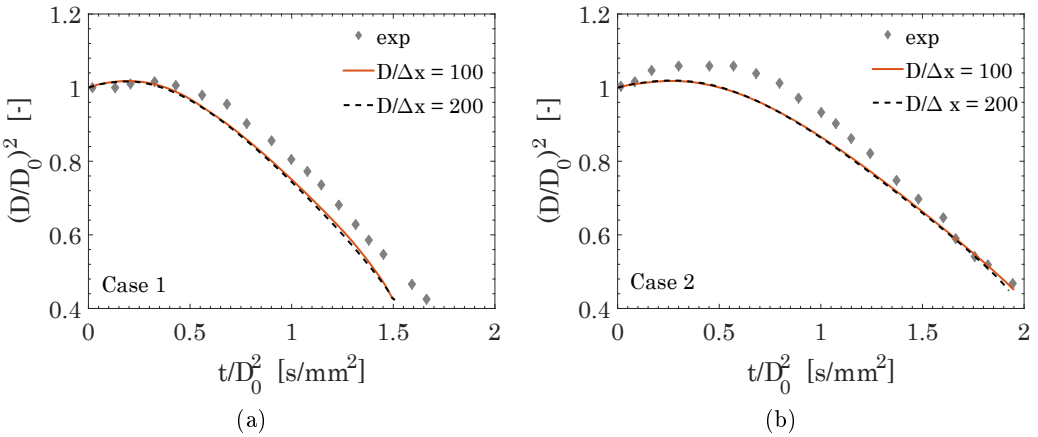

Figure 19: Grid refinement analysis for Cases 1 (a) and 2 (b) from Table 3.

- The mesh is then imported in `OpenFOAM`®. Finally, the symmetry plane is collapsed into a symmetry axis, providing an axisymmetric domain.

Finally, the accuracy of the result is then checked by a grid refinement analysis. In Figure 19, Cases 1 and 2 (from Table 3) are reported, with droplet resolutions $D/\Delta x = 100$ and 200. The coarsest case is based on the boundary layer thickness calculation (Equation 56) and it is shown to be accurate enough to provide mesh independence with further refinement.

Appendix B Implementing phase-change

This appendix provides a detailed explanation on how the phase-change process is implemented within the VOF method. In order to model the droplet size variation, source terms are added in the VOF function equation:

$$\frac{\partial \alpha}{\partial t} + \nabla \cdot (\mathbf{v}\alpha) = \frac{\dot{m}}{\rho} - \frac{\alpha}{\rho}\frac{D\rho}{Dt} \tag{57}$$

where the source terms represent the contribution of the evaporation/condensation rate (depending on the sign of $\dot{m}$) and the droplet dilation due to the change of density $\frac{D\rho}{Dt}$. This equation is solved in two steps, treating the advection and the source terms in a segregated approach, similarly to what happens in an operator-splitting technique: the interface transport is solved first, using the `isoAdvector` library, while the source terms are included in a second step.

The presence of an evaporation flux $\dot{m}$ generates an outflow velocity (Stefan flow) at the gas phase due to the density change involved. The velocity jump $[\mathbf{v}]$ is:

$$[\mathbf{v}] = \dot{m}\left(\frac{1}{\rho_L} - \frac{1}{\rho_G}\right)\mathbf{n} \tag{58}$$

The velocity jump is not explicitly imposed, but it arises from the solution of the continuity equation (in the pressure-velocity coupling). For evaporation cases it becomes:

$$\frac{1}{\rho}\frac{D\rho}{Dt} + \nabla \cdot \mathbf{v} = \dot{m}\left(\frac{1}{\rho_L} - \frac{1}{\rho_G}\right) \tag{59}$$

The additional term on the right-hand side provides the Stefan flow and the velocity jump. This source term is distributed on the interfacial cells (by means of $\nabla\alpha$), providing a non-sharp velocity field, following a CSF approach.
The main issue in modeling droplets evaporation is that the Stefan flow makes the interface advection problematic. The radial flux due to evaporation destabilizes the interface, affecting its sharpness and correct transport. As reported in the introduction, the main solutions involve the extension or the extrapolation of the liquid velocity to advect the interface. In this work an alternative approach is proposed, which is much simpler to implement.
The velocity and pressure fields are given by the PIMPLE algorithm, solving the following system of equations (Navier-Stokes and continuity):

$$\begin{cases} \frac{\partial(\rho\mathbf{v})}{\partial t} + \nabla \cdot (\rho\mathbf{v} \otimes \mathbf{v}) = \nabla \cdot \mu\left(\nabla\mathbf{v} + \nabla\mathbf{v}^T\right) - \nabla p + \rho\mathbf{g} \\ \frac{1}{\rho}\frac{D\rho}{Dt} + \nabla \cdot \mathbf{v} = \dot{m}\left(\frac{1}{\rho_L} - \frac{1}{\rho_G}\right) \end{cases} \tag{60}$$

The combination of these two equations results in a Laplace equation, which provides the pressure field p, subsequently used to correct and update the velocity $\mathbf{v}$. In this work we introduce a new velocity field $\mathbf{v}^*$ and a new pressure field p^* which satisfy the following system of equations:

$$\begin{cases} \frac{\partial(\rho\mathbf{v}^*)}{\partial t} + \nabla \cdot (\rho\mathbf{v}^* \otimes \mathbf{v}^*) = \nabla \cdot \mu\left(\nabla\mathbf{v}^* + \nabla\mathbf{v}^{*T}\right) - \nabla p^* + \rho\mathbf{g} \\ \frac{1}{\rho}\frac{D\rho}{Dt} + \nabla \cdot \mathbf{v}^* = 0 \end{cases} \tag{61}$$

This additional pressure-velocity coupling is equal to the standard one, but it does not contain the term due to evaporation $\dot{m}\left(\frac{1}{\rho_L} - \frac{1}{\rho_G}\right)$. The droplet will evaporate as usual (Equation 57), but the velocity field $\mathbf{v}^*$ will not include the Stefan flow. The strategy is to use the velocity $\mathbf{v}^*$ *only to advect the interface*, while the standard velocity $\mathbf{v}$ is used

to advect all the other fields (such as temperature, species etc.). In this way the interface will not be influenced by the normal evaporation flux (i.e. Stefan flow), maintaining its sharpness and making the advection algorithm much more stable. The methodology is relatively simple to implement, but it comes with some drawbacks:

- It is expensive: the method requires to solve two times the pressure-velocity coupling to obtain two velocity fields $\mathbf{v}$ and $\mathbf{v}^*$ and the two pressure fields p and p^*. This is often the most time consuming step;
- The interface is advected with the $\mathbf{v}^*$ field. The main hypothesis behind this strategy is that the radial flow does not influence the interface position. This is a very reasonable assumption for the cases of our interest. A suspended droplet generates a radial velocity towards an infinite gaseous environment (with respect to the droplet size). The outward radial flux can be safely assumed as symmetric around the droplet surface, meaning that the resulting momentum will be perfectly balanced over the droplet, providing no interface displacement. Of course, the method will not work for cases in which the Stefan flow directly affects the interface position. A typical example is the Leidenfrost effect [70]: when a small liquid droplet is brought close to a very hot surface, the repulsive force due to the Stefan flow makes the droplet hover over the surface without any physical contact. The vapor layer works as an insulator, preventing the whole liquid mass to reach the boiling point.

Nomenclature

Acronyms

ISS International Space Station

MULES Multidimensional Universal Limiter with Explicit Solution

$NC_{10}H_{22}$ n-decane

$NC_{16}H_{34}$ n-hexadecane

NC_7H_{16} n-heptane

VOF Volume Of Fluid

Greek letters

α marker function [−]

β thermal expansion coefficient $\left[\frac{1}{K}\right]$

Δh_{ev} evaporation enthalpy $\left[\frac{J}{kg}\right]$

$\hat{\phi}$ mixture gas-phase fugacity coefficient [−]

κ curvature $\left[\frac{1}{m}\right]$

μ dynamic viscosity $\frac{kg}{ms}$

ω mass fraction [−]

ϕ pure gas-phase fugacity coefficient [−]

ψ sphericity [−]

ρ density $\left[\frac{kg}{m^3}\right]$

σ surface tension $\left[\frac{N}{m}\right]$

ξ potential $\left[\frac{m^2}{s^2}\right]$

Roman letters

$\dot{m}$ evaporative flux $\left[\frac{kg}{m^3 s}\right]$

$\mathcal{D}$ mass diffusion coefficient $\left[\frac{m^2}{s}\right]$

$\mathbf{f}$ force $\left[\frac{N}{m^3}\right]$

$\mathbf{j}$ mass flux $\left[\frac{kg}{m^2 s}\right]$

$\mathbf{r}$ position vector $[m]$

$\mathbf{v}$ velocity $\left[\frac{m}{s}\right]$

C_p constant pressure specific heat $\left[\frac{J}{kgK}\right]$

D diameter $[m]$

Eo Eötvös number [−]

Gr Grashof number [−]

H	height of the mesh $[m]$
h	transfer coefficient $\left[\frac{W}{m^2 s}\right]$ or $\left[\frac{m}{s}\right]$
J	Chilton-Colburn factor $[-]$
k	thermal conductivity $\left[\frac{W}{mK}\right]$
M_w	molecular weight $\left[\frac{kg}{mol}\right]$
Ns	Number of species $[-]$
Nu	Nusselt number $[-]$
p	pressure $[Pa]$
p^0	vapor pressure $[Pa]$
p_{rgh}	dynamic pressure $[Pa]$
Pr	Prandtl number $[-]$
R	gas constant $\left[\frac{J}{molK}\right]$
r	distance $[m]$
Re	Reynolds number $[-]$
S	surface $\left[m^2\right]$
Sc	Sc number $[-]$
Sh	Sherwood number $[-]$
t	time $[s]$
T	temperature $[K]$
v	molar volume $\left[\frac{m^3}{mol}\right]$
W	basis radius of the mesh $[m]$
x	liquid phase mole fraction $[-]$
y	gas phase mole fraction $[-]$
Z	compressibility factor $[-]$

Subscripts

0	initial, reference
adj	adjacent
c	convective
d	diffusive
ext	external
G	gas
i	species i
int	cell at the interface
j	species j
L	liquid
M	mass, material
m	centripetal
s	surface
T	heat
x	x direction
y	y direction

References

[1] D. B. Spalding, The combustion of liquid fuels, in: Symposium (International) on combustion, Vol. 4, Elsevier, 1953, pp. 847–864.

[2] G. Godsave, Studies of the combustion of drops in a fuel spray—the burning of single drops of fuel, in: Symposium (International) on Combustion, Vol. 4, Elsevier, 1953, pp. 818–830.

[3] B. Abramzon, W. Sirignano, Droplet vaporization model for spray combustion calculations, International Journal of Heat and Mass Transfer 32 (9) (1989) 1605–1618.

[4] W. A. Sirignano, Fluid dynamics and transport of droplets and sprays, Cambridge university press, 1999.

[5] H. A. Dwyer, Calculations of droplet dynamics in high temperature environments, Progress in Energy and Combustion Science 15 (2) (1989) 131–158.

[6] H. Dwyer, B. Sanders, Detailed computation of unsteady droplet dynamics, in: Symposium (International) on Combustion, Vol. 20, Elsevier, 1985, pp. 1743–1749.

[7] C. Law, Unsteady droplet combustion with droplet heating, Combustion and Flame 26 (1976) 17–22.

[8] S. Kotake, T. Okazaki, Evaporation and combustion of a fuel droplet, International Journal of Heat and Mass Transfer 12 (5) (1969) 595–609.

[9] S. Sazhin, M. Al Qubeissi, R. Kolodnytska, A. Elwardany, R. Nasiri, M. Heikal, Modelling of biodiesel fuel droplet heating and evaporation, Fuel 115 (2014) 559–572.

[10] S. S. Sazhin, Advanced models of fuel droplet heating and evaporation, Progress in energy and combustion science 32 (2) (2006) 162–214.

[11] B. Abramzon, S. Sazhin, Droplet vaporization model in the presence of thermal radiation, International Journal of Heat and Mass Transfer 48 (9) (2005) 1868–1873.

[12] A. J. Marchese, F. L. Dryer, V. Nayagam, Numerical modeling of isolated n-alkane droplet flames: initial comparisons with ground and space-based microgravity experiments, Combustion and Flame 116 (3) (1999) 432–459.

[13] A. Cuoci, M. Mehl, G. Buzzi-Ferraris, T. Faravelli, D. Manca, E. Ranzi, Autoignition and burning rates of fuel droplets under microgravity, Combustion and Flame 143 (3) (2005) 211–226.

[14] T. I. Farouk, F. L. Dryer, Isolated n-heptane droplet combustion in microgravity: cool flames–two-stage combustion, Combustion and Flame 161 (2) (2014) 565–581.

[15] S. Okajima, S. Kumagai, Further investigations of combustion of free droplets in a freely falling chamber including moving droplets, in: Symposium (International) on Combustion, Vol. 15, Elsevier, 1975, pp. 401–407.

[16] S. Kumagai, T. Sakai, S. Okajima, Combustion of free fuel droplets in a freely falling chamber, in: Symposium (International) on Combustion, Vol. 13, Elsevier, 1971, pp. 779–785.

[17] C. Chauveau, I. Gökalp, D. Segawa, T. Kadota, H. Enomoto, Effects of reduced gravity on methanol droplet combustion at high pressures, Proceedings of the Combustion Institute 28 (1) (2000) 1071–1077.

[18] T. Farouk, Y. Xu, C. Avedisian, F. Dryer, Combustion characteristics of primary reference fuel (prf) droplets: Single stage high temperature combustion to multistage "cool flame" behavior, Proceedings of the Combustion Institute 36 (2) (2017) 2585–2594.

[19] T. Farouk, D. Dietrich, F. Alam, F. Dryer, Isolated n-decane droplet combustion–dual stage and single stage transition to "cool flame" droplet burning, Proceedings of the Combustion Institute 36 (2) (2017) 2523–2530.

[20] D. L. Dietrich, V. Nayagam, M. C. Hicks, P. V. Ferkul, F. L. Dryer, T. Farouk, B. D. Shaw, H. K. Suh, M. Y. Choi, Y. C. Liu, et al., Droplet combustion experiments aboard the international space station, Microgravity Science and Technology 26 (2) (2014) 65–76.

[21] A. Cuoci, A. E. Saufi, A. Frassoldati, D. L. Dietrich, F. A. Williams, T. Faravelli, Flame extinction and low-temperature combustion of isolated fuel droplets of n-alkanes, Proceedings of the Combustion Institute 36 (2) (2017) 2531–2539.

[22] A. Stagni, A. Cuoci, A. Frassoldati, E. Ranzi, T. Faravelli, Numerical investigation of soot formation from microgravity droplet combustion using heterogeneous chemistry, Combustion and Flame 189 (2018) 393–406.

[23] C. W. Hirt, B. D. Nichols, Volume of fluid (VOF) method for the dynamics of free boundaries, Journal of computational physics 39 (1) (1981) 201–225.

[24] M. Nabil, A. S. Rattner, interthermalphasechangefoam– A framework for two-phase flow simulations with thermally driven phase change, SoftwareX 5 (2016) 216–226.

[25] A. Georgoulas, M. Andredaki, M. Marengo, An enhanced VOF method coupled with heat transfer and phase change to characterise bubble detachment in saturated pool boiling, Energies 10 (3) (2017) 272.

[26] M. J. Nieves-Remacha, L. Yang, K. F. Jensen, OpenFOAM computational fluid dynamic simulations of two-phase flow and mass transfer in an advanced-flow reactor, Industrial & Engineering Chemistry Research 54 (26) (2015) 6649–6659.

[27] Z. Guo, D. Fletcher, B. Haynes, A review of computational modelling of flow boiling in microchannels, The Journal of Computational Multiphase Flows 6 (2) (2014) 79–110.

[28] J. Schlottke, B. Weigand, Direct numerical simulation of evaporating droplets, Journal of Computational Physics 227 (10) (2008) 5215–5237.

[29] N. Ghata, B. D. Shaw, Computational modeling of the effects of support fibers on evaporation of fiber-supported droplets in reduced gravity, International Journal of Heat and Mass Transfer 77 (2014) 22–36.

[30] N. Ghata, B. D. Shaw, Computational modeling of unsupported and fiber-supported n-heptane droplet combustion in reduced gravity: a study of fiber effects, Combustion Science and Technology 187 (1-2) (2015) 83–102.

[31] J. Brackbill, D. B. Kothe, C. Zemach, A continuum method for modeling surface tension, Journal of computational physics 100 (2) (1992) 335–354.

[32] S. J. Cummins, M. M. Francois, D. B. Kothe, Estimating curvature from volume fractions, Computers & structures 83 (6-7) (2005) 425–434.

[33] S. Popinet, Numerical models of surface tension, Annual Review of Fluid Mechanics 50 (2018) 49–75.

[34] G. Strotos, I. Malgarinos, N. Nikolopoulos, M. Gavaises, Predicting the evaporation rate of stationary droplets with the VOF methodology for a wide range of ambient temperature conditions, International Journal of Thermal Sciences 109 (2016) 253–262.

[35] R. Banerjee, Numerical investigation of evaporation of a single ethanol/iso-octane droplet, Fuel 107 (2013) 724–739.

[36] O. A. George, J. Xiao, C. S. Rodrigo, R. Mercadé-Prieto, J. Sempere, X. D. Chen, Detailed numerical analysis of evaporation of a micrometer water droplet suspended on a glass filament, Chemical Engineering Science 165 (2017) 33–47.

[37] K. Eisenschmidt, M. Ertl, H. Gomaa, C. Kieffer-Roth, C. Meister, P. Rauschenberger, M. Reitzle, K. Schlottke, B. Weigand, Direct numerical simulations for multiphase flows: An overview of the multiphase code FS3D, Applied Mathematics and Computation 272 (2016) 508–517.

[38] S. Popinet, An accurate adaptive solver for surface-tension-driven interfacial flows, Journal of Computational Physics 228 (16) (2009) 5838–5866.

[39] J. Roenby, H. Bredmose, H. Jasak, A computational method for sharp interface advection, Royal Society open science 3 (11) (2016) 160405.

[40] C. J. Greenshields, OpenFOAM user guide, OpenFOAM Foundation Ltd, version 3 (1).

[41] S. M. Damián, An extended mixture model for the simultaneous treatment of short and long scale interfaces, Ph.D. thesis, Universidad Nacional Del Litoral. Facultad de Ingenieria y Ciencias Hidricas (2013).

[42] R. B. Bird, Transport phenomena, Applied Mechanics Reviews 55 (1) (2002) R1–R4.

[43] D.-Y. Peng, D. B. Robinson, A new two-constant equation of state, Industrial & Engineering Chemistry Fundamentals 15 (1) (1976) 59–64.

[44] J. M. Smith, Introduction to chemical engineering thermodynamics, ACS Publications, 1950.

[45] R. Banerjee, K. M. Isaac, An algorithm to determine the mass transfer rate from a pure liquid surface using the volume of fluid multiphase model, International Journal of Engine Research 5 (1) (2004) 23–37.

[46] M. M. Francois, S. J. Cummins, E. D. Dendy, D. B. Kothe, J. M. Sicilian, M. W. Williams, A balanced-force algorithm for continuous and sharp interfacial surface tension models within a volume tracking framework, Journal of Computational Physics 213 (1) (2006) 141–173.

[47] F. Denner, F. Evrard, R. Serfaty, B. G. van Wachem, Artificial viscosity model to mitigate numerical artefacts at fluid interfaces with surface tension, Computers & Fluids 143 (2017) 59–72.

[48] A. Albadawi, D. Donoghue, A. Robinson, D. Murray, Y. Delauré, Influence of surface tension implementation in volume of fluid and coupled volume of fluid with level set

methods for bubble growth and detachment, International Journal of Multiphase Flow 53 (2013) 11–28.

[49] A. Q. Raeini, M. J. Blunt, B. Bijeljic, Modelling two-phase flow in porous media at the pore scale using the volume-of-fluid method, Journal of Computational Physics 231 (17) (2012) 5653–5668.

[50] A. Cuoci, A. Frassoldati, T. Faravelli, E. Ranzi, OpenSMOKE++: An object-oriented framework for the numerical modeling of reactive systems with detailed kinetic mechanisms, Computer Physics Communications 192 (2015) 237–264.

[51] C. L. Yaws, The Yaws Handbook of Physical Properties for Hydrocarbons and Chemicals: Physical Properties for More Than 54,000 Organic and Inorganic Chemical Compounds, Coverage for C1 to C100 Organics and Ac to Zr Inorganics, Gulf Professional Publishing, 2015.

[52] H. Ghassemi, S. W. Baek, Q. S. Khan, Experimental study on binary droplet evaporation at elevated pressures and temperatures, Combustion science and technology 178 (6) (2006) 1031–1053.

[53] R. Matlosz, S. Leipziger, T. Torda, Investigation of liquid drop evaporation in a high temperature and high pressure environment, International Journal of Heat and Mass Transfer 15 (4) (1972) 831–852.

[54] C. Morin, C. Chauveau, P. Dagaut, I. Goekalp, M. Cathonnet, Vaporization and oxidation of liquid fuel droplets at high temperature and high pressure: application to n-alkanes and vegetable oil methyl esters, Combustion science and technology 176 (4) (2004) 499–529.

[55] K. Han, C. Zhao, G. Fu, F. Zhang, S. Pang, Y. Li, Evaporation characteristics of dual component droplet of benzyl azides-hexadecane mixtures at elevated temperatures, Fuel 157 (2015) 270–278.

[56] D. Walton, The evaporation of water droplets. a single droplet drying experiment, Drying technology 22 (3) (2004) 431–456.

[57] C. Chauveau, F. Halter, A. Lalonde, I. Gokalp, An experimental study on the droplet vaporization: effects of heat conduction through the support fiber, in: Proc. of 22 nd Annual Conference on Liquid Atomization and Spray Systems (ILASS Europe 2008), Vol. 59, 2008, p. 61.

[58] M. Suzuki, H. Nomura, N. Hashimoto, Development of apparatus for microgravity experiments on evaporation and combustion of palm methyl ester droplet in high-pressure environments, Transactions of the Japan Society for aeronautical and space sciences, Space technology Japan 7 (ists26) (2009) Ph_43–Ph_48.

[59] H. Nomura, H. Rath, J. Sato, M. Kono, Effects of ambient pressure and natural convection on fuel droplet evaporation, 4th Asian-Pacific International Symposium on Combustion and energy Utilization (1997) 266–271.

[60] G. Gogos, S. Soh, D. N. Pope, Effects of gravity and ambient pressure on liquid fuel droplet evaporation, International journal of heat and mass transfer 46 (2) (2003) 283–296.

[61] C. Verwey, M. Birouk, Experimental investigation of the effect of natural convection on the evaporation characteristics of small fuel droplets at moderately elevated temperature and pressure, International Journal of Heat and Mass Transfer 118 (2018) 1046–1055.

[62] A. Azimi, A. Arabkhalaj, H. Ghassemi, R. S. Markadeh, Effect of unsteadiness on droplet evaporation, International Journal of Thermal Sciences 120 (2017) 354–365.

[63] W. Fang, Y. Jie, Y. Shaofeng, L. Rui, J. Jie, A new stationary droplet evaporation model and its validation, Chinese Journal of Aeronautics 30 (4) (2017) 1407–1416.

[64] G. Zhu, S. Aggarwal, Transient supercritical droplet evaporation with emphasis on the effects of equation of state, International Journal of Heat and Mass Transfer 43 (7) (2000) 1157–1171.

[65] J.-R. Yang, S.-C. Wong, An experimental and theoretical study of the effects of heat conduction through the support fiber on the evaporation of a droplet in a weakly convective flow, International journal of heat and mass transfer 45 (23) (2002) 4589–4598.

[66] H. Lamb, Hydrodynamics, Dover Publications, New York, 1945.

[67] D. K. Mandal, S. Bakshi, Internal circulation in a single droplet evaporating in a closed chamber, International Journal of Multiphase Flow 42 (2012) 42–51.

[68] D. K. Mandal, S. Bakshi, Evidence of oscillatory convection inside an evaporating multicomponent droplet in a closed chamber, Journal of colloid and interface science 378 (1) (2012) 260–262.

[69] J. Sim, H. G. Im, S. H. Chung, A computational study of droplet evaporation with fuel vapor jet ejection induced by localized heat sources, Physics of Fluids 27 (5) (2015) 053302.

[70] J. Bernardin, I. Mudawar, The leidenfrost point: experimental study and assessment of existing models, Journal of Heat Transfer 121 (4) (1999) 894–903.

Paper 2

An experimental and CFD modeling study of suspended droplets evaporation in buoyancy driven convection

A.E. Saufi[(a)], R. Calabria[(b)], F. Chiariello[(b)],
A. Frassoldati[(a)], A. Cuoci[(a)], T. Faravelli[(a)], P. Massoli[(b)]

[(a)]Department of Chemistry, Materials, and Chemical Engineering "G. Natta", P.zza Leonardo da Vinci 32, Milano, Italy

[(b)]Istituto Motori-CNR, Napoli, Italy

Chemical Engineering Journal (2019), vol. **375**, 122006

Abstract

A detailed analysis on the evaporation of acetic acid and ethylene glycol droplets is performed experimentally and numerically. The isolated droplet is positioned in a combustion chamber, suspended on a thermocouple and evaporated in buoyancy driven convection, following the thermal history throughout the droplet lifetime. The experiments provide quantitative and qualitative data on the evaporation physics of acetic acid, ethylene glycol and their mixture. The data are then modeled adopting the multiphase CFD code `DropletSMOKE++`, describing the flow field around the droplet, the heating rate and the evaporation process. The main novelty introduced in this work is a multiregion approach to describe the solid fiber, which allows to model the conjugate heat transfer with the liquid and the gas phase, as well as its impact on the droplet evaporation. `DropletSMOKE++` results show a good agreement with the experimental data, regarding both the diameter decay and the liquid temperature, whose internal distribution in the liquid is shown to be highly affected by the heat flux from the fiber (which can contribute up to $30-40\%$ in the total heat flux on the droplet). The effect of the thermocouple on the evaporation rate has been highlighted simulating the same experiments considering the solid as adiabatic, showing in this case a large underprediction of the vaporization rate and confirming the need of a detailed model for the fiber to correctly predict the vaporization phenomenon. The mixture evaporation has been investigated, emphasizing the importance of adopting a detailed thermodynamic model (which includes activity coefficients) and the impact of the mixture non-ideality on the evaporation process. The mixture also exhibits preferential vaporization, facilitated by the internal convection in the liquid phase.

Keywords: droplet, evaporation, DropletSMOKE, fiber, thermocouple, convection

1 Introduction

The study of the evaporation and combustion of isolated fuel droplets is currently an active area of research, mainly directed toward the better understanding and design of many engineering devices such as diesel engines and industrial burners. The CFD modeling of sprays relies on local source terms to describe the droplet heating, evaporation and combustion in a convective flow, usually based on semi-empirical correlations depending on dimensionless numbers (Re, Pr, Sc) [1, 2]. Detailed results based on the direct numerical resolution of the differential equations (DNS) can help to build or improve reliable sub-grid scale models for the description of the vaporization rate, the internal mixing and the differential evaporation (for multicomponent mixtures) for a single droplet. In fact, the analysis is significantly simplified neglecting the complex droplet-droplet interactions (coalescence, breakup, etc.), both from an experimental [3, 4] and theoretical [5, 6, 7] point of view.

In the last years, many fuels have been investigated concerning isolated droplet vaporization with a particular attention toward alternative fuels such as pyrolysis-oil (POs) [8, 9, 10]. Pyrolysis oils (POs) are black-brownish liquids obtained by the condensation of vapors during the fast pyrolysis of vegetable biomass . In this context, a fundamental research activity is performed within the Residue2Heat project [11], which aims at developing a concept for renewable residential heating using FPBO (Fast Pyrolysis Bio Oil), to develop a proper surrogate mixture able to mimic the behavior of the real bio-oil. A nine-component mixture (water, acetic acid, ethylene glycol, glycol aldehyde, vanillin, HMW-lignin, levoglucosan, 2,5-dimethylfuran, oleic acid) has been defined and experimentally verified in comparison with the corresponding FPBO in single droplet experiments [12, 11]. The experimental analyses and kinetic model development [13] were performed hierarchically, starting form pure components, then moving to their mixtures and finally the complete surrogate.

This work aims at analyzing, both experimentally and numerically, two of the proposed components for the bio-oil surrogate: acetic acid and ethylene glycol, as well as their mixture. The complex physics of the fuel droplets, suspended on a thin thermocouple in order to follow their thermal history, were studied in a single droplet combustion chamber by means of high speed shadowgraphs [12] to investigate evaporation process in detail. The heating rate at the thermocouple junction is provided by a resistive electric coil placed below the droplet, which induces buoyancy and an upward convective hot flow toward the liquid phase. The heating rate is firstly measured without the droplet and it is subsequently applied to the evaporation of acetic acid, ethylene glycol and their mixture,

providing as output data the squared diameter decay and the liquid temperature profile. Afterwards, the multiphase CFD code `DropletSMOKE++` [14] has been adopted to model the experiments, in order to obtain detailed data regarding the evaporation physics of the droplet. The `DropletSMOKE++` code, based on the VOF methodology, has been developed at Politecnico di Milano and it is specifically conceived for the detailed analysis of the evaporation of multidimensional fuel droplets in a convective flow. It has been validated against a large set of experimental data, with different fuels and in a wide range of operating conditions. In this work, the code has been further extended including the detailed description of the support fiber (i.e. the thermocouple), providing the temperature field of the fiber and a better insight on the heat transfer between the fluid and the solid phase. The literature on the topic includes the experimental and theoretical works of Yang et al. [15, 16], mainly concerning the impact of the fiber diameter on the evaporation rate. More recently, these analyses have been conducted by Rehman et al. [17], experimentally analyzing different supporting fiber sizes and materials and their effect on the droplet lifetime. Han et al. [18], studied this effect on multicomponent droplets, providing a numerical analysis based on a simple 1D model for both the droplet and the solid fiber and a quasi-steady state assumption for the gas phase. More detailed approaches have been proposed by Shringi et al. [19], also studying the impact of capillary fluxes on the droplet cooling, while Ghata et al. [20] implemented a VOF methodology for the fluid description, limiting however the study to reduced gravity conditions. Finally, Strizhak et al. [21] recently suggested a heat transfer model for tethered droplets, relying however on the Effective Thermal Conductivity model [6] for the temperature gradient and the circulation inside the droplets.

Concerning the CFD modeling, the main novelty of this work is the introduction of a multiregion approach, widely known in the CFD community for conjugate heat transfer problems, combined with the VOF methodology. This is applied to study the heat transfer of a three-phase system in which the solid fiber, the liquid droplet and the gaseous convective flow interact with each other. This is done without relying on any sub-model, semi-empirical correlation or approximate approach for the solid fiber or the droplet heating and vaporization, performing a complete detailed numerical simulation of the three phase system.

The paper organization includes a detailed description of the experimental device (combustion chamber) for the analysis of the droplet evaporation, followed by a brief presentation on the main features of the `DropletSMOKE++` code, presented in detail in the reference work [14], and its numerical implementation. The experimental heating rate detected by the thermocouple is then reconstructed and applied to the evaporation of

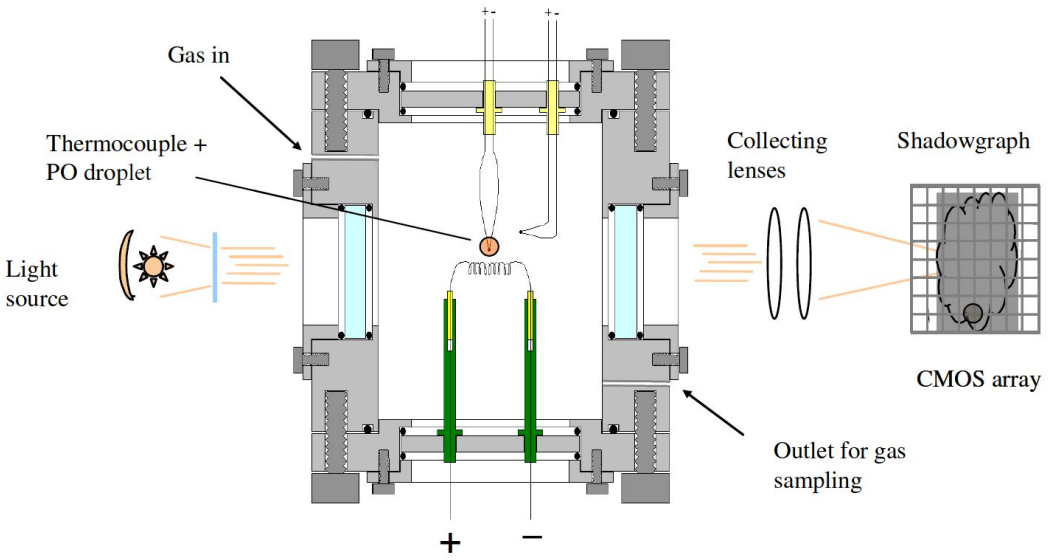

Figure 1: Experimental configuration

acetic acid, ethylene glycol and their mixture. The results are then presented and discussed, with a particular focus on the impact of the support fiber on the vaporization physics and on the liquid temperature distribution. An analysis on the mixture non-ideality is reported in order to stress the importance of a detailed thermodynamics to correctly predict the evaporation rate. Finally, the internal velocity field in the liquid phase is reported, highlighting its role in the preferential vaporization of the mixture.

2 Experimental configuration

The evaporation studies on fuel droplets discussed in this work were carried out in a combustion cell designed to analyze the thermal behavior of single fuel droplets. The cell allows to realize the experiments in a wide range of operating conditions, controlling the heating rate (up to 1000 K/s), the pressure (from 0.1 kPa to 10 MPa) and the atmosphere composition (usually nitrogen or air). The cell was originally realized in the framework of the European Project "COMBIO - A New Competitive Liquid Biofuel for Heating" [12], in order to study the combustion of pyrolysis oils and their emulsions up to a pressure of 10 MPa. From the geometrical point of view, the cell is a cylindrical chamber in stainless steel AISI 316 provided with four optical accesses for the realization of different experimental configurations and diagnostic. The experimental configuration is presented in Figure 1.

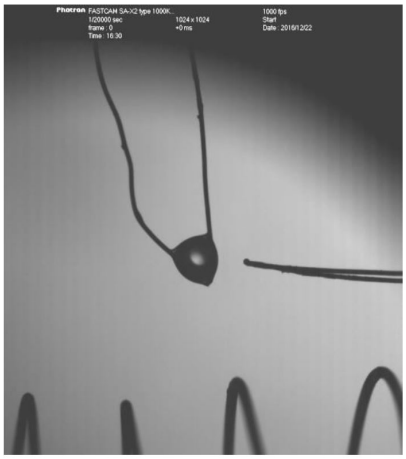

Figure 2: Detail of the suspended droplet

At the center of the cell a thermocouple is placed. The liquid fuel droplet is suspended on the thermocouple junction by means of a microsyringe (Figure 2). The heating of the fuel droplet is provided by an electric current passing through a coil of resistive material placed below the thermocouple, which releases heat by Joule effect. The evaporation of the droplet is followed by shadowgraph technique at high speed. A second thermocouple, placed laterally to the central one, is used to monitor the temperature in the area surrounding the droplet, which is particularly important for ignition experiments.
The thermocouples are of type K (chromel / allumel), with exposed junction, characterized by a good linearity of response in the range of $20°C$ -1200°C. In order to minimize intrusive effects of the thermocouple on the droplet thermal history, a wire diameter of $75\mu m$ has been adopted, while the junction diameter was limited to $125\mu m$. This choice has ensured a good adhesion of the droplet on the thermocouple junction even at high temperatures, when the surface tension and the viscosity of the fuel are considerably reduced. The signals of the thermocouples are acquired by means of the 4-channels transient recorder LeCroy Waverunner 104MXI-A. The image acquisition system is constituted by a CMOS high-speed (Photron Fastcam SA-X2) with a resolution of 1024x1024 pixels, 12-bit. The imaging is realized in shadowgraph configuration, in which the droplet is placed between a light source and the camera, with all these three elements perfectly aligned.

Movies obtained by the CMOS camera are saved as a sequence of individual images and analyzed with specific software for the extraction of relevant information. Through the analysis of the images of droplets in evaporation phase it is possible to extract

quantitative information concerning the phenomenology, such as the equivalent diameter of the droplet over the time. By the coupled analysis of the output images and the signals from the thermocouple, the thermal history and the whole evaporation process of the droplet can be fully reconstructed.

3 Mathematical model

3.1 Basic equations

In the VOF methodology [22, 23] a scalar marker function α is used to represent the liquid volumetric fraction of a two phase fluid, considering it as a single fluid with step-function properties. The α function varies from value 0 in the gas-phase to value 1 in the liquid phase and it is governed by the following transport equation:

$$\frac{\partial \alpha}{\partial t} + \nabla \cdot (\mathbf{v}\alpha) = -\frac{\dot{m}}{\rho} - \frac{\alpha}{\rho}\frac{D\rho}{Dt} \tag{1}$$

The source term $\dot{m}$ is the evaporation flux which changes the liquid volume, while the second term accounts for the liquid density variation. The interface tracking is coupled with a single Navier-Stokes equation, solved for both phases:

$$\frac{\partial (\rho \mathbf{v})}{\partial t} + \nabla \cdot (\rho \mathbf{v} \otimes \mathbf{v}) = \nabla \cdot \mu \left(\nabla \mathbf{v} + \nabla \mathbf{v}^T \right) - \nabla p + \rho \mathbf{g} \tag{2}$$

which provides the velocity fields. Finally, the energy equation is solved:

$$\rho C_p \left(\frac{\partial T}{\partial t} + \mathbf{v} \nabla T \right) = \nabla \cdot (k \nabla T) + \beta \frac{Dp}{Dt} - \sum_{i=0}^{Ns} \mathbf{j}_{d,i} C_{p,i} \nabla T - \sum_{i=0}^{Ns_L} \dot{m}_i \Delta h_{ev,i} \tag{3}$$

in which the interface cooling and the diffusion fluxes enthalpy of the species are included.

3.2 Thermodynamics and multicomponent evaporation model

The evaporation flux $\dot{m}_i$ is evaluated directly from the diffusion and convective fluxes at the gaseous interface, without the need of any particular evaporation model based on dimensionless numbers or empirical correlations [24]. We evaluate the surface mole fraction at the gas side, assuming thermodynamic equilibrium at the interface [25]:

$$y_i|_{int} = \frac{p_i^0(T)\phi_i\left(T, p_i^0\right) e^{\int_{p_i^0}^{p} \frac{v_{L,i}}{RT} dp} \gamma_i\left(T, p, x_i\right)}{p\hat{\phi}_i(T, p, y_i)} x_i|_{int} \tag{4}$$

where $p_i^0(T)$ is the vapor pressure of species i, ϕ_i is the gas-phase fugacity coefficient for the pure species and $\hat{\phi}_i$ is the gas-phase mixture fugacity coefficient. The exponential term represents the Poynting correction, while $x_i|_{int}$ and $y_i|_{int}$ are the liquid and gas mole fractions of species i. Finally, γ_i is the activity coefficient for non-ideal mixtures, evaluated with the UNIFAC approach [26]. The conversion to mass fraction is straightforward:

$$\omega_i^G|_{int} = \frac{M_{w,i}}{M_w} y_i|_{int} \tag{5}$$

This interfacial mass fraction $\omega_i^G|_{int}$ is evaluated on the whole liquid phase and then advected and diffused towards the gas phase, simulating the vapor transport:

$$\rho_G \left(\frac{\partial \omega_i^G}{\partial t} + \mathbf{v}\nabla\omega_i^G \right) = -\nabla \cdot \mathbf{j}_{d,i}^G \tag{6}$$

where the diffusive flux $\mathbf{j}_{d,i}^G$ is computed as [14]:

$$\mathbf{j}_{d,i}^G = -\rho^G \mathcal{D}_i^G \frac{M_{w,i}}{M_w} \nabla y_i \tag{7}$$

The vapor presence in the gas phase can now be used to compute the evaporating flux $\dot{m}_i$ for each species, accounting for both the convective and the diffusive fluxes:

$$\dot{m}_i = \left(\rho \mathbf{v} \omega_i^G|_{int} - \rho \mathcal{D}_i \frac{M_{w,i}}{M_w} \nabla y_i|_{int} \right) \nabla\alpha \tag{8}$$

where $|\nabla\alpha|$ accounts for the local surface area per unit volume, imposing the evaporation flux only at the interface. The vaporizing flux $\dot{m}_i$ is then included as a source term for the liquid species transport equation:

$$\frac{\partial \left(\rho_L \omega_i^L\right)}{\partial t} + \nabla \cdot \left(\rho_L \mathbf{v} \omega_i^L\right) = -\nabla \cdot \mathbf{j}_{d,i}^L - \dot{m}_i \tag{9}$$

where the diffusive flux in the liquid phase is computed with a pseudo-Fick approach [27]:

$$\mathbf{j}_{d,i}^L = -\rho^L \mathcal{D}_i^L \frac{M_{w,i}}{M_w} \nabla x_i \tag{10}$$

The final mass fraction field of species i is simply the superposition of the two fields:

$$\omega_i = \alpha\omega_i^L + (1-\alpha)\,\omega_i^G \tag{11}$$

3.3 Surface tension modeling

The main difficulty of the VOF approach is the modeling of surface tension driven flows. Very small droplets ($\sim$ 1-2 mm diameter) have a very large interface curvature κ, whose value is needed to compute the surface tension force $\mathbf{f}_s$:

$$\mathbf{f}_s = \sigma\kappa\nabla\alpha \tag{12}$$

The numerical evaluation of curvature κ from the α step-function is numerically challenging [28] and errors in this calculation lead to unphysical velocities around the interface called parasitic currents, which can easily propagate and eventually destroy the droplet. Many ways have been proposed to reduce this problem [29, 30], but none of them is able to completely eliminate spurious currents for the cases of our interest, concerning small evaporating droplets. In order to overcome this problem, a suspending force $\mathbf{f}_m$ directed towards the droplet center has been imposed, in order to keep it strongly held to the thermocouple junction even when gravity is present. In this system surface tension force $\mathbf{f}_s$ is not needed anymore and it can be neglected, eliminating parasitic currents directly from their source. The Navier-Stokes equation becomes:

$$\frac{\partial(\rho\mathbf{v})}{\partial t} + \nabla\cdot(\rho\mathbf{v}\otimes\mathbf{v}) = \nabla\cdot\mu\left(\nabla\mathbf{v} + \nabla\mathbf{v}^T\right) - \nabla p + \rho\mathbf{g} + \mathbf{f}_m \tag{13}$$

This by-passing technique has been proposed by Saufi et al. [14] and represents one of the strengths of our numerical code, since it allows to model small droplets dynamics without worrying about spurious currents. Surface tension is suppressed, eliminating the parasitic flows from their very source and allowing to model the whole evaporation process, whatever the droplet size. More details and analyses about this technique are presented in the specific work on the `DropletSMOKE++` code [14].

3.4 Multiregion approach for conjugate heat transfer

One of the main novelties of this paper is the implementation of a multiregion approach in order to account for the solid phase representing the thermocouple wire. The solid fiber rapidly conducts heat towards the droplet, representing an additional preferential path for the heat fluxes on the liquid phase, which can perturb the evaporation process [31, 15,

32]. In this work we implemented an extension of the `DropletSMOKE++` code, in which we combine the VOF methodology to describe the two-phase fluid and a multiregion approach for the sole solid region with a very high level of detail. The heat transfer across the phases can be modeled accounting for the real geometry of the system, with no need of semi-empirical correlations or approximate approaches to account for the fiber. The fluid and the solid regions are independently meshed, solved and connected by means of dynamic boundary conditions, providing a full detailed numerical simulation of the three-phase system. In particular, a simple heat conduction equation is solved for the solid phase:

$$\rho_s C_{p,s} \frac{\partial T_s}{\partial t} = \nabla \cdot (k_s \nabla T_s) \tag{14}$$

while the fluid temperature field is provided by Equation 3. The external surface of the solid fiber is the contact boundary between the phases. The boundary conditions which apply describe the conservation of heat fluxes across the boundary as well as the continuity of the temperature field. Equations 3 and 14 are solved in a closed loop until convergence. The solid properties values are $k_s = 29.7\ \frac{W}{mK}$, $\rho_s = 8600\ \frac{kg}{m^3}$ and $C_{p,s} = 523\ \frac{J}{kgK}$.

3.5 Fluid properties

The `OpenSMOKE++` library [33] is used to compute the fluid properties . The gas physical properties $(\rho, \mu, C_p, k, \mathcal{D}_i)$ are based on the kinetic theory of gases, while liquid properties $(\rho, \mu, C_p, k, \mathcal{D}_i,\ \Delta h_{ev,i})$ are evaluated based on the correlations available in the Yaws and Prausnitz [34, 35] databases and thermophysical definition of the FPBO mixture developed within the Residue2Heat project [11]. The mixture properties to be used in the governing equations can be then computed. For a generic property χ:

$$\chi = \chi_L \alpha + \chi_G \left(1 - \alpha\right) \tag{15}$$

4 Numerical methodology

The `DropletSMOKE++` code is based on the open-source framework `OpenFOAM`®, which allows to numerically solve the transport equations on complex geometries. The pressure-velocity coupling is implemented through the PIMPLE algorithm [36], while for the time discretization an implicit Euler method is adopted. A threshold Courant number ($\mathrm{Co} < 1$) governs the time-step value. Gauss linear upwind scheme is used for spatial discretization

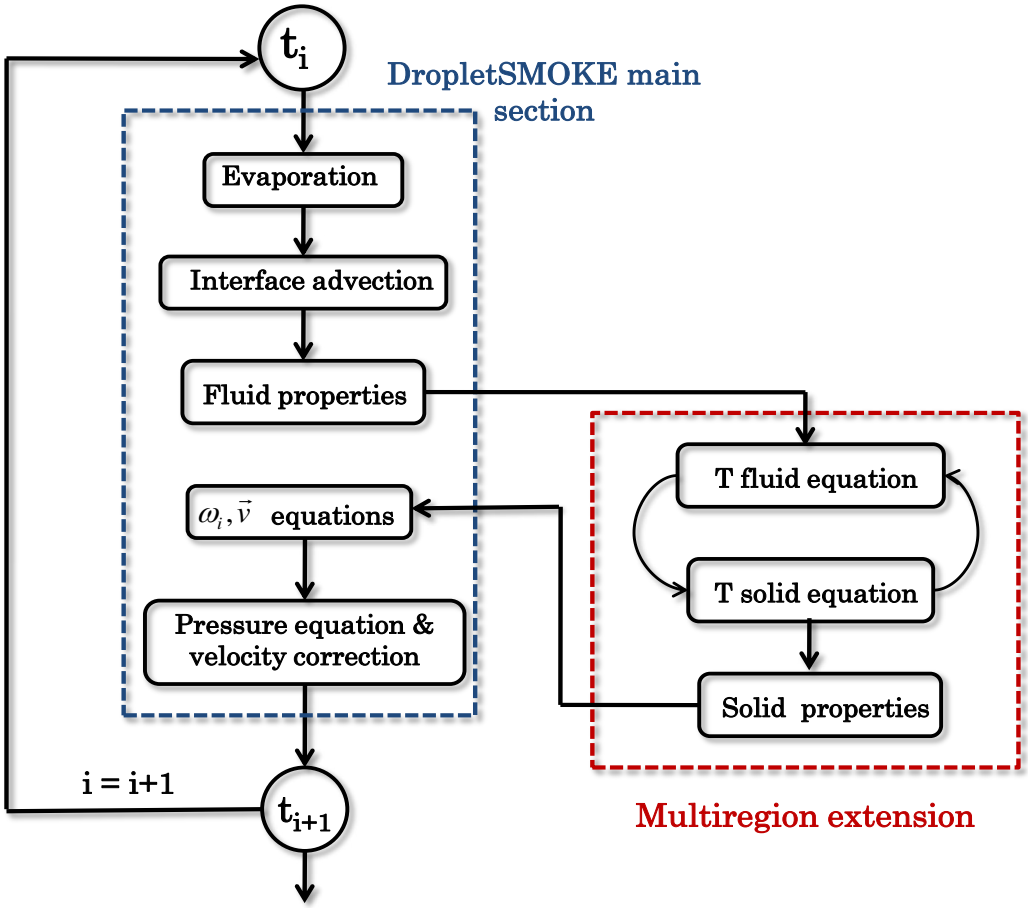

Figure 3: Numerical steps of the `DropletSMOKE++` code, including the multiregion extension for the description of the solid fiber.

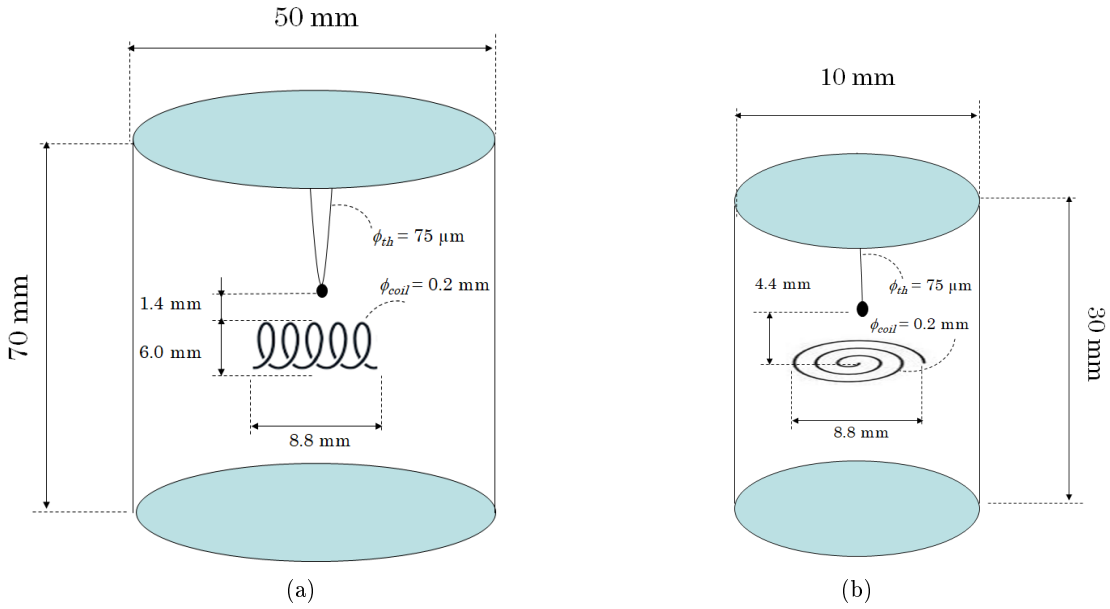

Figure 4: Detailed geometrical dimensions of the original experimental configuration in (a). Alternative configuration used for the CFD simulations in (b).

of convective terms, while an orthogonal correction is adopted for Laplacian terms. The structure of the code is reported in Figure 3, highlighting the multiregion extension.

4.1 An alternative configuration for the CFD modeling

The main geometrical dimensions of the experimental configuration (Figure 1) are reported in Figure 4 (a). The CFD simulation of this domain would require a full 3D simulations, since the presence of the coil and the double-wire thermocouple does not leave any symmetry in the system to be exploited. A 3D simulation would be very difficult, not only concerning the domain construction, but mainly because of the high computational cost of the simulations. Therefore, in order to model the experimental device with a reasonable computational cost, an alternative geometrical configuration has been adopted, characterized by the presence of axial symmetry.

This alternative configuration is represented by the cylindric geometry in Figure 4 (b). The following differences with respect to the original one (Figure 4 a) are introduced:

- Only a reduced portion of the whole domain is modeled, treating all the external boundaries of the new configuration as open (Figure 4 b). The droplet is positioned far enough from the chamber boundaries to consider the wall perturbation on the evaporation process negligible. This allows to significantly reduce the number of

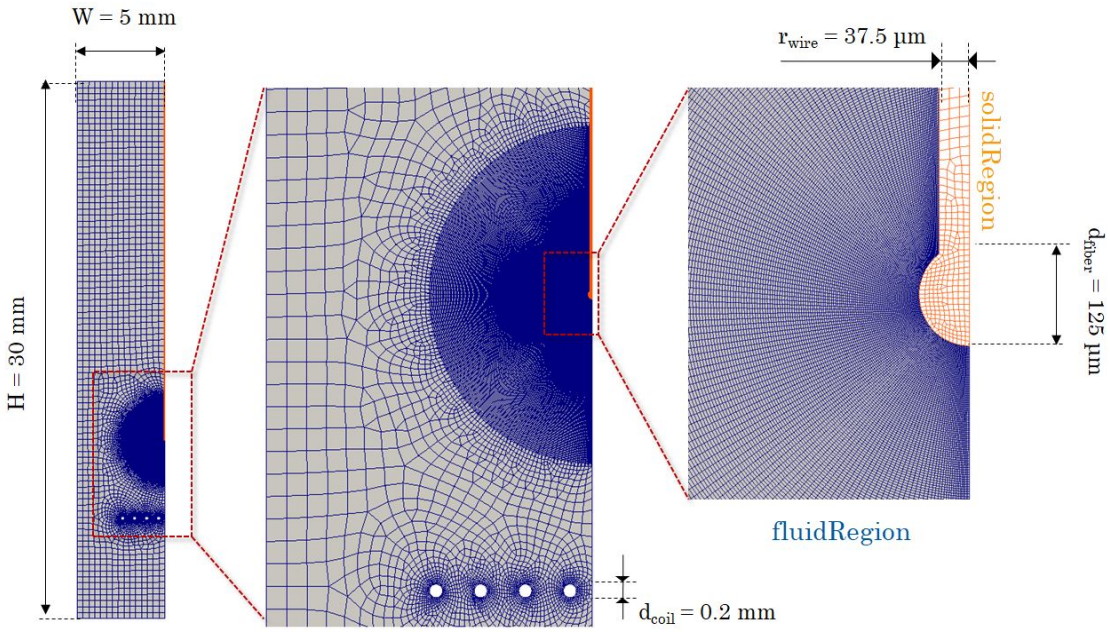

Figure 5: Multiregion computational mesh used for the CFD simulations at three increasing levels of detail, from left to right. The fluid region mesh is reported in blue color, the solid region mesh (fiber) is reported in orange.

computational cells.

- The thermocouple is modeled as a single vertical solid wire, approximate to a very thin cylinder, which ends with a small sphere representing the thermocouple junction. This creates an axial symmetry in the geometry which can be used to simplify the simulations.

- The original heating coil geometry is a horizontal metallic spring. In the alternative configuration in Figure 4 (b) it has been replaced with a planar single wire coil, which can be described within an axisymmetric geometry. The distance between the droplet and this planar coil in the new configuration is equal to the distance between the droplet and the axis of the horizontal spring in the real system (Figure 4 a). This is done to preserve the "average" distance of the heating system from the droplet, maintaining a realistic description of the experimental device.

4.1.1 Computational mesh

The computational mesh used for all the numerical cases proposed in this work has been built with the commercial CFD code `Ansys FLUENT`® v19.2 and subsequently imported

in OpenFOAM®. The mesh is reported in Figure 5. The geometry is 2D and axisymmetric, representing a slice of a cylinder having a radius $W = 5$ mm and a height $H = 30$ mm. The fluid region (blue color) and the solid region (orange color) are independently meshed and then connected. The solid region represents the metallic fiber, a vertical cylindric wire ($r_{wire} = 37.5\ \mu m$) ending with a small supporting sphere ($d_{fiber} = 125\ \mu m$), around which the liquid droplet will be suspended. The front view of the planar heating coil in the new configuration (Figure 4 b) is a series of circular holes (Figure 5), having a diameter $d_{coil} = 0.2$ mm. The number of cells is $\sim 60{,}000$, chosen by a sensitivity analysis on the cell size, with a maximum mesh non-orthogonality equal to 59.4 and a maximum Skewness of 1.4. A particularly fine mesh is imposed in the droplet region and around the heating coil.

4.2 Reconstruction of the heating rate

The metallic coil heats the surrounding atmosphere, moving the gas toward the droplet and triggering the evaporation process. However, the upward velocity of the hot gas and its temperature are generally not known, since they depend on the coil geometry, the current intensity and the material resistivity, which are usually not known with a sufficient accuracy. To overcome this problem, a preliminary experiment is performed in order to obtain the heating rate of the system:

- The droplet is taken out of the chamber. The thermocouple is now directly exposed to the gaseous phase.
- The coil is electrically heated, providing buoyancy and the upward convective flow
- The temperature at the thermocouple junction is measured, providing the temperature profile and the heating rate in that point.

An example of the experimental temperature profile is presented in Figure 6 (a). The temperature profile in a generic fixed point gives an indirect information on the fluid flow velocity $\mathbf{v}$ and the local temperature gradient ∇T:

$$\frac{\partial T}{\partial t} = -\mathbf{v}\nabla T + \frac{k}{\rho C_p}\nabla^2 T \tag{16}$$

The strategy is to perform a trial and error procedure, in which the boundary condition at the heating coil surface (Figure 5) is tuned in order to generate an upward flow which provides a temperature profile at the thermocouple equal to the experimental one (Figure 6 a). Once this is done, the droplet is suspended on the thermocouple and

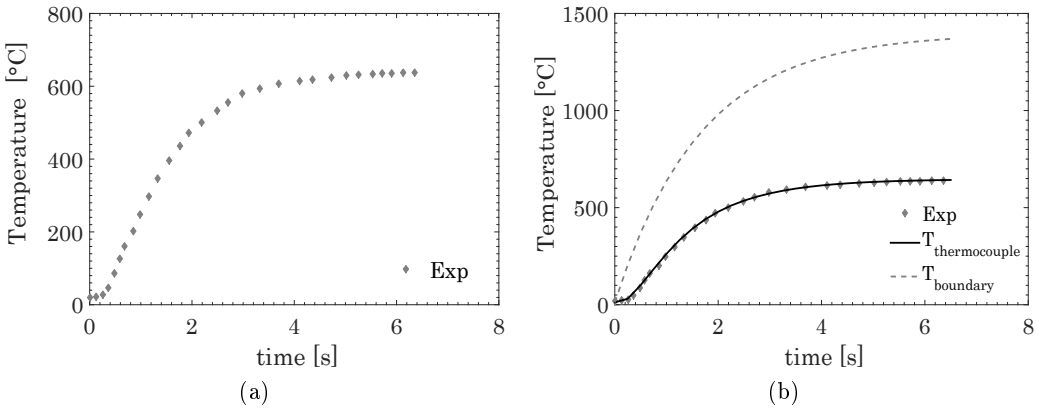

Figure 6: Experimental temperature profile at the thermocouple junction (a). Matching of the CFD results with the experiment (Figure b, black line vs. points) and the relative boundary condition profile (gray dashed line) at the coil surface.

evaporated, maintaining the same boundary condition at the coil surface.
There are many alternatives for the heating coil surface boundary condition. The best we found is represented by a time-varying boundary condition, imposed by a function of this type:

$$T(t) = T_\infty - (T_\infty - T_{amb})\, e^{-\xi t} \tag{17}$$

which physically represents the heating dynamics of the coil, which reaches a steady-state temperature T_∞ in an environment at $T_{amb} = 285$ K. The steady-state temperature of the coil T_∞ and ξ (the rate of approach to the steady state value T_∞) are the tuning parameters of the problem. Referring to Figure 6 (b), we need to find the optimal values of the parameters T_∞, ξ of the coil surface boundary condition (Equation 17, gray dashed line in Figure 6 b), that provide a heating rate at the thermocouple (black line in Figure 6 b) which fits the experiment. In the particular case presented in Figure 6, the tuning values are $T_\infty = 1670$ K, $\xi = 0.6\ s^{-1}$.

The CFD simulation of Figure 6 is presented in Figure 7, at three different times. In Figures 7 (a, b, c) the heating dynamics of the coil can be clearly seen, increasing the gas temperature over 1600 K in few seconds. The gas flow (Figures 7 d, e, f) moves upward because of the buoyancy and increases the fiber junction temperature ($\sim$ 900 K), with the heating rate presented in Figure 6 (a).

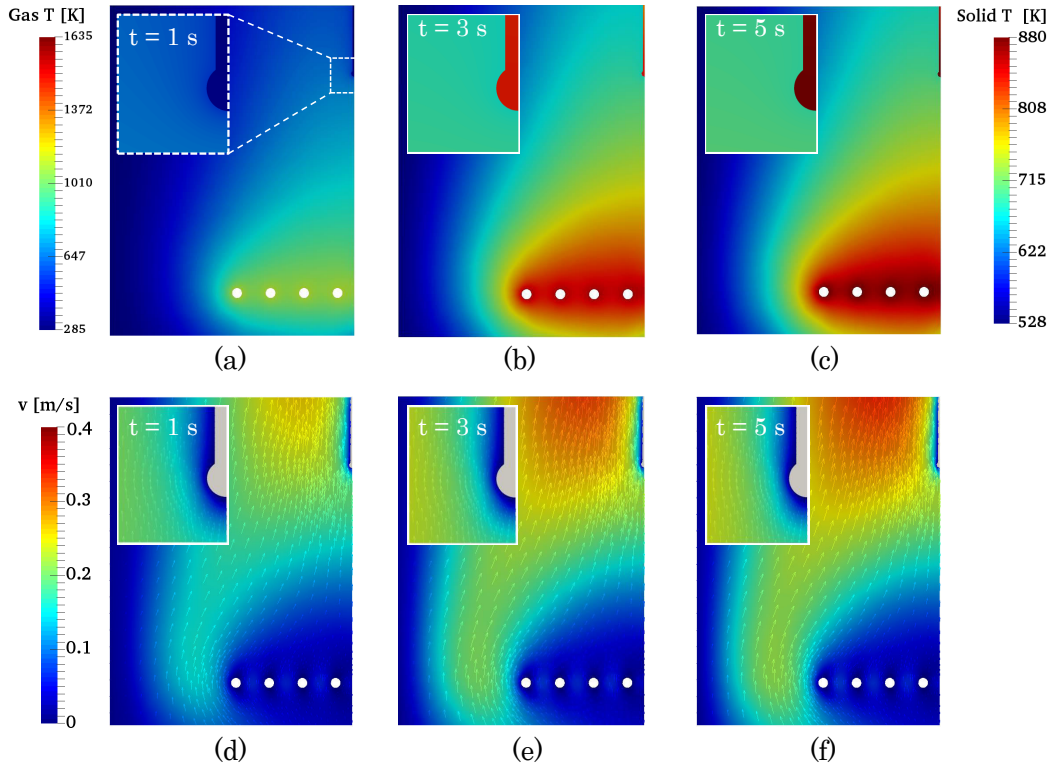

Figure 7: Numerical simulation for the heating rate reconstruction in Figure 6. Figures (a, b, c) report the temperature fields both in the gas and in the solid phase. Figures (d, e, f) report the velocity vector field of the gas phase. Pictures taken at times t= 1, 2, 5 s. In each picture, a detail of the solid fiber is shown.

Boundary	**v**	Temperature	ω_i	p
`inlet, outlet`	inletOutlet	inletOutlet	inletOutlet	$p = p_{ext}$
`outerWall`	inletOutlet	inletOutlet	inletOutlet	$p = p_{ext}$
`solidFiber`	noSlip	fluidCoupling	$\nabla\omega_i = 0$	$\nabla p = 0$
`heatingCoil`	noSlip	$T(t) = T_\infty - (T_\infty - T_{amb})\, e^{-\xi t}$	$\nabla\omega_i = 0$	$\nabla p = 0$

Table 1: Boundary conditions for velocity, temperature, species i mass fraction and pressure, to be compared with Figure 5. The time dependent condition at the heating wall is needed for the heating rate reconstruction.

4.3 Boundary conditions

The geometry has five boundaries, referring to Figure 5:

- `inlet, outlet`: the upper and bottom circular surfaces of the cylinder
- `outerWall`: external lateral surface of the cylinder
- `solidFiber`: the external surface of the solid vertical fiber (thermocouple), in contact with the fluid region
- `heatingCoil`: the external surface of the heating coil

Since we are not modeling the whole volume (Figure 4 a), but only a portion of it (Figure 4 b) the first three boundaries are open, in which an `inletOutlet` condition apply (a zero gradient condition, that switches to a fixed value condition if the velocity vector next to the boundary points inside the domain, e.g. backward flow). The temperature condition at the `solidFiber` boundary describes the heat transfer with the external fluid region, whereas it represents a wall for all the other variables (velocity, species etc.). The coupled heat transfer is included in the `turbulentTemperatureCoupledBaffleMixed` boundary condition, available in `OpenFOAM`® for conjugate heat transfer problems [36]. The `heatingCoil` boundary presents a time dependent condition for temperature, which is needed to develop the correct heating rate at the thermocouple (Equation 17). The boundary conditions are summarized in Table 1.

5 Description and modeling of the experimental cases

The multiregion code `DropletSMOKE++` is adopted to model the experimental data reported in Table 2. For each one of the cases an experimental heating rate at the thermocouple is provided and reconstructed (Table 3).

Case	Species	D_0 [mm]	T_L^0 [K]	T_G^0 [K]	p [atm]	Results
1	Acetic Acid	0.959	285	285	1	Figures 8, 9
2	Ethylene Glycol	0.940	285	285	1	Figure 10
3	Mixture	0.928	285	285	1	Figure 11, 14

Table 2: Experimental cases of evaporating droplets examined in this work.

Case	$T_{boundary}$ [K]
1	$T_1(t) = 1670 - (1670 - 285)\, e^{-0.6t}$
2	$T_2(t) = 1650 - (1650 - 285)\, e^{-0.6t}$
3	$T_3(t) = 1670 - (1670 - 285)\, e^{-0.65t}$

Table 3: Boundary condition at the `heatingCoil` boundary (Table 1, Figure 5) for the experimental cases in Table 2.

5.1 Pure components evaporation

The numerical simulation of Case 1 (Table 2) is presented in Figure 8, where the acetic acid mass fraction (a, b, c), the temperature (d, e, f) and the velocity vector (g, h, i) fields are reported at three different times. The heating coil generates an upward fluid flow starting the droplet evaporation process. The vapor distribution around the droplet (a, b, c) is not uniform, due to the different temperature on the droplet surface. The hot gas heats the droplet mainly from below, causing a higher evaporation rate in the lower region (b). Moreover, the presence of the fiber contributes to increase the local surface temperature close to the solid (b, c) where the liquid is more exposed to the hot boundary, as reported by Strizhak et al. [21] for suspended water droplets. In particular, the temperature behavior of the fiber is reported in Figures (d, e, f). Outside the liquid phase, the solid is directly exposed to the external gas and the absorbed heat flux is directly transferred to the center of the droplet, where the temperature approaches a steady-state temperature ($\sim 100°$ C). The temperature field inside the fiber can be considered one dimensional, as already reported in previous works [20, 16, 19].

The plots in Figure 9 report the normalized squared diameter decay of Case 1 (Figure a) and the liquid temperature profile measured by the thermocouple (Figure b). The temperature presents a sudden increase at the end of the experiment because the complete droplet evaporation exposes the thermocouple to the hot gas. The `DropletSMOKE++` code can predict the experimental values with a good accuracy for both the diameter and the liquid temperature, including the final heating of the fiber. In order to better analyze the

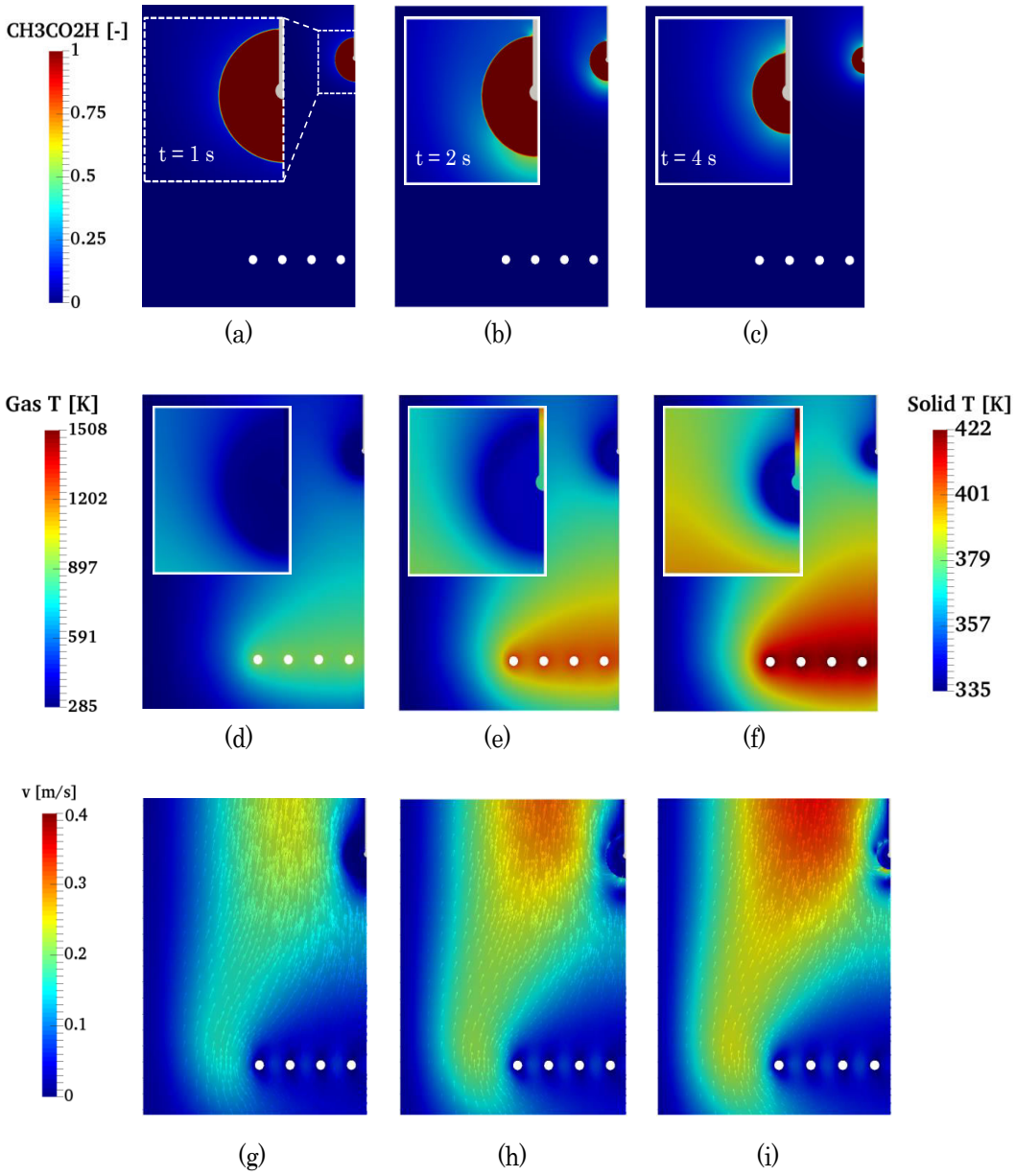

Figure 8: Numerical simulation of Case 1, Table 2. Evolution of the acetic acid mass fraction (a, b, c), gas and solid temperature (d, e, f) and vector velocity (g, h, i) fields for times t = 1 s, 2 s and 4 s.

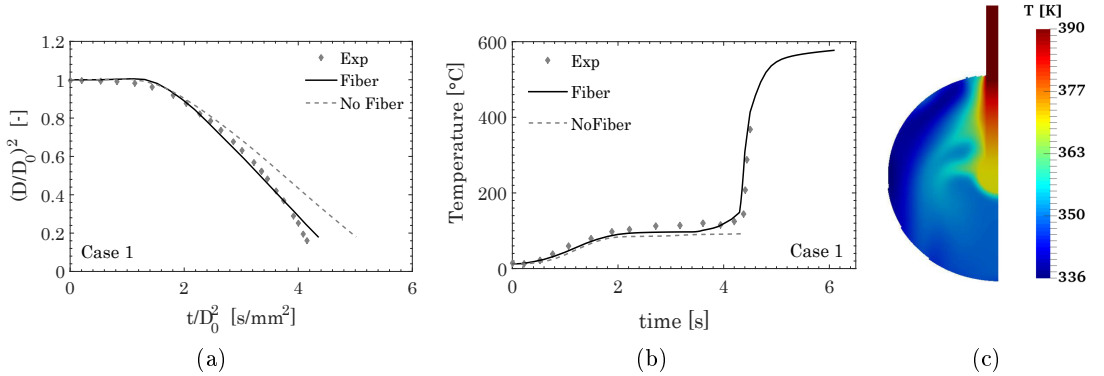

(a) (b) (c)

Figure 9: Normalized squared diameter decay (a) and liquid temperature profile (b) for Case 1, Table 2, evaporation of acetic acid. Comparison between experiments (gray points) and the `DropletSMOKE++` model, considering the heat transfer from the fiber (black line) and neglecting it (gray dashed line). Figure (c) reports the temperature distribution along the solid fiber and inside the liquid droplet at time t = 3 s.

impact of the fiber, the same simulation has been performed considering the `solidFiber` boundary as adiabatic. The main effect is a significant reduction of the evaporation rate (Figure a) and the consequent increased lifetime of the droplet. Coherently, the liquid temperature is slightly lower when the solid heat transfer contribution is not accounted for (Figure b).

In Figure 10 the results for Case 2 (Table 2) are presented, concerning ethylene glycol evaporation. The `DropletSMOKE++` code is still able to predict the experimental values with reasonable accuracy, even if some deviation can be seen toward the end of the droplet lifetime (Figure a). The evaporation rate is underestimated in the latest stages of the experiment, leading to larger diameters and a slightly lower liquid temperature (Figure 10 b). The same behavior, to a lesser extent, can be seen for acetic acid droplet simulations (Figure 9).

This phenomenon is probably due to the formation of bubbles inside the liquid phase, which can be clearly seen experimentally. The solid fiber directly conducts heat into the liquid phase, increasing the internal liquid temperature and reaching a steady-state temperature ($\sim$ 160 °C), not reached if the solid fiber is neglected (Figure 10 b). Moreover, the presence of the fiber surface facilitates the nucleation of bubbles on the solid surface, rapidly increasing the liquid consumption rate, the internal circulation and eventually the heat transfer on the droplet. The `DropletSMOKE++` code does not include a nucleation/boiling sub-model, considering the phase transition as purely superficial and not volumetric. This may cause an underestimation of the vaporization rate, leading to larger

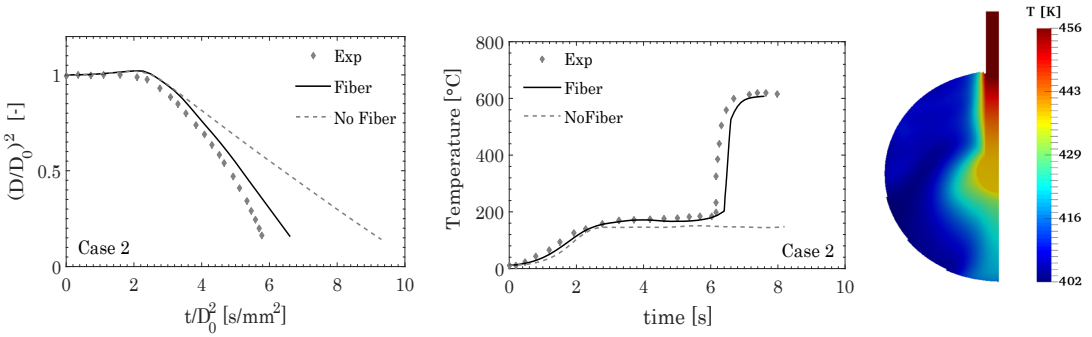

(a) (b) (c)

Figure 10: Normalized squared diameter decay (a) and liquid temperature profile (b) for Case 2, Table 2, evaporation of ethylene glycol. Comparison between experiments (gray points) and the `DropletSMOKE++` model, considering the heat transfer from the fiber (black line) and neglecting it (gray dashed line). Figure (c) reports the temperature distribution along the solid fiber and inside the liquid droplet at time t = 5s.

diameters toward the end of the droplet lifetime. As before, an additional simulation neglecting the solid heat transfer is presented, showing a significant underestimation of the vaporization rate as well as a lower steady state liquid temperature.

It is worth analyzing the temperature distribution in the liquid phase in order to emphasize the impact of the fiber. The temperature fields are reported in Figures 9 (c) for acetic acid (at time t = 3 s) and Figure 10 (c) for ethylene glycol (at time = 5 s), both for the liquid and the solid phase. The heat flux from the hot gas is conducted through the fiber, released in the liquid phase and distributed by the internal circulation. It is interesting to notice that the temperature distribution in the acetic acid droplet is more uniform if compared with ethylene glycol. This is due to the much higher viscosity of ethylene glycol, which reduces the internal velocities making the redistribution of the heat flux from the fiber more difficult. For both cases the maximum liquid temperature is found at the droplet center, where the liquid cannot evaporate. This creates favorable conditions for internal bubbles nucleation once the boiling temperature is reached (Figures 9 b, 10 b), indicating the reason for the slight delay of `DropletSMOKE++` with respect to the experiments at the end of the evaporation.

5.2 Mixture evaporation

Case 3 in Table 2 regards the evaporation of a 1:1 (volumetric) mixture of acetic acid and ethylene glycol. In this case we have two species in the liquid phase, which are diffused

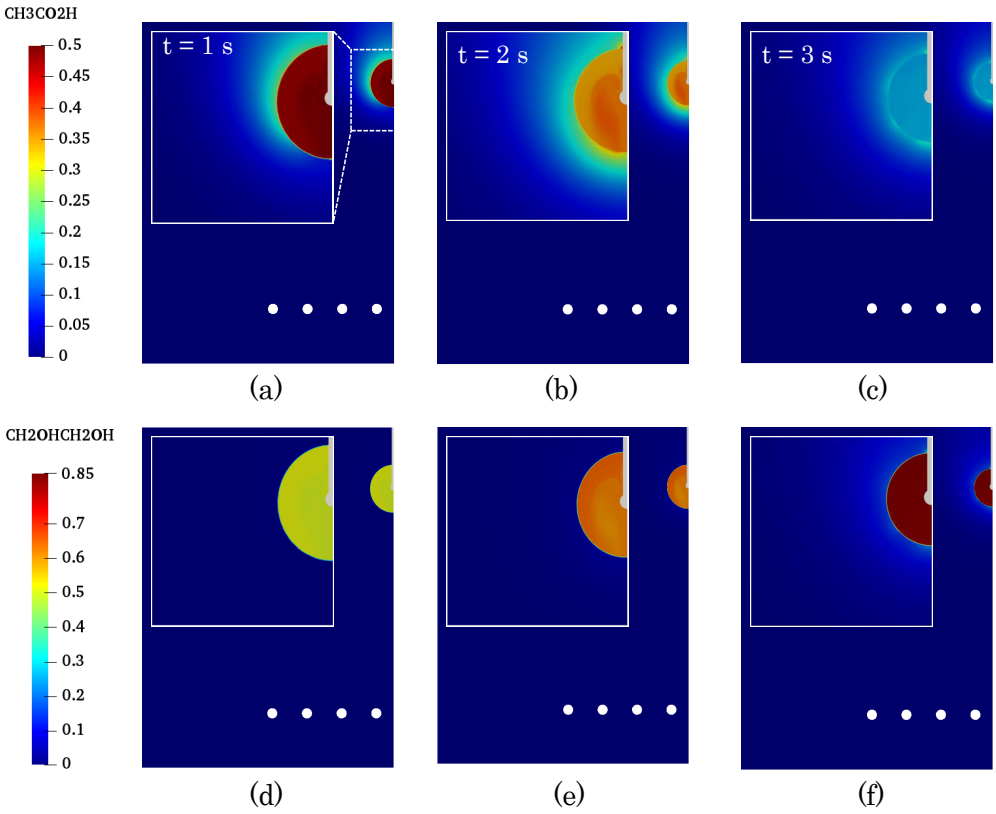

Figure 11: Numerical simulation of Case 3, Table 2. Evolution of the acetic acid (a, b, c) and ethylene glycol (d, e, f) mass fraction fields for times t = 1 s, 2 s and 3 s.

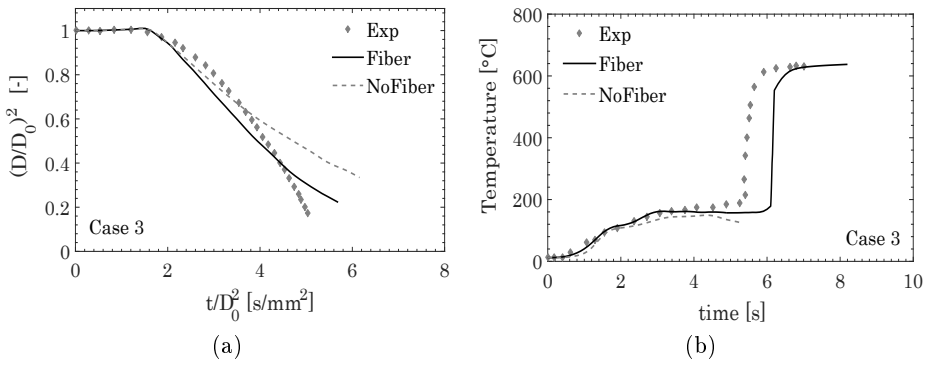

Figure 12: Normalized squared diameter decay (a) and liquid temperature profile (b) for Case 3, Table 2, evaporation of the mixture. Comparison between experiments (gray points) and the `DropletSMOKE++` model, considering the heat transfer from the fiber (black line) and neglecting it (gray dashed line). UNIFAC approach is used for γ_i.

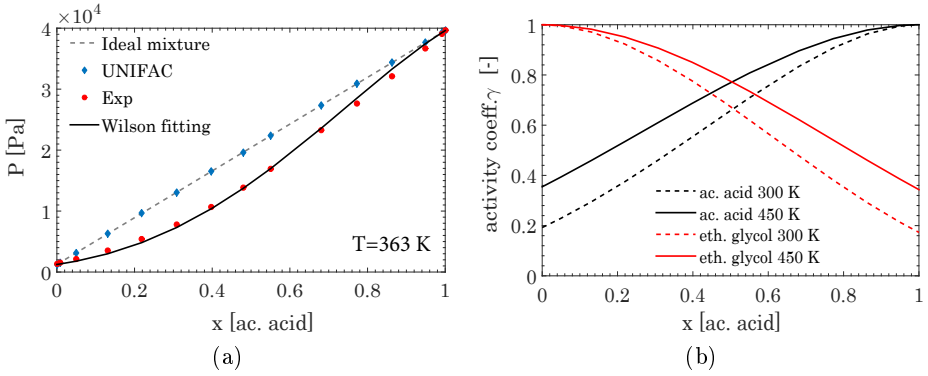

Figure 13: VLE behavior (at 363 K) of acetic acid-ethylene glycol mixtures (a) assuming ideal mixture and UNIFAC model for γ_i. The experimental data are taken from Schmid et al. [37] and the fitting is based on Wilson model. Figure (b) reports γ_i at 300 K and 450 K using the Wilson fitted model.

and advected by the internal velocity field. Figure 11 reports the evolution of acetic acid (a, b, c) and ethylene glycol (d, e, f) mass fraction. Ethylene glycol is the heavy species and it tends to concentrate in the droplet, while acetic acid evaporates faster. An internal mass fraction gradient is present (Figures b, e), which is rapidly homogenized by the strong internal convection.

Figure 12 reports the normalized squared diameter decay of Case 3 (Figure a) and the liquid temperature profile measured by the thermocouple (Figure b). While the liquid temperature is captured with good accuracy, the diameter decay shows a different trend. Comparing the model with the experiments, the evaporation is too fast at the initial stages and too slow towards the end of the vaporization process. Including the heat transfer with the fiber slightly improves the results (from the point of view of the droplet lifetime), but the qualitative trend does not change significantly. Moreover, since the final part of the evaporation is delayed, also the exposure of the thermocouple to the gas is shifted (Figure 12 b). Since this discrepancy only appears for Case 3, it is worth investigating the mixture thermodynamics in detail.

5.3 Wilson model for activity coefficients

The vapor-liquid equilibrium (VLE) data of acetic acid-ethylene glycol mixture are taken from the experimental values from Schmid et al. [37] and reported in Figure 13 (a) (red points). The data are taken at $T = 363$ K and show a slightly negative deviation from the Raoult's law, suggesting the need of a non-ideal mixture assumption for the system (since the vapor phase can be safely considered ideal). In this work the activity coefficients γ_i

of the species were computed with the UNIFAC approach [26], considering the functional groups present in the molecules. However, as can be clearly seen in Figure 13 (a), the UNIFAC method does not show a significant deviation from the mixture ideality and therefore it is not able to correctly predict the experimental data for this specific mixture. The modified UNIFAC [38] and the ASOG (Analytical Solution Of Groups) [39] methodologies predict a positive deviation of the VLE data from the ideality (not shown), leading to the fact that no predictive model for the activity coefficients can properly describe the acetic acid- ethylene glycol mixture. This may explain the discrepancy between the experiments and the CFD model in Figure 12 (a), since the mixture non-ideality can strongly affect the evaporation rate. In order to verify this hypothesis and overcome the lack of knowledge concerning the $\gamma_i\left(x_i\right)$ model, a fitting of the experimental data from Schmid et al. [37] has been performed using the Wilson model [40] for the activity coefficients γ_i of the binary mixture:

$$ln\gamma_1 = -ln\left(x_1 + x_2\Lambda_{1,2}\right) + x_2\left(\frac{\Lambda_{1,2}}{x_1 + x_2\Lambda_{1,2}} - \frac{\Lambda_{2,1}}{x_2 + x_1\Lambda_{2,1}}\right) \tag{18}$$

$$ln\gamma_2 = -ln\left(x_2 + x_1\Lambda_{2,1}\right) - x_1\left(\frac{\Lambda_{1,2}}{x_1 + x_2\Lambda_{1,2}} - \frac{\Lambda_{2,1}}{x_2 + x_1\Lambda_{2,1}}\right) \tag{19}$$

where:

$$\Lambda_{i,j} = \frac{v_j}{v_i}e^{-\frac{A_{i,j}}{RT}} \tag{20}$$

in which v represents the mole volume of the pure species. The two constants $A_{i,j}$ ($A_{1,2}$ and $A_{2,1}$) are the tuning parameters of the fitting procedure. The boiling pressure of the mixture can be easily calculated as a function of the acetic acid mole fraction x_1:

$$p\left(x_1\right) = p_2^0\gamma_2 + x_1\left(p_1^0\gamma_1 - p_2^0\gamma_2\right) \tag{21}$$

where p_i^0 is the vapor pressure of species i at $T = 363$ K. The two parameters $A_{1,2}$ and $A_{2,1}$ must be tuned in order to provide a boiling curve (Equation 21) which fits the experiments in Figure 13 (a). We obtain:

$$\Lambda_{1,2} = 0.977e^{\frac{1920.09}{RT}} \tag{22}$$

$$\Lambda_{2,1} = 1.022e^{\frac{1545.9}{RT}} \tag{23}$$

which inserted in Equations 18, 19 provide the activity coefficients of acetic acid and

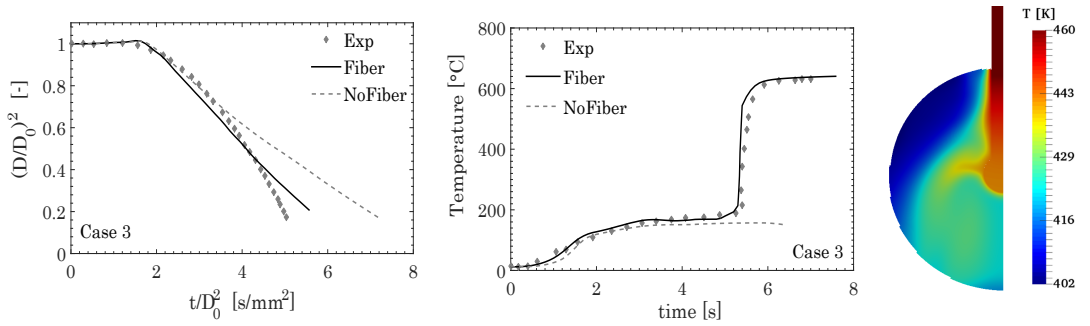

(a) (b) (c)

Figure 14: Normalized squared diameter decay (a) and liquid temperature profile (b) for Case 3, Table 2, evaporation of the mixture. Comparison between experiments (gray points) and the `DropletSMOKE++` model, considering the heat transfer from the fiber (black line) and neglecting it (gray dashed line). Wilson model used for γ_i. Figure (c) reports the temperature distribution along the solid fiber and inside the liquid droplet at time t = 2 s.

ethylene glycol in function of local composition and temperature. The γ_i curves are reported in Figure 13 (b) at 300 K (ambient T) and 450 K (maximum T reached during the evaporation, Figure 12 b). It is clear that the values of γ_i are far from ideality, especially within our domain of acetic acid concentration (from $\sim$ 0.5 to 0, Figure 11). This model works in the direction we need, since we expect the acetic acid evaporation to be slightly delayed at the initial stages (since $\gamma_{ac.acid} \sim 0.65 - 0.7$), increasing the vaporization rate of ethylene glycol towards the end (where $\gamma_{et.glycol}$ tends to 1).

Figure 14 reports the result obtained with the Wilson model for the activity coefficients, showing a significant improvement of the model prediction. The concavity of the squared diameter profile (Figure 12 a) is not present anymore, and the diameter decay is almost linear with time. As for the pure components cases, the final stages of the evaporation present a slight delay with respect to the experiments. The fiber heats the liquid from the inside 14 (c) and provides the conditions for possible bubbles nucleation which would enhance the vaporization rate. It is interesting to notice that the steady-state temperature (plateau) reached by the droplet is very similar to the ethylene glycol droplet case (Figure 10), even though the initial mixture is 1:1. Figure 11 (c) and (f) clearly show that at the time when the plateau is reached (around 3-4 s), the mixture composition is almost totally shifted toward ethylene glycol. The more volatile component (acetic acid) is almost completely evaporated.

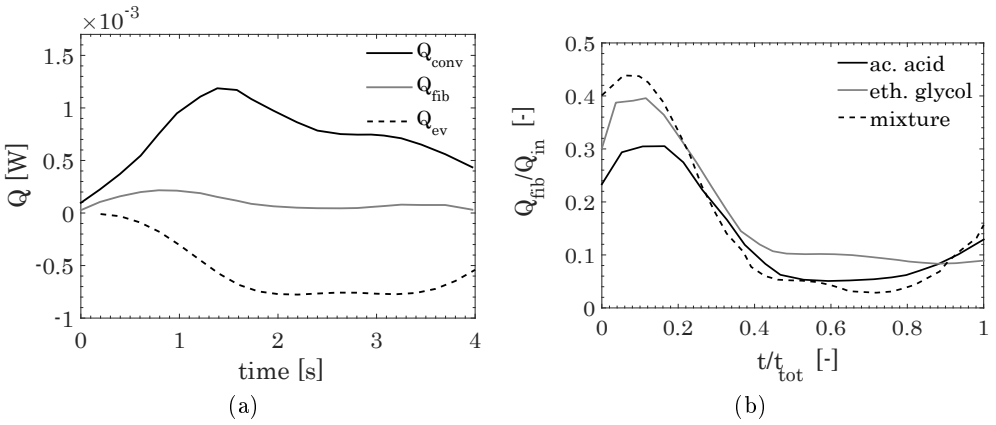

Figure 15: Heat fluxes contributions on the acetic acid droplet (Case 1, Table 2), divided in convective heat flux $\dot{Q}_{conv}$, evaporative flux $\dot{Q}_{ev}$ and heat conduction from the fiber $\dot{Q}_{fib}$ (a). Relative contribution of $\dot{Q}_{fib}$ to the total income $Q_{in} = \dot{Q}_{conv} + \dot{Q}_{fib}$ (b) for the three cases in Table 2.

5.4 Effect of the fiber on the droplet heating

It is clear from the previous results that the solid fiber can have a significant effect on the vaporization phenomena. It is interesting to quantitatively investigate the contribution of the fiber to the global heat flux on the droplet. To this purpose we performed a post-processing analysis on the heat fluxes on the liquid droplet, divided in:

- Heat flux on the droplet surface S

$$\dot{Q}_{conv} = \int_S (k\nabla T + \rho C_p T \mathbf{v})\, \mathbf{n} dS \tag{24}$$

- Evaporation flux

$$\dot{Q}_{ev} = \int_S \sum_i^{N_s} \dot{m}_i \Delta h_{ev,i} dS \tag{25}$$

- Conductive flux from the fiber surface S_f

$$\dot{Q}_{fib} = \int_{S_f} k_s \nabla T_s \mathbf{n} dS_f \tag{26}$$

The results are presented in Figure 15 (a) for the pure acetic acid droplet evaporation. The upward convective flow heats the thermocouple faster than the droplet, because

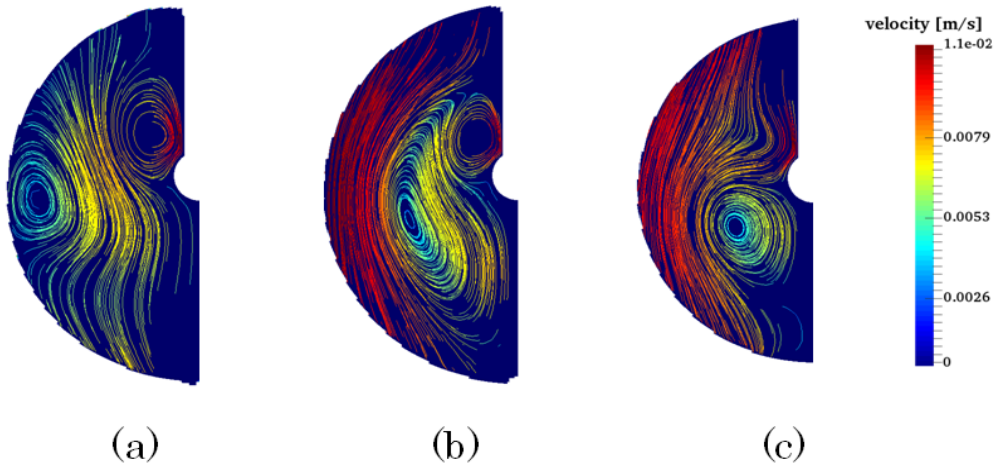

Figure 16: Flow field streamlines in the liquid phase, acetic acid droplet evaporation (Case 1, Table 2). Times t= 0.4 s (a), 1.2 s (b), 2 s (c).

of the initial surface cooling due to vaporization. This makes the fiber contribution significantly important at the initial stages of the evaporation process. Later on, the fiber contribution is stabilized at an almost constant value (due to the reaching of a constant droplet temperature) and has a sudden increase towards the end of the vaporization due to the complete droplet evaporation. This can be seen more in detail in Figure 15 (b), where the $\dot{Q}_{fib}$ contribution is highlighted through the ratio $\frac{\dot{Q}_{fib}}{\dot{Q}_{in}} = \frac{\dot{Q}_{fib}}{\dot{Q}_{conv}+\dot{Q}_{fib}}$, representing the relative contribution of the heat conduction from the fiber to the total heat flux income. The peak of the $\dot{Q}_{fib}$ contribution can reach $30-40\%$ of the total heat flux income at the very beginning of the vaporization (when the difference between the liquid and the fiber temperature is maximum), going down to $8-10\%$ throughout the process. This is however sufficient to provide a $10-15$ K increase in the droplet temperature (Figure 9) and a consequent reduced droplet lifetime. These results are in agreement with a few studies available in literature on the same topic. Yang et al. [16] investigated with a simple one-dimensional model the effect of supporting fibers on n-heptane and n-hexadecane droplet evaporation, showing the same qualitative trend we presented in our analysis. The importance of $\dot{Q}_{fib}$ at the early stage of the evaporation has also been described by Han et al. [18] and Harada et al. [31] for different support fibers, describing a situation in which the solid fiber has been sufficiently heated by the hot gases, while the droplet temperature is still low.

5.5 Internal circulation and preferential vaporization

The presence of internal convection in the droplet is a well known phenomenon from the experimental point of view. By means of Planar Laser-Induced Fluorescence and Particle Image Velocimetry [41, 42] and laser scattering [43, 44] it is possible to get an insight on the internal motion in the liquid phase.
Since we are solving for the whole velocity field, the liquid convection can also be visualized numerically. The internal velocity field for the acetic acid droplet evaporation are reported in Figure 16 for three different times. The main mechanism which leads to the formation of vortices in the liquid phase is the shear force applied on the interface by the external convection, as reported by Sirignano [2]. This can generate an internal flow field which can be of the order of $5 - 20\%$ of the free stream velocity [45]. Density gradients due to temperature differences inside the droplet usually have a secondary effect. The shear force induces the formation of a main vortex close to the droplet surface. This latter vortex, to enforce flow continuity, induces a second smaller vortex which rotates in opposite sense (Figure 16). The dimension of the main vortex is reduced during evaporation and its center is shifted toward the center of the droplet. This also causes a reduction of the second vortex and eventually its extinction (Figure 16 c). This is in agreement to what reported by the experimental work of Volkov et al. [41] on water droplets evaporation, where they detect a lower intensity of the internal convection as the evaporation proceeds.
It is important to point out that internal convection can have a major impact on the evaporation rate, especially concerning multicomponent droplets. If the volatilities of the components are very different (such as in real fuels), preferential vaporization can take place. This phenomenon is strongly dependent on the liquid flow field [46, 45]: if liquid convection is weak the droplet will most likely evaporate through "layers" (shell model), making internal diffusion the limiting step of the evaporation process. On the other hand, if internal convection is strong enough, the concentration of the components would be almost uniform in the liquid phase. The more volatile components are continuously transported toward the droplet surface, facilitating their preferential vaporization.
This can be clearly seen in Figure 12 (b) for the evaporation of the acetic acid-ethylene glycol mixture: before reaching the plateau, the droplet temperature is more irregular if compared to the pure monocomponent cases (Figures 9, 10 (b)) showing two changes in the profile concavity. This is behavior is typical of multi-stage vaporization and it is also exhibited by the diameter decay profile (Figure 12 a) where it is evident a change in the profile slope (i.e. the vaporization rate). The internal convection (Figure 16) plays a key

role in the preferential vaporization of the more volatile component (acetic acid in this case) because it significantly accelerates the internal mass transfer, which would be the limiting step in case of pure internal diffusion (in the absence of internal mixing). Finally it is worth noticing that when more realistic activity coefficients γ_i are accounted for (by the Wilson model, Figure 14) the preferential vaporization is smoothed and less evident. This is due to the stronger molecular interactions between the two components, which modify their relative volatility (Figure 13 a) and make the mixture evaporate similarly to monocomponent cases.

6 Conclusions

In this work we presented an experimental and numerical activity on the evaporation of suspended fuel droplets in a convective flow. Acetic acid and ethylene glycol (and their mixture) have been studied because of their importance as components of complex fuel surrogates. The droplets have been suspended on a support fiber in a small combustion chamber and evaporated in buoyancy driven convection, triggered by the electrical heating of a resistive coil placed under the droplet. The support fiber is a thermocouple, used to measure the heating rate and the liquid temperature of the droplet. The experiments have been then modeled with the multiphase CFD code `DropletSMOKE++`, based on the VOF methodology for the interface tracking. In this work the code was properly extended to account for the conjugate heat transfer between the solid support fiber and the fluid region (which includes both the liquid and the gas in the VOF description). The numerical results provide useful information on the flow field around and inside the droplet, as well as the gas, the liquid and the solid temperature distribution. The evaporation rate is shown to be largely underpredicted if the heat transfer from the support fiber is neglected (considering the boundary as adiabatic), both for acetic acid and ethylene glycol droplets. The multiregion approach effectively describes the additional heat flux conducted through the thermocouple, which clearly modifies the internal temperature distribution. The heat flux from the droplet center is advected inside the liquid phase and toward the surface, accelerating the vaporization and providing a good agreement with the experimental profiles. The `DropletSMOKE++` prediction of the mixture evaporation has been significantly improved using the activity coefficients obtained from a fitting of the VLE experiments, showing the inability of the available methods (UNIFAC, ASOG) to model the acetic acid-ethylene glycol mixture thermodynamics. Finally, the numerical results allowed to investigate the internal convection in the liquid phase and its formation mechanism. The strong internal mixing allows to preferentially vaporize

the more volatile component, leading to a double stage evaporation.
Future works will be focused on the extension of the evaporation model in order to consider the nucleation and boiling inside the liquid phase, as well as the introduction of a gas phase kinetics to simulate the combustion phenomenon.

Acknowledgments

The Residue2Heat project has received funding from the European Union's Horizon 2020 research and innovation programme under grant agreement No 654650.

Nomenclature

Acronyms

ASOG Analytical Solution Of Groups

CH_2OHCH_2OH Ethylene Glycol

CH_3CO_2H Acetic Acid

FPBO Fast Pyrolysis Bio Oil

UNIFAC UNIversal Functional-group Activity Coefficients

VLE Vapor-Liquid Equilibrium

VOF Volume Of Fluid

Greek letters

α marker function [−]

β thermal expansion coefficient $\left[\frac{1}{K}\right]$

χ generic fluid property [−]

Δh_{ev} evaporation enthalpy $\left[\frac{J}{kg}\right]$

γ activity coefficient [−]

$\hat{\phi}$ mixture gas-phase fugacity coefficient [−]

κ curvature $\left[\frac{1}{m}\right]$

μ dynamic viscosity $\frac{kg}{ms}$

ω mass fraction $[-]$

ϕ pure gas-phase fugacity coefficient $[-]$

ρ density $\left[\frac{kg}{m^3}\right]$

σ surface tension $\left[\frac{N}{m}\right]$

Roman letters

$\dot{m}$ evaporative flux $\left[\frac{kg}{m^3 s}\right]$

$\dot{Q}$ heat flux $[W]$

$\mathcal{D}$ mass diffusion coefficient $\left[\frac{m^2}{s}\right]$

$\mathbf{f}$ force $\left[\frac{N}{m^3}\right]$

$\mathbf{j}$ mass flux $\left[\frac{kg}{m^2 s}\right]$

$\mathbf{v}$ velocity $\left[\frac{m}{s}\right]$

C_p constant pressure specific heat $\left[\frac{J}{kgK}\right]$

D diameter $[m]$

H height of the mesh $[m]$

k thermal conductivity $\left[\frac{W}{mK}\right]$

M_w molecular weight $\left[\frac{kg}{mol}\right]$

Ns Number of species $[-]$

p pressure $[Pa]$

p^0 vapor pressure $[Pa]$

r radius $[m]$

t time $[s]$

T temperature $[K]$

v mole volume $\left[\frac{m^3}{mol}\right]$

W base radius of the mesh $[m]$

x liquid phase mole fraction $[-]$

y gas phase mole fraction $[-]$

Subscripts

0 initial, reference

amb ambient, external

$conv$ convective

d diffusive

ev evaporation

fib fiber

G gas

i species i

L liquid

s solid

References

[1] B. Abramzon, W. Sirignano, Droplet vaporization model for spray combustion calculations, International Journal of Heat and Mass Transfer 32 (9) (1989) 1605–1618.

[2] W. A. Sirignano, Fluid dynamics and transport of droplets and sprays, Cambridge university press, 1999.

[3] H. Ghassemi, S. W. Baek, Q. S. Khan, Experimental study on binary droplet evaporation at elevated pressures and temperatures, Combustion science and technology 178 (6) (2006) 1031–1053.

[4] K. Han, C. Zhao, G. Fu, F. Zhang, S. Pang, Y. Li, Evaporation characteristics of dual component droplet of benzyl azides-hexadecane mixtures at elevated temperatures, Fuel 157 (2015) 270–278.

[5] S. Sazhin, M. Al Qubeissi, R. Kolodnytska, A. Elwardany, R. Nasiri, M. Heikal, Modelling of biodiesel fuel droplet heating and evaporation, Fuel 115 (2014) 559–572.

[6] S. S. Sazhin, Advanced models of fuel droplet heating and evaporation, Progress in energy and combustion science 32 (2) (2006) 162–214.

[7] A. J. Marchese, F. L. Dryer, V. Nayagam, Numerical modeling of isolated n-alkane droplet flames: initial comparisons with ground and space-based microgravity experiments, Combustion and Flame 116 (3) (1999) 432–459.

[8] J. Piskorz, D. Scott, D. Radlein, Pyrolysis oils from biomass: Producing analyzing and upgrading, in: Symposium Series, Vol. 376, American Chemical Society Washington, DC, 1988.

[9] A. Oasmaa, C. Peacocke, et al., A guide to physical property characterisation of biomass-derived fast pyrolysis liquids, Technical Research Centre of Finland Espoo, 2001.

[10] A. Oasmaa, D. Meier, Norms and standards for fast pyrolysis liquids: 1. round robin test, Journal of Analytical and Applied Pyrolysis 73 (2) (2005) 323–334.

[11] Residue2Heat, `https://www.residue2heat.eu/`.

[12] R. Calabria, F. Chiariello, P. Massoli, Combustion fundamentals of pyrolysis oil based fuels, Experimental Thermal and Fluid Science 31 (5) (2007) 413–420.

[13] M. Pelucchi, C. Cavallotti, A. Cuoci, T. Faravelli, A. Frassoldati, E. Ranzi, Detailed kinetics of substituted phenolic species in pyrolysis bio-oils, Reaction Chemistry and Engineering.

[14] A. Saufi, A. Frassoldati, T. Faravelli, A. Cuoci, DropletSMOKE++: A comprehensive multiphase CFD framework for the evaporation of multidimensional fuel droplets, International Journal of Heat and Mass Transfer 131 (2019) 836–853.

[15] J.-R. Yang, S.-C. Wong, On the discrepancies between theoretical and experimental results for microgravity droplet evaporation, International Journal of Heat and Mass Transfer 44 (23) (2001) 4433–4443.

[16] J.-R. Yang, S.-C. Wong, An experimental and theoretical study of the effects of heat conduction through the support fiber on the evaporation of a droplet in a weakly

convective flow, International journal of heat and mass transfer 45 (23) (2002) 4589–4598.

[17] H. L.-u. Rehman, J. Weiss, P. Seers, Effect of heat conduction on droplet life time and evaporation rate under forced convection at low temperatures, Experimental Thermal and Fluid Science 72 (2016) 59–66.

[18] K. Han, G. Song, X. Ma, B. Yang, An experimental and theoretical study of the effect of suspended thermocouple on the single droplet evaporation, Applied Thermal Engineering 101 (2016) 568–575.

[19] D. Shringi, H. Dwyer, B. Shaw, Influences of support fibers on vaporizing fuel droplets, Computers & Fluids 77 (2013) 66–75.

[20] N. Ghata, B. D. Shaw, Computational modeling of the effects of support fibers on evaporation of fiber-supported droplets in reduced gravity, International Journal of Heat and Mass Transfer 77 (2014) 22–36.

[21] P. Strizhak, R. Volkov, G. Castanet, F. Lemoine, O. Rybdylova, S. Sazhin, Heating and evaporation of suspended water droplets: Experimental studies and modelling, International Journal of Heat and Mass Transfer 127 (2018) 92–106.

[22] C. W. Hirt, B. D. Nichols, Volume of fluid (VOF) method for the dynamics of free boundaries, Journal of computational physics 39 (1) (1981) 201–225.

[23] G. Tryggvason, R. Scardovelli, S. Zaleski, Direct numerical simulations of gas–liquid multiphase flows, Cambridge University Press, 2011.

[24] A. P. Pinheiro, J. M. Vedovoto, Evaluation of droplet evaporation models and the incorporation of natural convection effects, Flow, Turbulence and Combustion 1–22.

[25] J. M. Smith, Introduction to chemical engineering thermodynamics, ACS Publications, 1950.

[26] A. Fredenslund, R. L. Jones, J. M. Prausnitz, Group-contribution estimation of activity coefficients in nonideal liquid mixtures, AIChE Journal 21 (6) (1975) 1086–1099.

[27] J. Leffler, H. T. Cullinan Jr, Variation of liquid diffusion coefficients with composition. dilute ternary systems, Industrial & Engineering Chemistry Fundamentals 9 (1) (1970) 88–93.

[28] J. Brackbill, D. B. Kothe, C. Zemach, A continuum method for modeling surface tension, Journal of computational physics 100 (2) (1992) 335–354.

[29] S. Popinet, Numerical models of surface tension, Annual Review of Fluid Mechanics 50 (2018) 49–75.

[30] A. Albadawi, D. Donoghue, A. Robinson, D. Murray, Y. Delauré, Influence of surface tension implementation in volume of fluid and coupled volume of fluid with level set methods for bubble growth and detachment, International Journal of Multiphase Flow 53 (2013) 11–28.

[31] T. Harada, H. Watanabe, Y. Suzuki, H. Kamata, Y. Matsushita, H. Aoki, T. Miura, A numerical investigation of evaporation characteristics of a fuel droplet suspended from a thermocouple, International Journal of Heat and Mass Transfer 54 (1-3) (2011) 649–655.

[32] C. Chauveau, M. Birouk, F. Halter, I. Gökalp, An analysis of the droplet support fiber effect on the evaporation process, International Journal of Heat and Mass Transfer 128 (2019) 885–891.

[33] A. Cuoci, A. Frassoldati, T. Faravelli, E. Ranzi, OpenSMOKE++: An object-oriented framework for the numerical modeling of reactive systems with detailed kinetic mechanisms, Computer Physics Communications 192 (2015) 237–264.

[34] C. L. Yaws, The Yaws Handbook of Physical Properties for Hydrocarbons and Chemicals: Physical Properties for More Than 54,000 Organic and Inorganic Chemical Compounds, Coverage for C1 to C100 Organics and Ac to Zr Inorganics, Gulf Professional Publishing, 2015.

[35] R. C. Reid, J. M. Prausnitz, B. E. Poling, The properties of gases and liquids, McGraw Hill Book Co., New York, NY, 1987.

[36] C. J. Greenshields, OpenFOAM user guide, OpenFOAM Foundation Ltd, version 3 (1).

[37] B. Schmid, M. Döker, J. Gmehling, Measurement of the thermodynamic properties for the reactive system ethylene glycol–acetic acid, Fluid phase equilibria 258 (2) (2007) 115–124.

[38] J. Lohmann, R. Joh, J. Gmehling, From unifac to modified unifac (dortmund), Industrial & engineering chemistry research 40 (3) (2001) 957–964.

[39] A. Rizzi, J. F. Huber, Comparative calculations of activity coefficients in binary liquid mixtures at infinite dilution using the" solution of groups" model, Industrial & Engineering Chemistry Process Design and Development 20 (2) (1981) 204–210.

[40] F. A. Gothard, M. F. C. Ciobanu, D. G. Breban, C. I. Bucur, G. V. Sorescu, Predicting the parameters in the wilson equations for activity coefficients in binary hydrocarbon systems, Industrial & Engineering Chemistry Process Design and Development 15 (2) (1976) 333–337.

[41] R. Volkov, P. Strizhak, Research of temperature fields and convection velocities in evaporating water droplets using planar laser-induced fluorescence and particle image velocimetry, Experimental Thermal and Fluid Science 97 (2018) 392–407.

[42] R. Volkov, P. Strizhak, Measuring the temperature of a rapidly evaporating water droplet by planar laser induced fluorescence, Measurement 135 (2019) 231–243.

[43] D. K. Mandal, S. Bakshi, Evidence of oscillatory convection inside an evaporating multicomponent droplet in a closed chamber, Journal of colloid and interface science 378 (1) (2012) 260–262.

[44] D. K. Mandal, S. Bakshi, Internal circulation in a single droplet evaporating in a closed chamber, International Journal of Multiphase Flow 42 (2012) 42–51.

[45] C. K. Law, S. Prakash, W. Sirignano, Theory of convective, transient, multicomponent droplet vaporization, in: Symposium (International) on Combustion, Vol. 16, Elsevier, 1977, pp. 605–617.

[46] C. K. Law, Multicomponent droplet combustion with rapid internal mixing, Combustion and Flame 26 (1976) 219–233.

Paper 3

Direct numerical simulation of the combustion of a suspended droplet in normal gravity

A.E. Saufi, A. Frassoldati, T. Faravelli, A. Cuoci

Department of Chemistry, Materials, and Chemical Engineering "G. Natta", P.zza Leonardo da Vinci 32, Milano, Italy

Combustion and Flame (2020), submitted

Abstract

`DropletSMOKE++` is a multiphase CFD framework based on `OpenFOAM`®, originally developed and validated for suspended droplets evaporation in a gravity field and convective conditions. In this work the solver is further extended to account for gas-phase combustion introducing: (i) an operator-splitting methodology to efficiently solve the gas-phase chemistry with large kinetic mechanisms, (ii) a model for the flame radiative heat transfer and (iii) a double vaporization model to account for possible boiling. This allows to simulate the combustion of suspended fuel droplets in normal gravity with a detailed description of the gas-phase chemistry, representing the novelty and the main objective of this work. The numerical model is applied to simulate the vaporization, ignition and combustion of a methanol droplet suspended on a quartz fiber at different oxygen concentrations. The numerical results are compared with recent experimental data, showing a satisfactory agreement in terms of diameter decay, radial temperature profiles and sensitivity to the oxygen concentration in the gas-phase. In particular, the burning rate is found to be significantly affected by thermal conduction from the fiber, due to its relatively large size and the high temperatures involved in the combustion process. On the other hand the fiber perturbs the flame itself, providing a partial quenching close to its surface. The droplet combustion behavior has been compared to the one predicted in microgravity conditions, evidencing a lower standoff ratio, a higher flame temperature and an intense internal circulation. The gas-phase chemistry has been analyzed in terms of distribution of the main species in the gas phase, showing a local accumulation of (i) intermediate oxidation products at the fiber (due to the quenching) and (ii) water at the surface, which partially condenses on the droplet surface affecting the vaporization rate.

Keywords: droplet combustion, gravity, VOF, support fiber, methanol

1 Introduction

Spray and droplet combustion technologies are adopted in a large number of practical applications: power generation, propulsion, fuel injectors for diesel engines and aerospace applications. The combustion of a spray of droplets evolves through three main steps: (i) the atomization of the liquid, (ii) the vaporization of the fuel droplets and (iii) the ignition of the gas-phase and the subsequent combustion. Even though the numerical simulation of these systems is rapidly advancing, major difficulties remain due to the intrinsic complexity of the problem: droplets breakup, coalescence, surface tension instabilities, interactions with a turbulent gas flow are very complex phenomena, not yet fully understood [1, 2]. Evaporation and gas-phase combustion create large spatial temperature and concentration gradients, which further complicate the problem. Moreover, these phenomena are strongly coupled and they occur at very different temporal and spatial scales (several orders of magnitude), making their numerical modeling extremely expensive. Hence, the need of simplified but still physically representative configurations. In particular, the study of the evaporation and combustion of a single isolated droplet represented an essential step towards the better understanding of more complex systems, both experimentally and numerically. In the last decades researchers mainly focused on a simple, idealized condition in which a spherical droplet was investigated in microgravity [3, 4], because of the absence of buoyancy effects and droplet deformation. This was also attractive for the relatively simple mathematical modeling, exploiting the spherical symmetry of the system and leaving room for a more detailed chemistry description [5, 6]. This paved the way for the study of crucial aspects related to droplets combustion such as cool flames, multiple ignitions and extinction phenomena [7, 8]. Even if the microgravity condition still represents a valuable method for droplets analysis, there is a strong interest in considering more realistic situations in which convection and gravity play a significant role (like in sprays). The most common case is represented by the vaporization, ignition and combustion of a single droplet suspended on a fiber in normal gravity [9, 10, 11, 12, 13]. This system requires additional complexity in the mathematical description with respect to the zero-gravity case. In particular, a CFD multiphase model is required, including: (i) a robust numerical method for the interface localization and advection, (ii) the solution of both a gas and liquid velocity field, (iii) a reliable model for evaluating the evaporation rate in convective conditions and (iv) a multi-region approach to model the flame-fiber thermal interaction [14]. In this context, while noteworthy papers can be found for pure evaporation in normal gravity [15, 16, 17], very few numerical works on combustion are available and mainly limited to

non-shrinking, motionless droplets [18] or adopting one-step/global schemes for chemistry [19]. Recently, a skeletal mechanism (∼20 reactions) was used by Ghata et al. [20] within a multiphase approach, limiting however the application to microgravity conditions. To the authors knowledge, there is a lack of comprehensive models for droplets combustion in convective conditions, coupled with a detailed description of the gas-phase chemistry. The `DropletSMOKE++` solver [21, 22] is a multiphase CFD code specifically conceived to model the evaporation of pure and multicomponent suspended droplets (including i, ii, iii, iv). The main objective of this work is the extension of `DropletSMOKE++` to describe the combustion of suspended fuel droplets with a high level of detail, including:

- An operator-splitting approach to implement a detailed kinetic mechanism within a multiphase fluid dynamics;
- An optically-thin sub-model for the radiative heat transfer;
- A double vaporization model to account both for thermodynamically driven (evaporation) and thermally driven (boiling) cases.

The recent experimental work of Yadav et al. [23] on methanol droplets has been adopted as a benchmark case for the model validation: a methanol droplet is suspended with on a quartz vertical fiber (at ambient temperature and pressure) and ignited with a spark, tracking the combustion phenomena and the droplet characteristics over time. The numerical modeling of this configuration is the objective of this work and the paper organization reflects this purpose, including: a description of the main mathematical model (Section 3), the numerical methodology (Section 4) and the main numerical results compared with the experiments (Section 5). In addition, numerical analyses for the thermal effect of the fiber, the flame properties, the main species distribution and water condensation are provided, before moving to conclusions.

2 Experimental setup

The experiments are carried out in a closed combustion chamber (70x70x100 mm^3) in which a methanol droplet ($D_0 = 1.8$ mm) is suspended with a syringe on a quartz vertical fiber ($D_f = 0.6$ mm) at 300 K and atmospheric pressure. Two steel electrodes initiate the combustion, which is followed in two ways: a digital camera (60 fps) tracks the droplet surface regression, while a Mach Zehnder interferometer provides the whole temperature field distribution in a non-intrusive manner. More details about the experimental device can be found in the reference work [23].

3 Mathematical model

`DropletSMOKE++` is a multiphase CFD code based on the VOF methodology for the interface advection. In addition to the governing equations enforcing the conservation of momentum, energy and species mass, a detailed description of the interface thermodynamics is implemented (based on cubic Equations of State). The evaporation rate $\dot{m}$ is directly calculated from the gas-phase boundary layer and a multiregion approach for the thermal perturbation of the fiber on the droplet is included.

3.1 Interface advection

The VOF methodology [24] is an interface capturing method within an Eulerian formulation, adopting a marker function α to represent the fluid phases. The marker function α represents the liquid volumetric fraction, assuming value 0 in the gas-phase and value 1 in the liquid phase. The following equation for α is solved:

$$\frac{\partial \alpha}{\partial t} + \nabla \cdot (\mathbf{v}\alpha) = \frac{\dot{m}}{\rho} - \frac{\alpha}{\rho}\frac{D\rho}{Dt} \tag{1}$$

where the source terms represent the contribution of the evaporation/condensation rate (depending on the sign of $\dot{m}$) and the droplet dilation due to the change of density $\frac{D\rho}{Dt}$. The interface is advected using the `isoAdvector` library [25] developed by Roenby and Jasak, reconstructing the interface with a geometrical approach. The performances are superior to the MULES compressive scheme [26] commonly adopted in `OpenFOAM`®, in terms of shape preservation, volume conservation, interface sharpness and efficiency.

3.2 Governing equations

The velocity field is shared between the two phases, solving a single Navier-Stokes equation in the whole computational domain:

$$\frac{\partial (\rho \mathbf{v})}{\partial t} + \nabla \cdot (\rho \mathbf{v} \otimes \mathbf{v}) = \nabla \cdot \mu \left(\nabla \mathbf{v} + \nabla \mathbf{v}^T \right) - \nabla p_{rgh} - \mathbf{g} \cdot \mathbf{x} \nabla \rho \tag{2}$$

where $p_{rgh} = p - \mathbf{g} \cdot \mathbf{x}$ is the dynamic pressure, which greatly simplifies the definition of boundary conditions. The momentum equation is coupled with the following continuity equation:

$$\frac{1}{\rho}\frac{D\rho}{Dt} + \nabla \cdot \mathbf{v} = \dot{m} \left(\frac{1}{\rho_L} - \frac{1}{\rho_G} \right) \tag{3}$$

in which the term $\dot{m}\left(\frac{1}{\rho_L}-\frac{1}{\rho_G}\right)$ provides the interfacial velocity jump due to the phase-change (i.e. Stefan flow). Additionally, the energy equation is included:

$$\rho C_p\left(\frac{\partial T}{\partial t}+\mathbf{v}\nabla T\right)=\nabla\cdot(k\nabla T)-\nabla\cdot\mathbf{q}_{rad}-\nabla T\sum_i^{Ns}\mathbf{j}_i C_{p,i}-\sum_i^{Ns_L}\dot{m}_i\Delta h_{ev,i}-\sum_j^{N_R}R_j\Delta H_{R,j} \tag{4}$$

The term $\sum_i^{Ns_L}\dot{m}_i\Delta h_{ev,i}$ accounts for the interface cooling due to the evaporation of the Ns_L liquid species, while the term $\sum_j^{N_R}R_j\Delta H_{R,j}$ is the energy source term due to the N_R combustion reactions. $\mathbf{q}_{rad}$ describes the radiative heat transfer contribution. $\mathbf{j}_i$ are the diffusion fluxes based on the species mole fractions gradient ∇y_i [27]:

$$\mathbf{j}_i=-\rho\mathcal{D}_i\frac{M_{w,i}}{M_w}\nabla y_i \tag{5}$$

Finally, the chemical species in the gas phase have to be transported:

$$\frac{\partial\rho\omega_i^G}{\partial t}+\nabla\cdot\left(\rho\mathbf{v}\omega_i^G\right)=-\nabla\cdot\mathbf{j}_i+\sum_j^{N_R}R_j\nu_{i,j} \tag{6}$$

where the species source term $\sum_j^{N_R}R_j\nu_{i,j}$ is due to the N_R combustion reactions. $\nu_{i,j}$ represent the stoichiometric coefficient of the i-th species in the j-th reaction.

3.3 Interface thermodynamics

At the interface vapor-liquid equilibrium conditions are assumed. Adopting a cubic Equation of State (EoS), the general equation for a two-phase systems is [28]:

$$p_i^0(T)\,x_i\phi_i\left(T,p_i^0\right)e^{\int_{p_i^0}^{p}\frac{v_{L,i}}{RT}dp}\gamma_i(T,x_i)=py_i\hat{\phi}_i(T,p,y_i) \tag{7}$$

where $p_i^0(T)$ is the vapor pressure of species i, ϕ_i is the gas-phase fugacity coefficient for the pure species and $\hat{\phi}_i$ is the gas-phase mixture fugacity coefficient. The exponential term represents the Poynting correction, while x_i and y_i are the liquid and gas mole fractions of species i. γ_i is the activity coefficient for non-ideal mixtures. For fuels burning at atmospheric pressure, the equation can be well approximated with a modified Raoult's law:

$$p_i^0(T)\,x_i\gamma_i=py_i \tag{8}$$

The equilibrium gaseous mole fraction y_i is evaluated explicitly:

$$y_i = \frac{p_i^0(T)}{p} x_i \gamma_i \tag{9}$$

as well as the equilibrium gaseous mass fraction ω_i^G:

$$\omega_i^G = \frac{p_i^0(T)}{p} x_i \frac{M_{w,i}}{M_w} \gamma_i \tag{10}$$

and assigned to the whole liquid phase. Equation 6 is then solved to advect the gaseous species.

3.4 Evaporation rate

The vaporization flux of each liquid species $\dot{m}_i$ is directly calculated from the gas-phase diffusive contribution $\mathbf{j}_i$ (based on Equation 5) and the total flux $\dot{m}$ at the boundary layer:

$$\dot{m}_i = \mathbf{j}_i \nabla\alpha + \dot{m}\omega_i \tag{11}$$

where $\nabla\alpha$ applies the evaporation flux only at the interface. For monocomponent fuels $\dot{m}_i = \dot{m}$, so Equation 11 can be re-arranged to give the total evaporation rate $\dot{m}$:

$$\dot{m} = \frac{\mathbf{j}_i}{1-\omega_i} \nabla\alpha \tag{12}$$

which is equal to $\dot{m}_i$ for monocomponent fuels. If the dot product $\mathbf{j}_i \nabla\alpha$ is negative we have evaporation ($\dot{m} < 0$), otherwise we have condensation ($\dot{m} > 0$). In the same way, the evaporation rate for multicomponent fuels can be easily derived, obtaining:

$$\dot{m} = \frac{\sum_i^{N_{s,L}} \mathbf{j}_i}{1 - \sum_i^{N_{s,L}} \omega_i} \nabla\alpha \tag{13}$$

The total evaporation flux $\dot{m}$ is used as a source term in Equation 1. The evaporation flux of each species $\dot{m}_i$ (only needed for multicomponent cases) can be calculated with Equation 11 once $\dot{m}$ is known.

3.5 Droplet suspension

In normal gravity evaporation experiments, the surface tension force $\mathbf{f}_s$ suspends the liquid droplet against gravity:

$$\mathbf{f}_s = \sigma\kappa\delta_s\mathbf{n} \tag{14}$$

where κ is the interface curvature and $\boldsymbol{\delta}_s$ is a Dirac delta applied on the interface. Modeling surface tension is one of the main challenges in multiphase flows, especially at small scales, for two main reasons:

- The surface tension force is only applied at the interface and this makes its numerical discretization very difficult (i.e. the Dirac delta δ_s). Standard or trivial discretization methods are not able to perfectly balance the pressure gradient and the surface tension force, developing artificial velocity spikes at the interface (called spurious currents), which can eventually grow and break the droplet apart;
- Within a VOF approach the interface curvature κ is not easily accessible, due to the discontinuous nature of the marker α:

$$\kappa = \nabla \cdot \mathbf{n} = \nabla \cdot \left(\frac{\nabla \alpha}{|\nabla \alpha|} \right) \tag{15}$$

  which makes the interface normal ($\mathbf{n}$) calculation very difficult. Numerical errors on κ represents another source of spurious currents, in addition to incorrect interface discretizations.

These issue is very well known in literature [29, 30]: available solutions either rely on simple filtering of the α function [31, 32] or more rigorous methods both for the surface tension discretization (e.g. Ghost Fluid Method [33, 34]) and curvature computation (e.g. height functions [35, 30] or least-squares methods [36, 37]). While filtering techniques are proved to be non-consistent [38] and hardly generalizable, rigorous techniques require a great effort to be correctly implemented. In particular, the `OpenFOAM`® framework lacks in reliable models for surface tension driven flows and no valid and general solution has been proposed so far. Moreover, the aforementioned methods are not proved to efficiently work in evaporative conditions: the presence of evaporation further worsens the problem, since the Stefan flow tends to destabilize the interface thickness. The research in this sense is still at the beginning and only few results are available [39, 17].
In order to overcome this problem, a suspending force $\mathbf{f}_m$ directed towards the droplet center is introduced, in order to keep the droplet attached to the fiber and suspended in the presence of a gravity field. In this way the surface tension force is not needed anymore and it can be suppressed, eliminating parasitic currents directly from their source. The Navier-Stokes equation becomes:

$$\frac{\partial (\rho \mathbf{v})}{\partial t} + \nabla \cdot (\rho \mathbf{v} \otimes \mathbf{v}) = \nabla \cdot \mu \left(\nabla \mathbf{v} + \nabla \mathbf{v}^T \right) - \nabla p_{rgh} - \mathbf{g} \cdot \mathbf{x} \nabla \rho + \mathbf{f}_m \tag{16}$$

This methodology allows to model the droplet evaporation process whatever the droplet size, without worrying about the detrimental effect of spurious currents. More details about the implementation can be found in the `DropletSMOKE++` reference work [21].

3.6 Multiregion approach for conjugate heat transfer

The fuel droplet is suspended on a vertical fiber and evaporated under a normal gravity field. Numerous experimental and numerical analyses [40, 41, 42] showed that the tethering system can significantly affect the vaporization process from a thermal point of view. The solid is heated by the gaseous environment and conducts heat towards the droplet, providing a preferential path for the heat flux on the liquid. This phenomenon becomes extremely important in combustion processes (due to the high gas temperature) and when adopting large fiber diameters (due to the larger surface available for the heat transfer). The `DropletSMOKE++` code includes a multiregion approach to account for the fiber thermal perturbation, firstly presented in [22]. The heat transfer is modeled considering the real geometry of the fiber, with no need of semi-empirical correlations or approximate approaches to account for the tethering system. The fluid and the solid regions are independently meshed, solved and connected with dynamic boundary conditions, providing a full detailed numerical simulation of the three-phase system. The following equation is solved for the solid phase:

$$\rho_s C_{p,s} \frac{\partial T_s}{\partial t} = \nabla \cdot (k_s \nabla T_s) - \nabla \cdot \mathbf{q}_{rad,s} \tag{17}$$

while the fluid temperature field is provided by Equation 4 and $\mathbf{q}_{rad,s}$ is the radiative heat flux from the fiber. The external surface of the solid fiber is the contact boundary between the phases. The boundary conditions describe the conservation of heat fluxes across the boundary as well as the continuity of temperature.

3.7 Gas, liquid and solid properties

The fluid properties are computed with the `OpenSMOKE++` library [43]. In particular, the gas physical properties $(\rho, \mu, C_p, k, \mathcal{D}_i)$ are based on the kinetic theory of gases, while liquid $(\rho, \mu, C_p, k, \mathcal{D}_i,\ \Delta h_{ev,i},\ p_i^0)$ and solid $(\rho_s, C_{p,s}, k_s)$ properties are evaluated based on the correlations available in the Yaws and Prausnitz [44, 45] databases. The activity coefficient γ_i for non-ideal mixtures is calculated based on the UNIFAC approach [46]. Within a VOF approach, the mixture properties to be used in the governing equations are computed as follows (e.g. for density ρ):

$$\rho = \rho_L \alpha + \rho_G (1 - \alpha) \tag{18}$$

3.8 Combustion modeling

The `DropletSMOKE++` model has been extensively validated for evaporation cases against numerous experimental data [21, 22] in a wide range of operating conditions, both in natural and forced convection. In this work, the model is further extended to include the gas-phase combustion and related phenomena. In particular:

- In order to overcome the stiffness of reacting processes, the gas-phase chemistry implementation is based on an operator-splitting approach [47], separating transport and reaction terms. It was adopted and extensively validated in the `laminarSMOKE++` solver [48] for the modeling of laminar flames with very detailed kinetic mechanisms (hundreds of species and thousands of species). The detailed implementation will be reported in the numerical methodology section;

- An optically thin model is used for radiative heat transfer, considering H_2O, CO, CO_2 and CH_4 as main radiating species. This is justified by the small optical depth of the system ($a_p L|_{max} < 0.3$, where a_p is the maximum local average absorptivity and L the maximum length in the domain). Planck absorption coefficients $a_{p,i}$ are calculated for each species and averaged based on the species mole fractions to obtain a_p:

$$a_p = \sum_{i}^{Ns_r} y_i a_{p,i} \tag{19}$$

  where Ns_r are the number of radiating species. Radiation is included in the temperature equation as the divergence of the radiating flux:

$$\nabla \cdot \mathbf{q}_{rad} = 4 a_p \sigma \left(T^4 - T_{env}^4 \right) \tag{20}$$

  where σ is the Stefan-Boltzmann constant and $T_{env} = 300$ K. Radiation from the solid fiber is also considered in Equation 17, with $a_{p,s} = 0.93$ for quartz [44]:

$$\nabla \cdot \mathbf{q}_{rad,s} = 4 a_{p,s} \sigma \left(T_s^4 - T_{env}^4 \right) \tag{21}$$

- When a droplet evaporates evaporates in a mildly-hot (few hundreds degrees K) environment, the liquid surface reaches (after a transient period) a steady wet-bulb temperature, below the liquid boiling point T_b, due to the balance of the incoming heat flux and vaporization enthalpy (Equation 4). The internal liquid temperature is generally lower. The evaporation rate $\dot{m}$ in these conditions is governed by the species diffusion flux $\mathbf{j}_i$ from the surface (Equations 12, 13). On the other hand, the presence of a significant thermal perturbation from the fiber (typical case in combustion processes with a few thousands degrees K) can push the internal liquid temperature towards the boiling point T_b. In this case the liquid temperature profile should reach T_b and instantaneously flatten, remaining constant. However, Equation 4 cannot predict this profile discontinuity inside the liquid phase (the cooling term $\sum_i^{Ns_L} \dot{m}_i \Delta h_{ev,i}$ is zero outside the interface) and the internal droplet temperature would continue to increase above T_b. In fact, the heat flux per unit volume $\dot{q}$ acting on a point in the droplet is entirely used to vaporize the liquid, maintaining the local temperature constant. Therefore, the vaporization rate in the liquid phase should be calculated as:

$$\dot{m} = -\frac{\dot{q}}{\Delta h_{ev}} = -\frac{\rho C_p \frac{\partial T}{\partial t}}{\Delta h_{ev}} \tag{22}$$

  where Δh_{ev} is the vaporization enthalpy. Equation 22 is to be applied at every point in the liquid phase in which $T \geq T_b$. If the liquid is a monocomponent fuel, the species vaporization flux $\dot{m}_i$ is obviously equal to $\dot{m}$. Equation 22 is also valid for multicomponent droplets, with the only difference that the boiling temperature T_b depends on the local composition x_i through Raoult's law (Equation 8) and it should be calculated in every point in the liquid phase. In this case the vaporization flux $\dot{m}_i$ can be calculated from the equilibrium gas-phase mass fraction (Equation 10):

$$\dot{m}_i = \dot{m}\omega_i^G = \dot{m}\frac{p_i^0(T)}{p} x_i \frac{M_{w,i}}{M_w}\gamma_i \tag{23}$$

Since predicting bubbles nucleation and growth is extremely difficult (and beyond the purpose of this work), the internal boiling flux contribution ($T \geq T_b$) is redistributed on the droplet interface to evaluate the interface regression (Equation 1). It is important to point out that in principle boiling occurs at temperatures higher than T_b, due to the superheat needed for bubbles nucleation and to overcome the surface tension energy

	monocomponent	multicomponent
$\dot{m}$	$\begin{cases} \frac{\mathbf{j}_i}{1-\omega_i}\nabla\alpha & \text{if } T < T_b \\ -\frac{\rho C_p \frac{\partial T}{\partial t}}{\Delta h_{ev}} & \text{if } T \geq T_b \end{cases}$	$\begin{cases} \frac{\sum_i^{N_{s,L}} \mathbf{j}_i}{1-\sum_i^{N_{s,L}} \omega_i}\nabla\alpha & \text{if } T < T_b \\ -\frac{\rho C_p \frac{\partial T}{\partial t}}{\Delta h_{ev}} & \text{if } T \geq T_b \end{cases}$
$\dot{m}_i$	$\dot{m}$	$\begin{cases} \mathbf{j}_i\nabla\alpha + \dot{m}\omega_i & \text{if } T < T_b \\ \dot{m}\frac{p_i^0(T)}{p} x_i \frac{M_{w,i}}{M_w}\gamma_i & \text{if } T \geq T_b \end{cases}$

Table 1: Summary of the vaporization rates $\dot{m}$ (total) and $\dot{m}_i$ (for each species) for monocomponent and multicomponent liquids.

barrier. However, in the presence of heterogeneous nucleation (due to the presence of the fiber, impurities in the fuel etc.) we can safely assume the superheat to be negligible in this case. The vaporization rate calculations are summarized in Table 1 both for monocomponent and multicomponent droplets.

4 Numerical setup

The `DropletSMOKE++` solver is based on the `OpenFOAM`® framework, adopting a finite-volume discretization of the governing equations. These are solved in a segregated approach and adopting the PIMPLE algorithm, a combination between SIMPLE (Semi-Implicit Method for Pressure-Linked Equations) and PISO (Pressure Implicit Splitting of Operators), to manage the pressure-velocity coupling [49]. The time step size Δt is controlled by the CFL condition governed by the Courant number (Co<0.5), while time integration adopts an implicit Euler method. The spatial discretization is based on Gauss linear scheme for the convective terms, while an orthogonal correction is adopted for Laplacian (diffusive) terms.

4.1 The operator-splitting approach

The operator-splitting approach [47] is the numerical methodology adopted in this work to efficiently include the chemical reactions. The highly non-linear dependence on temperature and species concentration and the very stiff nature of the combustion chemistry make the direct numerical resolution of Equations 4 and 6 extremely difficult. The numerical strategy is the segregation of the transport term and the source term of the

governing equations within the same time step. For a generic variable ψ having source term $\mathbf{S}$ and transport term (diffusion, convection etc.) $\mathbf{T}$:

$$\frac{\partial \psi}{\partial t} = \mathbf{T}(\psi) + \mathbf{S}(\psi) \tag{24}$$

this equation in solved in three sub-steps (Strang splitting):

1. Integration of the source term $\mathbf{S}(\psi)$ over a time step $\Delta t/2$. The initial condition $\psi^{(0)}$ is from the previous time step.

$$\frac{\partial \psi}{\partial t} = \mathbf{S}(\psi) \tag{25}$$

2. Integration of the transport term $\mathbf{T}(\psi)$ over a time step Δt. The initial condition $\psi^{(1)}$ is the result of the first integration (Point 1).

$$\frac{\partial \psi}{\partial t} = \mathbf{T}(\psi) \tag{26}$$

3. Second integration of the source term $\mathbf{S}(\psi)$ over a time step $\Delta t/2$. The initial condition $\psi^{(2)}$ is the result of the second integration (Point 2).

$$\frac{\partial \psi}{\partial t} = \mathbf{S}(\psi) \tag{27}$$

The variables ψ are the species mass fractions ω_i and the temperature T. These are solved in a fully coupled approach for points 1 and 3, providing a stiff system of $Ns + 1$ (Ns species and T) non-linear ODE for each computational cell. These ODE systems are totally independent, since the source terms $\mathbf{S}(\psi)$ are local and do not depend on adjacent cells. This is equivalent to the solution of a network of Nc independent batch reactors, where Nc is the number of cells. The numerical resolution is based on the `OpenSMOKE++` library [43], specifically developed to efficiently solve stiff ODE systems and manage detailed kinetic mechanisms. On the other hand, point 2 is solved in a segregated manner for the Ns species and temperature T (as typically done in `OpenFOAM`®). Additional details about the implementation can be found in the work of Cuoci et al. [48] (for the `laminarSMOKE++` solver), as well as an extensive validation for laminar flames with detailed kinetic mechanisms. It is important to specify that reactions only occur in the gas-phase: within a VOF approach this requires the resolution of the reactive step only if $\alpha = 0$ in the computational cell of interest. The main numerical steps included in the `DropletSMOKE++` solver are summarized in Figure 1.

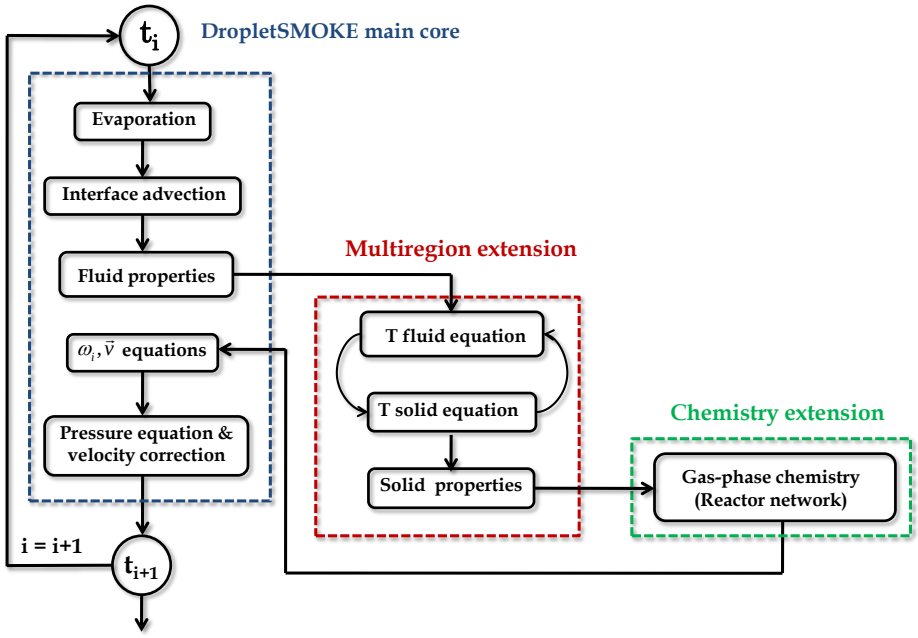

Figure 1: Numerical steps of the `DropletSMOKE++` code, including the multiregion extension for the description of the solid fiber and the reactor network for the combustion chemistry.

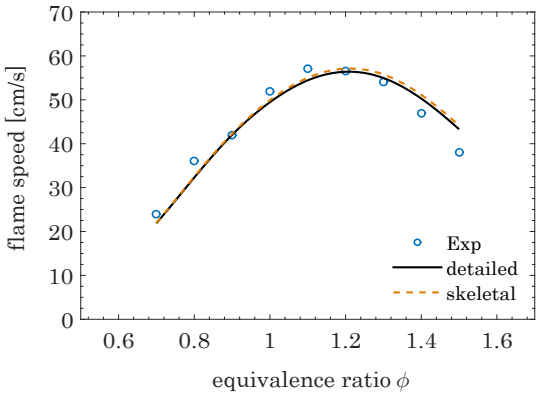

Figure 2: Experimental data of atmospheric laminar flame speeds of methanol at different equivalence ratios and $T_0 = 343$ K from Veloo et al. [50]. Comparison between detailed and skeletal mechanisms.

4.2 Kinetic mechanism

The kinetic mechanism for methanol combustion was obtained from the CRECK kinetic framework, which describes the pyrolysis, partial oxidation and combustion of hydrocarbons up to C_{16}. The C_0-C_3 mechanism [51] was recently updated following the works of Metcalfe [52] (for H_2/O_2 and C_1/C_2), Burke [53] (for C_3) and implementing the thermodynamics from Burcat database [54]. To limit the computational cost, the resulting mechanism (115 species, 1998 reactions) was finally reduced to a skeletal mechanism (20 species, 129 reactions) using the `DoctorSMOKE++` software [55], based on a combination of the Direct Relation Graph with Error Propagation (DRGEP) [56] and a species-targeted sensitivity analysis [57] with a maximum error on the ignition delay time set to 8%. The detailed and the reduced mechanisms are compared in Figure 2, in terms of methanol laminar flame speed. The reduced mechanism is available in the supplementary data.

4.3 Computational mesh

The computational mesh is built with the commercial CFD code `Ansys FLUENT`® v19.2 and then converted in `OpenFOAM`® format. The geometry represents a cylinder (radius L, height H) with a central vertical fiber (radius r) on which the droplet is suspended (Figure 3). Only a slice (5 degrees) of the total geometry is modeled exploiting the axial symmetry. The total number of cells is $\sim$ 92,000 for the fluid region and $\sim$ 10,000 for the solid region. The resulting droplet resolution is $D/\Delta x \sim 100$, necessary to solve the gas film thickness for the heat and mass transfer rates evaluation. A grid refinement analysis is reported in the appendix, proving mesh independence.

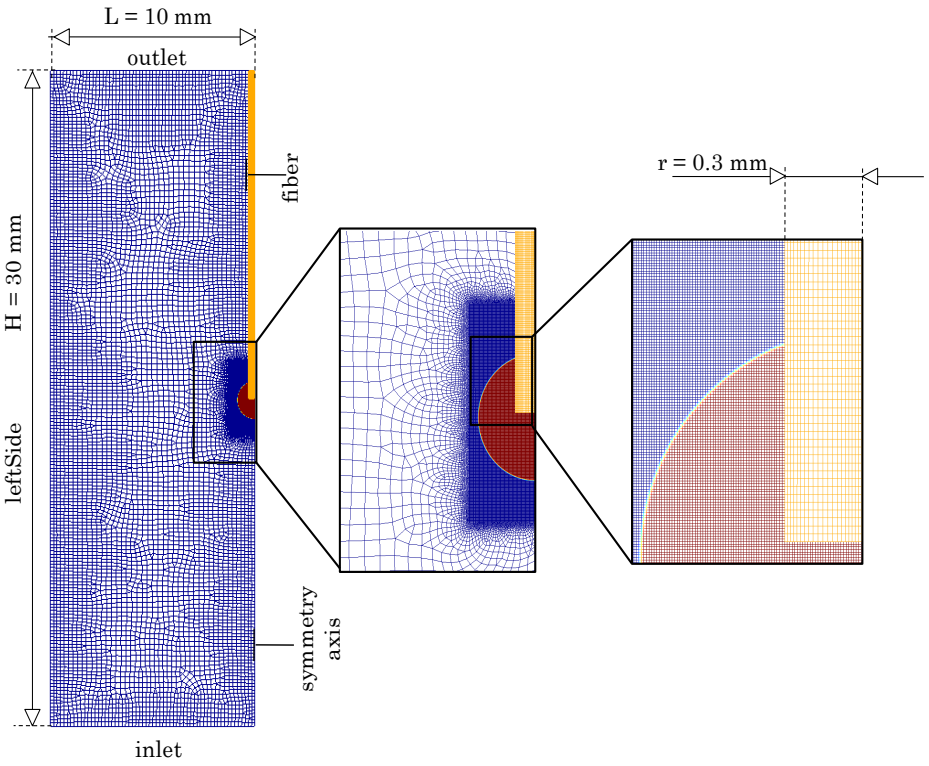

Figure 3: Computational mesh used in this work, with suspended droplet (red region) at three levels of detail. The fluid region (blue) and the solid region (orange) are separately meshed and connected, sharing the `fiber` boundary.

Boundary	$\mathbf{v}$	Temperature	ω_i	p
`inlet, outlet, leftSide`	open	open	open	$p = p_{ext}$
`fiber`	$\mathbf{v} = 0$	fluid-solid coupling	$\nabla\omega_i = 0$	$\nabla p = 0$

Table 2: Boundary conditions for velocity $\mathbf{v}$, temperature T, species mass fraction ω_i and pressure p. The mesh is presented in Figure 3.

The solid and the fluid regions are meshed independently and then connected with the shared boundary `fiber`. The fluid region is refined around the droplet to provide a sufficiently sharp interface and resolve the boundary layer. The resulting mesh is non-structured, with a non-orthogonality coefficient equal to 57 (safe values are < 70) and a maximum Skewness of 1.56 [49].

4.4 Boundary conditions

There are five boundaries in the computational domain named `leftSide`, `inlet`, `outlet`, `symmetry axis` and `fiber` (Figure 3). The computational geometry is smaller than the real one (in order to reduce the computational cost), therefore the external boundaries `leftSide`, `inlet` and `outlet` are considered open to not perturb the combustion process. Outlet boundary conditions are managed in `OpenFOAM`® as a zero gradient condition, which switches to a fixed value condition if the boundary velocity vector is directed inside the domain (backward flow). The `fiber` boundary condition enforces the thermal fluxes conservation and the continuity of the temperature profile. The coupled heat transfer is included in the `turbulentTemperatureCoupledBaffleMixed` boundary condition, available in `OpenFOAM`® for conjugate heat transfer problems [49]. A summary of the boundary conditions is presented in Table 2.

4.5 Parallelization

The `DropletSMOKE++` code works in parallel mode, adopting the Domain Decomposition Method already included in `OpenFOAM`®. Almost $\sim 95\%$ of the CPU time is used for the chemical step (the resolution of the ODE systems). Since this is a local step (no data transfer across the processors is needed), the parallelization efficiency is very high. The simulations presented in this work were run on a multi-processor machine (Intel Xeon X5675, 3.07 GHz). Using 60 processors the average CPU time was $\sim 90 - 100$ h.

Case	D_0 [mm]	y_{O_2} [-]
1	1.8	0.17
2	1.8	0.21
3	1.8	0.25

Table 3: Experimental cases of burning methanol droplets from Yadav et al. [23] examined in this work. y_{O_2} is the initial oxygen mole fraction in the gas-phase. $p = 1$ bar, $T = 300$ K.

5 Combustion of methanol droplets

5.1 Initial conditions

In this work three cases of methanol droplets combustion are considered, varying the oxygen mole fraction in the gas-phase. The cases are summarized in Table 3.
The spark ignition is simulated as a small sphere ($D = 0.1$ mm) having a temperature $T_{spark} = 2500$ K placed at 1 mm from the droplet surface. The spark is applied after a short time of pure evaporation (~ 0.02 s) to facilitate the ignition, for a total duration of 0.05 s. The initial conditions for the marker α and for the methanol mass fraction are shown in Figure 3. The fluid and solid initial temperatures are $T = 300$ K and the initial pressure is $p = 1$ bar.

5.2 Ignition and droplet combustion

The ignition and combustion dynamics of Case 2 is qualitatively presented in Figure 4 by means of temperature and methanol mass fraction fields. In Figure 5 the main combustion products (H_2O, CO_2, CO) and O_2 are presented in terms of mass fractions. The gas-phase ignites at $t \sim 0.07$ s, developing a buoyant diffusion flame. In Figure 4a the ignition spark is still visible close to the droplet surface.
It is useful to analyze the flame structure adopting a passive scalar Z [58]. Following Bilger's approach [59], we define the parameter β:

$$\beta = \frac{2}{M_{w,C}}\omega_C + \frac{1}{2M_{w,H}}\omega_H - \frac{1}{M_{w,O}}\omega_O \tag{28}$$

where the mass fraction of the k-th element (C, H, O) are calculated as:

$$\omega_k = \sum_i^{Ns} \omega_i N_{k,i} \frac{M_{w,k}}{M_{w,i}} \tag{29}$$

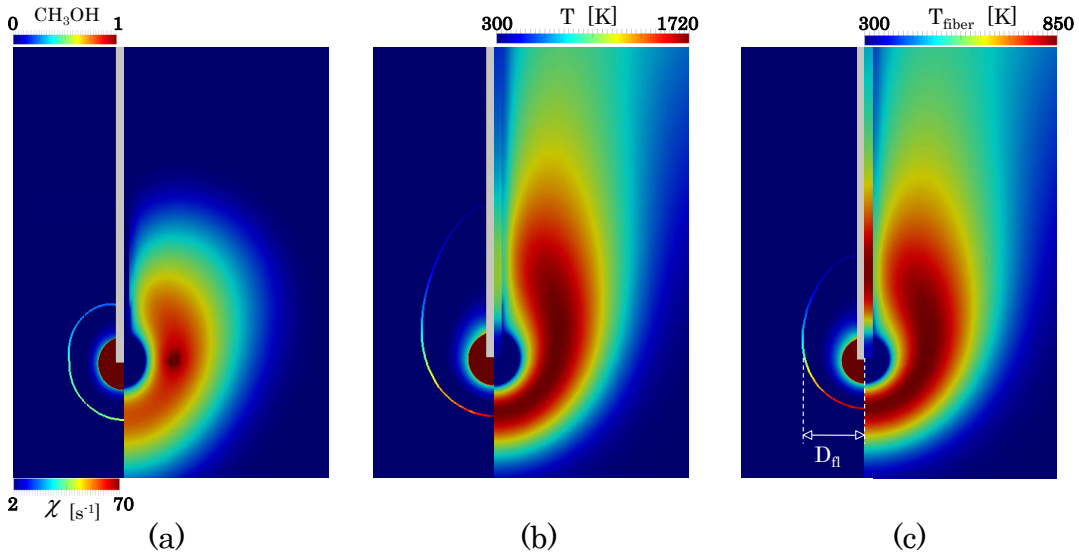

Figure 4: Case 2: 2D maps of methanol mass fraction (left), fluid and solid temperatures (right) at times $t = 0.07$ s (a), $t = 0.5$ s (b) and $t = 1$ s (c). On the left side the stochiometric passive scalar Z_{st} contour is shown, colored by the scalar dissipation rate $\chi = 2\mathcal{D}_{N_2}|\nabla Z|^2$ [58]. The flame diameter D_{fl} definition is evidenced in (c).

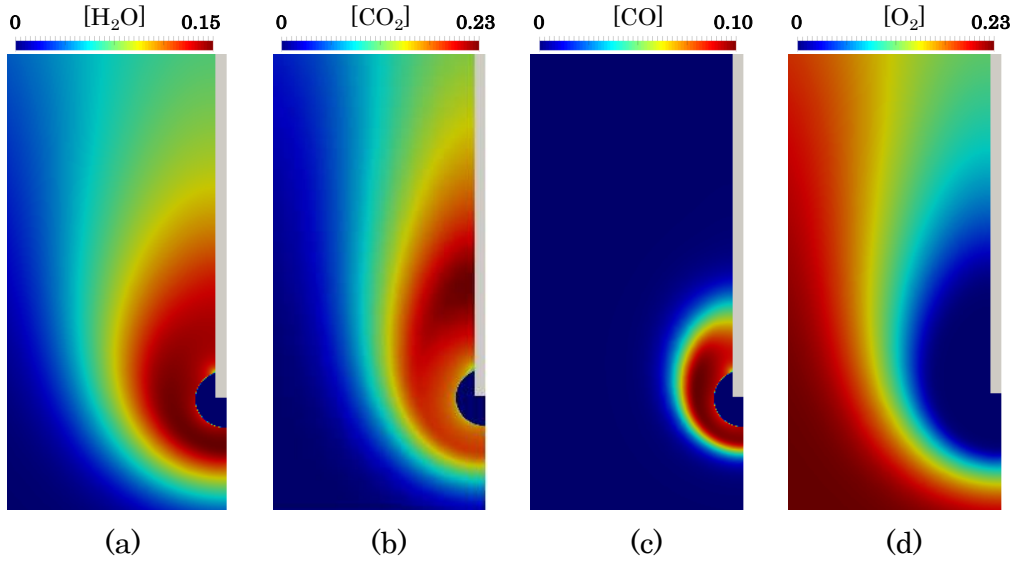

Figure 5: Case 2: 2D maps of H_2O (a), CO_2 (b), CO (c), O_2 (d) mass fractions. The gray region represents the fiber. Time $t = 0.67$ s.

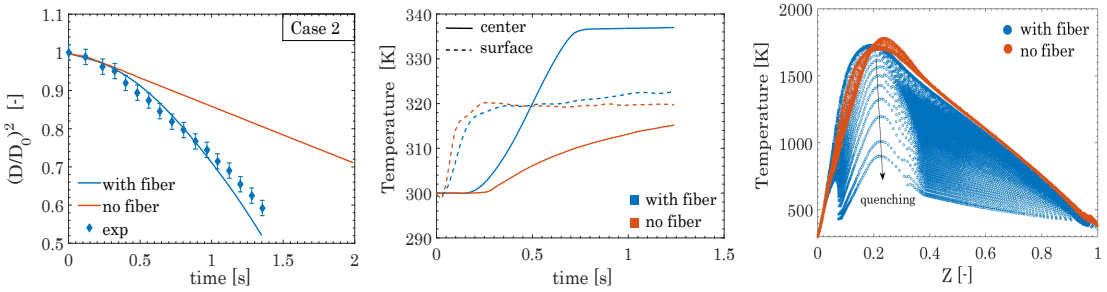

(a) (b) (c)

Figure 6: Effect of the fiber (Case 2): $(D/D_0)^2$ plot (a), droplet temperature (b) and T-Z scatterplot at $t = 0.67$ s (c). Experimental data from [23].

where $N_{k,i}$ is the number of atoms k in species i. The mixture fraction Z is defined as:

$$Z = \frac{\beta - \beta_{ox}}{\beta_{fuel} - \beta_{ox}} \tag{30}$$

The fuel composition used to calculate β_{fuel} is the gaseous composition at the droplet interface, including the dilution with the surrounding species. Therefore, Z assumes value 1 on the interface and 0 in the pure oxidizer. The stoichiometric Z_{st} is easily calculated imposing $\beta = 0$ (whatever the chemical reactions involved):

$$Z_{st} = -\frac{\beta_{ox}}{\beta_{fuel} - \beta_{ox}} \tag{31}$$

The Z_{st} isocontour is evidenced in Figure 4. It is colored by the local scalar dissipation rate χ:

$$\chi = 2\mathcal{D}_{N_2}|\nabla Z|^2 \tag{32}$$

The inverse of $|\nabla Z|^2$ is proportional to the flame thickness [58]. As an be seen in Figure 4, the lower part of the flame is thinner because it behaves similarly to a counterflow flame: the Stefan flow generated by the droplet vaporization is opposed to the upward flow due to buoyancy, tending to bring Z iso-surfaces closer and reducing the thickness of the reactive region. As a consequence, the highest concentration of radical species (OH, H, HO_2) are localized in this region. The flame becomes thicker in the upper part of the flame because of the absence of a significant relative velocity component normal to the Z iso-surfaces.

5.3 The thermal effect of the fiber

The temperature of the fiber increases due to the vicinity of the flame (up to ~ 850 K, Figure 4c) and this is known to affect the combustion process [14], creating a preferential path for the heat flux on the droplet (especially for large fiber diameters). In order to quantify the thermal perturbation caused by the fiber, Case 2 has also been simulated considering it as adiabatic. Figure 6a shows that if the fiber heat transfer is neglected the model is not able to predict the correct diameter decay, since the burning rate is strongly underestimated. In particular, two main processes govern the liquid temperature (Figure 6b): initially, after a slight decrease of T due to evaporation, the droplet surface receives heat from the flame, releasing vapor in the gas-phase and rapidly reaching an equilibrium temperature (i.e. wet-bulb temperature ~ 320 K). In the meantime the fiber temperature increases, conducting heat directly inside the liquid. Since evaporation is not possible inside the droplet, the temperature rapidly increases and reaches the boiling temperature T_b in the center. The evaporation rate evaluation switches to the boiling model (Table 1) and the temperature remains constant and equal to T_b (blue solid line in Figure 6b). This creates a situation in which the liquid surface evaporates at $T < T_b$, while the droplet interior boils ($T = T_b$).

At the initial stages the heat absorbed from the droplet surface governs the vaporization while the fiber plays a major role towards the end of the simulation (when the fiber is hotter and the droplet smaller), mainly affecting the internal temperature. If the fiber (Equation 17) and the boiling (Equation 22) are accounted for , the model predicts the burning rate (Figure 6a) with a reasonable accuracy.
Another interesting effect of the fiber is the partial quenching of the flame (Figure 4) close to the fiber surface, due to its thermal inertia. In Figure 6c a scatterplot of the temperature with respect to the passive scalar Z (Equation 30) is reported, showing a wide quenching region when the fiber is accounted for. Focusing on the $Z_{st} \sim 0.21$, the flame temperature decreases of ~ 1000 K approaching the fiber providing an incomplete combustion in this region. This effect is of primary importance since it leads to an accumulation of radicals and partial oxidation products at the fiber surface.

5.4 The effect of the oxygen concentration

In Figure 7a the numerical diameter decays of Cases 1, 2, 3 are presented and compared with the experiments. The numerical results have been shifted, so that time $t = 0$ represents the ignition time. The agreement is satisfactory, within the uncertainties of the experimental data. The explanation for the differences in the diameter decay

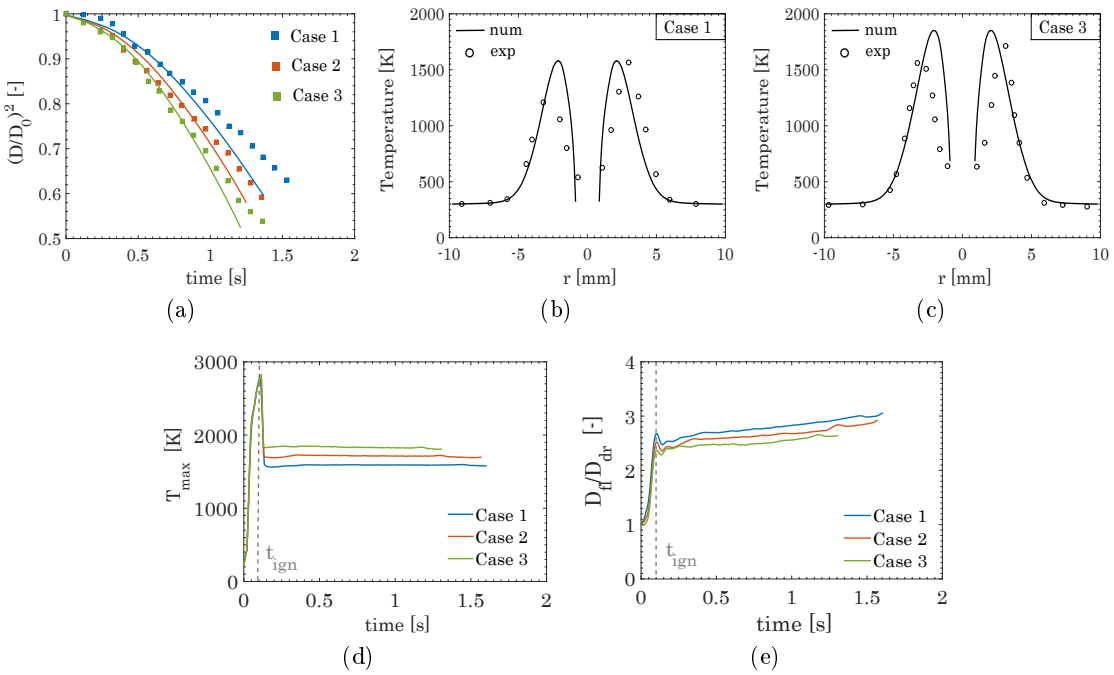

Figure 7: Effect of oxygen: $(D/D_0)^2$ plot of Cases 1, 2, 3 (a) and radial T profiles of Cases 1 (b) and 3 (c) at $t = 0.67$ s. Profiles of flame temperature T_{max} (d) and standoff ratio D_{fl}/D_{dr} (e) over time. Experimental data from [23].

is straightforward: increasing the oxygen concentration leads to a higher temperature of (i) the flame and thus (ii) of the fiber. Both induce a more intense vaporization of the liquid, increasing the burning rate and diminishing the droplet lifetime. The maximum temperature profile over time is reported in Figure 7d: after the ignition the flame temperature stabilizes at a constant value, which is higher for higher oxygen concentrations in the gas-phase. This can also be observed from the radial temperature profiles, taken along an horizontal line passing through the droplet center (for Cases 1, 3 in Figures 7b, 7c). The model predicts the experimental data with a reasonable accuracy, considering the error associated with the measurements (up to $\sim 10\%$, as reported in [23]). Experimental errors can also be seen in the slight asymmetry of the temperature profiles. The difference in the maximum flame temperatures is ~ 150 K, with the peak for Case 3 slightly closer to the droplet surface. As reported in the last section of this paper, the agreement with the experimental results concerning the radial temperature profile improves including water condensation on the droplet surface.
Finally, it is worth analyzing the flame position with respect to the droplet interface (standoff ratio) for the three cases (Figure 7e). The flame diameter D_{fl} is indicated in Figure 4 (c) and corresponds to the maximum horizontal distance of the Z_{st} isoline from the symmetry axis. The flame position with respect to the droplet surface slightly increases over time for all the three cases. The flame approaches the droplet surface increasing the oxygen concentration, since the stoichiometric condition at Z_{st} is satisfied closer to the droplet. The vicinity of the flame further increases the vaporization rate from the droplet, further enhancing the effect of the higher oxygen concentration. This is in agreement to what observed by other authors [60, 61].

5.5 The effect of gravity

The presence of a gravity field creates an upward buoyant flow ($v_{max} \sim 0.4$ m/s) once the flame is ignited and stabilized, which significantly influences the droplet combustion physics. The external convection forms a thin boundary layer which significantly affects the heat and mass transport rates. To better discuss and highlight the effects of gravity, we simulated the cases in Table 3 in microgravity conditions (μg), imposing $\mathbf{g} = \mathbf{0}$. The results are compared with the cases simulated in normal gravity in terms of flame temperature, standoff ratio (D_{fl}/D_{dr}), flame geometry and internal motion. The presence of external convection influences:

- *The droplet shape*: under a convective field the droplet geometry is no longer spherical, due to the deformation induced by the flow. On principle this can affect the

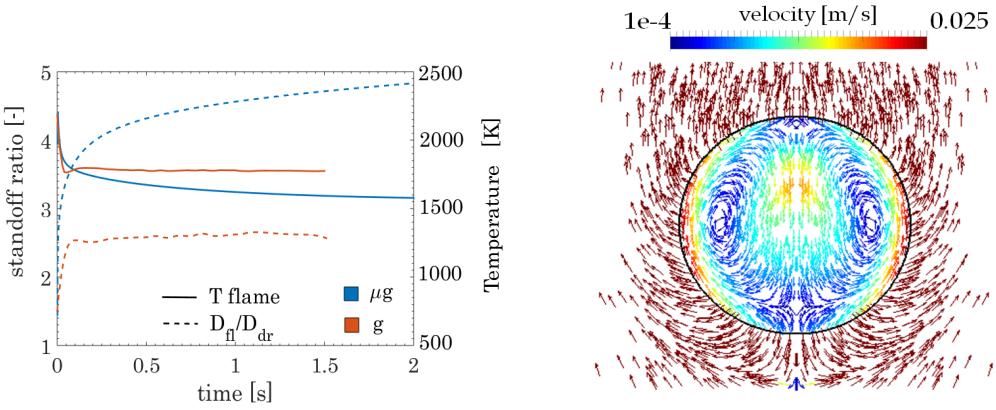

(a) (b)

Figure 8: Case 2: profiles of flame T and relative flame position D_{fl}/D_{dr} (standoff ratio) in microgravity and normal gravity (a). Two-phase velocity field around and inside the droplet (b), time t=1 s.

vaporization rate, since the surface area available for the vaporization is different. However, we noticed that for small droplets this is usually a minor effect [21] and that the sphericity coefficient ∼1 for most of the cases of our interest;

- *The flame geometry*: in microgravity the flame is spherical and its distance from the droplet increases after the ignition, reaching a value of ∼ 4-5 times the droplet diameter (Figure 8 a). As a consequence the flame temperature decreases, providing a possible radiative extinction if the flame diameter is large enough [8]. On the other hand, in normal gravity the flame is axisymmetric and much closer to the droplet, maintaining its relative position almost constant in time (it is actually slightly increasing). This is due to the convective transfer of oxygen to the reactive region (much faster than pure diffusion), which satisfies the stoichiometric requirement of the flame front at a shorter distance. The average flame thickness is significantly reduced, especially in the lower part of the flame.
  As a result, the flame temperature is practically constant in time and higher than the case in microgravity (of ∼ 250 K). Moreover, the flame further approaches the droplet surface when the oxygen concentration increases. We found this effect to be similar both in microgravity and normal gravity, indicating that the presence of convection does not significantly affect the response of the flame distance to the oxygen concentration;

- *The internal circulation*: in microgravity the heat transfer in the liquid phase

is mainly governed by conduction due to the absence of internal motion. When gravity is present, the buoyancy-driven convection induces an internal motion in the liquid phase (shear stress continuity) which significantly enhances the internal heat transfer [62]. Figure 8 (b) shows the two-phase velocity field for the burning droplet, highlighting the internal motion. As reported by many authors [2], the internal flow can be approximated as a Hill's vortex, having a toroidal core region within the droplet. The maximum velocity in the liquid phase ($\sim$ 2.5 cm/s) is an order of magnitude less than the relative gas-phase velocity ($\sim$ 30 cm/s), in agreement to what observed by Prakash and Sirignano [63].

It is worth noticing that the gas-phase velocity field exhibits a significant radial flow at the interface, due to the Stefan flow induced by the vaporization. Several authors observed that this radial flow leads to a significant reduction of the drag coefficient on the droplet [64, 65], due to the expansion of the gas-phase boundary layer which significantly reduces the viscous force on the droplet. As an additional effect, this can make the liquid velocity field much less sensitive to the external convection, reducing the intensity of the internal motion. Following a fairly complex theoretical analysis, Sadhal [66] observes that in the limit of extremely high radial flows the internal toroidal structure can be totally destroyed, due to the absence of a tangential component of the relative gas-phase velocity at the interface.

5.6 Distribution of the species in the gas phase

Once a passive scalar Z is defined (Equation 30), we can analyze the main species distribution (for Case 2 at $t = 0.67$ s) along the flame coordinate. The results are reported in Figures 9 and 10, highlighting the Z_{st}. In order to analyze the rate of production of the species in a simpler system, a 1D counterflow diffusion flame has been simulated with `OpenSMOKE++` [43], replicating the same conditions encountered in the droplet flame (in terms of χ, geometry, inlet T and composition). As already reported, most of the species have a peak in the high scalar dissipation rate (χ) region (low thickness), the lower part of the flame (Figure 9). The OH radical is slightly below the Z_{st} due to the need of O_2 for its formation, while the H radical peak is at Z_{st}. The HO_2 radical shows an interesting profile, with three peaks along Z: on the rich side, HO_2 is mainly produced by O_2+CH_2OH $\rightarrow$ HO_2+CH_2O, while on the lean side H+O_2+(M)$\rightarrow$$HO_2$+(M) is dominant, due to the high diffusivity of H which escapes the flame front. The intermediate HO_2 peak is due to the flame quenching at the fiber surface (clearly visible in the HO_2 mass fraction map in Figure 9c), which decreases the temperature and stabilizes HO_2. The important presence

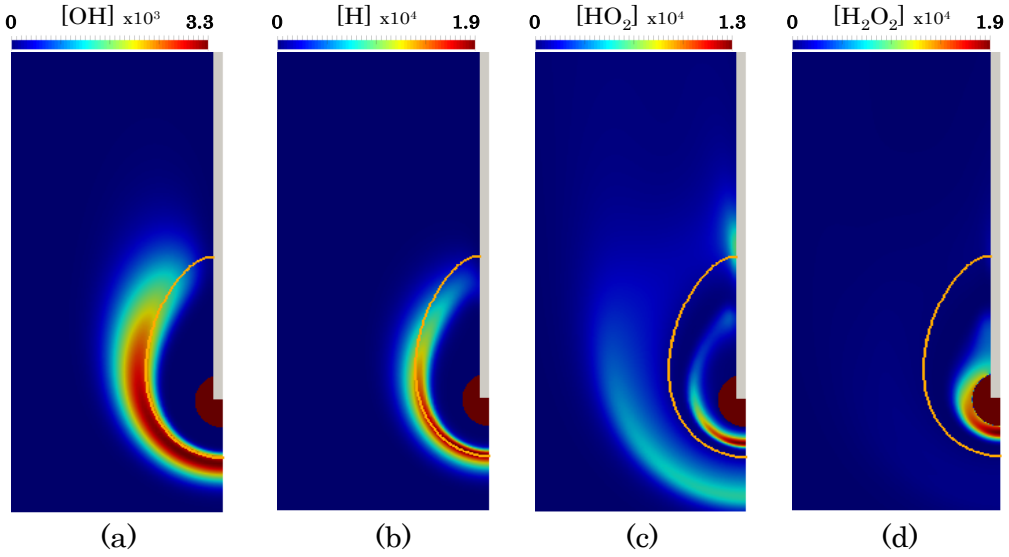

Figure 9: Case 2: 2D maps of OH (a), H (b), HO_2 (c), H_2O_2 (d) mass fractions. The orange solid line is the flame front (Z_{st}), the red region is the droplet. Time $t = 0.67$ s.

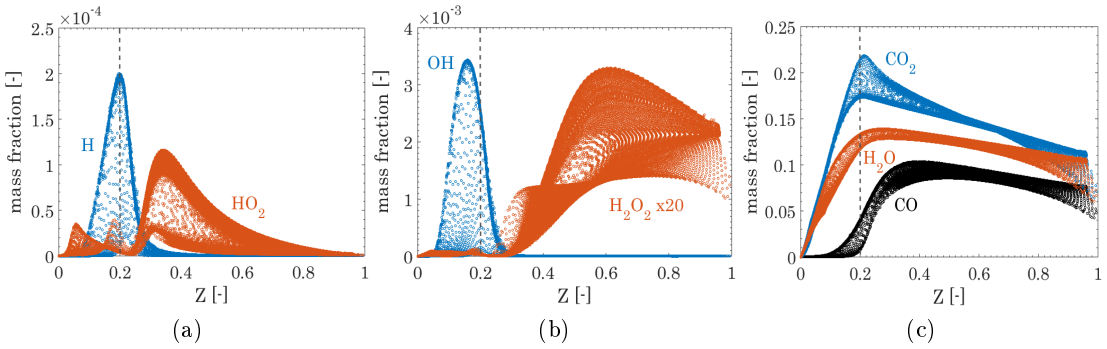

Figure 10: Case 2: ω_i-Z scatterplots of main species mass fractions at time $t = 0.67$ s.

of HO_2 for $Z > Z_{st}$ is also responsible for the hydrogen peroxide H_2O_2 formation (Figure 10b) through the abstraction reaction HO_2+CH_3OH→H_2O_2+CH_2OH, extensively investigated by other authors [67, 68]. At $Z < Z_{st}$, OH recombination reaction ($2OH \rightarrow H_2O_2$) is the main responsible for H_2O_2 formation in the lean region. At $Z \sim 0.35$ there is an intermediate peak (not clearly visibile due to the very low concentration), still due to the flame quenching at the fiber which locally cools the flame. The main combustion products are H_2O and CO_2 (Figure 10c), while CO is almost completely oxidized by OH at the flame front. With respect to the case without fiber, we notice a lower concentration of these species. It is worth noticing that CO, CO_2 and H_2O are present in significant amount at the droplet interface ($Z = 1$), because of back diffusion from the flame. Differently from CO and CO_2, water can condense on the droplet surface due to the low interface temperature ($\sim$ 320 K). This will be analyzed in the next section.

5.7 Absorption of water in the liquid phase

The water present among the combustion products in the gas-phase is miscible with methanol and it can condense on the droplet surface. If the liquid temperature is sufficiently high, water starts vaporizing as well and a two-component thermodynamics is established. This has been widely investigated in recent numerical and experimental works regarding alcohol combustion [69, 70, 61]. From the modeling point of view only few things change:

- The species equation must be solved also for the liquid phase. The only difference is that a source term $\dot{m}_i$ has to be included to account for the amount of species i lost at the liquid interface for evaporation ($\dot{m}_i < 0$) or added by condensation ($\dot{m}_i > 0$):

$$\frac{\partial \rho \omega_i^L}{\partial t} + \nabla \cdot \left(\rho \mathbf{v} \omega_i^L\right) = -\nabla \cdot \mathbf{j}_i^L + \dot{m}_i \tag{33}$$

  The equation for the gas-phase remains Equation 6. The diffusion coefficients $\mathcal{D}_i$ in the liquid phase (needed for the flux $\mathbf{j}_i^L$) are computed with the Leffler-Cullinan approach [71].

- The boiling temperature T_b is needed to trigger the boiling sub-model (Table 1). In a two-component mixture (water and methanol) T_b depends on the local composition and it should be calculated in every point in the liquid phase at every time step. This can be a very expensive procedure, since finding T_b involves the solution

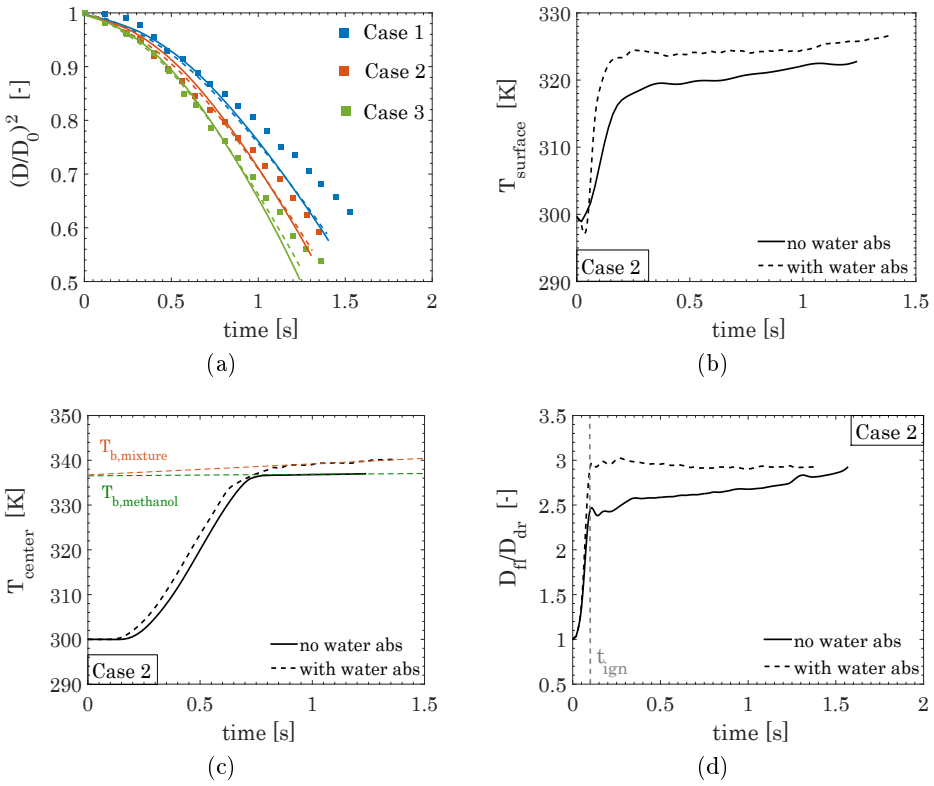

Figure 11: Effect of condensed water: $(D/D_0)^2$ plot of Cases 1, 2, 3 (a), surface temperature profiles (b), internal temperature profiles (c) and standoff ratio D_{fl}/D_{dr} profiles (d) of Case 2.

of a non-linear algebraic equation (Equation 8). It is much easier to adopt the local boiling pressure p_b:

$$\dot{m} = \begin{cases} \frac{\sum_i^{N_{s,L}} \mathbf{j}_i}{1-\sum_i^{N_{s,L}} \omega_i} \nabla\alpha, & \text{if } p > p_b \\ -\frac{\rho C_p \frac{\partial T}{\partial t}}{\Delta h_{ev}}, & \text{if } p \leq p_b \end{cases} \tag{34}$$

and similarly:

$$\dot{m}_i = \begin{cases} \mathbf{j}_i \nabla\alpha + \dot{m}\omega_i & \text{if } p > p_b \\ \dot{m}\frac{p_i^0(T)}{p} x_i \frac{M_{w,i}}{M_w}\gamma_i & \text{if } p \leq p_b \end{cases} \tag{35}$$

where the boiling pressure p_b can be directly calculated in every point of the liquid phase as:

$$p_b = \sum_{i}^{Ns_L} p_i^0 (T)\, x_i \gamma_i \tag{36}$$

In order to highlight the effect of the absorbed water on the droplet combustion, we simulated the three cases in Table 3 including the water condensation flux. This is done by simply initializing the initial fuel composition with a small amount of water ($\omega_0^L = 10^{-4}$ in this case). The results are reported in Figure 11.
Referring to Figure 11a, we can identify two main vaporization regimes of the methanol-water mixture. During the first period the droplet is consumed faster when water absorption is accounted for: this happens because of the condensation heat released on the surface, which increases the temperature (∼4-5 K). Since methanol is (initially) the main component of the two-phase mixture, it vaporizes faster [69]. This can be clearly seen in Figure 11b, where the surface temperatures for the two cases are reported. Later on, the amount of condensed water becomes significant and the droplet global vaporization rate is retarded (also because of methanol dilution). This effect seems to be more enhanced at high temperatures (Case 3) due to the higher water concentration in the gas-phase. Moreover, the water absorbed at the surface is transported (by diffusion and internal convection) inside the liquid phase, close to the fiber. The vaporization enthalpy of the methanol-water mixture locally increases ($\Delta h_{ev,water} > \Delta h_{ev,meth}$) and the internal boiling flux is diminished (Equation 22), further slowing the vaporization rate. At the droplet center the boiling conditions are reached for both cases ($T = T_b$, Figure 11c). While T_b is constant for pure methanol vaporization, it constantly increases for the mixture because of water absorption ($T_{b,water} > T_{b,meth}$) which changes the liquid composition. It is also worth analyzing the difference in the flame position with respect to the droplet surface (Figure 11d). The standoff ratio is higher due to the more intense methanol vaporization which pushes the flame farther. This is reflected by the comparison of the radial temperature profiles (previously shown in Figure 7 b,c) in Figures 12(a,b): when water absorption is included, the temperature maximum slightly shifts away from the droplet and improves the agreement with the experimental data. Lee and Law [69] also report the existence of a final evaporation stage in which the condensed water starts to vaporize again once reached a significant concentration in the liquid. However, we did not notice this phenomena in our case probably because of the relatively low amount of water absorbed. In particular, we noticed less than 10% (in mass) of water accumulation in the liquid phase at the end of the simulation (for all the cases). We found this effect to be negligible on the diameter decay (Figure 11a), since the vaporization rate is controlled

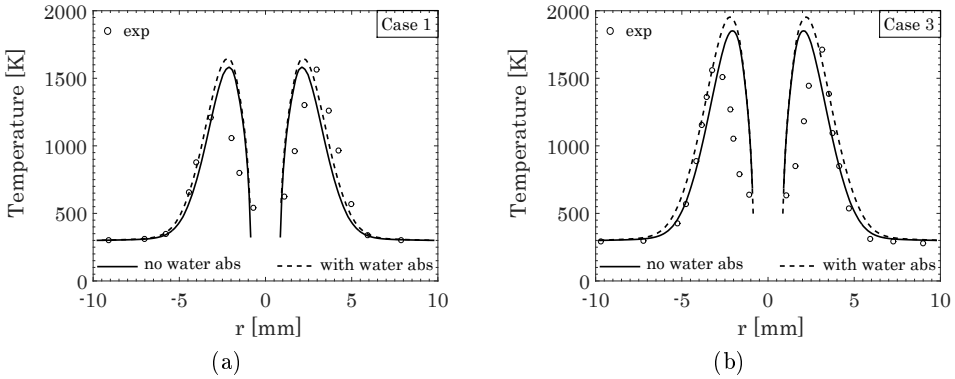

Figure 12: Effect of condensed water: radial temperature profiles for Case 1 (a) and Case 3 (b).

by the internal boiling (mainly methanol) induced by the fiber.

6 Conclusions

In this paper we presented a CFD computational framework for the numerical modeling of the combustion of suspended fuel droplets in normal gravity, accounting for: (i) the efficient numerical management of the gas-phase combustion through the operator-splitting approach (as well as a radiation model), (ii) a multiregion approach to model the thermal perturbation of the fiber, (iii) a vaporization model which includes the possibility of boiling in the liquid phase. The numerical model has been adopted to simulate the combustion of suspended methanol droplets from a recent experimental work. The agreement with the experimental data was satisfactory, both in terms of diameter decay and radial temperature profiles. In particular:

- The thermal perturbation of the fiber strongly affects the vaporization rate, conducting heat inside the liquid phase. The droplet interior is subjected to boiling, while the external surface evaporates by diffusion. A partial quenching of the flame occurs close to its surface, accumulating oxidized species;

- Higher oxygen concentrations increase the flame temperature, bring the flame closer to the droplet surface and diminishes the droplet lifetime;

- The presence of a buoyant flow provides an axisymmetric flame geometry, with a lower standoff ratio and a higher flame temperature if compared to microgravity.

Furthermore, the shear stress at the interface induces an circulation in the liquid phase, which enhances the internal heat transfer;

- The flame is thinner in the lower part of the droplet (high χ), where we found the peak of most of the radical species. A brief analysis of the distribution of species in the gas phase shed light on the chemical behavior of H and HO_2 radicals and on the quenching effect at the fiber;

- The water produced in the gas-phase condenses on the droplet surface, with two main effects: (i) an initial increase of the burning rate, due to the release of the condensation enthalpy at the droplet surface and (ii) a subsequent delay, because of water accumulation. The effect on the diameter decay is negligible, while the comparison of the radial temperature profiles slightly improves.

Further works will be focused on the combustion modeling of more complex fuels (such as n-alkanes and multicomponent fuels), investigating additional phenomena such as cool flames, soot formation and preferential vaporization.

Acknowledgments

We acknowledge the CINECA award under the ISCRA initiative, for the availability of high performance computing resources and support (ISCRA-B: HP10BGXWCZ).

Appendix A Grid refinement analysis

The sensitivity of the numerical results with respect to the mesh size is investigated in this appendix. Case 2 (Table 3) is simulated at three increasing levels of refinement: n=1 (37,000 cells), n=2 (92,000 cells) and n=3 (160,000 cells). The mesh is refined only in the fluid region, maintaining the proportions between the fine region (around the droplet) and the coarser one (outside the droplet). The analysis is made in terms of the variables reported in Table 4 at time $t = 0.5$ s. The values are compared with the continuum value at zero grid spacing, evaluated adopting the Richardson extrapolation [72]. The approximate orders of convergence are also calculated.
The code shows convergence orders between 1.7 and 2.3 for the examined variables. Even though n=3 is the most accurate case, the refinement level n=2 (92,000 cells) has been used in this work, since the computational time is significantly reduced. Adopting this resolution, the average error for the reported variables remains between 0.01% and 2%.

Variable	Refinement levels			∞	O
	n=1	n=2	n=3		
T_{flame}	1711.29	1760.2	1759.95	1759.83	2.2
$T_{surface}$	316.36	319.21	319.24	319.25	2.3
CO_{max}	0.109	0.118	0.117	0.1165	1.8
$CO_{2,max}$	0.248	0.236	0.234	0.233	1.8
H_2O_{max}	0.171	0.146	0.143	0.142	2.3
OH_{max}	0.00311	0.00373	0.00364	0.0036	1.7

Table 4: Grid refinement analysis for Case 2 at three different levels of resolution. The reference value ∞ is estimated through Richardson extrapolation. The approximate order of convergence O is also reported.

Nomenclature

Acronyms

VOF Volume Of Fluid

Greek letters

α VOF marker function [–]

β thermal expansion coefficient $\left[\frac{1}{K}\right]$

χ scalar dissipation rate $\left[s^{-1}\right]$

ΔH_R enthalpy of reaction $[J/kg]$

Δh_{ev} evaporation enthalpy $\left[\frac{J}{kg}\right]$

δ_s Dirac delta $\left[\frac{1}{m}\right]$

γ activity coefficient [–]

$\hat{\phi}$ mixture gas-phase fugacity coefficient [–]

κ curvature $\left[\frac{1}{m}\right]$

μ dynamic viscosity $\left[\frac{kg}{ms}\right]$

ν stoichiometric coefficient [–]

ω mass fraction [–]

ϕ pure gas-phase fugacity coefficient $[-]$

ψ generic variable

ρ density $\left[\frac{kg}{m^3}\right]$

σ surface tension $\left[\frac{N}{m}\right]$

Roman letters

$\dot{m}$ evaporation flux $\left[\frac{kg}{m^3 s}\right]$

$\dot{q}$ heat flux per unit volume $\left[\frac{W}{m^3}\right]$

$\mathcal{D}$ mass diffusion coefficient $\left[\frac{m^2}{s}\right]$

$\mathbf{f}$ force per unit volume $\left[\frac{N}{m^3}\right]$

$\mathbf{j}$ diffusion flux $\left[\frac{kg}{m^2 s}\right]$

$\mathbf{S}$ source term

$\mathbf{T}$ transport term

$\mathbf{v}$ velocity $\left[\frac{m}{s}\right]$

$\mathbf{x}$ position vector $[m]$

a_p absorption coefficient $[-]$

C_p constant pressure specific heat $\left[\frac{J}{kgK}\right]$

D diameter $[m]$

H height of the mesh $[m]$

k thermal conductivity $\left[\frac{W}{mK}\right]$

L base radius of the mesh $[m]$

M_w molecular weight $\left[\frac{kg}{mol}\right]$

Ns Number of species $[-]$

p pressure $[Pa]$

p^0 vapor pressure $[Pa]$

p_{rgh} dynamic pressure $[Pa]$

R reaction rate $\left[\frac{kg}{m^3 s}\right]$

r radius $[m]$

t time $[s]$

T temperature $[K]$

v molar volume $\left[\frac{m^3}{mol}\right]$

x liquid mole fraction $[-]$

y gas mole fraction $[-]$

Z mixture fraction $[-]$

Subscripts

0 initial, reference

b boiling

env ambient

f fiber

G gas

i i-th species

j j-th reaction

L liquid

rad radiative

s solid

References

[1] G. Tryggvason, R. Scardovelli, S. Zaleski, Direct numerical simulations of gas–liquid multiphase flows, Cambridge University Press, 2011.

[2] W. A. Sirignano, Fluid dynamics and transport of droplets and sprays, Cambridge university press, 1999.

[3] S. Okajima, S. Kumagai, Further investigations of combustion of free droplets in a freely falling chamber including moving droplets, in: Proceedings of the Combustion Institute, Vol. 15, Elsevier, 1975, pp. 401–407.

[4] D. L. Dietrich, J. B. Haggard Jr, F. L. Dryer, V. Nayagam, B. D. Shaw, F. A. Williams, Droplet combustion experiments in spacelab, in: Proceedings of the Combustion Institute, Vol. 26, Elsevier, 1996, pp. 1201–1207.

[5] A. J. Marchese, F. L. Dryer, V. Nayagam, Numerical modeling of isolated n-alkane droplet flames: initial comparisons with ground and space-based microgravity experiments, Combustion and Flame 116 (3) (1999) 432–459.

[6] A. Cuoci, M. Mehl, G. Buzzi-Ferraris, T. Faravelli, D. Manca, E. Ranzi, Autoignition and burning rates of fuel droplets under microgravity, Combustion and Flame 143 (3) (2005) 211–226.

[7] T. I. Farouk, F. L. Dryer, Isolated n-heptane droplet combustion in microgravity: cool flames–two-stage combustion, Combustion and Flame 161 (2) (2014) 565–581.

[8] A. Cuoci, A. E. Saufi, A. Frassoldati, D. L. Dietrich, F. A. Williams, T. Faravelli, Flame extinction and low-temperature combustion of isolated fuel droplets of n-alkanes, Proceedings of the Combustion Institute 36 (2) (2017) 2531–2539.

[9] D. C. K. Rao, S. Syam, S. Karmakar, R. Joarder, Experimental investigations on nucleation, bubble growth, and micro-explosion characteristics during the combustion of ethanol/jet a-1 fuel droplets, Experimental Thermal and Fluid Science 89 (2017) 284–294.

[10] M. A. Pfeil, L. J. Groven, R. P. Lucht, S. F. Son, Effects of ammonia borane on the combustion of an ethanol droplet at atmospheric pressure, Combustion and flame 160 (10) (2013) 2194–2203.

[11] C. Chauveau, I. Gökalp, D. Segawa, T. Kadota, H. Enomoto, Effects of reduced gravity on methanol droplet combustion at high pressures, Proceedings of the Combustion Institute 28 (1) (2000) 1071–1077.

[12] C. Chauveau, B. Vieille, I. Gökalp, D. Segawa, T. Kadota, A. Nakainkyo, Effects of gravitational acceleration on high pressure combustion of methanol droplets, Journal de Chimie Physique et de Physico-Chimie Biologique 96 (6) (1999) 1031–1037.

[13] B. Shaw, J. Wei, Combustion of methanol droplets in air-diluent environments with reduced and normal gravity, Journal of Combustion 587987.

[14] C. Chauveau, F. Halter, A. Lalonde, I. Gokalp, An experimental study on the droplet vaporization: effects of heat conduction through the support fiber, in: Proc. of 22 nd Annual Conference on Liquid Atomization and Spray Systems (ILASS Europe 2008), Vol. 59, 2008, p. 61.

[15] R. Banerjee, Numerical investigation of evaporation of a single ethanol/iso-octane droplet, Fuel 107 (2013) 724–739.

[16] O. A. George, J. Xiao, C. S. Rodrigo, R. Mercadé-Prieto, J. Sempere, X. D. Chen, Detailed numerical analysis of evaporation of a micrometer water droplet suspended on a glass filament, Chemical Engineering Science 165 (2017) 33–47.

[17] Y. Wang, X. Chen, X. Wang, V. Yang, Vaporization of liquid droplet with large deformation and high mass transfer rate, ii: Variable-density, variable-property case, Journal of Computational Physics 394 (2019) 1–17.

[18] B. Wang, A. Kronenburg, G. L. Tufano, O. T. Stein, Fully resolved DNS of droplet array combustion in turbulent convective flows and modelling for mixing fields in inter-droplet space, Combustion and Flame 189 (2018) 347–366.

[19] Y. Jin, B. Shaw, Computational modeling of n-heptane droplet combustion in air–diluent environments under reduced-gravity, International Journal of Heat and Mass Transfer 53 (25-26) (2010) 5782–5791.

[20] N. Ghata, B. D. Shaw, Computational modeling of unsupported and fiber-supported n-heptane droplet combustion in reduced gravity: a study of fiber effects, Combustion Science and Technology 187 (1-2) (2015) 83–102.

[21] A. Saufi, A. Frassoldati, T. Faravelli, A. Cuoci, DropletSMOKE++: A comprehensive multiphase CFD framework for the evaporation of multidimensional fuel droplets, International Journal of Heat and Mass Transfer 131 (2019) 836–853.

[22] A. Saufi, R. Calabria, F. Chiariello, A. Frassoldati, A. Cuoci, T. Faravelli, P. Massoli, An experimental and CFD modeling study of suspended droplets evaporation in buoyancy driven convection, Chemical Engineering Journal (2019) 122006.

[23] A. K. Yadav, A. Chowdhury, A. Srivastava, Interferometric investigation of methanol droplet combustion in varying oxygen environments under normal gravity, International Journal of Heat and Mass Transfer 111 (2017) 871–883.

[24] C. W. Hirt, B. D. Nichols, Volume of fluid (VOF) method for the dynamics of free boundaries, Journal of computational physics 39 (1) (1981) 201–225.

[25] J. Roenby, H. Bredmose, H. Jasak, A computational method for sharp interface advection, Royal Society open science 3 (11) (2016) 160405.

[26] S. S. Deshpande, L. Anumolu, M. F. Trujillo, Evaluating the performance of the two-phase flow solver interfoam, Computational science & discovery 5 (1) (2012) 014016.

[27] R. B. Bird, Transport phenomena, Applied Mechanics Reviews 55 (1) (2002) R1–R4.

[28] J. M. Smith, Introduction to chemical engineering thermodynamics, ACS Publications, 1950.

[29] J. Brackbill, D. B. Kothe, C. Zemach, A continuum method for modeling surface tension, Journal of computational physics 100 (2) (1992) 335–354.

[30] S. Popinet, An accurate adaptive solver for surface-tension-driven interfacial flows, Journal of Computational Physics 228 (16) (2009) 5838–5866.

[31] A. Albadawi, D. Donoghue, A. Robinson, D. Murray, Y. Delauré, Influence of surface tension implementation in volume of fluid and coupled volume of fluid with level set methods for bubble growth and detachment, International Journal of Multiphase Flow 53 (2013) 11–28.

[32] A. Q. Raeini, M. J. Blunt, B. Bijeljic, Modelling two-phase flow in porous media at the pore scale using the volume-of-fluid method, Journal of Computational Physics 231 (17) (2012) 5653–5668.

[33] R. P. Fedkiw, T. Aslam, B. Merriman, S. Osher, A non-oscillatory eulerian approach to interfaces in multimaterial flows (the ghost fluid method), Journal of computational physics 152 (2) (1999) 457–492.

[34] V. Vukčević, H. Jasak, I. Gatin, Implementation of the ghost fluid method for free surface flows in polyhedral finite volume framework, Computers & Fluids 153 (2017) 1–19.

[35] S. J. Cummins, M. M. Francois, D. B. Kothe, Estimating curvature from volume fractions, Computers & structures 83 (6-7) (2005) 425–434.

[36] E. Marchandise, P. Geuzaine, N. Chevaugeon, J.-F. Remacle, A stabilized finite element method using a discontinuous level set approach for the computation of bubble dynamics, Journal of Computational Physics 225 (1) (2007) 949–974.

[37] O. Desjardins, V. Moureau, H. Pitsch, An accurate conservative level set/ghost fluid method for simulating turbulent atomization, Journal of Computational Physics 227 (18) (2008) 8395–8416.

[38] S. Popinet, Numerical models of surface tension, Annual Review of Fluid Mechanics 50 (2018) 49–75.

[39] J. Palmore Jr, O. Desjardins, A volume of fluid framework for interface-resolved simulations of vaporizing liquid-gas flows, Journal of Computational Physics 399 (2019) 108954.

[40] T. Harada, H. Watanabe, Y. Suzuki, H. Kamata, Y. Matsushita, H. Aoki, T. Miura, A numerical investigation of evaporation characteristics of a fuel droplet suspended from a thermocouple, International Journal of Heat and Mass Transfer 54 (1-3) (2011) 649–655.

[41] J.-R. Yang, S.-C. Wong, On the discrepancies between theoretical and experimental results for microgravity droplet evaporation, International Journal of Heat and Mass Transfer 44 (23) (2001) 4433–4443.

[42] C. Chauveau, M. Birouk, F. Halter, I. Gökalp, An analysis of the droplet support fiber effect on the evaporation process, International Journal of Heat and Mass Transfer 128 (2019) 885–891.

[43] A. Cuoci, A. Frassoldati, T. Faravelli, E. Ranzi, OpenSMOKE++: An object-oriented framework for the numerical modeling of reactive systems with detailed kinetic mechanisms, Computer Physics Communications 192 (2015) 237–264.

[44] C. L. Yaws, The Yaws Handbook of Physical Properties for Hydrocarbons and Chemicals: Physical Properties for More Than 54,000 Organic and Inorganic Chemical Compounds, Coverage for C1 to C100 Organics and Ac to Zr Inorganics, Gulf Professional Publishing, 2015.

[45] R. C. Reid, J. M. Prausnitz, B. E. Poling, The properties of gases and liquids.

[46] A. Fredenslund, R. L. Jones, J. M. Prausnitz, Group-contribution estimation of activity coefficients in nonideal liquid mixtures, AIChE Journal 21 (6) (1975) 1086–1099.

[47] G. Strang, On the construction and comparison of difference schemes, SIAM journal on numerical analysis 5 (3) (1968) 506–517.

[48] A. Cuoci, A. Frassoldati, T. Faravelli, E. Ranzi, A computational tool for the detailed kinetic modeling of laminar flames: Application to C2H4/CH4 coflow flames, Combustion and Flame 160 (5) (2013) 870–886.

[49] C. J. Greenshields, OpenFOAM user guide, OpenFOAM Foundation Ltd, version 3 (1).

[50] P. S. Veloo, Y. L. Wang, F. N. Egolfopoulos, C. K. Westbrook, A comparative experimental and computational study of methanol, ethanol, and n-butanol flames, Combustion and Flame 157 (10) (2010) 1989–2004.

[51] E. Ranzi, A. Sogaro, P. Gaffuri, G. Pennati, T. Faravelli, A wide range modeling study of methane oxidation, Combustion science and technology 96 (4-6) (1994) 279–325.

[52] W. K. Metcalfe, S. M. Burke, S. S. Ahmed, H. J. Curran, A hierarchical and comparative kinetic modeling study of C1- C2 hydrocarbon and oxygenated fuels, International Journal of Chemical Kinetics 45 (10) (2013) 638–675.

[53] S. M. Burke, U. Burke, R. Mc Donagh, O. Mathieu, I. Osorio, C. Keesee, A. Morones, E. L. Petersen, W. Wang, T. A. DeVerter, et al., An experimental and modeling study of propene oxidation. part 2: Ignition delay time and flame speed measurements, Combustion and Flame 162 (2) (2015) 296–314.

[54] A. Burcat, B. Ruscic, et al., Third millenium ideal gas and condensed phase thermochemical database for combustion (with update from active thermochemical tables)., Tech. rep., Argonne National Lab.(ANL), Argonne, IL (United States) (2005).

[55] A. Stagni, A. Frassoldati, A. Cuoci, T. Faravelli, E. Ranzi, Skeletal mechanism reduction through species-targeted sensitivity analysis, Combustion and Flame 163 (2016) 382–393.

[56] P. Pepiot-Desjardins, H. Pitsch, An efficient error-propagation-based reduction method for large chemical kinetic mechanisms, Combustion and Flame 154 (1-2) (2008) 67–81.

[57] K. E. Niemeyer, C.-J. Sung, M. P. Raju, Skeletal mechanism generation for surrogate fuels using directed relation graph with error propagation and sensitivity analysis, Combustion and flame 157 (9) (2010) 1760–1770.

[58] T. Poinsot, D. Veynante, Theoretical and numerical combustion, RT Edwards, Inc., 2005.

[59] R. Bilger, S. Stårner, R. Kee, On reduced mechanisms for methane air combustion in nonpremixed flames, Combustion and Flame 80 (2) (1990) 135–149.

[60] T. Farouk, F. Dryer, Microgravity droplet combustion: effect of tethering fiber on burning rate and flame structure, Combustion Theory and Modelling 15 (4) (2011) 487–515.

[61] T. I. Farouk, F. L. Dryer, On the extinction characteristics of alcohol droplet combustion under microgravity conditions–a numerical study, Combustion and flame 159 (10) (2012) 3208–3223.

[62] C. K. Law, Recent advances in droplet vaporization and combustion, Progress in energy and combustion science 8 (3) (1982) 171–201.

[63] S. Prakash, W. Sirignano, Liquid fuel droplet heating with internal circulation, International Journal of Heat and Mass Transfer 21 (7) (1978) 885–895.

[64] R. Kurose, H. Makino, S. Komori, M. Nakamura, F. Akamatsu, M. Katsuki, Effects of outflow from the surface of a sphere on drag, shear lift, and scalar diffusion, Physics of Fluids 15 (8) (2003) 2338–2351.

[65] T. R. Jayawickrama, N. E. L. Haugen, M. U. Babler, M. A. Chishty, K. Umeki, The effect of stefan flow on the drag coefficient of spherical particles in a gas flow, International Journal of Multiphase Flow 117 (2019) 130–137.

[66] S. S. Sadhal, P. S. Ayyaswamy, Flow past a liquid drop with a large non-uniform radial velocity, Journal of Fluid Mechanics 133 (1983) 65–81.

[67] J. Li, Z. Zhao, A. Kazakov, M. Chaos, F. L. Dryer, J. J. Scire Jr, A comprehensive kinetic mechanism for CO, CH2O, and CH3OH combustion, International Journal of Chemical Kinetics 39 (3) (2007) 109–136.

[68] M. Pelucchi, S. Namysl, E. Ranzi, A. Frassoldati, O. Herbinet, F. Battin-Leclerc, T. Faravelli, An experimental and kinetic modelling study of n-C4C6 aldehydes oxidation in a jet-stirred reactor, Proceedings of the Combustion Institute 37 (1) (2019) 389–397.

[69] A. Lee, C. K. Law, An experimental investigation on the vaporization and combustion of methanol and ethanol droplets, Combustion science and technology 86 (1-6) (1992) 253–265.

[70] B. Zhang, F. Williams, Alcohol droplet combustion, Acta Astronautica 39 (8) (1996) 599–603.

[71] J. Leffler, H. T. Cullinan Jr, Variation of liquid diffusion coefficients with composition. dilute ternary systems, Industrial & Engineering Chemistry Fundamentals 9 (1) (1970) 88–93.

[72] P. J. Roache, P. M. Knupp, Completed richardson extrapolation, Communications in Numerical Methods in Engineering 9 (5) (1993) 365–374.

Paper 4

An accurate methodology for surface tension modeling in OpenFOAM®

A.E. Saufi[(a)], O. Desjardins[(b)], A. Cuoci[(a)]

[(a)]Department of Chemistry, Materials, and Chemical Engineering "G. Natta", P.zza Leonardo da Vinci 32, Milano, Italy

[(b)]Sibley School of Mechanical and Aerospace Engineering, Cornell University, Ithaca, NY, United States

International Journal of Multiphase Flow (2020), submitted

Abstract

In this paper a numerical methodology for surface tension modeling is presented, with an emphasis on the implementation in the OpenFOAM® framework. The methodology relies on a combination of (i) a well-balanced approach based on the Ghost Fluid Method (GFM), including the jump of density and pressure directly in the numerical discretization of the pressure equation, and (ii) Height Functions to evaluate the interface curvature, implemented, to the authors' knowledge, for the first time in OpenFOAM®. The method is able to significantly reduce spurious currents (almost to machine accuracy) for a stationary droplet, showing second order convergence both for the curvature and the interface shape. Accurate results are also obtained for additional test cases such as translating droplets, capillary oscillations and rising bubbles, for which numerical results are comparable to what obtained by other numerical codes in the same conditions. Finally, the Height Functions method is extended to include the treatment of contact angles, both for sessile droplets and droplets suspended under the effect of gravity, showing a very good agreement with the theoretical prediction.
The code works in parallel mode and details on the actual implementation in OpenFOAM® are included to facilitate the reproducibility of the results.

Keywords: OpenFOAM, Surface tension, Height Functions, Curvature, Spurious currents, Ghost Fluid Method

1 Introduction

The research on multiphase flows is of practical and fundamental interest for the scientific community, especially regarding energy and propulsion science. Liquid sprays and atomization processes are ubiquitous and the fundamental understanding of the physical phenomena involved paves the way to a more rational and focused design of many engineering devices (e.g for combustion, irrigation, coating). The transformation of a macro-scale liquid structure into small droplets involves several physical steps, including break-up, fragmentation and droplet coalescence, in addition to the phase-change process [1, 2]. Bubbly flows are also present in numerous applications, including boiling heat transfer, gas absorption and stirring in chemical engineering processes [3, 4]. The correct design of these systems requires a knowledge on the collective rising velocity of the bubbles, their distribution and the interaction with the liquid phase. The numerical analysis of these phenomena is very complex and requires a multiphase code able to efficiently handle the interface transport (based on VOF, level-set or front-tracking methods [5, 6, 7]), large density ratios and a detailed description of the surface tension force. In particular, this latter will be the main focus of this paper.
The accurate representation of surface tension is extremely delicate, especially at small scales, due to the singular nature of this force. This makes its implementation within a continuum mechanics context very challenging, in particular:

- The surface tension force only exists at the liquid-gas interface, posing a great problem concerning its discretization. It is well known that incorrect, approximate or trivial discretizations of the surface tension force lead to the formation of unphysical velocities around the interface (called spurious currents) due to the local numerical imbalance between the pressure gradient and the surface tension force [8, 9, 10]. Conversely, well-balanced numeric schemes are able to recover equilibrium solutions of specific cases. The simplest case is given by a motionless spherical droplet at zero gravity, described by the following (continuous) equation:

$$\frac{\partial (\rho \mathbf{v})}{\partial t} = -\nabla p + \sigma \kappa \delta_s \mathbf{n} = \mathbf{0} \tag{1}$$

  where δ_s is a Dirac delta of the interface position, κ is the curvature and $\mathbf{n}$ is the normal to the interface. The equilibrium solution for a two-dimensional droplet of diameter D is a discontinuous pressure field, with a pressure jump $[p]$:

$$[p] = \frac{2\sigma}{D} \tag{2}$$

If the numerical discretizations of the pressure gradient ∇p and surface tension force $\sigma\kappa\delta_s\mathbf{n}$ do not cancel out:

$$\frac{\partial(\rho\mathbf{v})}{\partial t} = -\nabla p + \sigma\kappa\delta_s\mathbf{n} \neq \mathbf{0} \tag{3}$$

a non-physical flow field (spurious current) will be generated as a consequence of this numerical imbalance. This flow generally grows in time, eventually destroying the droplet. The Continuum Surface Force (CSF) method [11] suffers particularly from this issue, due to the volumetric representation of the surface tension force via delta functions. Alternative methods directly approach the sharp discontinuity, such as the Ghost Fluid Method (GFM). The main strategy is an explicit treatment of the discontinuity, including the jump conditions directly in the numerical discretization. Introduced by Fedwik et al. [12] to handle discontinuities in compressible solvers, it has been extended to study detonations [13], to efficiently solve variable coefficients Poisson equations [14] and finally to treat the large density ratio typical of multiphase flows [15, 16, 17, 18], as well as the pressure jump due to surface tension (Equation 2). An extensive review by Lalanne et al. [19] analyzes the treatment of the viscosity jump with the GFM approach, based on the works of Kang [20] and Sussmann [21];

- The surface tension force is directly proportional to the interface curvature (Equation 1). Even if the surface tension force is discretized with a perfectly balanced method, this is generally not enough to eliminate spurious currents. The curvature gradients along the interface generate a flow, which may be physical (e.g. when a deformed droplet tends towards a spherical shape) or unphysical, when these variations are actually due to numerical errors in the curvature evaluation [11, 22]. This unphysical flow (spurious current) deforms the droplet, further complicating the curvature computation. This issue is particularly evident within a VOF method, because it requires the differentiation of a discontinuous function (i.e. α):

$$\kappa = \nabla \cdot \mathbf{n} = \nabla \cdot \left(\frac{\nabla\alpha}{|\nabla\alpha|} \right) \tag{4}$$

On the other hand, level-set methods adopt an iso-contour of a smooth function to track the interface, allowing an easier evaluation of the curvature through Equation

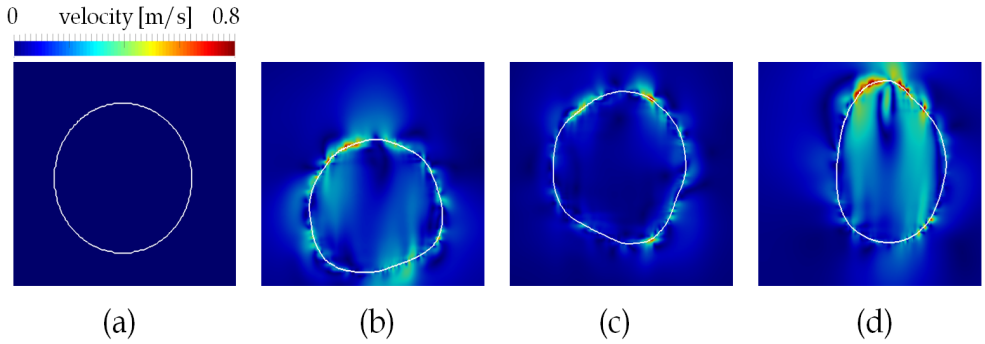

Figure 1: Spurious currents on a droplet of water ($D = 1$ mm, white contour) using the `interFoam` multiphase solver available in `OpenFOAM`® [33]. Times t = 0 (a), 0.04 (b), 0.1 (c) and 0.2 (d) s.

4.

The first solutions relied on the filtering of α, in order to handle smoother functions. However, many studies showed the inaccuracy and non-consistency of these methods [23, 24]. Widely used are Height Functions [22, 25], in which local heights are computed (from volume fractions) and differentiated in order to obtain the curvature. The main conditions is to have well defined heights, usually available when the droplet is well resolved. When this is not possible, least-squares methods can be used, based on discrete surfaces differentiation [26, 27, 16]. The interface is locally approximated by a quadratic form, from which the curvature can be analytically computed;

- Finally, the numerical treatment of gas-liquid-solid contact points is particularly important. The study of the contact angle between the solid and the interface is fundamental in many applications such as sessile and suspended droplets. In particular, in this latter the contact angle is provided by the equilibrium between surface tension force and the droplet weight. In case of transient systems, it also depends on the liquid and gas velocity fields (which ultimately act as additional forces on the droplet). It is necessary to use a stable methodology to predict the interface contact angle, depending on the local operating conditions. While it is relatively easy to deal with static contact angles [28], the description of a moving contact line implies a paradox: Navier Stokes equations with no-slip conditions produce an infinite viscous dissipation [29]. This has been addressed in several works [30, 31, 32] regarding contact angle hysteresis.

These aspects have been extensively treated in many works and recent numerical

implementations efficiently include all of them (e.g. Gerris [9], NGA [16]). In this work we want to focus on the `OpenFOAM`® framework, which lacks for a general comprehensive solver for surface tension driven flows. Most of the recent attempts are mainly based on smoothing-filtering techniques [34, 35] or simplified coupled VOF-Level Set methods [36, 37], which can be hardly generalized (uncertainty on the number-type of filters, choice of the interface thickness, re-initialization method etc.). Comprehensive reviews on the capabilities of the main multiphase solver in `OpenFOAM`® (`interFOAM`) for microfluidic applications [38, 39] clearly show large errors in the pressure jump prediction, a significant presence of spurious currents (Figure 1) and no mesh convergence (even first order) on the interface curvature. The objective of this paper is to fill this gap, providing a stable and accurate numerical methodology for `OpenFOAM`® able to overcome the aforementioned issues, allowing to correctly represent the surface tension effects in common systems. This is implemented as an extension of the `DropletSMOKE++` solver [40], a CFD multiphase code specifically conceived for the analysis of fuel droplets vaporization. Therefore:

- The Ghost Fluid Method (GFM) has been implemented to handle the density and the pressure gradients at the interface, providing a balanced and sharp discretization of these fields. This is based on the work of Vukcevic and Jasak [18], which has been further extended in this work to account for the pressure jump due to surface tension;
- The Height Functions method has been implemented to evaluate the interface curvature, to the authors' knowledge for the first time in `OpenFOAM`®. This method has been chosen due to its simplicity, good convergence properties and accurate results for sufficiently resolved interfaces;
- The Height Functions method is extended to treat contact lines, in order to predict contact angles for static (sessile droplets) and dynamic (suspended droplets) systems. This is partially based on the work of Dupont et al. [41] and Afkhami et al. [28].

The paper organization includes: (i) the main mathematical model, (ii) a detailed description of the Ghost Fluid Method and (iii) the Height Functions method. Details about the specific implementation in `OpenFOAM`® are also provided. The methodology is validated with classical test cases, including: static droplet equilibrium, translating droplets, capillary oscillations and bubbles rising in a dense fluid. Many of these tests have been already carried out by other authors and the comparison of their results with ours is provided as well. Finally, the contact angle treatment is presented, with

applications to sessile droplets and suspended droplets. The manuscript finishes with the conclusions.

2 Main mathematical model

2.1 Interface advection

The VOF methodology is adopted to transport the interface. The two phases are treated as a single fluid whose properties vary abruptly at the phase boundary. A scalar marker function α represents the liquid volumetric fraction, varying from value 0 in the gas-phase to value 1 in the liquid phase. The α advection equation is:

$$\frac{\partial \alpha}{\partial t} + \nabla \cdot (\mathbf{v}\alpha) = 0 \tag{5}$$

The interface transport is solved using the `isoAdvector` library developed by Roenby and Jasak [42]. `isoAdvector` performs a geometric advection of the interface, whose quality is superior to the MULES (Multidimensional Universal Limiter with Explicit Solution) compressive scheme by Weller [43] usually used in the `OpenFOAM`® multiphase solvers.

2.2 Navier-Stokes equations

A single Navier-Stokes equation is solved for both phases (one-fluid approach):

$$\frac{\partial (\rho \mathbf{v})}{\partial t} + \nabla \cdot (\rho \mathbf{v} \otimes \mathbf{v}) = \nabla \cdot \mu \left(\nabla \mathbf{v} + \nabla \mathbf{v}^T \right) - \nabla p + \rho \mathbf{g} + \sigma \kappa \delta_s \mathbf{n} \tag{6}$$

Taking out the continuity equation $\frac{\partial \rho}{\partial t} + \nabla \cdot (\rho \mathbf{v}) = 0$:

$$\rho \left(\frac{\partial \mathbf{v}}{\partial t} + \mathbf{v} \cdot \nabla \mathbf{v} \right) = \nabla \cdot \mu \left(\nabla \mathbf{v} + \nabla \mathbf{v}^T \right) - \nabla p + \rho \mathbf{g} + \sigma \kappa \delta_s \mathbf{n} \tag{7}$$

Following the work of Vukcevic and Jasak [18], we can write Equation 7 as:

$$\rho \left(\frac{\partial \mathbf{v}}{\partial t} + \mathbf{v} \cdot \nabla \mathbf{v} \right) = \nabla \cdot \mu \left(\nabla \mathbf{v} + \nabla \mathbf{v}^T \right) - \nabla p_d - \mathbf{g} \cdot \mathbf{x} \nabla \rho + \sigma \kappa \delta_s \mathbf{n} \tag{8}$$

where $p_d = p - \rho \mathbf{g} \cdot \mathbf{x}$ is the dynamic pressure. In this way gravity is considered as a contribution to the dynamic pressure jump. Working with incompressible flows, the density gradient $\nabla \rho$ is zero everywhere but at the interface. The same argument is valid for the surface tension force, as defined by the Dirac delta $\delta_s \mathbf{n}$ vector. These interfacial

contributions will be handled through the GFM and included directly in the discretization of the dynamic pressure p_d, hence, they can be eliminated from the equation:

$$\frac{\partial \mathbf{v}}{\partial t} + \mathbf{v} \cdot \nabla \mathbf{v} = \beta \nabla \cdot \mu \left(\nabla \mathbf{v} + \nabla \mathbf{v}^T \right) - \beta \nabla p_d \tag{9}$$

where $\beta = \frac{1}{\rho}$. The jump of dynamic pressure $[p_d]$ can be derived from the definition of p_d:

$$[p_d] = [p] - \left[\frac{1}{\beta} \right] \mathbf{g} \cdot \mathbf{x} \tag{10}$$

The jump of pressure $[p]$ is due to surface tension. Therefore:

$$[p_d] = \sigma \kappa - \left[\frac{1}{\beta} \right] \mathbf{g} \cdot \mathbf{x} \tag{11}$$

The main novelty of this work with respect to that of Vukcevic et al. [18] is the introduction of the surface tension term $\sigma\kappa$, which was not considered in their work.

2.3 Pressure equation

The PIMPLE algorithm [33], a combination between SIMPLE (Semi-Implicit Method for Pressure-Linked Equations) and PISO (Pressure Implicit Splitting of Operators) is used to manage the pressure-velocity coupling in `OpenFOAM`®, computing a velocity field which satisfies both momentum and continuity equation through an iterative procedure. Equation 8 is written in a semi-discretized form [44]:

$$a_P \mathbf{v}_P = \mathbf{H}\left(\mathbf{v}_N\right) - \beta \nabla p_d \tag{12}$$

where $\mathbf{H}\left(\mathbf{v}_N\right)$ matrix includes neighbor transport coefficients and source terms, while a_p are the diagonal coefficients of the matrix. The pressure gradient is not discretized at this point. We can derive the velocities at the cell centers:

$$\mathbf{v}_P = \frac{\mathbf{H}\left(\mathbf{v}_N\right)}{a_P} - \frac{1}{a_P} \beta \nabla p_d \tag{13}$$

and the face fluxes ϕ_f:

$$\phi_f = \frac{\mathbf{H}\left(\mathbf{v}_N\right)_f}{a_{P,f}} \cdot \mathbf{S}_f - \left(\frac{1}{a_P} \right)_f \beta_f \left(\nabla p_d \right)_f \cdot \mathbf{S}_f \tag{14}$$

The continuity equation for incompressible flows is:

$$\nabla \cdot \mathbf{v} = 0 \tag{15}$$

The final form of the pressure equation is (substituting Equation 13 in Equation 15):

$$\nabla \cdot \left(\frac{\mathbf{H}\left(\mathbf{v}_N\right)}{a_P} \right) = \nabla \cdot \left(\frac{1}{a_P} \beta \nabla p_d \right) \tag{16}$$

The finite volume discretization of this equation is [44]:

$$\sum_f \frac{\mathbf{H}\left(\mathbf{v}_N\right)_f}{a_{P,f}} \cdot \mathbf{S}_f = \sum_f \left(\frac{1}{a_P} \right)_f \beta_f \left(\nabla p_d \right)_f \cdot \mathbf{S}_f \tag{17}$$

The solution of Equation 17 gives a pressure field p_d that, inserted in 8, provides a conservative velocity field. The face fluxes ϕ_f are then reconstructed based on the new pressure gradient via Equation 14.
The pressure equation (Equation 17) involves three discontinuous fields at the free surface: (i) $\beta_f = \left(\frac{1}{\rho}\right)_f$, (ii) the dynamic pressure p_d and (iii) the viscosity μ included in the matrix $\mathbf{H}\left(\mathbf{v}_N\right)$. Their jump [ ] at the interface f is:

$$\left[\frac{1}{\beta_f} \right] = \rho_L - \rho_G \tag{18}$$

$$H_f = [p_d] = -\left[\frac{1}{\beta_f} \right] \mathbf{g} \cdot \mathbf{x}_f + \sigma \kappa_f = -\left(\rho_L - \rho_G \right) \mathbf{g} \cdot \mathbf{x}_f + \sigma \kappa_f \tag{19}$$

$$[\mu] = \mu_L - \mu_G \tag{20}$$

The density and pressure discontinuities will be treated with the GFM. Due to the inherent complexity of treating the viscosity jump within a GFM approach [19], a Continuum Surface Force method (CSF) is adopted for this term. The jump is smoothed across a few interfacial cells, making the viscosity field continuous:

$$\mu = \alpha \mu_L + \left(1 - \alpha\right) \mu_G \tag{21}$$

3 The Ghost Fluid Method (GFM)

Figure 2 reports a qualitative plot of the pressure jump $[p]$ at the free surface Γ. In `OpenFOAM`® every face f is shared between two adjacent cells called owner (O) and a

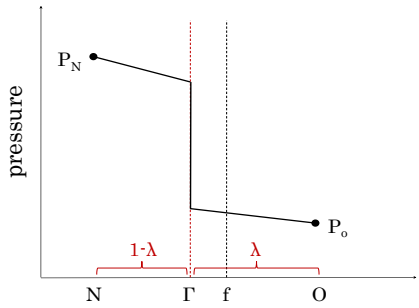

(a)

Figure 2: Pressure jump at the interface Γ, defined on the cell face f. λ is the relative interface position.

neighbour (N). Following Vukcevic et al. [18], an interfacial face f is defined when two adjacent cells N (neighbour) and O (owner) are respectively "wet" ($\alpha > 0.5$) and "dry" ($\alpha < 0.5$), satisfying the following equation:

$$(\alpha_N - 0.5)(\alpha_O - 0.5) < 0 \tag{22}$$

The interface Γ will be between the cells O and N, but we do not know where. The dimensionless relative position of the interface (with respect to cell O) is λ and it is defined as:

$$\lambda = \frac{\alpha_O - 0.5}{\alpha_O - \alpha_N} \tag{23}$$

In Equation 17 the term $\beta_f (\nabla p_d)_f$ is the only one which requires special attention. An ordinary discretization of the pressure gradient at the cell face $(\nabla p_d)_f$ would be (for orthogonal meshes):

$$(\nabla p_d)_f = \frac{p_O - p_N}{|\mathbf{d}|} \tag{24}$$

where $\mathbf{d}$ is the distance vector (from O to N). As can be seen in Figure 3 (a), this implementation leads to incorrect values of the face gradient. On the other hand, the GFM exploits the knowledge of the pressure jump at the interface Γ (Equation 19), allowing to derive one-sided extrapolated values of the pressure field which can be used to discretize the pressure gradient. Let us refer to Figure 3 (b), considering cell N a liquid cell. Knowing the values of p_N and p^+ it is easy to derive the value p_o^+ at cell O by linear extrapolation. This latter is called "ghost value", since it is defined on the other

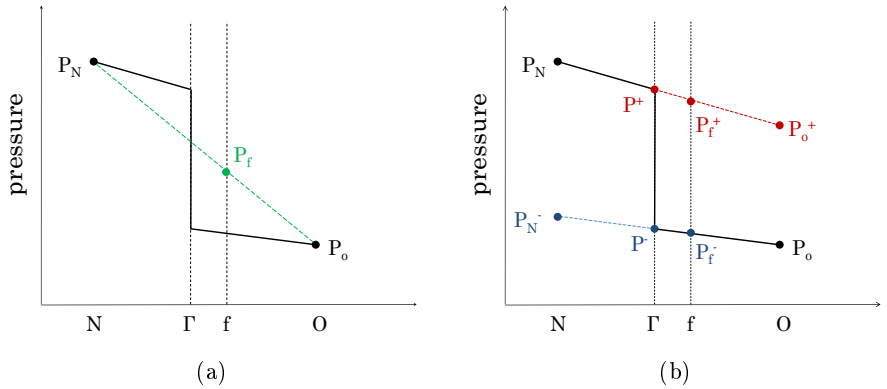

Figure 3: Ordinary interpolation in presence of a jump at the free surface, leading to incorrect gradients (Figure a). Correct gradient evaluation through one-sided extrapolation of interface values (Figure b).

side of the interface Γ (on the gas phase in this case). The same is valid for the gas side (cell O) and its liquid side extrapolation p_N^- at cell N. The pressure gradient has now two different formulations, depending on the position with respect to the interface Γ:

$$(\nabla p_d)_f\Big|_N = \frac{p_O^+ - p_N}{|\mathbf{d}|} \tag{25}$$

$$(\nabla p_d)_f\Big|_O = \frac{p_N^- - p_O}{|\mathbf{d}|} \tag{26}$$

where the extrapolated values p_O^+ and p_N^- are linked by interfacial pressure jump H_f (Equation 19). The jump H_f requires the position vector $\mathbf{x}_f$ of the interface Γ (easily defined based on λ):

$$\mathbf{x}_f = \mathbf{x}_O + \lambda|\mathbf{d}| \tag{27}$$

and the face interpolated values of the curvature κ_f (accessible knowing the cell-centered curvature values in cells N and O). The interfacial jump H_f is therefore directly included in the discretization of the pressure equation. The detailed derivation of the extrapolated values p_O^+ and p_N^- can be found in the reference work of Vukcevic et al. [18]. The final GFM discretization of the pressure Laplacian (for orthogonal meshes) in Equation 16 is the following:

- If the owner cell O is "wet" ($\alpha > 0.5$):

$$\nabla \cdot \left(\frac{1}{a_P} \beta \nabla p_d \right) \Big|_O = \sum_f \left(\frac{1}{a_P} \right)_f \frac{|\mathbf{S}_f|}{|\mathbf{d}|} \frac{\beta^L \beta^G}{\beta_w} \left(p_N - p_O - H_f \right) \tag{28}$$

$$\nabla \cdot \left(\frac{1}{a_P} \beta \nabla p_d \right) \Big|_N = \sum_f \left(\frac{1}{a_P} \right)_f \frac{|\mathbf{S}_f|}{|\mathbf{d}|} \frac{\beta^L \beta^G}{\beta_w} \left(p_O - p_N + H_f \right) \tag{29}$$

where $\beta_w = \lambda \beta^G + (1 - \lambda) \beta^L$.

- If the owner cell O is "dry" ($\alpha < 0.5$):

$$\nabla \cdot \left(\frac{1}{a_P} \beta \nabla p_d \right) \Big|_O = \sum_f \left(\frac{1}{a_P} \right)_f \frac{|\mathbf{S}_f|}{|\mathbf{d}|} \frac{\beta^L \beta^G}{\beta_d} \left(p_N - p_O - H_f \right) \tag{30}$$

$$\nabla \cdot \left(\frac{1}{a_P} \beta \nabla p_d \right) \Big|_N = \sum_f \left(\frac{1}{a_P} \right)_f \frac{|\mathbf{S}_f|}{|\mathbf{d}|} \frac{\beta^L \beta^G}{\beta_d} \left(p_O - p_N + H_f \right) \tag{31}$$

where $\beta_d = \lambda \beta^L + (1 - \lambda) \beta^G$.

The face flux ϕ_f is reconstructed based on the new pressure gradient (discretized explicitly with GFM) according to Equation 14:

- If the owner O is "wet":

$$\phi_f = \frac{\mathbf{H}\left(\mathbf{v}_N\right)_f}{a_{P,f}} \cdot \mathbf{S}_f - \left(\frac{1}{a_P} \right)_f \frac{|\mathbf{S}_f|}{|\mathbf{d}|} \frac{\beta^L \beta^G}{\beta_w} \left(p_N - p_O - H_f \right) \tag{32}$$

- If the owner O is "dry":

$$\phi_f = \frac{\mathbf{H}\left(\mathbf{v}_N\right)_f}{a_{P,f}} \cdot \mathbf{S}_f - \left(\frac{1}{a_P} \right)_f \frac{|\mathbf{S}_f|}{|\mathbf{d}|} \frac{\beta^L \beta^G}{\beta_d} \left(p_N - p_O - H_f \right) \tag{33}$$

Finally, the cell-centered velocity $\mathbf{v}$ can be reconstructed from the face fluxes ϕ_f. Equations 28 to 33 have to be used for interfacial faces only (defined by Equation 22). For the other faces, ordinary discretization applies.

3.1 Details on the `OpenFOAM`® implementation

The main algorithm for the implementation of the Ghost Fluid Method in `OpenFOAM`® is here reported, including the main code lines:

1. Localize the interfacial faces: create a surface scalar field `interfacialFace`, which assumes value 1 if Equation 22 is satisfied and 0 otherwise;

2. Construct the surface scalar field λ, the relative position of the interface (Equation 23);

3. Construct the surface vector field `interfacePosition`, the interface position $\mathbf{x}_f$ (Equation 27);

4. Compute the interpolated value of the curvature $\kappa_f = \kappa_O \lambda + \kappa_N (1 - \lambda)$. The cell values of κ are computed with the Height Functions method, as explained in the dedicated section. Construct the surface scalar field `surfaceTensionJump` as $\sigma \kappa_f$;

5. Construct the surface scalar field `Jump`, the jump H_f across the interfacial face (Equation 19). Consider that the jump on the face has opposite sign depending if it is "seen" from the owner side or from the neighbour side. In `OpenFOAM`® we have:

```
if (alpha1.ref()[owner[facei]] > 0.5)
Jump.ref()[facei] =
(rhoL-rhoG)*(g.value() & interfacePosition.ref()[facei])
+ surfaceTensionJump.ref()[facei];

else
Jump.ref()[facei] =
-(rhoL-rhoG)*(g.value() & interfacePosition.ref()[facei])
- surfaceTensionJump.ref()[facei];
```

6. Compute the values $\beta_w = \lambda \beta^G + (1 - \lambda) \beta^L$ and $\beta_d = \lambda \beta^L + (1 - \lambda) \beta^G$;

7. Construct the Laplacian finite volume matrix `fvmLaplacian` (Equations 28 to 31):

   (a) The resulting discretization matrix is symmetric, it is sufficient to specify the upper matrix coefficient a_{upp} of the Laplacian (describing the effect of the neighbour cell on the owner). If not defined, the lower coefficient will be automatically set the same. For every face:

   - If the owner is "wet":

$$a_{upp} = \left(\frac{1}{a_P} \right)_f \frac{|\mathbf{S}_f|}{|\mathbf{d}|} \frac{\beta^L \beta^G}{\beta_w} \tag{34}$$

in OpenFOAM® the term $\left(\frac{1}{a_P}\right)_f |\mathbf{S}_f|$ is called `raUfMagSf`. So:

```
fvmLaplacian.upper()[facei]
= deltaCoeff.ref()[facei]*raUfMagSf.ref()[facei]*
betaL.ref()[facei]*betaG.ref()[facei]/betaW.ref()[facei];
```

- If the owner is "dry":

$$a_{upp} = \left(\frac{1}{a_P}\right)_f \frac{|\mathbf{S}_f|}{|\mathbf{d}|} \frac{\beta^L \beta^G}{\beta_d} \tag{35}$$

in OpenFOAM®:

```
fvmLaplacian.upper()[facei]
= deltaCoeff.ref()[facei]*raUfMagSf.ref()[facei]*
betaL.ref()[facei]*betaG.ref()[facei]/betaD.ref()[facei];
```

- If the face is not interfacial, standard interpolation applies to β:

$$a_{upp} = \left(\frac{1}{a_P}\right)_f \frac{|\mathbf{S}_f|}{|\mathbf{d}|} \beta_f \tag{36}$$

in OpenFOAM®:

```
fvmLaplacian.upper()[facei]
= deltaCoeff.ref()[facei]*raUfMagSf.ref()[facei]* beta.ref()[facei];
```

(b) The diagonal term d is:

$$d = -\sum_f a_{upp} \tag{37}$$

It is very easy in OpenFOAM® to do this operation:

```
fvmLaplacian.negSumDiag();
```

(c) The source terms are antisymmetric. This means that for each interfacial face the additional flux (due to the jump H_f) from the owner O and the neighbour N cancel out, providing a perfectly balanced scheme. For every interfacial face:

- If the owner cell O is wet (Equations 28 and 29):
  - Owner contribution:

$$\left(\frac{1}{a_P}\right)_f \frac{|\mathbf{S}_f|}{|\mathbf{d}|} \frac{\beta^L \beta^G}{\beta_w} H_f \tag{38}$$

– Neighbour contribution:

$$-\left(\frac{1}{a_P}\right)_f \frac{|\mathbf{S}_f|}{|\mathbf{d}|}\frac{\beta^L\beta^G}{\beta_w}H_f \tag{39}$$

- If the owner cell O is dry (Equations 30 and 31):
  – Owner contribution:

$$\left(\frac{1}{a_P}\right)_f \frac{|\mathbf{S}_f|}{|\mathbf{d}|}\frac{\beta^L\beta^G}{\beta_d}H_f \tag{40}$$

  – Neighbour contribution:

$$-\left(\frac{1}{a_P}\right)_f \frac{|\mathbf{S}_f|}{|\mathbf{d}|}\frac{\beta^L\beta^G}{\beta_d}H_f \tag{41}$$

The face contributions must be summed to provide the cell centered source term. In `OpenFOAM`® we created a volume scalar field `sourceLaplacian` in which:

```
forAll(owner, facei)
{
sourceLaplacian.ref()[owner[facei]]
+=  fvmLaplacian.upper()[facei]*Jump.ref()[facei];
sourceLaplacian.ref()[neighbour[facei]]
-=  fvmLaplacian.upper()[facei]*Jump.ref()[facei];
}
```

There is no need to distinguish between wet and dry cells, it has been already done constructing `fvmLaplacian`. Finally:

```
fvmLaplacian.source() = sourceLaplacian;
```

8. Solve the pressure equation (Equation 17) using `fvmLaplacian`;
9. Reconstruct the face fluxes `phi` on the faces (Equations 32 and 33). In `OpenFOAM`®:

```
phi.ref()[facei]
= phiHbyA.ref()[facei] - fvmLaplacian.upper()[facei]*
(
p.ref()[neighbour[facei]]-p.ref()[owner[facei]]-Jump.ref()[facei]
```

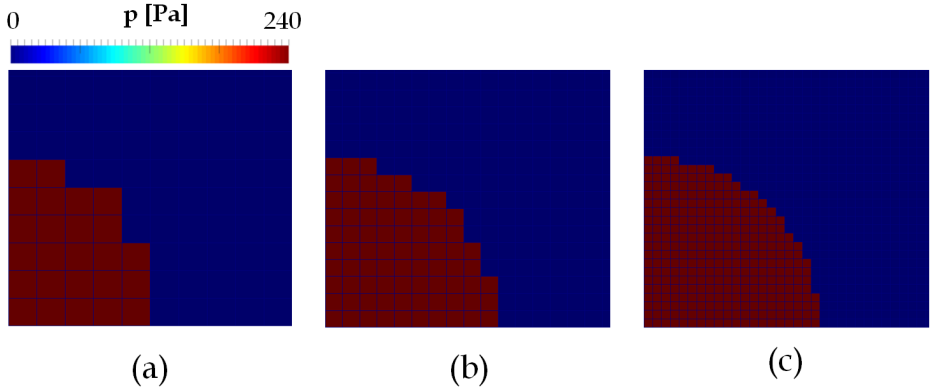

Figure 4: Numerical equilibrium solution (pressure p) for a 2D droplet at zero gravity using the Ghost Fluid Method (GFM) for pressure discretization. The curvature is prescribed $\kappa_f = 2000\ m^{-1}$, providing a pressure jump equal to $[p] = 240$ Pa. Three droplet resolutions $\frac{D}{\Delta x} = 10$ (a), 20 (b), 40 (c) at time $t = 0.01$ s.

```
);
```

again, no need to distinguish between wet and dry cells, the difference is included in `fvmLaplacian.upper()`;

10. Reconstruct the cell-centered velocity values $\mathbf{v}$. In OpenFOAM®:

```
U = fvc::reconstruct(phi);
```

It is important to follow these steps not only for the internal faces, but also for the boundary ones, in order to be able to perform parallel computations.

3.2 Static test case

As reported by Francois et al. [8], a consistent discretization method should be able to recover an exact balanced solution for a static droplet (Equation 1) when the interface curvature κ_f is prescribed exactly. A 2D droplet ($D = 1$ mm) is considered, with equal density and viscosity for both gas and liquid $\rho = 1\ kg/m^3$, $\mu = 10^{-4}\ Pa \cdot s$. The curvature κ_f is imposed equal to the analytical value $\frac{1}{R} = 2000\ m^{-1}$. The surface tension is $\sigma = 0.012$ N/m. The relative Laplace number La:

$$La = \frac{\rho D \sigma}{\mu^2} \tag{42}$$

La	$D/\Delta x$	$\|\mathbf{v}\|_{max}$ [m/s]	Ca
1200	10	$2.60 \cdot 10^{-13}$	$2.16 \cdot 10^{-15}$
	20	$1.60 \cdot 10^{-12}$	$1.33 \cdot 10^{-14}$
	40	$2.72 \cdot 10^{-12}$	$2.27 \cdot 10^{-14}$
	100	$1.44 \cdot 10^{-12}$	$1.20 \cdot 10^{-14}$

Table 1: Spurious currents analysis for a Laplace number $La = 1200$ at four different droplet resolutions $D/\Delta x = 10, 20, 40, 100$, by means of $|\mathbf{v}|_{max}$ and capillary number Ca. Time $t = 0.01$ s.

is equal to 1200. The pressure jump due to surface tension equals the total pressure jump (since gravity is zero):

$$H_f = \sigma \kappa_f = 240 \ Pa \tag{43}$$

Four droplet resolutions have been adopted $\frac{D}{\Delta x} = 10, 20, 40, 100$. The results are presented in Figure 4 and in Table 1 in terms of maximum velocity $|\mathbf{v}|_{max}$ and capillary number Ca:

$$Ca = \frac{\mu |\mathbf{v}|_{max}}{\sigma} \tag{44}$$

The equilibrium solution is numerically well recovered, providing a perfectly sharp pressure field. Spurious currents are reduced to machine precision (round off), because of the well-balanced discretization adopted. This holds for all the grid resolutions.

3.3 Dynamic test case

In order to test (only qualitatively) a dynamic case, gravity has been activated maintaining the same initial conditions (Figure 4). The surface tension pressure jump across the interface is still $\sigma \kappa_f = 240 \ Pa$. Figure 5 reports the pressure field of the falling droplet at four different times, for three droplet resolutions $\frac{D}{\Delta x} = 20, 40, 100$. Differently from the static case, the total pressure jump H_f is not constant because it includes the gravity contribution (Equation 19). The GFM maintains a perfectly sharp representation of the pressure field. The droplet falls as if there was no surface tension acting on the interface, because we are disregarding the variation of curvature along the interface. This will be the focus of the next section.

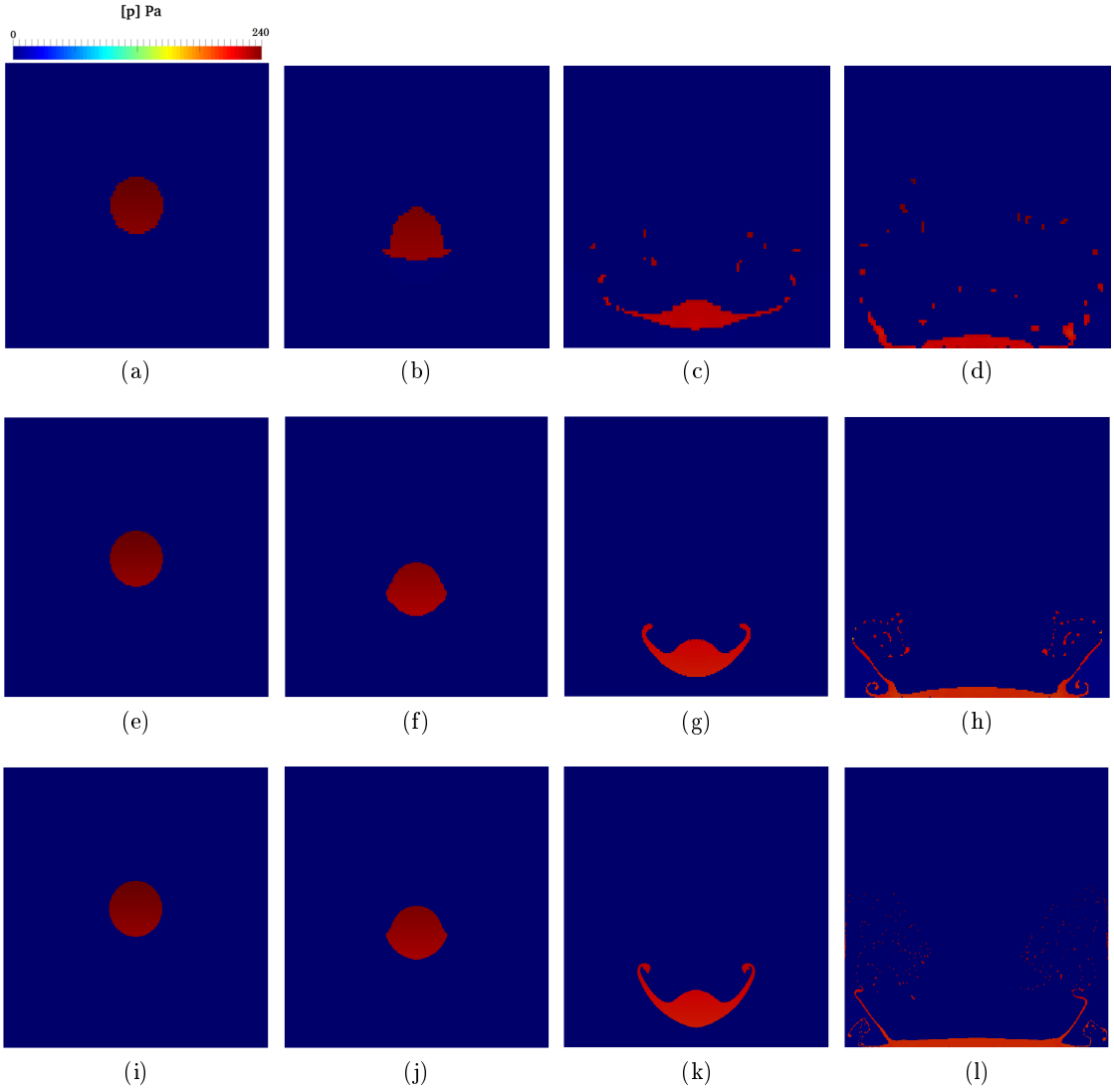

Figure 5: Numerical simulation of a falling droplet at three different droplet resolutions $\frac{D}{\Delta x} = 20$ (a, b, c, d), $\frac{D}{\Delta x} = 40$ (e, f, g, h) and $\frac{D}{\Delta x} = 100$ (i, j, k, l). The surface tension pressure jump is imposed equal $[p] = 240$ Pa. Times $t = 0.002$ s (a, e, i), $t = 0.012$ s (b, f, j), $t = 0.024$ s (c, g, k), $t = 0.036$ s (d, h, l).

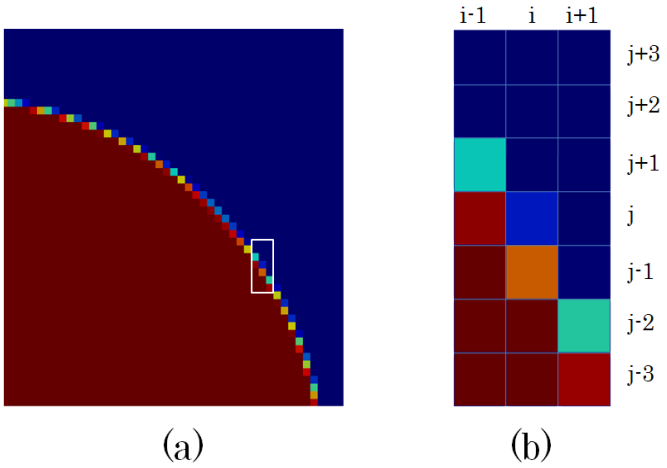

Figure 6: A 3x7 vertical stencil constructed around the interfacial cell (i,j).

4 Curvature evaluation: Height Functions

Every interfacial face f, defined in Equation 22, is shared between two adjacent cells: owner O and neighbour N. As stated in Equation 19, the jump at the interface H_f requires the value of the face interpolated curvature κ_f, therefore the cell-centered values of the curvature κ are necessary in cells O and N for every interfacial face f. We will call these cells "interfacial cells". In this work, we implemented the Height Functions method for the cell-centered curvature calculation.
In the Height Functions method the curvature is obtained by a direct differentiation of local heights, defined for every interfacial cell. Referring to Figure 6, a 3x7 vertical stencil is constructed for every interfacial cell (i, j). The liquid volume fractions (VOF function) are summed up for every cell (multiplied by the vertical cell size Δy) for each of the i columns, obtaining three local heights h_i:

$$h_i = \sum_{j-3}^{j+3} \alpha_{i,j} \Delta y \tag{45}$$

In order to avoid differentiating multi-valued functions, we can also choose an horizontal stencil: the choice is based on the largest component of the interface normal $\mathbf{n}$ in the (i, j) cell:

- if $|n_y| > |n_x|$ we choose a 3x7 vertical stencil;
- if $|n_x| > |n_y|$ we choose a 3x7 horizontal stencil.

The heights represent the position of the interface with respect to the stencil base. Adopting a second order finite difference scheme, we can calculate the first derivative $h'_{i,j}$:

$$h'_{i,j} = \frac{h_{i+1} - h_{i-1}}{2\Delta x} \tag{46}$$

the second derivative $h''_{i,j}$:

$$h''_{i,j} = \frac{h_{i+1} - 2h_i + h_{i-1}}{\Delta x^2} \tag{47}$$

and finally the cell-centered curvature $\kappa_{i,j}$ (in 2D):

$$\kappa_{i,j} = \frac{h''_{i,j}}{\left(1 + h'^2_{i,j}\right)^{3/2}} \tag{48}$$

The curvature is then interpolated at the interface Γ, based on the relative interface position λ (Equation 23):

$$\kappa_f = \lambda\kappa_N + (1 - \lambda)\,\kappa_O \tag{49}$$

Finally, this face-centered curvature value can be used to construct the pressure jump in Equation 19 for the GFM pressure discretization.
This is a standard Height Functions method, because it adopts a fixed stencil for every interfacial cell (i, j). Alternative methods include adaptive stencils [9, 45], for which the size changes depending on the local interface topology (using from 3x3 up to 3x9 stencils) and rotated stencil which are aligned to the interface normal [46].

4.1 Details on the `OpenFOAM`® implementation

The concept behind the use of Height Functions is simple and relatively easy to implement (if compared to discrete surface fitting or spline interpolation [47, 48]). As described before, we use fixed 3x7 stencils (vertical or horizontal, depending on the interface normal **n** direction) for all the interfacial cells. To our knowledge there was no attempt in literature to develop a Height Functions method for the `OpenFOAM`® framework. While in structured finite-difference CFD codes it is immediate to construct a stencil around a cell (using the (i, j) indices), the `polyMesh` mesh description of `OpenFOAM`® (based around faces) makes it more difficult. Hence, the need of a specific description.

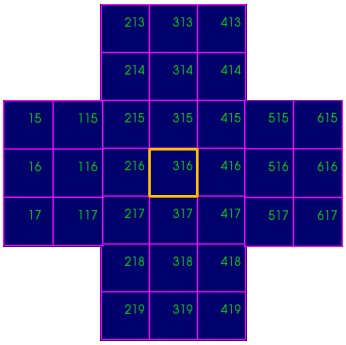

(a)

$$\mathbf{V} = \begin{pmatrix} 213 & 313 & 413 \\ 214 & 314 & 414 \\ 215 & 315 & 415 \\ 216 & 316 & 416 \\ 217 & 317 & 417 \\ 218 & 318 & 418 \\ 219 & 319 & 419 \end{pmatrix} \quad \text{(b)}$$

$$\mathbf{H} = \begin{pmatrix} 17 & 16 & 15 \\ 117 & 116 & 115 \\ 217 & 216 & 215 \\ 317 & 316 & 315 \\ 417 & 416 & 415 \\ 517 & 516 & 515 \\ 617 & 616 & 615 \end{pmatrix} \quad \text{(c)}$$

Figure 7: Example of a vertical and horizontal stencils for the cell 316 (a). Corresponding **V** (b) matrix, for the vertical stencil and **H** (c) matrix for the horizontal stencil.

4.1.1 Stencils construction

In this work we build all the necessary stencils *in pre-processing*, to be more efficient during the simulation. The main algorithm for the stencils construction is coded in a pre-processing function, which only requires the mesh:

1. For every cell in the entire domain construct a 3x3 square stencil around it. This is easily done creating an object of the class `CPCCellToCellStencil`, for which only the mesh information is needed:

   ```
   CPCCellToCellStencil initialStencil(mesh);
   labelList squareStencil = initialStencil[celli];
   ```

   The `squareStencil` list contains the *global* indices of the initial 3x3 stencil in `celli`;

2. Extend the stencil in the vertical direction, adding two rows at the top and at the bottom. For each cell `cellj` in the 3x3 stencil (`squareStencil`):

   (a) Find the 4 adjacent cells:

   ```
   labelList adjacentCells = mesh.cellCells()[ squareStencil[cellj] ];
   ```

   (b) Choose the cell `cellk` in the vertical direction, checking that the vector:

```
vector normal = mesh.C()[adjacentCells[cellk]]-
 mesh.C()[squareStencil[cellj]];
```

points upwards (or downwards) and that `cellk` is not already included in the stencil. We have now a 3x5 stencil;

(c) Repeat the extension (a, b) using the 3x5 stencil, to obtain a 3x7 stencil;

3. Store the 21 cells indices of the vertical stencil in a 3x7 matrix **V**. The matrix elements are sorted as presented in Figure 7 (b);

4. Do the same operation on the `squareStencil` (point 2) in the horizontal direction (adding two columns to the left and two columns to the right);

5. Store the 21 cells indices of the horizontal stencil in a 3x7 matrix **H**. The matrix elements are sorted as presented in Figure 7 (c);

6. If a cell in the domain does not allow to build the complete stencil (e.g. close to the boundary), ignore the cell. We will focus on these cells when dealing with contact angles.

Adopting this pre-processing methodology, every cell in the domain is already linked to its two stencils (**V** and **H**). Therefore, we do not need to construct a stencil at every iteration during run-time, since everything is already tabulated. The great advantage arises when parallel computations are handled. A single processor only has access to its internal cells and to the boundary cells of adjacent processors, making the stencil construction difficult and expensive. In our case this is not necessary, since the stencils are already pre-computed for every cell before the domain partitioning and remain available to the processor throughout the simulation.

4.1.2 Heights calculation

At this point we have two matrices for every cell `celli` of the domain:

- a 3x7 matrix **V** containing the 21 global indices of the vertical stencil (Figure 7 b);
- a 3x7 matrix **H** containing the 21 global indices of the horizontal stencil (Figure 7 c);

During the simulation, the stencil cells (and their α values) must be called. For each interfacial face (Equation 22):

1. Select the owner and neighbour cell of the face. For each one:
2. Calculate the interface normal as $\mathbf{n} = \frac{\nabla \alpha_s}{|\nabla \alpha_s|}$. α_s is a smoothed α field, which helps to calculate the normals with better accuracy. A recursive interpolation smoothing is used in this work:

   ```
   alphaSmooth = fvc::average(fvc::interpolate(alpha));
   ```

   which is repeated a few times (3-4 times is enough);
3. Choose the correct stencil:
   (a) If n_y is the largest component of the interface normal $\mathbf{n}$, choose the vertical stencil matrix $\mathbf{V}$;
   (b) If n_x is the largest component of the interface normal $\mathbf{n}$, choose the horizontal stencil matrix $\mathbf{H}$;
4. Calculate the heights (Equation 45), and the cell-centered curvature (Equation 48);
5. Interpolate the curvature to the face f (Equation 49) to obtain κ_f;
6. Proceed to the GFM discretization of the pressure equation.

It is important to point out that sometimes 3x3 or 3x5 stencils are sufficient to compute discrete heights and obtain a the same curvature value provided by the 3x7 stencil (if the upper/lower rows only add full/empty cells). However, as stated by Popinet [9] 3x7 stencils may not be enough in some cases and 3x9 stencils can be necessary. In the cases presented in this work strong deformations of the interface are not present and 3x7 stencils are safe to compute build consistent heights for curvature calculation. Moreover, in order to have defined heights for all interfacial cells, the droplet must be well resolved. If the curvature radius approaches the mesh size, switching to curve fitting methods would be the best option.

5 Equilibrium of a circular droplet

In a circular droplet at zero gravity the pressure jump at the interface should perfectly balance the surface tension force. The test case from Popinet [9] is adopted and used for comparison: a circular interface is initialized at the center of the domain and it is given enough time to relax to its numerical equilibrium shape. Only a quarter of the circle is

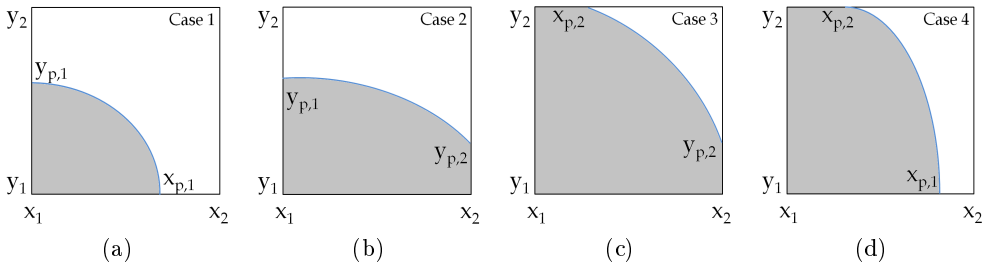

Figure 8: Four possible configurations for the intersection between a quarter of a circular interface and the cell.

Case	Area
1	$F(x_{p,1}) - F(x_1) - (x_{p,1} - x_1)\, y_1$
2	$F(x_2) - F(x_1) - (x_2 - x_1)\, y_1$
3	$F(x_2) - F(x_{p,2}) + (x_{p,2} - x_1)\, y_2 - (x_2 - x_1)\, y_1$
4	$F(x_{p,1}) - F(x_{p,2}) + (x_{p,2} - x_1)\, y_2 - (x_{p,1} - x_1)\, y_1$

Table 2: Computation of the grey area for the four cases in Figure 8.

considered. In order to reach the numerical equilibrium (Equation 2) three conditions are required:

- A perfectly balanced discretization method;
- An accurate methodology for curvature calculation;
- An *exact* initialization of the circular interface.

The Ghost Fluid Method and the Height Functions are used for pressure discretization and curvature calculation. The last point requires a brief discussion.

5.1 Interface initialization

A circular interface at rest has a constant curvature. An equilibrium solution ($\mathbf{v}=\mathbf{0}$) can be reached if the curvature deviations are minimized along the interface, providing a uniform κ value. However, this does not imply that the actual curvature value will be accurate (i.e converging). In fact, mesh convergence towards the exact value is usually not achievable, unless the droplet is *exactly* initialized [49, 50]. This is not a trivial task and many recent works aimed at giving an accurate methodology for general surfaces initialization on polyhedral meshes [51, 52]. In this work we propose a relatively simple methodology, based on the direct integration of the analytical expression $f(x)$ of a

quarter of a circle:

$$f(x) = \sqrt{R^2 - x^2}dx \tag{50}$$

where R is the radius. The following algorithm is implemented for the circle initialization. For each cell in the domain:

- The four vertex coordinates $\mathbf{w}_1(x_1, y_1)$, $\mathbf{w}_2(x_2, y_1)$, $\mathbf{w}_3(x_2, y_2)$, $\mathbf{w}_4(x_1, y_2)$ of the cell are extracted;
- For each vertex $\mathbf{w}_i$ the distance function ψ_i is computed:

$$\psi_i = |\mathbf{w}_i| - R \tag{51}$$

- If all the vertices are inside the droplet ($\psi < 0$), set $\alpha = 1$;
- If all the vertices are outside the droplet ($\psi > 0$), set $\alpha = 0$;
- Otherwise, the cell contains the interface. In this case:
  - Calculate the intersections $x_{p,1}, x_{p,2}, y_{p,1}, y_{p,2}$ of the circle with the cell faces x_1, x_2, y_1, y_2;
  - Depending on the position of the intersections (Figure 8), compute the area delimited by the curve and the cell faces. The integration of 50 is analytical:

$$F(x) = \int_0^x f(x) = \frac{R^2}{2}\left[\frac{x}{R}\sqrt{1 - \left(\frac{x}{R}\right)^2} + asin\left(\frac{x}{R}\right)\right] \tag{52}$$

    The area formulae are reported in Table 2.

This methodology can be rapidly implemented, it is very accurate and does not depend on the mesh adopted. The obvious drawback is the non-generality of the method, only valid for this specific case.

5.2 Test case setup

The droplet diameter is $D = 1$ mm. Density and viscosity are equal for gas and liquid: $\rho = 1\ kg/m^3$, $\mu = 10^{-4}\ Pa \cdot s$. Three surface tension values are used ($\sigma = 0.0012, 0.012, 0.12$ N/m) to obtain three cases at different Laplace numbers $La = 120, 1200, 12000$. As reported by Popinet [9] the velocity scale of the problem regards the capillary waves originated from the droplet:

La	$D/\Delta x$	$\|\mathbf{v}\|_{max}$ [m/s]	Ca
120	10	$6.81 \cdot 10^{-9}$	$5.67 \cdot 10^{-10}$
	20	$7.95 \cdot 10^{-9}$	$6.62 \cdot 10^{-10}$
	40	$5.70 \cdot 10^{-11}$	$4.75 \cdot 10^{-12}$
	100	$9.95 \cdot 10^{-11}$	$8.29 \cdot 10^{-12}$
1200	10	$1.32 \cdot 10^{-9}$	$1.10 \cdot 10^{-11}$
	20	$8.68 \cdot 10^{-9}$	$7.23 \cdot 10^{-11}$
	40	$2.94 \cdot 10^{-8}$	$2.45 \cdot 10^{-10}$
	100	$1.18 \cdot 10^{-8}$	$9.83 \cdot 10^{-11}$
12000	10	$6.70 \cdot 10^{-9}$	$5.58 \cdot 10^{-12}$
	20	$3.14 \cdot 10^{-7}$	$2.62 \cdot 10^{-10}$
	40	$1.48 \cdot 10^{-7}$	$1.23 \cdot 10^{-10}$
	100	$6.36 \cdot 10^{-7}$	$5.30 \cdot 10^{-10}$

Table 3: Spurious currents analysis for the 2D static droplet. Results at $La = 120, 1200, 12000$ and four different droplet resolutions $D/\Delta x = 10, 20, 40, 100$, by means of $L_\infty(\mathbf{v})$ error norm $|\mathbf{v}|_{max}$ and capillary number Ca. Time $t = T_\nu = 0.01$ s.

$$v_\sigma = \sqrt{\frac{\sigma}{\rho D}} \tag{53}$$

while the dissipation of this velocity occurs in a time scale T_ν:

$$T_\nu = \frac{D^2}{\nu} \tag{54}$$

where ν is the kinematic viscosity. In order to test the accuracy of the surface tension implementation it is fundamental to run the test case for a time $t \sim T_\nu$, in order to properly dissipate the initial interface perturbation. The surface tension implementation is explicit and the CFL condition for surface tension driven flows requires a minimum time step size [11] for stability:

$$\Delta t_{min} = \sqrt{\frac{\rho \Delta x^3}{\pi \sigma}} \tag{55}$$

The numerical result are presented in terms the following error norms, for velocity $\mathbf{v}$:

$$L_\infty(\mathbf{v}) = max(|\mathbf{v}|) \tag{56}$$

curvature κ:

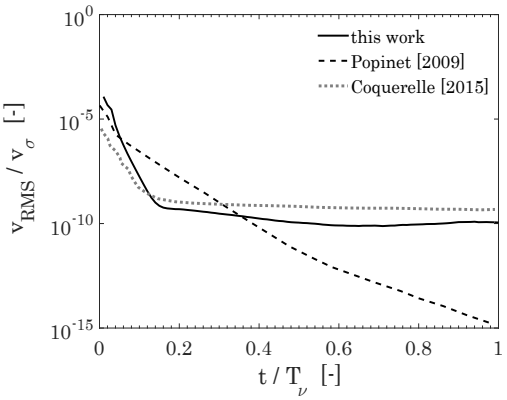

Figure 9: Dimensionless root mean square (RMS) velocity profile over time, for $La = 1200$. Comparison with the results from Popinet [9] and Coquerelle [49].

$$L_\infty(\kappa) = \frac{1}{\kappa_{ex}} max\left(|\kappa_i - \kappa_{ex}|\right) \tag{57}$$

and interface shape:

$$L_2(shape) = \sqrt{\frac{\sum_i (\alpha_i - \alpha_{ex})^2}{\sum_i}} \tag{58}$$

$$L_\infty(shape) = max\left(|\alpha_i - \alpha_{ex}|\right) \tag{59}$$

where α_{ex} is the exact α field from the initialization. The three cases ($La = 120, 1200, 12000$) are run at four different droplet resolutions $\frac{D}{\Delta x} = 10, 20, 40, 100$ to investigate the mesh convergence.

5.3 Spurious currents

Table 3 reports the L_∞ error norm for the velocity field $|\mathbf{v}|_{max}$ and the relative capillary number Ca for the three Laplace numbers (120, 1200, 12000) at four different resolution of the droplet. The residual parasitic currents are extremely low, even reaching the machine precision in some cases. As expected, the $|\mathbf{v}|_{max}$ values are located along the diagonal axis (at $\sim 45°$, where $n_y \sim n_x$) due to the lower accuracy of Height Functions in this region [9]. The capillary number remains well below 10^{-9} and the result do not significantly change further reducing the time step size.

Parasitic currents are also analyzed over time in Figure 9 for $La = 1200$. The RMS velocity is made dimensionless using v_σ, while the dimensionless time τ is referred to

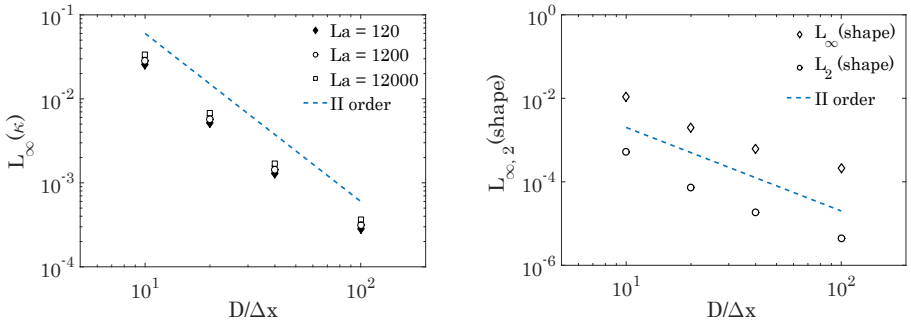

Figure 10: Mesh convergence analysis for the L_∞ error norm for curvature κ (a) at different Laplace numbers. L_∞ and L_2 error norms for shape (b) at $La = 12000$.

T_ν. The RMS velocity initially shows a strong exponential decrease (due to viscous dissipation) followed by a slower one, around the value $\sim 10^{-10}$. The same occurs for all La numbers. The results are between the ones obtained by Popinet [9] and Coquerelle [49] for the same case. Even though parasitic currents do not completely vanish within T_ν, they remain very low and we did not notice any interference with the accuracy of the curvature calculation.

5.4 Mesh convergence

The accuracy of the simulations is assessed by a mesh convergence analysis on the curvature κ and the numerical droplet shape. Results are presented in Figure 10. We observe close to second-order accuracy both for curvature and droplet shape, with a very weak dependence on the Laplace number. The $L_2(\kappa)$ norm (not shown) coincides with $L_\infty(\kappa)$, indicating a very uniform value of the curvature along the interface. Even for coarse resolutions the error values remain very small and comparable to what obtained by other studies [9].

Concerning the velocity field, in Table 3 spurious currents become close to round off errors refining the mesh for $La = 120$. However, we could not recover a similar mesh convergence for $La = 1200$ and $La = 12000$, in which spurious currents slightly increase with mesh refinement. This behavior is not new in literature [55] and apparently tends to occur at high Laplace numbers. To better investigate this aspect we compared our results at $La = 12000$ with other available studies in Figure 11 in terms of capillary number Ca. The works of Desjardins [16], Herrmann [54] and Coquerelle [49] are based on a Level-Set approach and show mesh convergence at different orders (from ~ 1 to $\sim$

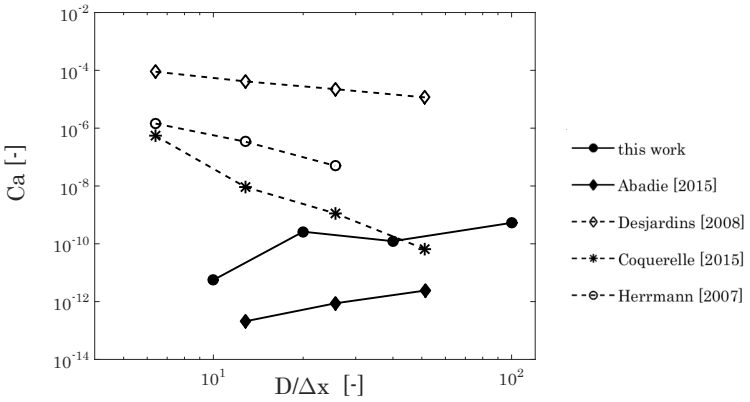

Figure 11: Capillary number convergence with mesh refinement, $La = 12000$. Comparison with the works of Abadie [53], Desjardins [16], Coquerelle [49] and Herrmann [54]. Dashed lines for level-set based methods, solid lines for VOF methods.

3). Abadie [53] instead performed a large comparative study on the effect of the interface advection on surface tension modeling, showing that a combination of a geometric interface reconstruction for VOF (i.e. PLIC) and Height Functions for curvature can actually lead to a non-decreasing velocity error for higher resolutions (Figure 5 in [53], also reported here in Figure 11 for comparison). Similar results have been reached by Popinet and Zaleski comparing front-tracking methods and PLIC/VOF (Figure 6 in [56]). Owkes and Desjardins also show non-converging capillary numbers for a standard mesh-aligned height functions method (Table 1 in [46]). Interestingly, they could avoid this adopting normal-aligned stencil in order to reduce curvature errors (especially when $n_x \sim n_y$), even though the issue seems to persist at high La numbers ($> 10^6$).
As reported by Abadie (Table 1 in [53]), residual spurious currents for VOF methods coupled with Height Functions are most likely due to numerical errors in the advection step rather than inaccurate curvature calculation. Indeed, accurate methods such Height Functions are able to capture small fluctuations of the interface position due to advection errors. In our case `isoAdvector` by Roenby and Jasak [42] is used to reconstruct and advect the interface. The authors report slightly worse results in the advection for low time steps (Co < 0.5) and this was also previously observed by Ubbink and Issa [57]. In our case the time step is controlled by surface tension and it is orders of magnitude lower than the one dictated by the Courant number. Refining the mesh further enhances this effect (since $\Delta t \sim \Delta x^{3/2}$) and we believe it probably introduces additional errors in the advection step. The effect of the interface advection on spurious currents is further analyzed in the next section.

La	$D/\Delta x$	$\lvert\mathbf{v}-\mathbf{v}_0\rvert_{max}$ [m/s]	Ca
120	10	$7.76 \cdot 10^{-3}$	$6.46 \cdot 10^{-4}$
	20	$4.69 \cdot 10^{-3}$	$3.39 \cdot 10^{-4}$
	40	$5.25 \cdot 10^{-3}$	$4.37 \cdot 10^{-4}$
	100	$1.52 \cdot 10^{-2}$	$1.26 \cdot 10^{-3}$
1200	10	$2.55 \cdot 10^{-2}$	$2.10 \cdot 10^{-4}$
	20	$1.88 \cdot 10^{-2}$	$1.56 \cdot 10^{-4}$
	40	$2.31 \cdot 10^{-2}$	$1.92 \cdot 10^{-4}$
	100	$8.80 \cdot 10^{-2}$	$7.33 \cdot 10^{-4}$
12000	10	$8.21 \cdot 10^{-2}$	$6.84 \cdot 10^{-5}$
	20	$6.15 \cdot 10^{-2}$	$5.12 \cdot 10^{-5}$
	40	$1.03 \cdot 10^{-1}$	$8.58 \cdot 10^{-5}$
	100	$4.04 \cdot 10^{-1}$	$3.36 \cdot 10^{-4}$

Table 4: Spurious currents analysis for the 2D translating droplet. Results at $La = 120, 1200, 12000$ and four different droplet resolutions $D/\Delta x = 10, 20, 40, 100$, by means of relative velocity error norm $\lvert\mathbf{v}-\mathbf{v}_0\rvert_{max}$ and capillary number Ca. Time $t = T_U$.

6 Translating droplet

In order to investigate the combined accuracy of the advection scheme, the curvature calculation and surface tension discretization, a droplet subjected to a uniform constant velocity field $\mathbf{v}_0$ is considered, as firstly proposed in [9]. The exact solution in the moving reference frame is the same as for the static case. This test case is much more problematic, since the advection errors directly impact the curvature estimation and therefore the velocity field. The new time scale of the problem is:

$$T_U = \frac{D}{|\mathbf{v}_0|} \tag{60}$$

As for the static droplet test, three Laplace numbers $La = 120, 1200, 12000$ are considered. Gas and liquid properties are unchanged. The velocity is prescribed in the horizontal direction and it is chosen in order to maintain a constant Weber number:

$$We = \frac{\rho|\mathbf{v}_0|^2 D}{\sigma} = 0.4 \tag{61}$$

meaning that for higher surface tensions (i.e. higher La numbers) a stronger velocity field is imposed. We have:

- $|\mathbf{v}_0| = 0.69$ m/s for $La = 120$

- $|\mathbf{v}_0| = 2.19$ m/s for $La = 1200$
- $|\mathbf{v}_0| = 6.93$ m/s for $La = 12000$

The simulations are run for a total time $t = T_U$ at four different droplet resolutions $D/\Delta x = 10, 20, 40, 100$. The capillary number Ca is based on the moving reference frame:

$$Ca = \frac{\mu |\mathbf{v} - \mathbf{v}_0|_{max}}{\sigma} \tag{62}$$

The results are summarized in Table 4. The capillary numbers in this case are 7-8 orders of magnitudes higher than for the static test, clearly indicating that the main spurious currents magnifier is the advection scheme. This is in agreement to what obtained by Abadie (Figure 18 in [53]): in particular for VOF/PLIC/Height Functions methods he shows that the ratio between the capillary number of translating and static droplet can reach up to 10^9, while it is close to unity for level-set based approaches. We also compared the dimensionless RMS velocity profile to Popinet results [9] in Figure 12 (a), showing very similar results: oscillations of frequency $\sim \frac{|\mathbf{v}_0|}{\Delta x}$ and no convergence towards the exact solution. On overall, the maximum error on the relative velocity is below 5% for all the cases, which is usually acceptable for common applications. In Figure 12 (b) the L_∞ norm on the curvature is shown for $La = 12000$. Mesh convergence cannot be reached, both for this work and the results from Popinet [9]. These results underline the need of a tighter coupling between surface tension scheme and interface advection, in order to reach more accurate solutions in more representative cases.

7 Oscillating droplet

A slightly elliptical shape is imposed as initial condition for a 2D liquid droplet, which tends to recover a spherical geometry due to surface tension-induced oscillations. The perturbed surface of the droplet is given in polar coordinates:

$$R(\theta) = R_0 [1 + \epsilon cos(2\theta)] \tag{63}$$

The droplet ($D = 1$ mm) is centered at (0,0) and it is deformed by a factor $\epsilon = 0.04$. The surface tension is $\sigma = 0.07$ N/m, while the density ratio is 100. The viscosity of both fluids is set to zero. The inviscid condition makes the test case more stringent, since spurious currents cannot be limited by a physical viscosity. In fact, oscillations decay is present anyway due to numerical dissipation. The analytical solution for small

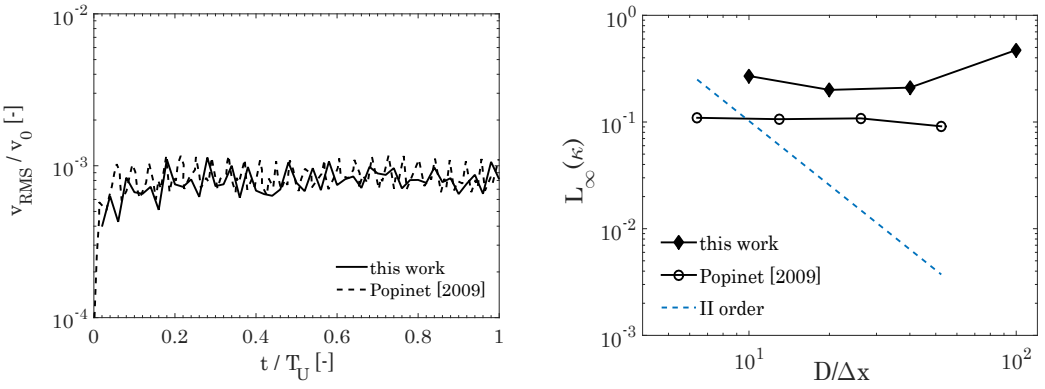

Figure 12: RMS velocity profile over the time (a) and L_∞ error norm on curvature κ (b) for the translating droplet test. Comparison with the results by Popinet [9].

perturbations has been derived by Lamb [58]. The oscillation frequency ω for a 2D droplet is:

$$\omega = \sqrt{\frac{6\sigma}{(\rho_L + \rho_G)\, R^3}} \tag{64}$$

Four droplet resolutions have been adopted $\frac{D}{\Delta x} = 10, 20, 40, 100$. The results are reported in Figure 13 in terms of maximum relative position on the x axis (a) and convergence of the relative error on the oscillation frequency:

$$error = \frac{|\omega - \omega_{ex}|}{\omega_{ex}} \tag{65}$$

where the numerical frequency is averaged over the first three periods.

The oscillation of the interface position is in very good agreement with the analytical solution, reaching an error of $\sim 1\%$ at the finest level. The mesh convergence analysis shows first order convergence on the frequency. The coarse solution suffers from significant numerical diffusion, which is almost totally recovered refining the mesh.

8 Rising bubble

A more complex test case is represented by a gas bubble rising in a dense liquid under the effect of gravity. Analytical solutions are not available for this case and a simple comparison of the bubble shapes with experimental or other numerical works is not

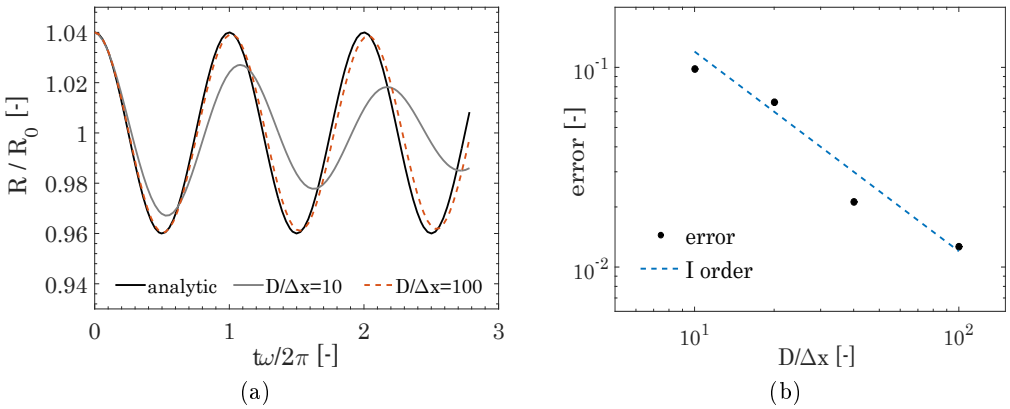

Figure 13: Oscillations of a 2D inviscid liquid droplet (a): comparison between analytical solution (black line) and numerical results on the coarsest (grey line) and finest (dashed line) mesh. Mesh convergence in (b).

Test case	ρ_L	ρ_G	μ_L	μ_G	$\lvert\mathbf{g}\rvert$	σ	Eo
1	1000	100	10	1	0.98	24.5	10

Table 5: Physical parameters for the bubble rising test case.

sufficient to verify the accuracy of the results [10]. Hysing et al. [59] provided an accurate reference solution for this test, adopting different numerical codes under different conditions, representing a valid numerical benchmark for comparison. The domain is [1 x 2] m and the bubble ($D = 0.5$ m) is initially positioned at (0.5, 0.5). The physical parameters are defined in Table 5. The Eotvos number (based on the liquid properties) is defined as:

$$Eo = \frac{\rho_L g D^2}{\sigma} \tag{66}$$

The quantitative results are given in terms of center of mass y_c of the bubble:

$$y_c = \frac{\int_S y dS}{\int_S dS} \tag{67}$$

rising velocity of the bubble v_c:

$$v_c = \frac{\int_S v_y dS}{\int_S dS} \tag{68}$$

and bubble circularity c:

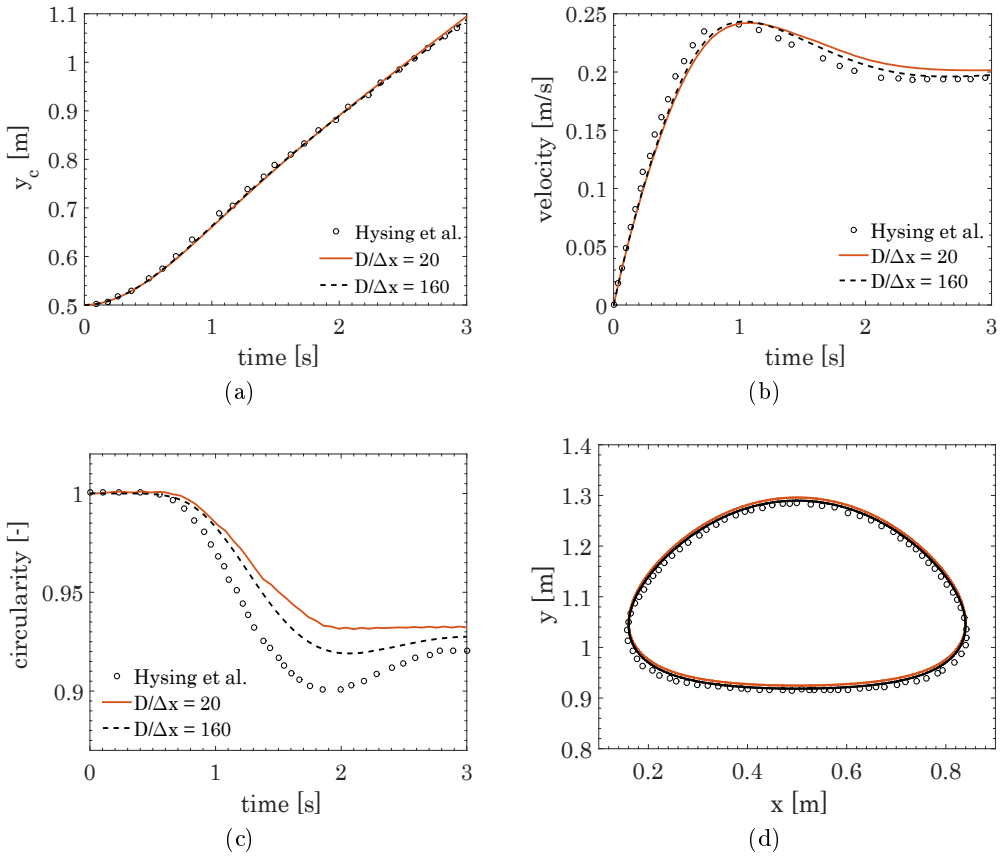

Figure 14: Numerical results for the bubble center of mass y_c (a), rising velocity v_c (b), circularity c (c) and final bubble shape (d) (at $t = 3$ s). Coarsest mesh (orange line) and finest mesh (black line) compared with the reference results from Hysing et al. [59] (circles).

$$c = \frac{\pi D}{p} \tag{69}$$

The bubble perimeter p is calculated as:

$$p = \int_S |\nabla \alpha| dS \tag{70}$$

where S is the planar surface occupied by the bubble. These parameters allow to track the motion of the bubble and to quantitatively evaluate the quality of the numerical results and the comparison with reference numerical works. A mesh convergence analysis is also performed, running the simulations at four different resolutions $D/\Delta x = 20, 40, 80, 160$. The results are presented in Figure 14 and Table 6.
In the work of Hysing et al. [59] three different numerical codes are used to assess the convergence of the results: TP2D (Transport Phenomena in 2D) [60], FreeLIFE (free-Surface Library of Finite Element) [61] and MoonNMD (Mathematics and object-oriented Numerics in MagDeburg) [62]. All of the three codes give almost identical results, therefore only the TP2D code will be used as a comparison in this work. It is based on a finite-element discretization method, adopting a level-set approach for the interface advection. The interface re-initialization (always needed for level-set approaches) is based on the fast marching method, while surface tension is included by a direct integration over the interface contour. The comparison in Figure 14 shows a very good agreement between the results, especially regarding the center of mass of the bubble y_c (a) (almost coincident). The rising velocity v_c (b) in our work shows a slight delay in the maximum value, whereas the terminal velocity (asymptotic value) is well recovered. Most deviations are found in the circularity profile (c), probably due to the difficulty of using Equation 70 to calculate the bubble perimeter: in fact, the bubble shape and position (d) is in excellent agreement with the reference work. It is worth noticing that quite good results are already obtained with the coarsest solution and they further improve with the refinement level.

Table 6 shows the sensitivity of the results to the refinement level and the approximate order of convergence of the main measures. The numerical results converge towards a solution (with orders from $\sim$1 to $\sim$3) which is slightly different from the one obtained by Hysing et al. [59]: while the final bubble position $y_c|_{t=3}$ and the maximum velocity $v_{c,max}$ are very similar, small deviations are present in the other quantities. Similar discrepancies from the reference work have been noticed by Coquerelle et al. [49], especially regarding the minimum in the circularity profile. Nevertheless, we believe the results are satisfactory and in line with the reference work, especially considering the multiple

Measure	$D/\Delta x$				O	Ref. [59]
	20	40	80	160		
c_{min}	0.9313	0.9213	0.9197	0.9190	2.1	0.9012 ± 0.0001
$t\|_{c_{min}}$	2.201	2.103	2.042	2.033	1.8	1.9
$v_{c,max}$	0.2421	0.2424	0.2430	0.2433	1.1	0.2419 ± 0.0002
$t\|_{v_{max}}$	1.079	1.029	1.019	1.018	2.9	$0.921 \leqslant t \leqslant 0.932$
$y_c\|_{t=3}$	1.094	1.088	1.087	1.0879	1.7	1.081 ± 0.001

Table 6: Numerical results at different resolutions for the rising bubble test case. Comparison with the reference results from Hysing et al. [59].

differences in the numerical codes (advection method, discretization approach, surface tension treatment, flow solvers etc.) which makes a complete adherence of the results very difficult.

9 Contact angles

Referring to Figure 15, the contact angle is defined as the angle given by the intersection of the gas-liquid interface with the solid line. This defines a boundary condition for the VOF function, in which at the boundary cell the interface normal must satisfy the contact angle condition. As reported in the introduction, working with interface normals can be dangerous due to the large numerical errors arising from differentiating a discontinuous function. In this work the contact angle boundary condition is implemented as an extension of the Height Functions method for curvature calculation, following the work of Afkhami et al. [28]. The Height Functions method requires three heights h_0, h_1 and h_2 for the curvature calculation. At the boundary cell only two heights are available h_1, h_2, requiring the construction of a "ghost" height h_0 which includes the contact angle condition:

$$h_0 = h_1 + \Delta x tan\theta \tag{71}$$

It is very easy to implement this in `OpenFOAM`®:

1. In pre-processing, if a cell belongs to the boundary a complete stencil cannot be built. Fill the missing column (ghost) with a representative label (e.g. -1);

2. During runtime, if a stencil contains the value -1 it means that the relative cell is at the boundary. Calculate the two available heights as usual, while the remaining

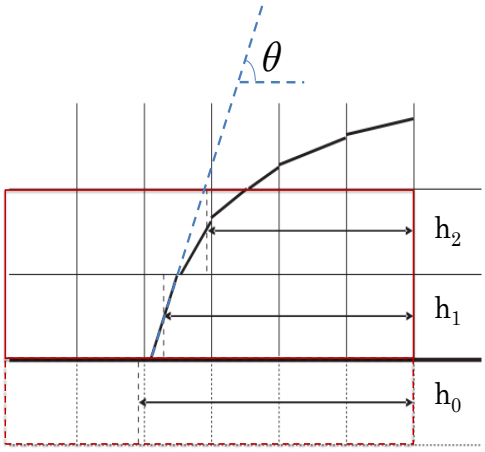

Figure 15: Height functions implementation of the static contact angle.

one as:

```
heights[0] = heights[1]+Deltax*Foam::tan(theta);
```

where `theta` is the assigned contact angle;

3. Once the three heights are available, the curvature at the boundary cell can be easily calculated (Equation 48).

9.1 2D Sessile droplets

A semicircular 2D liquid droplet ($D = 1$ mm, $D/\Delta x = 100$) is placed on a horizontal surface (sessile drop). The contact angle condition (Equation 71) is enforced at the boundary cell curvature calculation. The total simulation time is set to $t = 0.1$ s. The curvature gradient at the boundary induces a flow, deforming the interface until a steady-state condition is reached (in which the curvature is uniform). The resulting circular cap is analyzed by means of apparent radius R, height e, length L and residual spurious currents. The analytical solution is available [41]:

$$R = R_0 \sqrt{\frac{\pi}{2\left(\theta - sin\theta cos\theta\right)}} \tag{72}$$

$$e = R\left(1 - cos\theta\right) \tag{73}$$

$$L = 2Rsin\theta \tag{74}$$

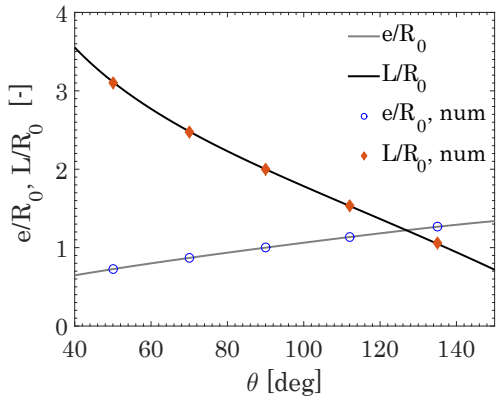

Figure 16: Comparison between analytical and numerical solutions for static droplets contact angles in terms of e/R_0 and L/R_0.

θ $[deg]$	$\lvert\mathbf{v}\rvert_{max}$ [m/s]	Ca
50	$2.2 \cdot 10^{-4}$	$3.14 \cdot 10^{-7}$
70	$2.4 \cdot 10^{-4}$	$3.42 \cdot 10^{-7}$
90	$2.9 \cdot 10^{-4}$	$4.14 \cdot 10^{-7}$
112	$3.2 \cdot 10^{-4}$	$4.57 \cdot 10^{-7}$
135	$3.8 \cdot 10^{-4}$	$5.42 \cdot 10^{-7}$

Table 7: Residual spurious currents for 2D static sessile droplets (Figure 17).

The qualitative results (VOF function) are reported in Figure 17 for different static contact angles θ. The comparison with the analytical solution is very good for both for the e, L parameters (Figure 16). The residual spurious currents and the relative capillary number are reported in Table 7. Compared to the results for the equilibrium of a circular droplet (Table 3) we notice an increase in the capillary number, which however remains under 10^{-6} for all the cases. This has also been reported by Dupont et al. [41].

9.2 Droplet suspension on a vertical fiber

A very stringent test is the suspension of small droplets against the gravity field on a thin vertical fiber, as usually done in many experimental works (Figure 18 a). In this case the contact angle with the solid fiber cannot be fixed, since it depends on multiple factors such as the droplet weight, the fiber geometry, the surface tension etc. For a 2D droplet having a radius R and length L it is possible to derive the equilibrium contact angle with a balance of forces:

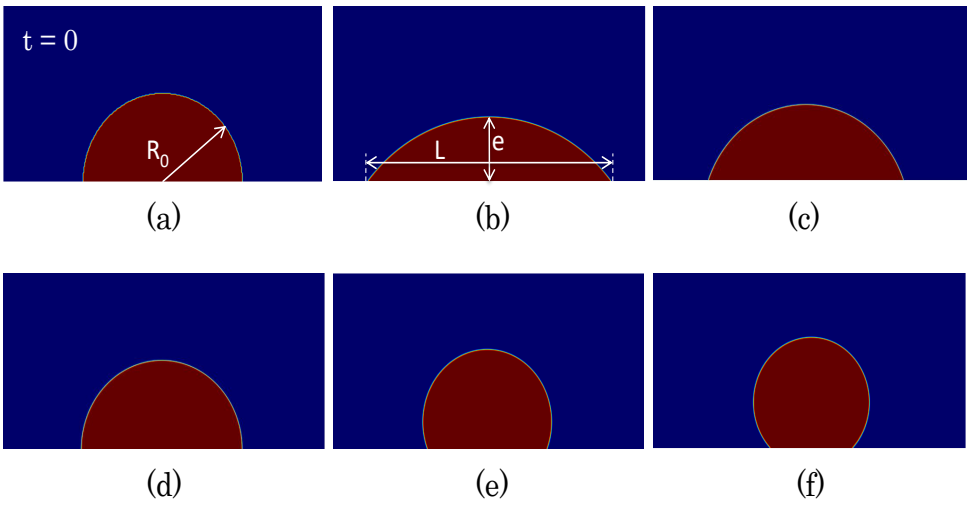

Figure 17: α initial condition for static contact angles analysis (a). Steady-state droplet shapes for $\theta = 50°$ (b), $\theta = 70°$ (c), $\theta = 90°$ (d), $\theta = 112°$ (e) and $\theta = 135°$ (f).

$$\rho_L \pi R^2 L = 2L\sigma cos\theta \tag{75}$$

$$cos\theta = \frac{\rho_L \pi R^2}{2\sigma} \tag{76}$$

As described in the previous section (Figure 15), at the boundary cell we need to find the value of the "ghost height" h_0 that satisfies the contact angle condition (Equation 71). Imposing Equation 76 as a boundary condition is not sufficient, since it is an equilibrium solution which does not account for transient situations (e.g. convective flow around the droplet). In fact, the numerical model should predict the contact angle dynamics depending on the local conditions (droplet weight and shape, surface tension, velocity etc.) and automatically find a steady-state situation independently of Equation 76. Referring to Figure 18 (b), the numerical strategy consists in finding the value of the "ghost height" h_0^* at the boundary cell (point A) *that cancels the local momentum balance* [41]. For each boundary cell cut by the interface:

1. We derive the pressure jump H_f^* which provides $\phi_f = 0$. The reconstructed face flux is given by Equations 32 and 33:

   - if the owner is wet:

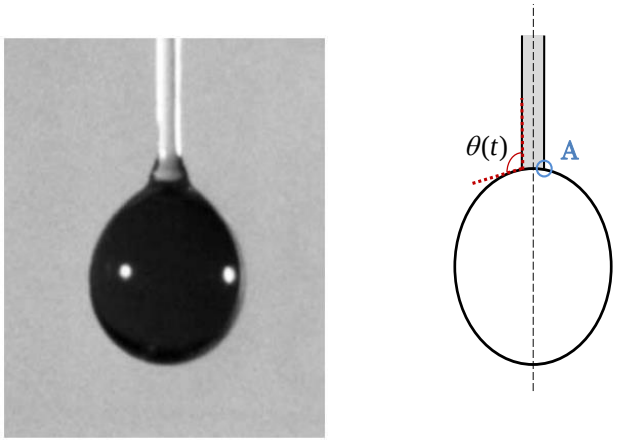

Figure 18: Water droplet suspended on a vertical fiber [63] in Figure (a). Sketch of the same droplet highlighting the dynamic contact angle θ and the contact point A in Figure (b).

$$H_f^* = p_N - p_O - \frac{\frac{\mathbf{H}(\mathbf{v}_N)_f}{a_{P,f}} \cdot \mathbf{S}_f}{\left(\frac{1}{a_P}\right)_f \frac{|\mathbf{S}_f|}{|\mathbf{d}|} \frac{\beta^L \beta^G}{\beta_w}} \tag{77}$$

- if the owner is dry:

$$H_f^* = p_N - p_O - \frac{\frac{\mathbf{H}(\mathbf{v}_N)_f}{a_{P,f}} \cdot \mathbf{S}_f}{\left(\frac{1}{a_P}\right)_f \frac{|\mathbf{S}_f|}{|\mathbf{d}|} \frac{\beta^L \beta^G}{\beta_d}} \tag{78}$$

In `OpenFOAM`®:

```
Jump.ref()[facei]= p.ref()[neighbour[facei]]-p.ref()[owner[facei]]
-phiHbyA.ref()[facei]/laplacian.upper()[facei];
```

where the surfaceScalarField `phiHbyA` $= \frac{\mathbf{H}(\mathbf{v}_N)_f}{a_{P,f}} \cdot \mathbf{S}_f$;

2. We calculate the value of the face-centered curvature κ^* which provides an interfacial jump equal to H_f^* (Equation 19):

$$\kappa^* = \frac{H_f^* + (\rho_L - \rho_G)\, \mathbf{g} \cdot \mathbf{x}_f}{\sigma} \tag{79}$$

In `OpenFOAM`®:

```
if (alpha1.ref()[owner[facei]] > 0.5)
double curvature = (Jump.ref()[facei]-
(rhoL-rhoG)*(g.value() & interfacePosition.ref()[facei]))/
surfaceTension.ref()[facei];

else
double curvature = -(Jump.ref()[facei]+
(rhoL-rhoG)*(g.value() & interfacePosition.ref()[facei]))/
surfaceTension.ref()[facei];
```

The face-centered value `curvature` is then assigned to both the owner and the neighbour of the interfacial face `facei`;

3. The value of the "ghost" height h_0^* is obtained by solving the following non-linear algebraic equation:

$$\kappa^* - \frac{\frac{h_2 - 2h_1 + h_0^*}{\Delta x^2}}{\left(1 + \left(\frac{h_2 - h_0^*}{2\Delta x}\right)^2\right)^{3/2}} = 0 \tag{80}$$

4. Finally, the contact angle can be easily derived as:

$$\theta^* = atan\left(\frac{h_0^* - h_1}{\Delta x}\right) \tag{81}$$

It is important to specify that only Equations 77, 78 are necessary for the method to work, since the jump H_f^* the only information actually used by the GFM method. Equations 79, 80 and 81 are however useful to know the value of θ^* that cancels the momentum balance, which can be compared with the theoretical prediction.

This is an iterative procedure, since the interfacial jump H_f^* is derived explicitly, adopting the pressure field of the previous time step (Equations 77 and 78). Multiple iterations of the Poisson equation are needed to find the correct pressure field that cancels the local momentum balance. However, we noticed that a single iteration is actually enough for the procedure to work. The actual face flux ϕ_f is slightly different from zero, but it tends to cancel over time. This allows to save significant computational time, avoiding the iterations.

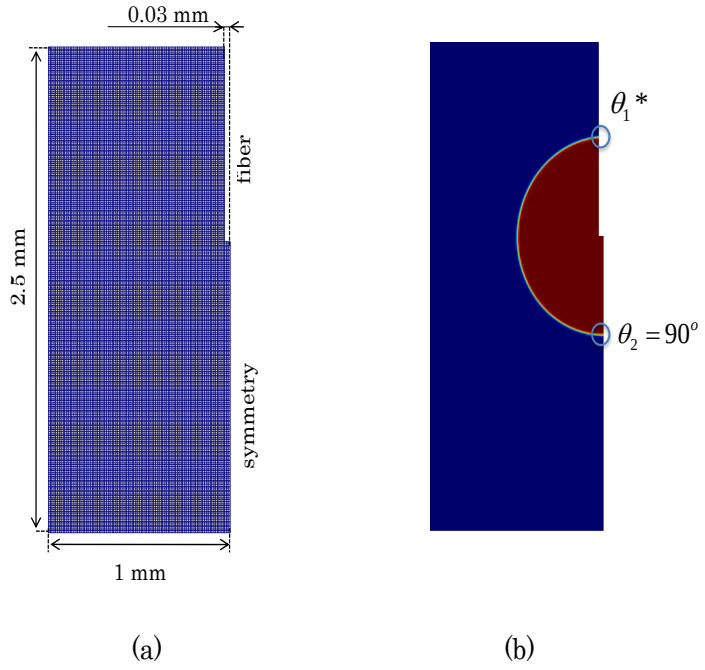

Figure 19: 2D computational mesh used for suspended droplets simulations (a). VOF initial condition (b) for the droplet, with boundary conditions for contact angles.

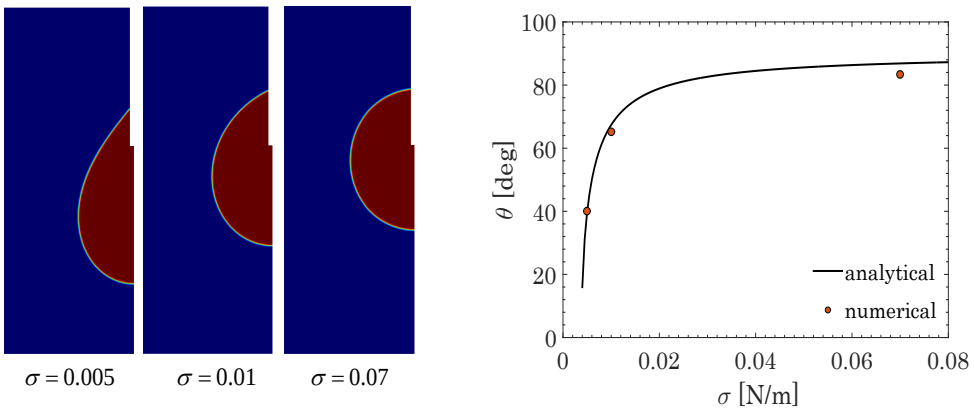

(a) (b)

Figure 20: Comparison between analytical and numerical solutions for 2D suspended droplets contact angles at different surface tension values. Steady-state condition.

9.2.1 2D droplet suspension

To validate the method, a 2D liquid droplet ($D = 1$ mm, $\rho_L = 1000\ kg/m^3$) is placed on a thin vertical fiber as shown in Figure 19. Only half of the droplet is modeled due to symmetry conditions. At the symmetry boundary the contact angle is imposed equal to $\theta_2 = 90°$ (using the method reported for the sessile droplets). The fiber boundary is a wall, where a `noSlip` condition apply for velocity. On this boundary, the contact angle θ_1^* is calculated as jjust described in this section. The other boundaries are open. Three different surface tension values have been adopted ($\sigma = 0.005, 0.01, 0.07$ N/m) and the numerical results are compared with the analytical solution given by Equation 76. The results are reported in Figure 20.

As expected, lower surface tensions provide a more deformed droplet shape. The contact point is not perfectly fixed due to the choice of avoid multiple iteration within the same time step. This is especially true for the lowest surface tension case ($\sigma = 0.005$ N/m), because of the longer dynamics needed to reach the steady-state condition. The agreement with the theoretical prediction is good, with a slight deviation for $\sigma = 0.07$ N/m. In Table 8 the residual spurious currents are reported, showing results comparable to the sessile droplets cases.

9.2.2 2D axisymmetric droplet suspension

The axisymmetric geometry is often used to save computational time with respect to full 3D simulations. In particular, suspended droplets usually exhibit axisymmetric geometry

σ [N/m]	$\|\mathbf{v}\|_{max}$ [m/s]	Ca
0.005	$6.1 \cdot 10^{-4}$	$1.2 \cdot 10^{-5}$
0.01	$3.4 \cdot 10^{-4}$	$3.4 \cdot 10^{-6}$
0.07	$4.3 \cdot 10^{-5}$	$6.1 \cdot 10^{-7}$

Table 8: Residual spurious currents for 2D suspended droplets (Figure 20).

if a vertical support fiber is adopted. From the theoretical and numerical points of view, the only difference is that a second curvature must be accounted for (perpendicular to the interface and to the plane containing the droplet). This is easily calculated from the 2D heights already available [64]:

$$\kappa_2 = \frac{1}{|\mathbf{x}|\sqrt{1+h'^2}} \tag{82}$$

where $\mathbf{x}$ is the distance of the interface perpendicularly to the symmetry axis. The interface position is defined by the exact location of the height, which must be used to compute $|\mathbf{x}|$. Therefore:

- if a vertical stencil is adopted for the cell (i,j):

$$|\mathbf{x}| = x_{i,j} \tag{83}$$

- if a horizontal stencil is adopted for the cell (i,j):

$$|\mathbf{x}| = x_{i,j} - 3.5\Delta x + h_i \tag{84}$$

  where $x_{i,j}$ is the x coordinate of the interfacial cell center.

At the cell (i,j) the total curvature $\kappa_{i,j}$ is then the sum of the two principal curvatures:

$$\kappa_{i,j} = \frac{h''_{i,j}}{\left(1+h'^2_{i,j}\right)^{3/2}} + \frac{1}{|\mathbf{x}|\sqrt{1+h'^2_{i,j}}} \tag{85}$$

This second curvature represents an additional contribution to the pressure jump, which is then handled by the GFM. All the treatment of the contact angles remains the same. The only difference is that Equation 80 becomes:

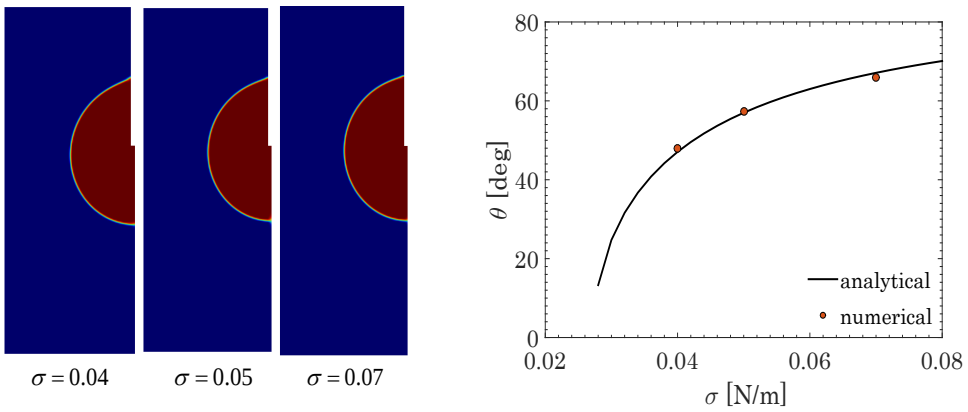

(a) (b)

Figure 21: Comparison between analytical and numerical solutions for 2D axisymmetric suspended droplets contact angles at different surface tension values. Steady state condition.

$$\kappa^* - \frac{\frac{h_2-2h_1+h_0^*}{\Delta x^2}}{\left(1+\left(\frac{h_2-h_0^*}{2\Delta x}\right)^2\right)^{3/2}} - \frac{1}{|\mathbf{x}|\sqrt{1+\left(\frac{h_2-h_0^*}{2\Delta x}\right)^2}} = 0 \tag{86}$$

in order to account for the second curvature. The theoretical value of the contact angle for 2D axisymmetric droplets (or 3D ones) can be easily derived by a balance of forces on the suspended droplet:

$$\frac{4}{3}\pi R^3 \rho_L = \sigma \pi d_F cos\theta \tag{87}$$

where d_F is the fiber diameter. We obtain:

$$cos\theta = \frac{4\rho_L g R^3}{3\sigma d_F} \tag{88}$$

We repeat the same test done for 2D droplets, suspending 2D axisymmetric droplets on a vertical fiber for different surface tension values ($\sigma = 0.04, 0.05, 0.07$ N/m). The computational mesh in Figure 19 (a) remains the same, but the symmetry plane is collapsed into a symmetry axis. In this configuration the new domain is a slice of a cylinder with a thin vertical cylindrical fiber on the axis on which the droplet is suspended. The results are reported in Figure 21 and Table 9.

The droplet deformation is now much less evident and only localized close to the contact point. The agreement with the theoretical value is satisfactory for all the three

σ [N/m]	$\|\mathbf{v}\|_{max}$ [m/s]	Ca
0.04	$1.1 \cdot 10^{-4}$	$2.7 \cdot 10^{-7}$
0.05	$6.5 \cdot 10^{-5}$	$1.3 \cdot 10^{-7}$
0.07	$6.6 \cdot 10^{-4}$	$9.4 \cdot 10^{-7}$

Table 9: Residual spurious currents for 2D axisymmetric droplets (Figure 21).

cases. The residual spurious currents are comparable to what obtained for the 2D droplet suspension.

10 Conclusions

In this work we presented an accurate methodology for the modeling of surface tension driven flows in the `OpenFOAM`® framework. The Ghost Fluid Method (GFM) is implemented for the numerical discretization of the pressure equation, including the jump due to surface tension and gravity, while the cell-centered values of the curvature are evaluated adopting Height Functions. The methodology shows a significant reduction of spurious currents for a 2D stationary droplet, close to machine accuracy. The curvature and the interface shape show second order convergence towards the exact solution, with a weak dependence on the Laplace number. The capillary number does not always converge with mesh refinement, especially at high Laplace numbers, probably due to the sensitivity of Height Functions to errors in the interface advection. This is confirmed by the translating droplet test case, which clearly indicates the interface advection as the main spurious currents magnifier rather than the curvature calculation errors, in line to what reported by other authors.
The methodology is also tested to analyze (i) capillary oscillations in a perturbed liquid droplet, exhibiting first order convergence on the frequency value and (ii) a bubble rising in a dense fluid, showing excellent agreement with the reference numerical solution in terms of bubble position, rising velocity and interface shape. Finally, the Height Functions method is extended for the modeling of contact angles, with applications to sessile droplets and suspended droplets, both in 2D and 2D axisymmetric configurations. The agreement with the theoretical solution is satisfactory.
Future works will focus on the extension of the methodology to variable fluid properties and the implementation of phase-change.

Acknowledgments

We acknowledge the CINECA award under the ISCRA initiative, for the availability of high performance computing resources and support.

This following appendix is not part of the submitted paper, but it is worth including them in this manuscript to better support the numerical methodology of the work.

Appendix A The centripetal force

In the three previous papers surface tension was not modeled, due to (i) the very limited capability of `OpenFOAM`® to deal with surface tension driven flows and the (ii) detrimental effect that spurious currents have on the dynamics of small droplets, especially when evaporating. Hence, a centripetal force $\mathbf{f}_m$ has been introduced to suspend the droplet against gravity (Paper 1):

$$\mathbf{f}_m = \rho\alpha\nabla\xi \tag{89}$$

where:

$$\xi = \xi_0 \frac{R_f}{r} \tag{90}$$

where ξ_0 is the force intensity and R_f the fiber radius. The introduction of this centripetal force may impact the droplet physics, in particular:

- The droplet shape;
- The internal circulation.

The indirect effect is on the internal heat transfer (due to convection in the liquid phase) and, hence, on the vaporization rate. The effect of the droplet shape has been analyzed in Paper 1, showing that, for small droplets (the ones of our interest), the shape does not significantly differ from a spherical one. We also found that the impact of the intensity of the centripetal force on the vaporization rate was very limited, indicating a negligible effect of the force field on the internal convection.

The aim of this work (Paper 4) was to overcome this issue and an accurate methodology for surface tension was developed and successfully tested in a wide range of static

and dynamic conditions. Given the results of this work, the effect of the centripetal force can be analyzed more in detail by the direct comparison of (i) droplets suspended with the centripetal force and (ii) droplets suspended with surface tension. To this purpose, we simulated the dynamics of a droplet suspended on a vertical fiber and immersed in an upward convective field. Three different velocities of the gas-phase are adopted: (i) $v = 0.1$ m/s, (ii) $v = 0.2$ m/s and (iii) $v = 0.5$ m/s (to cover the typical convective velocities of our interests). For each case the droplet is suspended by the following forces:

- Centripetal force, with intensities ξ_0:
  - $\xi_0 = 0.5$;
  - $\xi_0 = 1$;
  - $\xi_0 = 2$;
- Surface tension ($\sigma = 0.05$ N/m);

The convective field induces an internal circulation with a structure similar to a Hill's vortex. The results are reported in Figure 22 in terms of internal velocity field. We assume the cases with surface tension (a, e, i) to be *exact*, working as a benchmark for comparison with the other simulations. The maximum velocity in the liquid phase is one order of magnitude lower than the one in the gas-phase, in agreement with the work of Sirignano [2]. Both suspension methods (surface tension and centripetal force) correctly reproduce the structure of the Hill's vortex for all the external velocities. No significant difference is noticeable between the two suspension methods in terms of velocity magnitude and there is a very low sensitivity to the intensity of the centripetal force. Some differences from the exact case (i.e. with surface tension) can be noticed for $v = 0.1$ m/s (b-d), probably due to the very low induced internal velocity which makes it more sensitive to the centripetal force. From this analysis it is clear that the adoption of very low intensity of the centripetal force (b, f, j) is the best way to ensure a qualitatively and quantitatively good results with respect to the exact case, since the internal velocity field would be mainly subjected to the interface shear stress. This is confirmed in Figure 23 where the internal mean velocity magnitude is reported in time for all the cases. After an initial transition period (in which the droplet is stabilizing), the steady-state condition shows a constant mean velocity for all the cases, slightly higher for the cases suspended with the centripetal force. Again, no appreciable difference is detected using different intensities ξ_0 to suspend the droplet.
The overall effect on the evaporation rate was shown in Paper 1, in which the adoption of

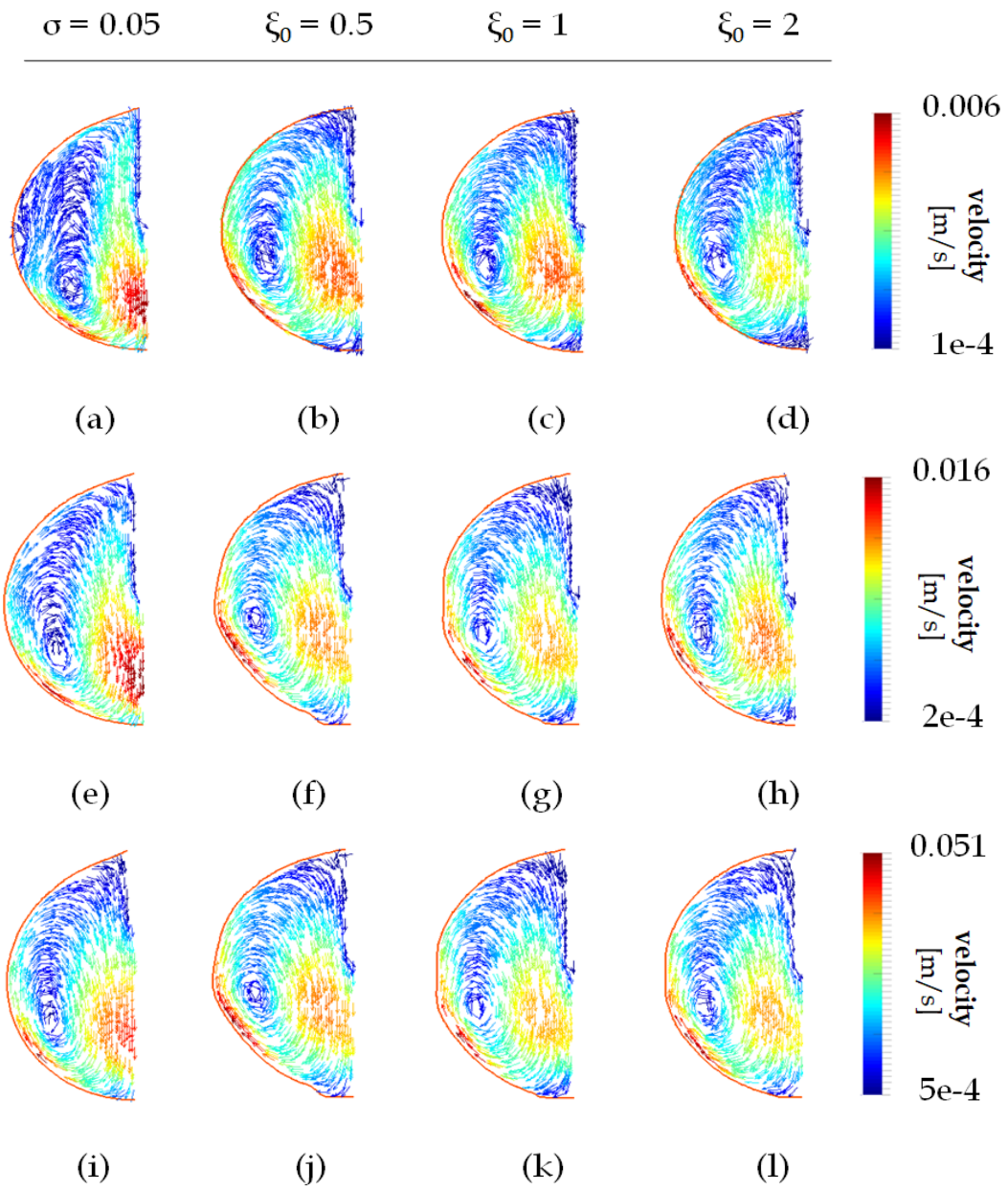

Figure 22: Internal circulation of a droplet suspended with surface tension (a, e, i) and centripetal force at different intensities. Three gas-phase convective velocities $v = 0.1$ (a-d), $v = 0.2$ (e-h) $v = 0.5$ (i-l) m/s. Time $t = 1$ s.

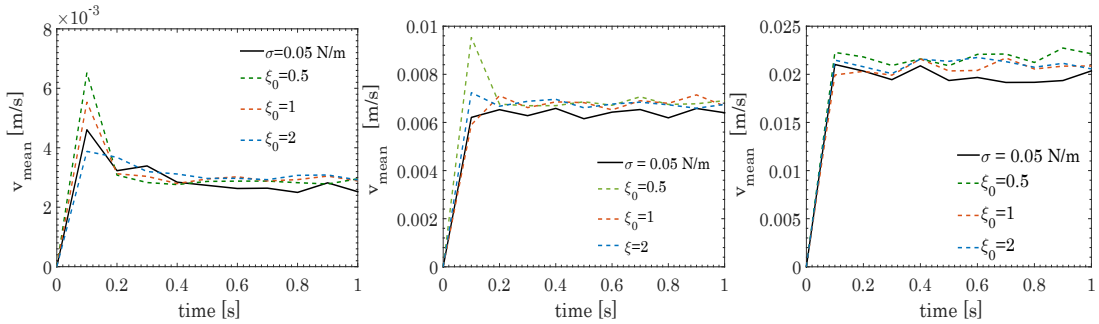

Figure 23: Mean velocity in the liquid phase for external convective velocities $v = 0.1$ (a), $v = 0.2$ (b) $v = 0.5$ (c) m/s.

the extreme values of the intensity ξ_0 (the minimum needed to suspend the droplet and the maximum which provided a perfectly spherical droplet) showed only a very limited difference in the evaporation rate. This leads to the conclusion that, even with different values of ξ_0, the internal heat transfer remains much faster than the gas-phase heat transfer and does not represent a rate determining step. It is clear, however, that in order to better represent the physics of the problem in terms of the internal velocity field structure, the best option is to adopt *the minimum value* of ξ_0 needed to suspend the droplet. The only minor drawback is a "more dynamic" transition period (Figure 23) required from the droplet to find a steady-state shape, which is less evident for high ξ_0 values that tend to stabilize the droplet.

Nomenclature

Acronyms

CSF Continuum Surface Force

GFM Ghost Fluid Method

PLIC Piecewise Linear Interface Calculation

RMS Root Mean Square

VOF Volume Of Fluid

Greek letters

α VOF marker function [–]

β reciprocal of density $\left[\frac{m^3}{kg}\right]$

$\Delta x, y$ cell size $[m]$

δ_s Dirac delta $\left[\frac{1}{m}\right]$

ϵ deformation factor $[-]$

κ curvature $\left[\frac{1}{m}\right]$

λ relative position of the interface $[-]$

μ dynamic viscosity $\left[\frac{kg}{ms}\right]$

ν kinematic viscosity $[m/s^2]$

ω frequency $\left[s^{-1}\right]$

ϕ velocity face flux $\left[m^3/s\right]$

ψ distance $[m]$

ρ density $\left[\frac{kg}{m^3}\right]$

σ surface tension $\left[\frac{N}{m}\right]$

θ angle [degree, rad]

Θ_s Heaviside function $[-]$

Roman letters

$\mathbf{d}$ distance vector $[m]$

$\mathbf{g}$ gravitational acceleration $\left[\frac{m}{s^2}\right]$

$\mathbf{n}$ interface normal $[-]$

$\mathbf{S}$ surface vector $\left[m^2\right]$

$\mathbf{v}$ velocity $\left[\frac{m}{s}\right]$

$\mathbf{w}$ vertex position vector $[m]$

$\mathbf{x}$ position vector $[m]$

c circularity $[-]$

Ca capillary number $[-]$

D diameter $[m]$

Eo Eotvos number $[-]$

F integral function

H total pressure jump $[Pa]$

h height $[m]$

L error norm

La Laplace number $[-]$

p perimeter $[m]$

p pressure $[Pa]$

p_d dynamic pressure $[Pa]$

R radius $[m]$

T time scale $[s]$

t time $[s]$

v_σ capillary wave velocity $[m/s]$

We Weber number $[-]$

Subscripts

0 initial, reference

d dry

ex exact

f face-centered value

G gas

L liquid

N neighbour

O owner

P cell-centered value

s smoothed

w wet

References

[1] B. Abramzon, W. Sirignano, Droplet vaporization model for spray combustion calculations, International Journal of Heat and Mass Transfer 32 (9) (1989) 1605–1618.

[2] W. A. Sirignano, Fluid dynamics and transport of droplets and sprays, Cambridge university press, 1999.

[3] D. Juric, G. Tryggvason, Computations of boiling flows, International journal of multiphase flow 24 (3) (1998) 387–410.

[4] C. Delale, S. Nas, G. Tryggvason, Direct numerical simulations of shock propagation in bubbly liquids, Physics of Fluids 17 (12) (2005) 121705.

[5] C. W. Hirt, B. D. Nichols, Volume of fluid (VOF) method for the dynamics of free boundaries, Journal of computational physics 39 (1) (1981) 201–225.

[6] M. Sussman, E. Fatemi, P. Smereka, S. Osher, An improved level set method for incompressible two-phase flows, Computers & Fluids 27 (5-6) (1998) 663–680.

[7] G. Tryggvason, B. Bunner, A. Esmaeeli, D. Juric, N. Al-Rawahi, W. Tauber, J. Han, S. Nas, Y.-J. Jan, A front-tracking method for the computations of multiphase flow, Journal of Computational Physics 169 (2) (2001) 708–759.

[8] M. M. Francois, S. J. Cummins, E. D. Dendy, D. B. Kothe, J. M. Sicilian, M. W. Williams, A balanced-force algorithm for continuous and sharp interfacial surface tension models within a volume tracking framework, Journal of Computational Physics 213 (1) (2006) 141–173.

[9] S. Popinet, An accurate adaptive solver for surface-tension-driven interfacial flows, Journal of Computational Physics 228 (16) (2009) 5838–5866.

[10] S. Popinet, Numerical models of surface tension, Annual Review of Fluid Mechanics 50 (2018) 49–75.

[11] J. Brackbill, D. B. Kothe, C. Zemach, A continuum method for modeling surface tension, Journal of computational physics 100 (2) (1992) 335–354.

[12] R. P. Fedkiw, T. Aslam, B. Merriman, S. Osher, A non-oscillatory eulerian approach to interfaces in multimaterial flows (the ghost fluid method), Journal of computational physics 152 (2) (1999) 457–492.

[13] R. P. Fedkiw, T. Aslam, S. Xu, The ghost fluid method for deflagration and detonation discontinuities, Journal of Computational Physics 154 (2) (1999) 393–427.

[14] X.-D. Liu, R. P. Fedkiw, M. Kang, A boundary condition capturing method for poisson's equation on irregular domains, Journal of computational Physics 160 (1) (2000) 151–178.

[15] E. Olsson, G. Kreiss, A conservative level set method for two phase flow, Journal of computational physics 210 (1) (2005) 225–246.

[16] O. Desjardins, V. Moureau, H. Pitsch, An accurate conservative level set/ghost fluid method for simulating turbulent atomization, Journal of Computational Physics 227 (18) (2008) 8395–8416.

[17] W. Bo, J. W. Grove, A volume of fluid method based ghost fluid method for compressible multi-fluid flows, Computers & Fluids 90 (2014) 113–122.

[18] V. Vukčević, H. Jasak, I. Gatin, Implementation of the ghost fluid method for free surface flows in polyhedral finite volume framework, Computers & Fluids 153 (2017) 1–19.

[19] B. Lalanne, L. R. Villegas, S. Tanguy, F. Risso, On the computation of viscous terms for incompressible two-phase flows with level set/ghost fluid method, Journal of Computational Physics 301 (2015) 289–307.

[20] M. Kang, R. P. Fedkiw, X.-D. Liu, A boundary condition capturing method for multiphase incompressible flow, Journal of Scientific Computing 15 (3) (2000) 323–360.

[21] M. Sussman, K. M. Smith, M. Y. Hussaini, M. Ohta, R. Zhi-Wei, A sharp interface method for incompressible two-phase flows, Journal of computational physics 221 (2) (2007) 469–505.

[22] S. J. Cummins, M. M. Francois, D. B. Kothe, Estimating curvature from volume fractions, Computers & structures 83 (6-7) (2005) 425–434.

[23] M. Williams, D. Kothe, E. Puckett, Accuracy and convergence of continuum surface tension models, Fluid dynamics at interfaces (1998) 294–305.

[24] G. Tryggvason, R. Scardovelli, S. Zaleski, Direct numerical simulations of gas–liquid multiphase flows, Cambridge University Press, 2011.

[25] G. Bornia, A. Cervone, S. Manservisi, R. Scardovelli, S. Zaleski, On the properties and limitations of the height function method in two-dimensional cartesian geometry, Journal of Computational Physics 230 (4) (2011) 851–862.

[26] R. Chiodi, O. Desjardins, A reformulation of the conservative level set reinitialization equation for accurate and robust simulation of complex multiphase flows, Journal of Computational Physics 343 (2017) 186–200.

[27] E. Marchandise, P. Geuzaine, N. Chevaugeon, J.-F. Remacle, A stabilized finite element method using a discontinuous level set approach for the computation of bubble dynamics, Journal of Computational Physics 225 (1) (2007) 949–974.

[28] S. Afkhami, M. Bussmann, Height functions for applying contact angles to 2d vof simulations, International journal for numerical methods in fluids 57 (4) (2008) 453–472.

[29] C. Huh, L. Scriven, Hydrodynamic model of steady movement of a solid/liquid/fluid contact line, Journal of colloid and interface science 35 (1) (1971) 85–101.

[30] S. Afkhami, S. Zaleski, M. Bussmann, A mesh-dependent model for applying dynamic contact angles to vof simulations, Journal of computational physics 228 (15) (2009) 5370–5389.

[31] S. Wang, O. Desjardins, 3d numerical study of large-scale two-phase flows with contact lines and application to drop detachment from a horizontal fiber, International Journal of Multiphase Flow 101 (2018) 35–46.

[32] M. Renardy, Y. Renardy, J. Li, Numerical simulation of moving contact line problems using a volume-of-fluid method, Journal of Computational Physics 171 (1) (2001) 243–263.

[33] C. J. Greenshields, OpenFOAM user guide, OpenFOAM Foundation Ltd, version 3 (1).

[34] M. Aboukhedr, A. Georgoulas, M. Marengo, M. Gavaises, K. Vogiatzaki, Simulation of micro-flow dynamics at low capillary numbers using adaptive interface compression, Computers & Fluids 165 (2018) 13–32.

[35] A. Q. Raeini, M. J. Blunt, B. Bijeljic, Modelling two-phase flow in porous media at the pore scale using the volume-of-fluid method, Journal of Computational Physics 231 (17) (2012) 5653–5668.

[36] A. Ferrari, M. Magnini, J. R. Thome, A flexible coupled level set and volume of fluid (flexclv) method to simulate microscale two-phase flow in non-uniform and unstructured meshes, International Journal of Multiphase Flow 91 (2017) 276–295.

[37] A. Albadawi, D. Donoghue, A. Robinson, D. Murray, Y. Delauré, Influence of surface tension implementation in volume of fluid and coupled volume of fluid with level set methods for bubble growth and detachment, International Journal of Multiphase Flow 53 (2013) 11–28.

[38] S. S. Deshpande, L. Anumolu, M. F. Trujillo, Evaluating the performance of the two-phase flow solver interfoam, Computational science & discovery 5 (1) (2012) 014016.

[39] F. Jamshidi, H. Heimel, M. Hasert, X. Cai, O. Deutschmann, H. Marschall, M. Wörner, On suitability of phase-field and algebraic volume-of-fluid openfoam® solvers for gas–liquid microfluidic applications, Computer Physics Communications 236 (2019) 72–85.

[40] A. Saufi, A. Frassoldati, T. Faravelli, A. Cuoci, DropletSMOKE++: A comprehensive multiphase CFD framework for the evaporation of multidimensional fuel droplets, International Journal of Heat and Mass Transfer 131 (2019) 836–853.

[41] J.-B. Dupont, D. Legendre, Numerical simulation of static and sliding drop with contact angle hysteresis, Journal of Computational Physics 229 (7) (2010) 2453–2478.

[42] J. Roenby, H. Bredmose, H. Jasak, A computational method for sharp interface advection, Royal Society open science 3 (11) (2016) 160405.

[43] S. M. Damián, An extended mixture model for the simultaneous treatment of short and long scale interfaces, Ph.D. thesis, Universidad Nacional Del Litoral. Facultad de Ingenieria y Ciencias Hidricas (2013).

[44] H. Jasak, Error analysis and estimation for the finite volume method with applications to fluid flows.

[45] M. Sussman, M. Ohta, Improvements for calculating two-phase bubble and drop motion using an adaptive sharp interface method, Fluid Dyn. Mater. Process 3 (1) (2007) 21–36.

[46] M. Owkes, O. Desjardins, A mesh-decoupled height function method for computing interface curvature, Journal of Computational Physics 281 (2015) 285–300.

[47] Y. Renardy, M. Renardy, Prost: a parabolic reconstruction of surface tension for the volume-of-fluid method, Journal of computational physics 183 (2) (2002) 400–421.

[48] I. Ginzburg, G. Wittum, Two-phase flows on interface refined grids modeled with vof, staggered finite volumes, and spline interpolants, Journal of Computational Physics 166 (2) (2001) 302–335.

[49] M. Coquerelle, S. Glockner, A fourth-order accurate curvature computation in a level set framework for two-phase flows subjected to surface tension forces, Journal of Computational Physics 305 (2016) 838–876.

[50] J. López, C. Zanzi, P. Gómez, R. Zamora, F. Faura, J. Hernández, An improved height function technique for computing interface curvature from volume fractions, Computer methods in applied mechanics and engineering 198 (33-36) (2009) 2555–2564.

[51] S. Bnà, S. Manservisi, R. Scardovelli, P. Yecko, S. Zaleski, Numerical integration of implicit functions for the initialization of the vof function, Computers & Fluids 113 (2015) 42–52.

[52] S. Bnà, S. Manservisi, R. Scardovelli, P. Yecko, S. Zaleski, Vofi—a library to initialize the volume fraction scalar field, Computer Physics Communications 200 (2016) 291–299.

[53] T. Abadie, J. Aubin, D. Legendre, On the combined effects of surface tension force calculation and interface advection on spurious currents within volume of fluid and level set frameworks, Journal of Computational Physics 297 (2015) 611–636.

[54] M. Herrmann, A balanced force refined level set grid method for two-phase flows on unstructured flow solver grids, Journal of computational physics 227 (4) (2008) 2674–2706.

[55] D. J. Harvie, M. Davidson, M. Rudman, An analysis of parasitic current generation in volume of fluid simulations, Applied mathematical modelling 30 (10) (2006) 1056–1066.

[56] S. Popinet, S. Zaleski, A front-tracking algorithm for accurate representation of surface tension, International Journal for Numerical Methods in Fluids 30 (6) (1999) 775–793.

[57] O. Ubbink, R. Issa, A method for capturing sharp fluid interfaces on arbitrary meshes, Journal of Computational Physics 153 (1) (1999) 26–50.

[58] H. Lamb, Hydrodynamics, Dover Publications, New York, 1945.

[59] S.-R. Hysing, S. Turek, D. Kuzmin, N. Parolini, E. Burman, S. Ganesan, L. Tobiska, Quantitative benchmark computations of two-dimensional bubble dynamics, International Journal for Numerical Methods in Fluids 60 (11) (2009) 1259–1288.

[60] S. Turek, Efficient Solvers for Incompressible Flow Problems: An Algorithmic and Computational Approache, Vol. 6, Springer Science & Business Media, 1999.

[61] N. Parolini, Computational fluid dynamics for naval engineering problems, Tech. rep., EPFL (2004).

[62] V. John, G. Matthies, Moonmd–a program package based on mapped finite element methods, Computing and Visualization in Science 6 (2-3) (2004) 163–170.

[63] D. Walton, The evaporation of water droplets. a single droplet drying experiment, Drying technology 22 (3) (2004) 431–456.

[64] C. Pozrikidis, J. H. Ferziger, Introduction to theoretical and computational fluid dynamics, Physics Today 50 (1997) 72.

Part III

Conclusions

Conclusions

In this thesis work we presented a multiphase CFD framework for the modeling of isolated droplets. The solver (called `DropletSMOKE++`) accounts for the presence of external flow and for the influence of a gravity field, allowing to numerically model the evaporation and combustion of isolated droplets in convective conditions.

We can summarize the main novelties of the work in three points:

1. The first point is the development of a general and complex numerical model for isolated droplet combustion, based on an interface-resolved approach (VOF methodology). This allows to describe in detail the (i) interface transport and (ii) the flow field in both phases. With respect to existing works, the novelty is the extension of the model for the coupled description of: (iii) the heat and mass transfer phenomena based on the resolution of the boundary layer, (iv) the thermodynamics at the interface based on cubic Equations of State, (v) the thermal effect of the suspending fiber, (vi) the phase-change process (evaporation, boiling and condensation), (vii) the radiative heat transfer and (viii) the combustion chemistry. In particular, phenomena from (iv) to (viii) are usually applied only to sphero-symmetric models, whereas applications to interface-resolved simulation are scarce. Among these, we indicate (v) and (viii) as the most innovative points of the present work;

2. The second point is the applicability and practical use of the code to model a wide range of real systems involving isolated droplets: microgravity droplets, evaporation in forced and natural convection, multicomponent droplets, suspended droplet combustion, showing a good agreement with experimental data. To the author's opinion, this specific objective was made possible by four factors:

    - The completeness of the model, which describes a large spectrum of physical phenomena. To accurately predict the droplet dynamics it is fundamental to

include these phenomena and study their mutual interaction (e.g. effect of the fiber on the flame quenching, effect of gravity on the flame geometry etc.);

- The adoption of the `OpenFOAM`® framework, which include: embedded discretization methods, flexible object-oriented programming, and the capability of managing complex unstructured polyhedral grids (including multiregion domains), fundamental for the application to real systems;

- The adoption of the `OpenSMOKE++` library, for the rapid and efficient calculation of the transport properties (density, viscosity, thermal conductivity, diffusion coefficients, fugacity etc.) in function of temperature, pressure and local composition, necessary to predict essential phenomena (e.g. buoyancy, droplet dilation, preferential diffusion, non-ideal thermodynamics). In addition, `OpenSMOKE++` significantly simplifies the management of large kinetic schemes for the gas-phase combustion;

- The relaxation of two very critical aspects in droplets vaporization modeling: *surface tension*, by the introduction of the suspending force field to suspend the droplet and avoid spurious currents, and the *advection-evaporation coupling*, by the introduction of an additional velocity field, free of the Stefan flow effect, to advect the interface (Paper 1). These modifications to have a very small impact on the model accuracy, but dramatically reduce the numerical effort required by the model. This comes at the price of a lower generality, making these assumptions suitable only for axisymmetric suspended droplets. Hence, the third point;

3. The third point is the implementation of an accurate methodology for modeling surface tension in small droplets and bubbles, based on a combination of Ghost Fluid Method (GFM) for the equations discretization and Height Functions for the curvature evaluation (Paper 4). This work has been carried out to (i) extend the current `OpenFOAM`® capability to simulate multiphase flows at small-scales (extremely limited at the moment), showing results comparable to the state of the art in literature, and (ii) to start abandoning the use of the suspending force field for the droplet stabilization. Not coincidentally, a significant part of Paper 4 focused on the implementation of a stable and consistent method for droplet suspension, which represents one of the objectives (and novelties) of this work.

Outlooks

This is a multidisciplinary work, touching different fields from thermodynamics, to transport phenomena to multiphase fluid dynamics and, hence, the possible applications and further improvements are numerous. Providing a long list of these would be unnecessary and dispersive, whereas it is better to concentrate on few significant, but reasonable goals:

- First of all, the coupling between the surface tension methodology and `DropletSMOKE++` is required. This would allow to model the vaporization of suspended droplets avoiding the use of the suspending force field and apply the code to different configurations (e.g. falling droplets). The extension of the surface tension methodology to variable fluid properties is relatively easy, but fundamental to study interesting phenomena (e.g. Marangoni effect). However, the coupling with the phase-change process (evaporation in particular) is probably the most challenging aspect, due to instabilities in the interface advection. Moreover, the presence of surface tension requires more stringent time step sizes, which significantly increases the computational effort. Possible solutions in this sense include specific algorithms for the implicit implementation of surface tension, but not very convincing methods exist so far. Further investigations are fundamental in this sense;

- A systematic study on multicomponent droplets would be very important. Among the different phenomena involving complex fuels, the most interesting is probably the preferential vaporization. It is well known that internal circulation plays a key role in triggering the preferential evaporation of the species and this work can be useful for the numerical investigation of this phenomenon. An ideal line of research would involve the construction of a "map" defining the necessary conditions to trigger preferential vaporization, in terms of internal circulation, external convection and fluid temperatures. This would be very beneficial for the development of reduced sub-models for multicomponent mass transfer in sprays;

- Since this work includes the possibility of modeling combustion, an analogous approach could be adopted to investigate the autoignition of isolated droplets in convective conditions (very close to what happens in a diesel engine). This would help defining the optimal autoignition conditions for a wide range of configurations. The drawback is that autoignition simulations require a low-temperature chemistry, which significantly increases the size of the kinetic mechanism. Efficient methods for reducing the computational cost of the chemistry step will be fundamental (e.g.

adaptive chemistry reduction), since it is (by far) the most consuming process in the simulation;

- Finally, we suggest the possibility to study interacting droplets. This kind of investigation necessarily requires an interface-resolved approach, like the one provided in this work. The vaporization and combustion of droplet arrays (groups of 3, 5 droplets) can be simulated to analyze the mutual interaction of the droplets, very similarly to what occurs in a spray system. This can be interesting in defining of the particle size distribution in a vaporizing spray, as well as to design the ideal configurations to maximize the collective vaporization rate.

Appendix A

Governing equations

The objective of this appendix is to derive the governing equations at the foundation of this research, highlighting the key assumptions and model approximations.

A.1 Conservation laws

The most important concept behind all the innumerable forms of transport equations is nothing but a mathematical translation of the logical assertion:

$$Accumulation = IN - OUT + FORM \tag{A.1}$$

which, applied to a specific *control volume* CV and written in mathematical terms for a generic variable Φ, becomes:

$$\int_V \frac{\partial \Phi}{\partial t} dV = -\int_S \Phi \mathbf{v} \cdot \mathbf{n} dS - \int_S \mathbf{D}(\Phi) \cdot \mathbf{n} \, dS + \int_V F(\Phi) dV \tag{A.2}$$

where the volume V and the external surface S are referred to the chosen CV. The physical interpretation is evident: the rate of change of a quantity Φ over V is given by the net *convective* $\Phi \mathbf{v} \cdot \mathbf{n}$ and *diffusive* $\mathbf{D}(\Phi) \cdot \mathbf{n}$ flux through S and the rate of Φ formation $F(\Phi)$ over V. Generally, Φ can represent every variable[1], which integrated over the volume V provides a *physical quantity* that is governed by a conservation law:

- **Density**, whose integration over V gives the *total mass*

$$\Phi = \rho$$

[1] The variable Φ can be either a scalar or a vector. In the latter case it will be indicated as $\mathbf{\Phi}$.

This leads to the *continuity equation.*

- **Species partial density**, whose integration over V gives the *total mass of that species*

$$\Phi = \rho_i$$

This leads to the *species equation.*

- **Specific energy**, whose integration over V gives *the total energy*

$$\Phi = \sum_{i=1}^{n_s} \rho_i \hat{E}_i$$

This leads to the *energy equation.*

- **Specific momentum**, whose integration over V gives *a momentum*[2]

$$\mathbf{\Phi} = \rho \mathbf{v}$$

This leads to the *momentum equation*, which anticipates the well known *Navier-Stokes equations.*

Before proceeding in the specific definition of each conservation law, it is better to write the surface integrals in Equation A.2 exploiting the divergence theorem (or Ostrogradskij, Gauss theorem), reported here for a *vector* variable $\mathbf{\Phi}$:

$$\int_S (\mathbf{\Phi} \cdot \mathbf{n})\, dS = \int_V (\nabla \cdot \mathbf{\Phi})\, dV \tag{A.3}$$

therefore:

$$\int_V \frac{\partial \Phi}{\partial t} dV = -\int_V \nabla \cdot (\Phi \mathbf{v})\ dV - \int_V \nabla \cdot \mathbf{D}(\Phi) dV + \int_V F(\Phi) dV \tag{A.4}$$

This must be valid *whatever* the chosen volume V, so Equation A.2 can be written in a *differential form* removing the volume integrals:

$$\frac{\partial \Phi}{\partial t} = -\nabla \cdot (\Phi \mathbf{v}) - \nabla \cdot \mathbf{D}(\Phi) + F(\Phi) \tag{A.5}$$

Equation A.5 is nothing but Equation A.2, just referred to a point instead of a volume.

[2]Momentum meant as *linear translational* momentum (mass $\times$ velocity) in $\left[kg\frac{m}{s}\right]$.

Continuity equation

As already shown before, it is sufficient to replace the generic quantity Φ with the density ρ.

$$\frac{\partial \rho}{\partial t} = -\nabla \cdot (\rho \mathbf{v}) - \nabla \cdot \mathbf{D}(\rho) + F(\rho) \tag{A.6}$$

The diffusion flux $\mathbf{D}(\rho)$ is a vector and it is usually written as $\mathbf{j}_i$ for a single species i. Here the diffusion term $\nabla \cdot \mathbf{D}(\rho)$ is global and represents the sum of *all* the diffusive fluxes of the species, which is null by definition [3]. The formation term $F(\rho)$ is null as well, since total mass cannot be produced. Thus we have:

$$\frac{\partial \rho}{\partial t} + \nabla \cdot (\rho \mathbf{v}) = 0 \tag{A.7}$$

Conservation of species

Replacing the general quantity Φ with the partial density (or massive concentration in $\frac{kg}{m^3}$) of the i_{th} species, ρ_i:

$$\frac{\partial \rho_i}{\partial t} = -\nabla \cdot (\rho_i \mathbf{v}) - \nabla \cdot \mathbf{D}(\rho_i) + F(\rho_i) \qquad\qquad i = 1...n_s \tag{A.8}$$

and the formation rate $F(\rho_i)$ of species i is defined as:

$$F(\rho_i) = R_i = \sum_{j=1}^{n_r} \Omega_j \nu_{ij} \tag{A.9}$$

where Ω_j is the mass rate of the j_{th} reaction and ν_{ij} the stoichiometric coefficient of species i in reaction j. n_r is the total number of reactions in the kinetic mechanism. Positive ν_{ij} provides the *production* of a generic species i, while negative ν_{ij} lead to its *destruction*. Their sum gives the net *formation* rate $F(\rho_i) = R_i$.
The density of species ρ_i can also be written as the product $\rho\omega_i$ and this leads [4] to:

[3] This condition is expressed by the fact that the sum of all the diffusive fluxes of the species present in the system must be zero:

$$\mathbf{D}(\rho) = \sum_{i=1}^{n_s} \mathbf{j}_i = \mathbf{0}$$

[4] It's interesting to notice that during the derivation the continuity equation has been used:

$$\frac{\partial \rho\omega_i}{\partial t} + \nabla \cdot (\rho\omega_i \mathbf{v}) = \omega_i \left(\frac{\partial \rho}{\partial t} + \nabla \cdot (\rho \mathbf{v}) \right) + \rho \left(\frac{\partial \omega_i}{\partial t} + \mathbf{v} \cdot \nabla \omega_i \right) = \rho \left(\frac{\partial \omega_i}{\partial t} + \mathbf{v} \cdot \nabla \omega_i \right)$$

$$\rho\left(\frac{\partial\omega_i}{\partial t}+\mathbf{v}\cdot\nabla\omega_i\right)=-\nabla\cdot\mathbf{j}_i+\sum_{j=1}^{n_r}\Omega_j\nu_{ij}\qquad i=1...n_s \tag{A.10}$$

Conservation of momentum

Substituting $\mathbf{\Phi}$ by the specific momentum $\rho\mathbf{v}$:

$$\frac{\partial(\rho\mathbf{v})}{\partial t}=-\nabla\cdot(\rho\mathbf{v}\otimes\mathbf{v})-\nabla\cdot\mathbf{D}(\rho\mathbf{v})+F(\rho\mathbf{v}) \tag{A.11}$$

where $\otimes$ indicates a *dyadic* product ($\mathbf{v}\otimes\mathbf{v}$ is a second order tensor).
It is easy to notice that a momentum balance is nothing but a balance of *forces*. Therefore the rate of change of momentum can be expressed as the sum of the forces acting on the point, which can be:

- **Surface forces**
  - Pressure, described by the tensor $\underline{\underline{\mathbf{p}}}$
  - Shear stresses, described by the tensor $\underline{\underline{\boldsymbol{\tau}}}$
- **Volume forces**
  - Gravity $\rho\mathbf{g}$
  - Electromagnetic, Coriolis, or general forces per unit of volume $\mathbf{f}$

Therefore:

$$\frac{\partial(\rho\mathbf{v})}{\partial t}=-\nabla\cdot(\rho\mathbf{v}\otimes\mathbf{v})-\nabla\cdot\underline{\underline{\boldsymbol{\sigma}}}+\rho\mathbf{g}+\mathbf{f} \tag{A.12}$$

where $\underline{\underline{\boldsymbol{\sigma}}}=\underline{\underline{\boldsymbol{\tau}}}+\underline{\underline{\mathbf{p}}}$ is the *stress tensor*, accounting for shear stresses $\underline{\underline{\boldsymbol{\tau}}}$ and pressure $\underline{\underline{p}}$. The pressure tensor is diagonal and isotropic with $p_x=p_y=p_z=p$, therefore its divergence is equal to the pressure gradient ∇p. The divergence of $\underline{\underline{\boldsymbol{\sigma}}}$ replaces the usual diffusion term, while the sum $(\rho\mathbf{g}+\mathbf{f})$ replaces the formation term F, assuming the more coherent meaning of *net external* applied *force*.
A further simplification (imposing other forces than gravity $\mathbf{f}=0$) can be made to obtain the final form:

$$\frac{\partial(\rho\mathbf{v})}{\partial t}+\nabla\cdot(\rho\mathbf{v}\otimes\mathbf{v})=-\nabla\cdot\underline{\underline{\boldsymbol{\tau}}}-\nabla p+\rho\mathbf{g} \tag{A.13}$$

Conservation of energy

This equation is in principle a general conservation of *all* types of energy; kinetic, potential and internal, whose sum has been called $\hat{E}_i$ for the species i:

$$\frac{\partial}{\partial t}\sum_{i=1}^{n_s}\rho_i\hat{E}_i = -\nabla\cdot\left(\mathbf{v}\sum_{i=1}^{n_s}\rho_i\hat{E}_i\right) - \nabla\cdot\mathbf{D}(\hat{E}_i) + F(\hat{E}_i) \tag{A.14}$$

where

$$\hat{E}_i = \hat{U}_i(T,P,\omega_i) + \hat{K}(\mathbf{v}_i) + \hat{Z}(z) \tag{A.15}$$

The formation term $F(\hat{E}_i)$ is null, since energy cannot be produced, but only transformed. It is possible to refer it as a volume power source, for instance an external heat supply $\dot{Q}$ or generic fields of forces $\mathbf{f}_i$ acting on the species providing work. The diffusion term $\mathbf{D}(\hat{E}_i)$ is the *conductive* vector $\mathbf{q}$. Writing the equation in a more specific way:

$$\frac{\partial}{\partial t}\sum_{i=1}^{n_s}\rho_i\hat{E}_i = -\nabla\cdot\left(\mathbf{v}\sum_{i=1}^{n_s}\rho_i\hat{E}_i\right) - \nabla\cdot\left(\mathbf{v}\cdot\underline{\underline{\boldsymbol{\sigma}}}\right) - \nabla\cdot\mathbf{q} + \dot{Q} \tag{A.16}$$

where $\nabla\cdot\left(\mathbf{v}\cdot\underline{\underline{\boldsymbol{\sigma}}}\right)$ describes friction effects of stresses $\underline{\underline{\boldsymbol{\sigma}}}$ through the dot product with $\mathbf{v}$. It is usually neglected. $\dot{Q}$ normally accounts for sparks, lasers or radiative heat.
This equation is definitely too general for our purposes and some assumptions have to be made in order to obtain something simpler [5]. All the details about the derivation can be found in specific textbooks:

$$\rho\hat{Cp}\frac{DT}{Dt} = \beta T\frac{Dp}{Dt} - \underline{\underline{\boldsymbol{\tau}}} : \nabla\mathbf{v} - \nabla\cdot\mathbf{q} - \nabla T\cdot\sum_{i=1}^{n_s}\mathbf{j}_i\hat{Cp}_i + \dot{Q} - \sum_{j=1}^{n_r}\Omega_j\Delta H_j^R \tag{A.17}$$

This equation is usually simplified to give:

$$\rho\hat{Cp}\frac{DT}{Dt} = \beta T\frac{Dp}{Dt} - \nabla\cdot\mathbf{q} - \nabla T\cdot\sum_{i=1}^{n_s}\mathbf{j}_i\hat{Cp}_i + \dot{Q} - \sum_{j=1}^{n_r}\Omega_j\Delta H_j^R \tag{A.18}$$

$\beta T\frac{Dp}{Dt}$ accounts for enthalpy effects caused by strong pressure variations, $\nabla T\cdot\sum_{i=1}^{n_s}\mathbf{j}_i\hat{Cp}_i$ describes the different enthalpy of diffusive fluxes [6], while the last term represents the

[5] The Lagrangian derivative $\frac{DT}{Dt} = \frac{\partial T}{\partial t} + \mathbf{v}\cdot\nabla T$ is introduced for brevity

[6] If the specific heat $\hat{Cp}_i$ is considered to be constant for all species i, the whole term is null, since $\nabla T\cdot\hat{C}_p\sum_{i=1}^{n_s}\mathbf{j}_i = \mathbf{0}$

net heat power locally released by the reactions.

A.2 Constitutive equations

The equations derived so far are actually not directly applicable, since they contain terms which are apparently not related to the unknown the equation is describing. These terms have been called *diffusive fluxes* and, in order for the equation to be solved, it is necessary to rewrite them as a function of the transported variables.

- $\nabla \cdot \mathbf{j}_i$ must be written in function of the mass fraction ω_i
- $\nabla \cdot \underline{\underline{\boldsymbol{\tau}}}$ must be written in function of the velocity $\mathbf{v}$
- $\nabla \cdot \mathbf{q}$ must be written in function of the temperature T

The relation [7] between a variable and its flux is generally called *constitutive equation.*

Material diffusion

In this sub-section the main models for the material diffusive fluxes are presented, from the most complex to the simplest one.

Stefan-Maxwell diffusion model

In this case the material flux is calculated with its very definition:

$$\mathbf{j}_i = \rho \omega_i \mathbf{v}_{i,d} \tag{A.19}$$

where the $\mathbf{v}_{i,d}$ is the diffusion velocity of species i. The sum $\mathbf{v}_{i,d} + \mathbf{v} = \mathbf{v}_i$ is the velocity of species i. This is calculated by solving the following system:

$$\nabla y_i = \sum_{k=1}^{n_s} \frac{y_i y_k}{\mathcal{D}_{ik}} (\mathbf{v}_{k,d} - \mathbf{v}_{i,d}) + (\omega_i - y_i) \frac{\nabla p}{p} + \frac{\rho}{p} \sum_{k=1}^{n_s} \omega_i \omega_k (f_i - f_k) \qquad i = 1, ..n_s \tag{A.20}$$

[7] Actually it is not necessary to write a diffusive flux in function of the *same* variable which the equation is describing. This is done here just for simplicity and because it is the most common approach, but in principle a diffusive term can be written in function of whatever variable, since mathematically it is only needed to close the system. However, physically this must be supported by experimental evidence and many phenomena have been observed and studied (thermophoresis, Dufour effect, Stefan-Maxwell model for diffusion coefficients etc.).

where $\mathcal{D}_{ik}$ is the binary diffusivity of species i in species k, y_i and ω_i are respectively the molar and the mass fraction of species i.
The system A.20 makes the material flux of species i to be a function of the gradients of *all* the species, not only of its own one. This is therefore the most general and complete model for diffusion fluxes, whose drawback lies in the high computational cost.

Fick's law

Concerning the material diffusive term, Fick's law provides a very simple relation between the mass fraction of a species and its flux, which allows to avoid the huge computational cost of Stefan-Maxwell approach:

$$\mathbf{j}_i = -\rho \mathcal{D}_i \nabla \omega_i \tag{A.21}$$

where $\mathcal{D}_i$ is the molecular diffusivity of species i in the mixture.
This constitutive equation cannot be used alone, because it does not satisfy the closure of diffusive material fluxes. An additional equation is needed to correct this behavior.
Diffusion velocities $\mathbf{v}_{i,d}$ can be recovered combining A.21 and A.19.

$$\mathbf{v}_{i,d} = -\frac{\mathcal{D}_i \nabla \omega_i}{\omega_i} \tag{A.22}$$

and corrected in order to close the sum of the diffusion fluxes. Equation A.21 is used in this work in function of the species *mole fraction*:

$$\mathbf{j}_i = -\rho \mathcal{D}_i \frac{M_{w,i}}{M_w} \nabla y_i \tag{A.23}$$

Thermal diffusion

Fourier's law

The expression for the thermal flux has a strong analogy with the Fick's law already described.

$$\mathbf{q} = -k \nabla T \tag{A.24}$$

where k is the thermal conductivity. This parameter is strongly dependent on temperature and on composition (especially when the mixture contains species with very different properties).
The term in Equation A.18 which accounts for the enthalpy of material diffusion fluxes

is sometimes written as a conductive flux as well, because of the dependence on ∇T, providing a *total* conductive flux $\mathbf{q}_T$:

$$\mathbf{q}_T = -\nabla T \left(k + \sum_{i=1}^{n_s} \mathbf{j}_i \hat{C} p_i \right) \tag{A.25}$$

Momentum diffusion

Newton's law

This is the most complex case because it is necessary to link the shear stress term $\underline{\underline{\boldsymbol{\tau}}}$, which is a *tensor*, with velocity $\mathbf{v}$, which is a *vector*. Let us start from a simpler case, in which only one component of the shear stress tensor is linked with a velocity component. This is possible through the *Newton's law*:

$$\tau_{yx} = -\mu \frac{\partial v_x}{\partial y} \tag{A.26}$$

where μ is the *dynamic viscosity*.

In a generic system all the tensor components have to be taken into account. The generalization of the Newton's law is:

$$\tau_{ij} = -\mu \left(\frac{\partial v_i}{\partial j} + \frac{\partial v_j}{\partial i} \right) + \left(\frac{2}{3}\mu - \zeta \right) \nabla \cdot \mathbf{v} \tag{A.27}$$

where ζ is called *dilatational viscosity*. This fluid property is often not considered: for gases is negligible compared to the dynamic viscosity, while for incompressible flows the whole second term is canceled.[8] It is possible to write the same equation in a tensorial form:

$$\underline{\underline{\boldsymbol{\tau}}} = -2\mu \underline{\underline{\mathbf{D}}} + \frac{2}{3}(\mu - \zeta)(\nabla \cdot \mathbf{v}) \underline{\underline{\mathbf{I}}} \tag{A.28}$$

where $\underline{\underline{\mathbf{D}}}$ is called *rate of strain tensor*, defined as:

$$\underline{\underline{\mathbf{D}}} = \frac{1}{2} \left[\nabla \mathbf{v} + (\nabla \mathbf{v})^T \right] \tag{A.29}$$

[8] The continuity equation 3.4 written for incompressible flows becomes:

$$\nabla \cdot \mathbf{v} = 0$$

A.3 Extension to multiphase systems

Within a one-fluid approximation the extension of the governing equation to multiphase systems is straightforward. The fluid properties (density, viscosity etc.) change discontinuously. Interfacial physics only exists at the interface and requires the introduction of a Dirac delta distribution $\delta\mathbf{n}$ to describe the singular nature of these terms. These are:

- Surface tension force $\mathbf{f}_s$

$$\mathbf{f}_s = \sigma\kappa\delta\mathbf{n} \tag{A.30}$$

  where κ is the interfacial curvature. This is to be applied to the momentum equation.

- Phase-change $\dot{m}$

  to be applied to the continuity equation (for the Stefan flow description) and to the temperature equation (for the interface cooling description).

The final version of the governing equations at the foundation on this research work are:

1. Interface transport (VOF methodology)

$$\frac{\partial\alpha}{\partial t} + \nabla\cdot(\mathbf{v}\alpha) = \frac{\dot{m}}{\rho} - \frac{\alpha}{\rho}\frac{D\rho}{Dt} \tag{A.31}$$

2. Continuity equation

$$\frac{1}{\rho}\frac{D\rho}{Dt} + \nabla\cdot\mathbf{v} = \dot{m}\left(\frac{1}{\rho_L} - \frac{1}{\rho_G}\right) \tag{A.32}$$

3. Species equation

$$\rho\frac{D\omega_i}{Dt} = -\nabla\cdot\mathbf{j}_i + \sum_{j=1}^{n_r}\Omega_j\nu_{ij} \tag{A.33}$$

4. Energy equation (without pressure term and with radiation)

$$\rho\hat{Cp}\frac{DT}{Dt} = -\nabla\cdot\mathbf{q}_T - \nabla\cdot\mathbf{q}_{rad} - \sum_{j=1}^{n_r}\Omega_j\Delta H_j^R + \sum_{i=1}^{n_{s,L}}\dot{m}_i\Delta h_{ev,i} \tag{A.34}$$

5. Momentum equation

$$\rho \frac{D\mathbf{v}}{Dt} = -\nabla \cdot \underline{\underline{\boldsymbol{\tau}}} - \nabla p + \rho \mathbf{g} + \sigma \kappa \delta \mathbf{n} \tag{A.35}$$

The evaporation flux expression is needed to close the model, as well as the Dirac delta discrete approximation:

- Monocomponent phase-change flux

$$\dot{m} = \frac{\mathbf{j}_i}{1 - \omega_i} \delta \mathbf{n} \tag{A.36}$$

- Multicomponent phase-change flux

$$\dot{m} = \frac{\sum_i^{N_{s,L}} \mathbf{j}_i}{1 - \sum_i^{N_{s,L}} \omega_i} \delta \mathbf{n} \tag{A.37}$$

$$\dot{m}_i = \mathbf{j}_i \delta \mathbf{n} + \dot{m} \omega_i \tag{A.38}$$

- Dirac delta

$$\delta \mathbf{n} = \nabla \alpha \tag{A.39}$$